The Dissertation Committee for Mahdy Shirdel
Certifies that this is the approved version of the following dissertation:

Development of a Coupled Wellbore-Reservoir Compositional Simulator for Damage Prediction and Remediation

Committee:

Kamy Sepehrnoori, Supervisor

Gary A. Pope

Kishore Mohanty

Mojdeh Delshad

Dale D. Erickson

Development of a Coupled Wellbore-Reservoir Compositional Simulator for Damage Prediction and Remediation

by

Mahdy Shirdel, B.M.E, M.S.E.

Dissertation

Presented to the Faculty of the Graduate School of
The University of Texas at Austin
in Partial Fulfillment
of the Requirements
for the Degree of

Doctor of Philosophy

The University of Texas at Austin
August 2013

To

my wife

Sahar

without her support none of this would be possible

Acknowledgments

I would like to express my sincere gratitude to my supervising professor, Dr. Kamy Sepehrnoori, for his continuous guidance, support, and encouragement. I have learned a lot from his profound insight, keen observations, and vast knowledge. I am privileged to have had an opportunity to work with him.

I appreciate the time, valuable comments, and feedback of my committee members, Dr. Gary A. Pope, Dr. Mojdeh Delshad, Dr. Kishore Mohanty, and Dr. Dale Erickson. Special thanks go to Dr. Chowdhury Mamun for review and comments in my dissertation.

I would like to acknowledge the staff of the Petroleum and Geosystems Engineering Department at The University of Texas at Austin, Dr. Roger Terzian, Michelle Mason, Joanna Castillo, Cheryl Kruzie, Frankie Hart, and Mary Pettengill for their technical and administrative support.

Special thanks to my friends Abolghasem (Abe) Kazeminia, Hamed Darabi and Saeedeh Mohebbinia for their indispensable help and knowledge sharing about PHREEQC, UTCOMP and Asphaltene phase behavior modeling, Victor Magri and Ali Abouei for their valuable technical discussions and help in providing the user's manual and technical guide for UTWELL. I also enjoyed technical discussions with Dr. Walter Fair, Dr. Abdoljalil Varavei, Dr. Mohammad H. Kalaei and Dr. Paulo Ribeiro.

I sincerely thank the financial support provided by Abu Dhabi National Oil Company and Reservoir Simulation JIP at the Center for Petroleum and Geosystem Engineering Department at The University of Texas at Austin.

August 2013

Abstract

Development of a Coupled Wellbore-Reservoir Compositional Simulator for Damage Prediction and Remediation

Mahdy Shirdel, Ph.D.
The University of Texas at Austin, 2013

Supervisor: Kamy Sepehrnoori

During the production and transportation of oil and gas, flow assurance issues may occur due to the solid deposits that are formed and carried by the flowing fluid. Solid deposition may cause serious damage and possible failure to production equipment in the flow lines. The major flow assurance problems that are faced in the fields are concerned with asphaltene, wax and scale deposition, as well as hydrate formations. Hydrates, wax and asphaltene deposition are mostly addressed in deep-water environments, where fluid flows through a long path with a wide range of pressure and temperature variations (Hydrates are generated at high pressure and low temperature conditions). In fact, a large change in the thermodynamic condition of the fluid yields phase instability and triggers solid deposit formations. In contrast, scales are formed in aqueous phase when some incompatible ions are mixed.

Among the different flow assurance issues in hydrocarbon reservoirs, asphaltenes are the most complicated one. In fact, the difference in the nature of these molecules with respect to other hydrocarbon components makes this distinction. Asphaltene molecules are the heaviest and the most polar compounds in the crude oils, being insoluble in light n-alkenes and readily soluble in aromatic solvents. Asphaltene is attached to similarly structured molecules, resins, to become stable in the crude oils. Changing the crude oil composition and increasing the light component fractions destabilize asphaltene molecules. For instance, in some field situations, CO_2 flooding for the purpose of enhanced oil recovery destabilizes asphaltene. Other potential parameters that promote asphaltene precipitation in the crude oil streams are significant pressure and temperature variation.

In fact, in such situations the entrainment of solid particulates in the flowing fluid and deposition on different zones of the flow line yields serious operational challenges and an overall decrease in production efficiency. The loss of productivity leads to a large number of costly remediation work during a well life cycle. In some cases up to \$5 Million per year is the estimated cost of removing the blockage plus the production losses during downtimes. Furthermore, some of the oil and gas fields may be left abandoned prematurely, because of the significance of the damage which may cause loss about \$100 Million.

In this dissertation, we developed a robust wellbore model which is coupled to our in-house developed compositional reservoir model (UTCOMP). The coupled wellbore/reservoir simulator can address flow restrictions in the wellbore as well as the near-wellbore area. This simulator can be a tool not only to diagnose the potential flow assurance problems in the developments of new fields, but also as a tool to study and design an optimum solution for the reservoir development with different types of flow

assurance problems. In addition, the predictive capability of this simulator can prescribe a production schedule for the wells that can never survive from flow assurance problems.

In our wellbore simulator, different numerical methods such as, semi-implicit, nearly implicit, and fully implicit schemes along with blackoil and Equation-of-State compositional models are considered. The Equation-of-State is used as state relations for updating the properties and the equilibrium calculation among all the phases (oil, gas, wax, asphaltene). To handle the aqueous phase reaction for possible scales formation in the wellbore a geochemical software package (PHREEQC) is coupled to our simulator as well.

The governing equations for the wellbore/reservoir model comprise mass conservation of each phase and each component, momentum conservation of liquid, and gas phase, energy conservation of mixture of fluids and fugacity equations between three phases and wax or asphaltene. The governing equations are solved using finite difference discretization methods.

Our simulation results show that scale deposition is mostly initiated from the bottom of the wellbore and near-wellbore where it can extend to the upper part of the well, asphaltene deposition can start in the middle of the well and the wax deposition begins in the colder part of the well near the wellhead. In addition, our simulation studies show that asphaltene deposition is significantly affected by CO_2 and the location of deposition is changed to the lower part of the well in the presence of CO_2.

Finally, we applied the developed model for the mechanical remediation and prevention procedures and our simulation results reveal that there is a possibility to reduce the asphaltene deposition in the wellbore by adjusting the well operation condition.

Table of Contents

List of Tables

List of Figures

Chapter 1: Introduction

In this chapter, we discuss the scope of this dissertation and the main objectives pursued and achieved in this research. In addition, we introduce the structure and the different chapters of the dissertation in the following sections.

1.1 DESCRIPTION OF THE PROBLEM

During oil production, multiphase flow commonly occurs in different sections of a flow-line such as the wellbore, the tubing, and the surface equipment. Despite vast research efforts in this area, the complexity of multiphase flow combined with other processes still remains a challenging problem. The detrimental effect of different flow assurance issues and of perturbation of flow fields by solid particle deposition has also added to the challenge of realistic wellbore modeling in reservoir simulators.

The major flow assurance problems faced in the fields concern asphaltene, wax, and scale deposition, as well as hydrate formation. Hydrate, wax and asphaltene deposition are mostly addressed in deep-water environments, where fluid flows through a long path with a wide range of pressure and temperature variations. In fact, a significant change in the thermodynamic condition of the fluid yields phase instability and solid deposit formation. In contrast, scales are formed in aqueous phase when incompatible ions are mixed.

New advancements in the enhanced oil recovery processes have been encountered to some of the described flow assurance issues as well. Recently, there are some field projects in the Middle East suggesting that the application of CO_2 for a miscible gas flooding can cause asphaltene precipitation issues in the wellbores and near wellbore, where the production system can become inefficient.

In fact, in such situations the entrainment of solid particulates in the flowing fluid and deposition on different zones of the flow line yields serious operational challenges and an overall decrease in production efficiency. The loss of productivity leads to a large number of costly remediation works during a well-life cycle. In some cases, up to $5 Million per year is the estimated cost of removing the blockage plus the production losses during downtimes. Furthermore, some of the oil and gas fields may be left abandoned prematurely, because of the significance of the damage which may cause loss of about $100 Million.

Therefore, in this dissertation we proposed the development of a robust coupled wellbore/reservoir model which can address these flow restrictions in the wellbore as well as in the near-wellbore area. As a matter of fact, this simulator can be a tool, not only to diagnose the potential flow assurance problems in the developments of new fields, but also to study and design an optimum solution for the reservoir development with different types of flow assurance problems. In addition, the predictive capability of this simulator can prescribe the best production schedule for the wells that can otherwise never overcome flow assurance problems.

To the best of our knowledge, there is no other simulator that can handle the flow assurance issues, including asphaltene, wax, and scale formation, in a unified framework with the flexibility to work in standalone mode or in conjunction with a reservoir simulator.

1.2 RESEARCH OBJECTIVES

A great deal of research has been conducted to study the phase behavior of asphaltene, the wax precipitation, the formation of geochemical scale, and the dynamic aspect of solid particle deposition in petroleum industry. However, development of a comprehensive and integrated model of the particle deposition in the wellbore and reservoir is lacking. The main objective of this dissertation is implementation of the particular flow assurance issues related to asphaltene, wax precipitation and deposition, as well as scale formation and deposition into a multiphase, multi-component wellbore simulator that can be coupled with compositional reservoir simulators (i.e. UTCOMP). This simulator, which we call UTWELL in this work, can predict the multiphase flow and the flow barriers in the entire system from reservoir up to the surface facilities. It can also evaluate the well performance in different production and injection scenarios.

The challenging problems that were solved during development of UTWELL simulator include:

- Multiphase flow in the wellbores and pipelines with a detailed analysis of the numerical performance of the models
- Development of a fully compositional wellbore model
- Phase behavior modeling of asphaltene and wax precipitation
- Implementation of a robust geochemical reaction module in the wellbore simulator
- Flocculation of solid particle and entrainment from reservoir to the wellbore
- Development of appropriate solid particle deposition models with transportation modules in the wellbore

In this dissertation, we discuss the formulations along with the modifications we adopted for UTWELL and the methodologies we used to integrate the modules together to develop a multi-purpose simulator.

1.3 BRIEF DESCRIPTION OF THE CHAPTERS

In Chapter 2, we review the literature on existing models for multiphase flow in wellbores, phase behavior of asphaltene, wax, and geochemical reactions of scales, and solid particle deposition. In Chapter 3, we discuss the formulation of multiphase flow models in UTWELL. We spend several sections to fully explain the details of this part, since we believe that these formulations have not been well-delivered in the petroleum literature. Chapter 4 introduces the thermal wellbore model with the details of well heat transfer interactions with its ambience. Wellbore heat transfer model is crucial for the energy equation and an accurate temperature modeling. In Chapter 5, different methodologies to solve the system of transport equations are presented and the validation of the model results against analytical solutions and other commercial software is discussed. Chapter 6 presents the phase behavior of asphaltene and wax and the reaction models for geochemical scales formation. Chapter 7 explains the detailed modeling approach for solid particle deposition, making distinctions among asphaltene, scale, and wax. In Chapter 8, we combine the particle deposition models with the multiphase transport equations to address the movement of particles in the flow line. Chapter 9 discusses the coupling methods between wellbore and reservoir models and the solution approach for the convergence of both domains. Chapter 10 explains the possible applications of UTWELL simulator for remediation processes. In Chapter 11, we present the summary of the dissertation and the concluding remarks and we recommend the tasks that can be accomplished for further developments in UTWELL.

Finally, in Appendix A we discuss the reservoir model (UTCOMP) and the well models, in Appendix B we explain Equation-of-State compositional models that are used for fluid property calculations, and in Appendix C we review additional fluid property calculation models using black oil approach. We also discuss the derivation of general balance equations and the basic assumption of the model development in Appendix D. We show the common unit conversion factors that were used in the code in Appendix E. Moreover, in Appendix F and G we explain the keywords in UTWEL and several sample input data that were used in our simulations, respectively.

Chapter 2: Background and Literature Review

In the following sections, we review the related papers for development of an integrated wellbore model, thermodynamics of asphaltene and wax precipitation, the chemical reactions of scales, and the dynamic aspect of solid deposition.

2.1 MULTIPHASE FLOW MODELING IN WELLBORES

Over the last few years, a number of numerical and analytical wellbore simulators have been developed for multiphase and single-phase flow in the wellbores. One of the simplest approaches to compute multiphase flow variables in the wellbore is using empirical correlations. This approach is based on experimental data obtained at a certain range of liquid and gas velocities. In the literature, there are different correlations for multiphase flow calculation. Dukler and Cleveland (1964) and Hagedorn and Brown (1965) are the most commonly employed correlations for oil wells. Orkiszewski's (1967) is the most common correlation for gas wells with gas/liquid ratio above 50,000 scf/bbl. Other researchers, such as Duns and Ros (1963), Eaton, et al. (1967), Beggs and Brill (1973), and Mukherjee and Brill (1983), have also introduced different experimental correlations for multiphase flow in vertical and inclined pipes. In most commercial reservoir simulators, these correlations are still used for calculating well flow performances. However, these correlations are fundamentally based on limited experimental conditions, which are necessarily not valid for all cases.

Another approach to model multiphase flow is using fundamental and mechanistic transport equations. Since transport equations are based on the conservation of mass, momentum, and energy, results obtained from these equations are more reliable and more predictable. Yuan and Zhou (2009) compared correlation-based and mechanistic models with experimental data. As is observed from their comparison, correlation-based models are valid only in a certain range of velocities. Mechanistic models however give acceptable results at a wide range of liquid and gas velocities.

Among the most well-known mechanistic models prevailing in the literature are as follows: Taitel and Dukler (1976) and Taitel, et al. (1980) pioneered mechanistic modeling by introducing different flow regimes and explaining criteria for the transition between the flow regimes. Subsequently, Ozon, et al. (1987), Hasan and Kabir (1988), Xiao, et al. (1990), Ansari, et al. (1994), Petalas and Aziz (2000), and Gomez, et al. (2000) presented the mechanistic modeling of two-phase flow in wellbores and pipes.

A simplified version of mechanistic model to calculate multiphase flow variables is the homogeneous model. In this model, the mixture of fluids is assumed to be flowing with no slippage between the phases and the average bulk flow properties are incorporated into a pseudo-fluid. The homogenous model is simple to implement, but inaccurate for high density and viscosity contrast fluids. For this reason, in order to improve the homogenous model, an auxiliary equation is applied to calculate the velocity difference between the moving phases. The homogenous model with slippage between the phases upgrades to the drift flux model, where the mixture velocity is related to the gas and liquid velocities by a correlation (Mishima and Ishii, 1984). Despite the fact that the drift flux model considers slippage between the phases by a correlation, it still suffers from the incorrect interphase momentum transfer between fluids in separated flows. Drift flux models are mostly desirable for dispersed flows, where one phase is continuous and the other phase is dispersed bubbles in the continuous phase. Extending drift flux models to separated flows, such as annular, and slug flow can be also possible with an appropriate definition of drift flux parameters (Hasan and Kabir, 2007, Shi et al. 2005).

Although drift flux models are not quite mechanistic for multiphase flow simulation, they have several advantages for use in reservoir simulations. In fact, drift flux models, unlike two-fluid models, are continuous, differentiable, and relatively fast to compute.

Two-fluid and multiple-fluid models, usually referred to as mechanistic models, are most comprehensive for multiphase flow simulations in wellbores. These models are based on separated flows for each phase, where the slippage between the phases is considered via interphase shear stresses. The interphase shear stress terms mainly contribute to drag forces between the fluids, which control the slippage of one phase over the other phase.

In the mechanistic models, defining the interphase momentum terms requires a set of closure relationship equations. These closure relationship equations are functions of different flow parameters, plus flow regimes and spatial distribution of the fluids in the flow. Since flow regime transition strongly affects the interphase momentum equations, different researchers have studied the details of flow-regime effect in mechanistic modeling for various flow conditions and flow trajectories.

Ansari et al. (1994) presented a comprehensive mechanistic model for upward two-phase flow in wellbores, which formulated the flow pattern detection as well as the magnitude of momentum transfer between the phases in different flow patterns. Ansari et al. (1994) evaluated their model against experimental and field data available in Tulsa University Fluid Flow Project (TUFFP) and showed good agreement between their model and the data.

Later Kaya et al. (1999) extended the mechanistic modeling of two-phase flow to deviated wells. They adopted the flow pattern models from Barnea (1987) and Taitel et al. (1980) for dispersed bubble flow, from Chokshi (1994) model with some modifications for churn and slug flow, and from Ansari et al. (1994) model for annular flow.

For the horizontal flow trajectory, several models have also been developed by different researchers. Taitel and Dukler (1976) proposed reliable flow map detection in horizontal wells/pipes by dividing the flow regimes into stratified and non-stratified. The main criterion for transition between stratified to non-stratified flow regimes is according to the Kelvin-Helmholtz stability. In addition, Taitel and Dukler (1976) considered intermittent, bubbly and annular flow regimes in their flow map as well.

Since the closure relationship equation in the momentum equations is based on different flow regimes, discontinuities in those equations are inevitable. Discontinuities in a model can cause convergence problems during simulation. Hence, to avoid that, especially in transient models, proper modifications are required to smooth the momentum equations. Details of the flow regimes transition are discussed in Chapter 3.

In addition to the discontinuity problem in two-fluid models, hyperbolic nature of the two-fluid model equation can also add to the deficiency of the model. In certain circumstances, two-fluid models can become ill-posed and consequently unstable. This problem, regardless of the numerical approach used for solving the equations, has been reported by many researchers in multiphase flow area, such as Lyczkowski et al. (1975), No and Kazimi (1981), Song and Ishii (2000), Dinh et al. (2003), and Liao et al. (2008) .

Hence, in two-fluid models, extra care is needed to avoid instability issues. Usually in the two-fluid models, some non-conservative terms are added to avoid imaginary eigenvalues (RELAP5 (2012); No and Kazimi (1981)). In Chapter 3, we will discuss this issue in details.

Compared to the simplified mechanistic approaches, such as homogenous and drift-flux models, two-fluid models are computationally more challenging and numerically unstable without appropriate modifications. Despite these challenges, two-fluid and even multi-fluid models have been used in many commercial pipeline and wellbore simulators due to the better accuracy and strong capabilities, compared to those of non-mechanistic models.

The multi-fluid approach has been applied in the commercial pipeline simulators OLGA (Bendikesen, et al., 1991), LedaFlow (Kongsberg Oil and Gas Technologies); and research simulators RELAP5 (2012) and CATHARE (Micaelli, 1987). Other researchers, in the likes of Stone et al., 1989, Winterfeld, 1989, Almehaideb et al., 1989, Pourafshary, 2007, and Pourafshary et al., 2009, have also developed transient two-fluid models for wellbore-reservoir simulation. In addition, some other researchers, Hasan and Kabir (1996, 1997) and Livescu et al. (2009) have also developed homogenous or drift flux models for wellbore-reservoir simulation with the capability to capture flow variables with reasonable accuracies.

Bendiksen et al. (1991) presented a standalone, extended two-fluid model, OLGA, with a pseudo-compositional approach for fluid properties calculation. Separated mass balance for gas, bulk liquid and liquid droplets, three momentum equations for the continuous bulk fluids and liquid droplet, and one energy equation for the mixture of fluid were solved. The steady-state pressure drop, liquid holdup phase velocities, and temperature were obtained from the equations. Different flow regimes, such as stratified and annular mist (considered as a separated flow), bubbly flow and slug flow (considered as distributed flows) were included in the calculation. Bendiksen et al. (1991) compared their model with SINTEF experimental data and showed good agreement between the model and the experimental data.

Stone et al. (1989) presented a fully implicit, blackoil, three-dimensional reservoir simulator coupled to a blackoil and one-dimensional wellbore simulator. They mainly targeted a horizontal well for wellbore-reservoir system in their study. They also used a two-fluid model considering different flow regimes for the wellbore model. Stone et al. (1989) solved oil, water and gas mass balance, liquid/gas momentum balance energy equation simultaneously with reservoir equations in their model. They also considered parallel flow in the inner tubing and outer annuli and slant angle effect. Stone et al. (1989) validated their model against field data and showed a good agreement between their model results and field data. Stone et al. (1989) also discussed the stability of their model. They showed that in the high velocity condition, where bubbly and slug flows were generated, their model was less stable.

Winterfeld (1989) explained the application of a wellbore-reservoir simulator for pressure build-up tests. In his study, a transient, isothermal wellbore model was fully coupled to a blackoil, two-dimensional (r-z) reservoir simulator. The wellbore mechanistic model was a two-fluid model with some simplifications in interphase closure relations. Winterfeld (1989) showed good agreement between model results and field data for bottom-hole pressure build-up test.

Almehaideb et al. (1989) presented an isothermal, blackoil wellbore model coupled to a blackoil reservoir simulator. In their study, the effect of phase segregation in the wellbore during concurrent water and gas injection and the effect of multiphase flow in a pressure build-up test were investigated. They explained that the two-fluid model as well as a mixture momentum equation could be used for the wellbore model. Almehaideb et al. (1989) solved oil, water, and gas mass balance equations and liquid/gas momentum balance equations simultaneously with reservoir equations. They calculated liquid and gas superficial velocities, wellbore pressure, free gas mass fraction and water mass fraction as the primary variables in their wellbore model. Almehaideb et al. (189) showed how gas and water injection rate and gas quality vary in different layers of a reservoir in a lab-scale test. They validated their model with some limited data points from experimental results. They also illustrated the gas solubility effect on pressure build-up and compared two-fluid model and mixture model results for a pressure build-up test.

Recently, more comprehensive compositional wellbore-reservoir models have been introduced by different researchers. Pourafshary (2007) and Pourafshary et al. (2009) developed a thermal, blackoil wellbore simulator to model transient fluid flow and a thermal, compositional wellbore simulator to model semi-steady state flow. The model was applied for vertical wells and was explicitly coupled to a compositional reservoir simulator, General Purpose Adaptive Simulator (GPAS) (Wang et al., 1999; Han et al., 2007). Pourafshary (2007) applied the coupled wellbore-reservoir simulator for a pressure build-up test and showed the back flow, the after-flow phenomenon, and the phase segregation in the wellbore. He also compared his model with field data and showed good agreement.

Pourafshary et al. (2009) presented the development of thermal compositional coupled wellbore-reservoir simulator. They performed simulation on producing well with different case studies for crude oil, condensate gas, and volatile oil. He demonstrated that the blackoil approach was not accurate for representation of condensate and volatile oil flows in the wellbore.

Hasan and Kabir (1996), and Hasan et al. (1997; 1998) presented a blackoil model for single and two-phase flow in wellbores coupled to the reservoir. They applied a hybrid numerical model for the wellbore and an analytical single-phase model for the reservoir. Material balances for each phase, one momentum balance equation for the mixture, and energy balance were solved to obtain pressure, velocity, temperature, and fluid density in the wellbore. To calculate the liquid fraction (holdup) at each segment of the wellbore, Hasan et al. (1998) tracked the migration of gas bubbles throughout the wellbore. They used the wellbore-reservoir model for well test analysis application.

Livescu et al. (2009) developed a fully-coupled thermal compositional wellbore model. Mass conservation for each component, momentum conservation, and energy equation for the mixture of the fluids were solved to obtain pressure, temperature, and holdup profiles in the complete flow line. They used the drift-flux model to consider the slippage between the phases. In their study, different cases for thermal process and different well geometries were presented.

2.2 ASPHALTENE AND WAX PRECIPITATION

Asphaltene and wax precipitation in the tubing and surface facilities are the most common flow assurance issues during the production of hydrocarbon reservoirs. Applications of CO_2 and light hydrocarbon gas injection have also introduced additional issues to the asphaltene formation in the reservoirs (Tuttle, 1983). In fact, the presence of light components in the crude oil enhances destabilization of asphaltene. Thus, asphaltene precipitation is commonly observed not only in heavy oil reservoirs, but also in conventional oil reservoirs.

Several researchers have investigated the parameters affecting asphaltene precipitation and deposition in the production system. Heavy component content in the crude oil is the main factor for the precipitation and deposition of asphaltene in the reservoir and wellbore. However, saturate components fraction (Carbognani, et al. 1999) and resin concentration in the crude oil (Lichaa, 1977 and Hammami, et al. 1998) also influence asphaltene precipitation. Pressure and temperature variation also affect the amount of asphaltene precipitation, decreasing the fluid pressure until bubble point pressure increases asphaltene precipitation. However, decreasing the pressure to below the bubble point pressure decreases asphaltene precipitation. In fact, pressure reduction causes more expansion in the relative volume fraction of the light components with respect to heavy components. This behavior is similar to that of adding light hydrocarbon fraction in the fluid which destabilizes asphaltene. In contrast, below bubble point pressure, the stability of asphaltene in the fluid is increased. Decreasing pressure to below bubble point, light components are evaporated and the remaining fluid becomes more asphaltene soluble (Haskett and Tertera, 1965). The temperature effect on asphaltene formation is not well understood thus far. Some researchers suggest that increasing temperature enhances asphaltene precipitation. However, asphaltene precipitation decreases in a two-phase condition by increasing temperature, since light components are evaporated and asphaltene solubility increases in the remaining fluid.

Compared to asphaltene precipitation, the wax problem more than likely occurs in low temperatures where long chain of alkanes and cycloalkanes are crystallized. In the upper part of the tubing system or in offshore pipelines and wells in the sea beds where the temperature is drastically lowered, wax precipitation is facilitated. In addition, wax precipitation can be combined with asphalatene precipitation in some circumstances. In contrast to asphaltene, wax molecules are non-polar and the solubility of these components changes differently with fluid composition.

For asphaltene precipitation, most of the models are based on the classical Flory Huggins polymer solution theory. Leontaritis and Mansoori (1987) proposed a colloidal model, which assumed asphaltene particles were suspended solids in crude oil.

Chung (1992) and Nghiem et al. (1993) also used cubic Equation-of-State approach combined with solid model for asphaltene precipitation. In this method, asphaltene solid phase is the single component which reaches to equilibrium condition with the components in the liquid and vapor phases. The thermodynamic properties of the asphaltene phase are attributed to the pure single component of the heavyset component of the hydrocarbon mixture which is assigned as the asphatlene component in the characterized fluid.

Victorov and Firoozabadi (1996) discussed the micellization of asphaltene and proposed thermodynamic micellization models for asphaltene precipitation. Micellization model assumes that asphaltene molecules form a micellar core and the resin molecules are absorbed on the surface of this core for micelle stabilization. Gibbs free energy minimization principle is used for determining the structure and concentration of the micelle.

Recently, new equations of state have been developed to deal with asymmetric mixtures (i.e., mixtures containing molecules with large size differences) and associating molecules such as polar components. Chapman et al. (1990) developed a new Equation-of-State based on Statistical Associating Fluid Theory (SAFT). Later Gross and Sadowski (2001) modified SAFT Equation-of-State to Perturbed-Chain SAFT Equation-of-State (PC-SAFT EOS). PC-SAFT and SAFT EOS have shown promising results in modeling the phase equilibrium of systems containing heavy hydrocarbons such as asphaltene (Gonzalez et al., 2005; Gonzalez et al., 2007). Since these Equations-of-State consider the interaction of the molecules correctly, they have better prediction potential for asphaltene precipitation.

Kontogeorgis et al. (1996) also developed another Equation-of-State for asphaltic systems introducing Cubic Plus Association Equation-of-State (CPA EOS). This model was originally developed for multiphase equilibrium of systems containing associating fluids. CPA EOS is a combination of a simple cubic Equation-of-State (e.g. Peng-Robinson or Soave-Redlich-Kwong) with an association term similar to the one used in SAFT EOS.

Although PC-SAFT and CPA EOSs predict more accurate results for asphatlene precipitation than cubic EOSs, they are computationally more expensive and challenging than cubic EOSs are.

Other hydrocarbon components that can cause flow assurance issues are wax-forming components. In comparison to asphaltene, the thermodynamics of wax precipitation is better understood in the literature. In fact, the nature of wax phase is different from paraffinic components of the oil. Wax forming components can crystallize and precipitate in cool temperature. Since the paraffinic components are not associated to other components via polar sites, their phase behavior can be modeled by less sophisticated Equation-of-State models.

For wax precipitation modeling, different approaches such as the multi-solid model (Lira-Galeana, et al. 1996), ideal solid solution model (Erickson, et al. 1993, Pedersen, et al. 1991), non-ideal solid solution models (Won 1986) are available in the literature. The most realistic method used in the literature is Won's (1986) model, which considers non-ideal solutions for liquid and solid. However, since a large number of parameters are involved in this model, a simplified or a modified version of it is applied in the simulations of wax precipitation. For instance, the Computer Modeling Group (CMG) PVT simulator uses a modified version of Won's (1986) model, by introducing an equation for fugacity of components in the solid phase.

A number of researchers have also studied asphaltene and wax deposition in porous media and have developed numerical reservoir simulators to study these processes in the reservoir scale. Nghiem et al. (1993) developed the EOS compositional reservoir simulator in CMG software; Qin et al. (2001) developed the explicit asphaltene model in the EOS compositional reservoir simulator UTCOMP and Fazelipour (2007) developed a fully implicit EOS compositional model for asphaltene precipitation in the reservoir.

2.3 GEOCHEMICAL SCALE FORMATION

Another flow assurance issue that is investigated in this dissertation concerns with geochemical scales generation and deposition in the wellbore. In contrast to wax and asphaltene, this flow assurance is related to the aqueous phase and the active ions that can react in this phase. Geochemical scale deposition is initiated from reservoir or in the junctions that incompatible ions are comingled.

In fact, after drilling and producing the wells, the equilibrium state between the fluids' compositions will change, and in response to this, the process of scaling may begin. Thermodynamics and kinetics of the dissolved molecules and ions govern the formation of a specific type of scale. The geology (mineralogy) of the formation and the composition of the in-situ fluids as well could be of importance to these processes. The typical mineral scales found in the oilfield can be classified under two major generic families: carbonates or sulfates. However, there are other complex salts of iron such as the sulfide, oxides, and carbonates that can pose similar or even more difficult challenges when removing or inhibiting scaling.

Once the scaling process is initiated in the wellbore and near-wellbore, an array of problems emerges, such as plugging the tubular and the pore spaces inside the formation. The scale buildup in the formation contributes significantly to the total skin value by restricting the flow channels (paths) in the formation as well as increasing the pressure drop in the near-wellbore area.

Most of the published articles in the field of geochemical scales formation have focused primarily on understanding the main drivers of the scaling process as well as testing and analyzing chemicals used for remedial/inhibition jobs to mitigate the serious impact of these depositions. For instance, Crabtree et al. (1999) and Ramastad et al. (2004) have discussed the mechanism for crystallization and nucleation growth of scales.

In addition, Nancollas et al. (1979) and Sorbie and Laing (2004) proposed the mechanisms for crystal growth inhibitors.

However, in recent years several researchers have paid attention to the modeling of geochemical reactions in porous media. Rocha et al. (2001) developed a geochemical model with the necessary transport equations to accurately simulate the flow and diffusion of ions, but only for single-phase flow.

Bedrikovsestky et al. (2003) presented the mathematical and laboratory modeling of oilfield scaling of Barium Sulfate. They presented the effect of porous media on the $BaSO_4$ scaling kinetics and showed that the kinetics rate constant of $BaSO_4$ is proportional to flow velocity.

Delshad and Pope (2003) have also simulated the precipitation of Barium Sulfate with an equilibrium model and focused their study on the effect of seawater desulfurization and sulfate deposition using a University of Texas in house simulator (UTCHEM). In this study, they also presented the effect of dispersion on the distribution of the solid precipitates in the reservoir during the injection of incompatible water into the reservoir.

Moreover, Tomson et al. (2009) also discussed the effect of kinetics and the thermodynamic equilibrium model on scale formation in the reservoirs and pipelines. They concluded that since the thermodynamic models are far more reliable than the kinetics model, for the correct prediction of geochemical scales precipitation, reliable models for kinetics are required.

2.4 ASPHALTENE AND SCALE DEPOSITION MODELS IN WELLBORES

After precipitation of the solid particle in the continuous phase, the deposition process starts. In some occasions solid particles are very small at the beginning of precipitation and with time elapsing they aggregate and become larger. This process, which is called aggregation process, can be a step between precipitation and deposition or at the same time of precipitation. Once aggregation occurs, the solid particles become larger and the deposition process is expedited due to the larger momentum of solid particles.

For modeling the deposition of solid particle in the wellbore and near-wellbore, appropriate approaches should be applied. Since the flow regime in the reservoir may change from laminar to turbulent in the wellbore, separate deposition models are necessary for each domain. Ali and Islam (1998) and Wang and Civan (2001) have proposed deposition models in porous media; these consider the adsorbed and plugged portion of particles. However, several other researchers have proposed particle fouling models in the pipe for turbulent and laminar flows. In this study, we mainly focus on the deposition models in the wellbore.

The particle fouling models are categorized into two main approaches: i) classical concept of turbulent flow and eddy diffusion (Lin et al., 1953; Friedlander and Johnstone, 1957; Beal, 1970; Davis, 1983; Escobedo and Mansoori, 1995); ii) stochastic approach, such as those based on random-walk (Hutchinson et al., 1971; Cleaver and Yates, 1975).

Lin et al. (1953) were the first to demonstrate a thorough classical approach of mass transfer between a turbulent fluid stream and the wall. They offered an analogy with momentum transfer in the turbulent flow to derive the mass transfer of particles. In fact, Lin et al. (1953) used von Karman's (1935) analysis for the velocity and eddy viscosity distribution in three different flow regions. They introduced the mass transfer equation by incorporating the same eddy viscosity distributions found by von Karman (1935). Lin et al. (1953) mostly addressed the diffusion mechanism for small particles (< 0.1 micron) and calculated the concentration profile in the wall layer and buffer zone. They compared their model deposition rate results with experimental data for turbulent gas stream and showed fairly good agreement. Other researchers, who applied the classical approach, followed a similar method as Lin et al. (1953) with some modifications.

In contrast to previous researchers, Cleaver and Yates (1975) and Hutchinson et al. (1971) followed a different route, applying a probabilistic theory, to develop the particle deposition model. They implemented a simple mechanistic model, disregarding the classical flow regions and the boundary conditions, in their calculation.

Recently, Eskin et al. (2011) also discussed the detailed analysis of asphaltene particle deposition in the turbulent flow streams with a similar approach for particulate fouling models. Eskin et al. (2011) showed a theoretical model and experimental results, performed in a Couette device, for asphaltene deposition. In addition, they further developed a model for asphaltene particle size distribution and the mechanism of particles transport from fluid bulk to the pipe surface in their model.

Moreover, Ramirez-Jaramillo et al. (2005) proposed a multiphase, multi-component wellbore model to predict asphaltene deposition in standalone wells. They also discussed an asphaltene deposition model along with the effect of asphaltene particle on the rheology of the flowing fluid. Ramirez-Jaramillo et al. (2005) used asphaltene deposition models similar to wax deposition. Vargas (2009) also developed a simulation tool that predicts the asphaltene precipitation and deposition in the pipelines. In this model, a single-phase model was developed that accounts for the kinetics of asphaltene deposition, precipitation, and aggregation. Vargas (2009) showed fairly good agreement of their simulation results with test tube experimental data

2.5 WAX DEPOSITION MODELS IN WELLBORES

Due to different molecular structure of wax components and the crystallization of wax phase in the flow lines, the mechanism of wax deposition is slightly different from asphaltene and scale. Wax deposition models, likewise the wax precipitation models, have been extensively studied for the past few decades and many researchers have proposed different correlations for wax deposition and have incorporated the models into multiphase flow simulation for the wellbores.

Brown et al. (1993) developed a thermodynamic model for wax precipitation and a kinetic model for deposition of wax and rate of wax buildup in single-phase flow simulation. In the deposition model, Brown et al. (1993) considered shear and molecular diffusion mechanisms as the main deposition mechanisms. They also compared their model against experimental data and showed reasonable agreement between the prediction model and the experimental data, after tuning the model.

In the same fashion, Rygg et al. (1998) also developed a multiphase flow wax deposition model, which predicts wax deposition in wells and pipelines during turbulent flow regimes. Rygg et al.'s (1998) deposition in the model is also based on molecular diffusion and shear dispersion.

Singh et al. (2000) launched a fundamental study of wax deposition by including aging process in the deposition models. They presented a model system of wax and oil mixture to understand the ageing process of the wax-oil gels which hardens the wax deposit with time. They showed that the rate of aging process depends on the oil flow rate and the wall temperature.

Matzain (2001) proposed a similar mechanism for wax deposition; however, he extended the model to multiphase flow. He incorporated the flow regime effects on heat and mass transfer in wax deposition models. He also performed laboratory experiments for wax deposition in a flow loop, choosing two test fluids as waxy crude oil from South Pelto field in Gulf of Mexico and natural gas supplied by Oklahoma Natural Gas Co. He showed that the proposed models have good agreement with the experimental results.

Moreover, Hernandez et al. (2004) developed paraffin deposition model under single-phase flow condition with consideration of shear stripping, deposit ageing, flow regimes, temperature gradient, and fluid properties. They proposed a new deposition model that incorporates the kinetic resistance effect which avoids the equilibrium assumption for wax concentration in the interface of wax deposit.

Chapter 3: Multiphase Flow Models in the Wellbores and Pipelines

The fluid flow model for wellbore is well established for single-phase flow with limited applications in gas reservoirs or gas pipelines. Introducing the second phase as a concurrent or counter-current gas/liquid flow leads to flow models computationally more challenging and time consuming. At many of the flow conditions in the hydrocarbon reservoirs, we have multiphase flow and thus application of single-phase flow might be very inaccurate.

In this chapter, we introduce mechanistic models for single-phase and multiphase flow models for wellbore with all the details of transport equations. We explain the governing transport equations, numerical stability of the models, and flow regime detections in multiphase flow, constitutive relations, phasic wall momentum interactions, interphase mass transfer and state relations. Although these items have been discussed in many papers and research reports, we believe putting these sections together will be useful for the upcoming chapters and will ease understanding of multiphase flow in wellbores and pipes for more complex fluids.

3.1 SINGLE PHASE FLOW EQUATIONS

Single-phase flow can occur in the gas production wells, water injection wells, or superheated steam injection wells at certain conditions where condensation or evaporation of the continuous phase has not occurred. Although single-phase flow in the entire system may not be maintained, formulation of single-phase models can be useful for our development purposes and further extensions to multiphase flow codes. In addition, single-phase models can be used for multiphase flow simulations with some precautions, if the mixture of the phases can be assumed homogenous. UTWELL is capable of using single-phase model for injection wells and production wells. Usually this module is applied to well test analysis for single-phase pressure drawdown and build-up tests.

The governing equations in single-phase flow model consist of one mass conservation equation and one momentum conservation equation. In Appendix D derivation of general balance equations for single-phase flow are discussed in detail. However, incorporating the basic assumption for one-dimensional models and neglecting the turbulence effect, the balance equations in single-phase flow becomes

$$\frac{\partial \rho}{\partial t} + \frac{1}{A}\frac{\partial A\rho u}{\partial x} = \dot{\psi}, \tag{3.1}$$

$$\frac{\partial \rho u}{\partial t} + \frac{\partial \rho u^2}{\partial x} + \left(144.0 g_c\right)\frac{\partial P}{\partial x} + \rho g sin\theta + \frac{\tau \pi D}{A} = 0, \tag{3.2}$$

where ρ is the density of the fluid, u is the actual velocity, P is the pressure, τ is the wall shear stress, D is the diameter of the pipe, A is the cross section of the pipe, $\dot{\psi}$ is the source/sink term in mass influx, and $\left(144.0 g_c\right)$ is the field unit conversion factor. To obtain the flow variable, these equations are solved along with appropriate wall-phase shear friction equations and state relations presented in Sections 3.7 and 3.9.

3.2 MULTIPHASE FLOW EQUATIONS

Multiphase flow can occur in many occasions during oil production and transportation in hydrocarbon reservoirs. In the past few decades, development of robust multiphase flow models for hydrocarbon transportation has been aggressively expanded by many researchers and commercial developers in the petroleum industry. Accurate modeling of multiphase flow in the wells can be advantageous not only for production optimization but also for flow line designs.

Although multiphase flow models can yield better approximation of the flow variables, the complexity of the models has added some restrictions to full applications of these models. For instance, most of the multiphase flow models for the wellbores have been developed in 1D along the well trajectory and cross-sectional average schemes have been used to represent the fluids in the flow line. In fact, a full 3D model for the wellbore can be very computationally time-consuming and inefficient for a set of simulation studies. Hence, for development purposes of multiphase flow in the wellbore, we need to make some assumptions listed as follows:

- One-dimensional flow is assumed along the trajectory of the well in horizontal, deviated, and vertical inclinations. This assumption is reasonable for the wellbores and pipelines with small diameter. Considering a long well in the order of 1000 ft with a small diameter in the order of 1 ft, one-dimensional assumption for the flow path is reasonable.
- Eulerian time and spatial averaging are applied (Appendix D).
- The liquid phase consists of oil/water mixture. In case water exists in the flow, liquid properties are calculated by volumetric and mass averaging between water and oil. This assumption is valid when the slippage between oil and water is negligible. For the cases that oil viscosity is not very large no slip assumption is reasonable for the liquid mixture. However, for heavy oil systems the oil/water slippage should be considered.
- For the three-phase flow cases, oil and water slippage is included using a drift-flux correlation for the liquid mixture.
- In addition to source or sink mass flow rate, another term is also considered which is calculated by well indices values for each phase.

- Interface shear force, wall shear force, and spatial geometry of flow are modified for different flow regimes. A smooth transition is required for drag force changes in the momentum equations.
- Both gas and liquid phases have identical pressure and temperature. This is a reasonable assumption in many cases. In the cases that gas flow rate is not much larger than liquid, and gas expansion effect is not significant, temperature and pressure of different phases are approximately the same.
- Local thermodynamic equilibrium is considered between the phases. Compositional and blackoil approaches are applied to calculate the fluid properties and state relations. If appropriate gridblock and time step sizes are assumed in order for the hydrocarbon components and the aqueous phase components to remain in the gridblock the equilibrium assumption is reasonable. In fact, this assumption is reasonable as long as gas and liquid slippage effect is not very large.

In the following sections, we discuss the transport equations in detail and emphasize on the assumptions that we applied to our modeling approach. In Appendix D, we also discuss the detail of derivation of general balance equations for multiphase flow models and present the inclusion of the assumptions in our models.

3.2.1 Mass Conservation Equations

Since oil and gas phases are a mixture of hydrocarbon components, we derive our mass conservation equations from mass conservation of hydrocarbon components. Afterward, we can sum up the mass conservation of components in each hydrocarbon phase to obtain the mass conservation of hydrocarbon phases.

Assuming, *k* to be the hydrocarbon component in the gas and oil phase, the mass conservation of component *k* becomes

$$\frac{\partial\left(\hat{\rho}_o\alpha_o x_k+\hat{\rho}_g\alpha_g y_k\right)}{\partial t}+\frac{1}{A}\frac{\partial\left(A\hat{\rho}_o\alpha_o u_o x_k+A\hat{\rho}_g\alpha_g u_g y_k\right)}{\partial x}=\dot{\hat{\psi}}_{ok}+\dot{\hat{\psi}}_{gk},\ k = 1,\ \ldots,\ nc \qquad (3.3)$$

$\hat{\rho}_o$ and $\hat{\rho}_g$ are the molar density of oil and gas phases, α_o and α_g are the volume fractions of oil and gas, x_k and y_k are the compositions of component *k* in the oil and gas phases, u_o and u_g are the phases actual velocities and $\dot{\hat{\psi}}_{ok}$ and $\dot{\hat{\psi}}_{gk}$ are the molar influxes of component *k* in oil and gas phases . If we integrate Equation (3.3) over all components, we obtain the total mass conservation of the hydrocarbon fluids as follows:

$$\frac{\partial \sum_{k=1}^{nc}\left(\hat{\rho}_o\alpha_o x_k+\hat{\rho}_g\alpha_g y_k\right)}{\partial t}+\frac{1}{A}\frac{\partial \sum_{k=1}^{nc} A\left(\hat{\rho}_o\alpha_o u_o x_k+\hat{\rho}_g\alpha_g u_g y_k\right)}{\partial x}=\sum_{k=1}^{nc}\dot{\hat{\psi}}_{ok}+\dot{\hat{\psi}}_{gk}, \qquad (3.4)$$

$$\frac{\partial\left(\hat{\rho}_o\alpha_o+\hat{\rho}_g\alpha_g\right)}{\partial t}+\frac{1}{A}\frac{\partial\left(A\hat{\rho}_o\alpha_o u_o+A\hat{\rho}_g\alpha_g u_g\right)}{\partial x}=\dot{\hat{\psi}}_o+\dot{\hat{\psi}}_g. \qquad (3.5)$$

If we split Equation (3.5) into oil and gas phases, we will obtain

$$\frac{\partial\left(\rho_o\alpha_o\right)}{\partial t}+\frac{1}{A}\frac{\partial\left(A\rho_o\alpha_o u_o\right)}{\partial x}=\dot{\psi}_o-\mathit{\Gamma}_g, \qquad (3.7)$$

$$\frac{\partial\left(\rho_g\alpha_g\right)}{\partial t}+\frac{1}{A}\frac{\partial\left(A\rho_g\alpha_g u_g\right)}{\partial x}=\dot{\psi}_g+\mathit{\Gamma}_g, \qquad (3.8)$$

where $\mathit{\Gamma}_g$ is the interphase mass transfer term between oil and gas, $\dot{\psi}_o$ and $\dot{\psi}_g$ are oil and gas mass influx terms and ρ_o and ρ_g are oil and gas mass density. As can be seen, Equation (3.3) can be converted to Equations (3.7) and (3.8) by reducing the component based mass conservation equation to the phase based mass conservation equation. Along with an appropriate definition of interphase mass transfer term, Equations (3.7) and (3.8) can decrease the number of primary unknowns in our system of equations. This approach may lead to faster simulation run time as well as to application of the state relations, using either black oil or compositional phase property calculations, in a unified format.

The other mass conservation we can consider in our system of equations includes the water phase. Similar to Equation (3.8), for water phase we have

$$\frac{\partial(\rho_W \alpha_W)}{\partial t} + \frac{1}{A}\frac{\partial(A\rho_W \alpha_W u_W)}{\partial x} = \dot{\psi}_W . \tag{3.9}$$

α_W is the water volume fraction, u_W is the water velocity, and $\dot{\psi}_w$ is the mass influx term which is calculated from productivity indices of reservoir and wellbore. This term is discussed in detail in Chapter 9.

3.2.2 Momentum Conservation Equation with Homogenous Approach

One of the simplest approaches to calculate the velocity of phases in the multiphase flow model is using momentum equation for the mixture of fluids. In this method, we assume the entire fluid moving with the same velocity, no slippage and the momentum interactions exerted to the bulk of fluid

$$u_g = u_o = u_W = u_m . \tag{3.10}$$

Hence, in a homogenous model, we combine the mixture properties and solve the momentum equation for the bulk of the fluid to obtain u_m.

$$\frac{\partial\left(\rho_m u_m\right)}{\partial t}+\frac{\partial\left(\rho_m u_m^2\right)}{\partial x}+\left(144.0 g_c\right)\frac{\partial P}{\partial x}+\rho_m g \sin\theta+\frac{\tau_m \pi D}{A}=0. \tag{3.11}$$

In Equation (3.11), ρ_m is the mixture density which is calculated by volumetric averaging:

$$\rho_m=\rho_g\alpha_g+\rho_o\alpha_o+\rho_w\alpha_w \tag{3.12}$$

Since no slippage assumption is not always maintained in multiphase flow simulations, due to high density and viscosity contrast between the phases, homogenous models cannot be widely applied in the multiphase flow systems. For this reason, we need to incorporate some constitutive models in the momentum equations to include the slippage effect between the phases. To accomplish this, two different methodologies exist in the literature that we explain in detail in the next sections. In one method, a drift-flux correlation is used for the gas, oil and water phase velocities as a function of bulk volumetric average velocity and the drift velocities (Ishii, 1977). In the second method, separate momentum equations are used for each phase, inclusive of the interphase forces in the momentum equations for each phase. Usually in the second method, the phase is divided into gas and liquid and the equations are solved for the bulk of gas and the bulk of liquid (two-fluid models). Although separate momentum equations can be extended to as many number of phases exist, solving the equations for more than two phases can add more challenges in the definition of the interphase forces.

3.2.3 Momentum Conservation Equation with Drift-flux Approach

In the drift-flux modeling approach, the slippage of phases can be included in the velocity calculations using the model proposed by Ishii (1977)

$$u_g = C_0 J + V_d . \tag{3.13}$$

In Equation (3.13), J is volumetric average velocity of the bulk, V_d is the drift velocity and C_0 is the profile parameter (or distribution coefficient). Therefore, once we are able to calculate the volumetric average velocity of the bulk from the momentum equation, we can calculate the velocity of gas from Equation (3.13). Using average velocity equation, we can calculate the liquid velocity as well.

Referring to Equation (3.11), considering phase velocity slippage, the momentum equation is reformulated as follows:

$$\frac{\partial\left(\rho_m u_m\right)}{\partial t}+\frac{\partial\left(\rho_g \alpha_g u_g^2+\rho_o \alpha_o u_o^2+\rho_w \alpha_w u_w^2\right)}{\partial x}+\left(144.0 g_c\right)\frac{\partial P}{\partial x}+\rho_m g sin\theta+\frac{\tau_m \pi D}{A}=0. \tag{3.14}$$

Since velocities of gas, oil and water are no longer equal to the average velocity of the bulk fluid; the momentum equation becomes a function of phase velocities and mass average velocity, u_m,

$$u_m=\frac{\rho_g \alpha_g u_g+\rho_o \alpha_o u_o+\rho_w \alpha_w u_w}{\rho_m} . \tag{3.15}$$

Furthermore, in the drift-flux model proposed by Ishii (1977), volumetric average velocity is used; hence, to be able to use u_m in drift-flux correlation, certain modification is required. In addition, to extend the drift-flux model to calculate gas, oil, and water velocities, two pairs of systems (first, liquid and gas and second, oil and water) are considered. Hence, the mixture average velocity is used to calculate the liquid and gas velocities and the liquid average velocity is used to obtain oil and water velocities. With a correct definition of profile parameters and drift velocities for each system; the gas, liquid, oil, and water velocities are defined as follows:

$$u_g = C_1^{gl} u_m + vd_1^{gl}, \tag{3.16}$$

$$u_l = C_2^{gl} u_m + vd_2^{gl}, \tag{3.17}$$

$$u_o = C_1^{ow} u_m + vd_1^{ow}, \tag{3.18}$$

$$u_w = C_2^{ow} u_m + vd_2^{ow}. \tag{3.19}$$

In Section 3.6.1, we will discuss the details of correlations (3.16) though (3.19).

3.2.4 Momentum Conservation Equations with Two-fluid Approach

In the two-fluid modeling approach, instead of considering velocity slippage via drift-flux correlations, separate momentum equations are used for each phase (i.e. liquid and gas). In this method, the interaction forces between the phases and between phases and walls are included in the momentum equations of each phase to honor the force balance in each phase.

At this point, we assume that oil and water mixture creates a liquid phase with no slippage between oil and gas, and all the liquid properties are the average properties of oil and water. However, later we add the drift-flux model to the liquid phase to consider the slippage between water and oil. Hence, considering only gas/liquid phases in our system, the momentum conservation equations of gas and liquid phases in non-stratified flow become

$$\frac{\partial\left(\alpha_g\rho_g u_g\right)}{\partial t}+\frac{\partial\left(\alpha_g\rho_g u_g^2\right)}{\partial x}+\left(144.0g_c\right)\alpha_g\frac{\partial P}{\partial x}+\alpha_g\rho_g B_x+ \\ \alpha_g\rho_g u_g FWG-\Gamma_g u_{gi}+\alpha_g\rho_g\left(u_g-u_l\right)FIG=0, \tag{3.20}$$

$$\frac{\partial\left(\alpha_l\rho_l u_l\right)}{\partial t}+\frac{\partial\left(\alpha_l\rho_l u_l^2\right)}{\partial x}+\left(144.0g_c\right)\alpha_l\frac{\partial P}{\partial x}+\alpha_l\rho_l B_x+ \\ \alpha_l\rho_l u_l FWL+\Gamma_g u_{li}+\alpha_l\rho_l\left(u_l-u_g\right)FIL=0. \tag{3.21}$$

In the Equations (3.20) and (3.21), each term corresponds to the following:

$\frac{\partial\left(\alpha_g\rho_g u_g\right)}{\partial t}$: Momentum accumulation term;

$\frac{\partial\left(\alpha_g\rho_g u_g^2\right)}{\partial x}$: Momentum convection term in axial direction;

$\left(144.0g_c\right)\alpha_g\frac{\partial P}{\partial x}$: Pressure gradient;

$\alpha_g\rho_g B_x$: Body forces (i.e. gravity, pumps);

$\alpha_g\rho_g u_g FWG$: Phasic wall friction;

$\Gamma_g u_{gi}$: Interphase mass transfer momentum;

$\alpha_g\rho_g\left(u_g-u_l\right)FIG$: Interphase drag friction.

Equations (3.20) and (3.21) can be further simplified to Equations (3.22) and (3.23) by incorporating the mass balance equations of liquid and gas:

$$\alpha_g \rho_g \frac{\partial u_g}{\partial t} + \alpha_g \rho_g \frac{\partial u_g^2}{2\partial x} + (144.0 g_c)\alpha_g \frac{\partial P}{\partial x} + \alpha_g \rho_g B_x + \\ \alpha_g \rho_g u_g FWG + \Gamma_g (u_g - u_{gi}) + \dot{\psi}_g u_g + \alpha_g \rho_g \left(u_g - u_l\right) FIG = 0, \tag{3.22}$$

$$\alpha_l \rho_l \frac{\partial u_l}{\partial t} + \alpha_l \rho_l \frac{\partial u_l^2}{2\partial x} + (144.0 g_c)\alpha_l \frac{\partial P}{\partial x} + \alpha_l \rho_l B_x + \\ \alpha_l \rho_l u_l FWL - \Gamma_g (u_l - u_{li}) + \dot{\psi}_l u_l + \alpha_l \rho_l \left(u_l - u_g\right) FIL = 0. \tag{3.23}$$

To close the system of momentum equations, we should also consider momentum conservation in the interphase as well. In fact, the summation of liquid and gas momentums, Equations (3.20) and (3.21), should always yield the mixture momentum equation with no extra terms. Hence, to satisfy this condition we should have

$$-\Gamma_g u_{gi} + \alpha_g \rho_g \left(u_g - u_l\right) FIG + \Gamma_g u_{li} + \alpha_l \rho_l \left(u_l - u_g\right) FIL = 0 \tag{3.24}$$

Thus, if we assume

$$u_{gi} = u_{li} = u_i, \tag{3.25}$$

$$\alpha_g \rho_g FIG = \alpha_l \rho_l FIL = \alpha_l \rho_l \alpha_g \rho_g FI, \tag{3.26}$$

Equation (3.24) is always honored. u_i and FI are interphase velocity and interphase friction force coefficient, respectively, which are defined in Section 3.6.2.

Equations (3.22) and (3.23) are the final versions of momentum conservation equations for non-stratified flows. However, when we have stratified flow, as shown in Figure 3.1, another gravity term is added to the momentum equation, which is because of the liquid volume fraction gradient in the axial direction. This effect has not been considered in Equations (3.22) and (3.23).

As can be seen in Figure 3.1, in the stratified flow with the gas volume fraction α_g in a cross-section, the liquid level h_l with respect to the bottom of the pipe can be obtained from the following equations:

$$\pi\alpha_g = \beta - sin\beta cos\beta, \tag{3.27}$$

$$h_l = D\left(\frac{1+cos\beta}{2}\right). \tag{3.28}$$

Accordingly, the pressure equilibrium in the transverse direction of stratified flow also maintains the following relations between pressure at the top, P_g (gas occupying zone), pressure at the interface, P_I, and pressure at the bottom , P_l, (liquid occupying zone):

$$P_g = P_I - \rho_g B_y h_g \tag{3.29}$$

$$P_l = P_I + \rho_l B_y h_l \tag{3.30}$$

If we rewrite the force balance per unit volume exerted to the gas phase, inclusive of the interphase pressure, we will obtain

$$F_{BG}.\Delta x = \left(-\alpha_g \bar{P}_g\Big|_{x+\Delta x} + \alpha_g \bar{P}_g\Big|_x\right) + P_I\left(\alpha_g\Big|_{x+\Delta x} - \alpha_g\Big|_x\right), \tag{3.31}$$

$$F_{BG} = -\frac{\partial\left(\alpha_g \bar{P}_g\right)}{\partial x} + P_I\frac{\partial \alpha_g}{\partial x},$$

$$F_{BG} = -\alpha_g\frac{\partial \bar{P}_g}{\partial x} + \left(P_I - \bar{P}_g\right)\frac{\partial \alpha_g}{\partial x}. \tag{3.32}$$

In the same fashion for the liquid phase we can obtain F_{BL} as

$$F_{BL} = -\alpha_l \frac{\partial \bar{P}_l}{\partial x} + \left(P_I - \bar{P}_l\right)\frac{\partial \alpha_l}{\partial x}. \tag{3.33}$$

If we replace $\bar{P}_g = \frac{P_I + P_l}{2}$ and $\bar{P}_l = \frac{P_I + P_g}{2}$ as functions of P_I in Equations (3.32) and (3.32) and perform further rearrangement in the equations, we obtain

$$F_{BG} = -\alpha_g \frac{\partial P_I}{\partial x} + \frac{\alpha_g}{\left(\frac{\partial \alpha_g}{\partial h_g}\right)} \rho_g B_y \frac{\partial \alpha_g}{\partial x}, \tag{3.34}$$

$$F_{BL} = -\alpha_l \frac{\partial P_I}{\partial x} - \frac{\alpha_l}{\left(\frac{\partial \alpha_l}{\partial h_l}\right)} \rho_l B_y \frac{\partial \alpha_l}{\partial x}, \tag{3.35}$$

where $B_y = gsin\theta$ and $\left(\frac{\partial \alpha_g}{\partial h_g}\right) = \left(\frac{\partial \alpha_l}{\partial h_l}\right) = \frac{4sin\beta}{\pi D}$. Also, if we replace P_I in Equations (3.34) and (3.35) as functions of calculated average bulk pressure $(P = \bar{P}_g \alpha_g + \bar{P}_l \alpha_l)$ we obtain

$$F_{BG} = -\alpha_g \frac{\partial P}{\partial x} + \alpha_g \alpha_l (\rho_l - \rho_g) B_y \frac{\partial y}{\partial x}, \tag{3.36}$$

$$F_{BL} = -\alpha_l \frac{\partial P}{\partial x} - \alpha_g \alpha_l (\rho_l - \rho_g) B_y \frac{\partial y}{\partial x}, \tag{3.37}$$

where $\frac{\partial y}{\partial x}$ is the liquid level gradient with respect to the center of pipe in axial direction.

In Equations (3.22) and (3.23), we already had $\alpha_g \frac{\partial P}{\partial x}$ and $\alpha_l \frac{\partial P}{\partial x}$ as the only force balance terms. If we update those equations for stratified flow, our momentum equations for gas and liquid phases are upgraded to

$$\begin{aligned}&\alpha_g \rho_g \frac{\partial u_g}{\partial t} + \alpha_g \rho_g \frac{\partial u_g^2}{2\partial x} + (144.0 g_c)\alpha_g \frac{\partial P}{\partial x} - \alpha_g \alpha_l \left(\rho_l - \rho_g\right) B_y \frac{\partial y}{\partial x} + \alpha_g \rho_g B_x + \\ &\alpha_g \rho_g u_g FWG + \Gamma_g (u_g - u_{gi}) + \dot{\psi}_g u_g + \alpha_g \rho_g \left(u_g - u_l\right) FIG = 0,\end{aligned} \tag{3.38}$$

$$\begin{aligned}&\alpha_l \rho_l \frac{\partial u_l}{\partial t} + \alpha_l \rho_l \frac{\partial u_l^2}{2\partial x} + (144.0 g_c)\alpha_l \frac{\partial P}{\partial x} + \alpha_g \alpha_l \left(\rho_l - \rho_g\right) B_y \frac{\partial y}{\partial x} + \alpha_l \rho_l B_x + \\ &\alpha_l \rho_l u_l FWL - \Gamma_g (u_l - u_{li}) + \dot{\psi}_l u_l + \alpha_l \rho_l \left(u_l - u_g\right) FIL = 0.\end{aligned} \tag{3.39}$$

3.3 EIGENVALUE ANALYSIS OF MULTIPHASE FLOW EQUATIONS

Among the different multiphase flow models, two-fluid model can offer better accuracy in the simulations. However, from the early stage of development of two-fluid models, there were inherent instability problems in the solutions. Javier (1965) attributed this issue to the non-hyperbolic system of equations (No and Kazimi, 1981). In addition, Richtmyer and Morton (1967) showed that ill-posedness of the Initial Value Problems (IVP), regardless of the difference scheme, can cause stability problems. In fact, ill-posedness suggests that the results of the model do not reflect the real flow physics. Lyczkowski (1976) also analyzed the characteristics of the equations and showed that complex characteristics in the two-fluid model can cause rapid error growth and consequently stability issues. Other researchers (Gidaspow, 1974, Ramshaw and Trapp, 1978, Song and Ishii, 2000) have also argued the ill-posedness of two-fluid models and showed that the governing equations may not possess real characteristics when the relative velocity between liquid and gas exceeds a critical value. This critical value can be related to the Kelvin-Helmholtz stability condition for stratified flow (Issa and Kempf, 2003).

More recently, Hwang (2003) also presented some detailed mathematical analysis of two-fluid models and showed different numerical accuracy of the model in hyperbolic and non-hyperbolic conditions. He also suggested that in some limited time, the results of non-hyperbolic model could be accurate. In addition, Prosperetti (2007) showed that the loss of hyperbolicity causes non-physical solutions and instability to a disturbance of any wavelengths, such as machine error.

In this section, we discuss the stability of different multiphase flow models (homogenous, drift-flux, and two-fluid) by analyzing the characteristics of the equations. This analysis is crucial to understand the stable conditions of our models. In addition, we will discuss on the remedies for stability issues in the following sections.

3.3.1 Mathematical Stability of IVP, Ill-Posed Problems

A physical formulation is well-posed if its solution exists, is unique, and depends continuously on the boundary condition (No and Kazimi, 1981). Therefore, to check the well-posed condition of a system of equations, one should check the stability and the uniqueness of the solutions.

If we assume our system of equations has a general matrix form of

$$[A]\frac{\partial U}{\partial t}+[B]\frac{\partial U}{\partial x}=[C], \tag{3.40}$$

where U is the vector of variables, $[A]$ and $[B]$ are coefficient matrices and $[C]$ the sink/source terms, and

$$U(0,x)=u_0(x)\,,\; a \le x \le b\,, \tag{3.41}$$

$$U(t,a)=u\ \ (a)\,,U(t,b)=u\ \ (b). \tag{3.42}$$

our system is well-posed if the solution of Equation (3.40) exists, is unique and depends continuously on both initial and boundary conditions. In addition, this system is defined as hyperbolic if all values of the characteristics of Equation (3.40) are distinct and real. Lax (1958) also introduced the well-posed condition of a problem in linear partial differential equations, similar to the condition as defied for hyperbolic systems. The characteristic root of the Equation (3.40) is obtained from

$$\left|\lambda A - B\right| = 0\,. \tag{3.43}$$

3.3.2 Characteristic Roots of Multiphase Flow Equations

To analyze the characteristic roots of the different modeling approaches, we solve Equation (3.43) for each modeling approach. Afterward, we discuss on the regions where characteristic roots may become imaginary.

In the homogenous model we have

$$\frac{\partial(\rho_m)}{\partial t} + \frac{\partial(\rho_m u_m)}{\partial x} = \dot{\psi}_l + \dot{\psi}_g,$$

$$\frac{\partial(\rho_m u_m)}{\partial t} + \frac{\partial\left(\rho_m u_m^2\right)}{\partial x} + \left(144.0 g_c\right)\frac{\partial P}{\partial x} = -\rho_m g sin\theta - \frac{\tau_m \pi D}{A}.$$

Replacing the density derivative with pressure derivative, using the definition of fluid mixture compressibility, we obtain

$$\frac{\partial(\rho_m)}{\partial t} = \frac{\partial(\rho_m)}{\partial P}\frac{\partial P}{\partial t},$$

$$\frac{\partial(\rho_m)}{\partial x} = \frac{\partial(\rho_m)}{\partial P}\frac{\partial P}{\partial x},$$

$$C_m = \frac{\partial(\rho_m)}{\partial P}$$

$$C_m\frac{\partial P}{\partial t} + u_m C_m\frac{\partial P}{\partial x} + \rho_m\frac{\partial u_m}{\partial x} = \dot{\psi}_l + \dot{\psi}_g \tag{3.44}$$

$$u_m C_m\frac{\partial P}{\partial t} + \rho_m\frac{\partial u_m}{\partial t} + 2\rho_m u_m\frac{\partial u_m}{\partial x} + C_m u_m^2\frac{\partial P}{\partial x} + \left(144.0g_c\right)\frac{\partial P}{\partial x} = -\rho_m g sin\theta - \frac{\tau_m \pi D}{A} \tag{3.45}$$

Assuming

$$U{=}\left[u_m,P\right]^T, \tag{3.46}$$

$$\left[A\right] = \begin{bmatrix} 0 & C_m \\ \rho_m & u_m C_m \end{bmatrix}, \tag{3.47}$$

$$\left[B\right] = \begin{bmatrix} \rho_m & u_m C_m \\ 2\rho_m u_m & u_m^2 C_m + 1 \end{bmatrix}, \tag{3.48}$$

the characteristic roots of the homogenous model become

$$\begin{vmatrix} -\rho_m & C_m\lambda - u_m C_m \\ \rho_m\lambda - 2\rho_m u_m & u_m C_m \lambda - u_m^2 C_m - 1 \end{vmatrix} = 0 \rightarrow \lambda = u_m \pm \sqrt{\frac{1}{C_m}}. \tag{3.49}$$

As can be seen, the characteristic roots of the homogenous model are always real. Hence, the homogenous model is always hyperbolic and well-posed.

In the same fashion, we can analyze the characteristic roots of the drift-flux model. The system of equations in the drift flux model can be written as

$$\frac{\partial(\alpha_l\rho_l)}{\partial t}+\frac{\partial(\alpha_l\rho_l u_l)}{\partial x}=\dot{\psi}_l-\Gamma_g, \tag{3.50}$$

$$\frac{\partial(\rho_m)}{\partial t}+\frac{\partial(\rho_m u_m)}{\partial x}=\dot{\psi}_l+\dot{\psi}_g, \tag{3.51}$$

$$\frac{\partial(\rho_m u_m)}{\partial t}+\frac{\partial\left(\rho_m u_m^2\right)}{\partial x}+\left(144.0g_c\right)\frac{\partial P}{\partial x}=-\rho_m g sin\theta-\frac{\tau_m\pi D}{A}. \tag{3.52}$$

Using Equations (3.50) through (3.52), the variables vector and the matrix coefficients of the drift-flux model become

$$U=\left[\alpha_l,u_m,P\right]^T, \tag{3.53}$$

$$[A]=\begin{bmatrix}\rho_l & 0 & \frac{\alpha_l}{C_l}\\ 0 & 0 & \frac{1}{C_m^2}\\ 0 & \rho_m & \frac{u_m}{C_m^2}\end{bmatrix}, \tag{3.54}$$

$$[B]=\begin{bmatrix}\rho_l u_l & \alpha_l\rho_l\left(1-\alpha_g C_0\right) & \frac{\alpha_l u_l}{C_l^2}\\ 0 & \rho_m & \frac{u_m}{C_m^2}\\ 0 & 2\rho_m u_m & \frac{u_m^2}{C_m^2}+1\end{bmatrix}. \tag{3.55}$$

Accordingly, the characteristic equations of the drift-flux model are obtained as

$$\begin{vmatrix} \lambda\rho_l - \rho_l u_l & -\alpha_l \rho_l \left(1-\alpha_g C_0\right) & \dfrac{\lambda\alpha_l}{C_l^2} - \dfrac{\alpha_l u_l}{C_l^2} \\ 0 & -\rho_m & \dfrac{\lambda}{C_m^2} - \dfrac{u_m}{C_m^2} \\ 0 & \lambda\rho_m - 2\rho_m u_m & \dfrac{\lambda u_m}{C_m^2} - \dfrac{u_m^2}{C_m^2} - 1 \end{vmatrix} = 0 \tag{3.56}$$

Solving Equation (3.56) yields the characteristic roots of the drift flux model as

$$\lambda = u_l,$$
$$\lambda = u_m \pm C_m.$$

Similar to homogenous model, the characteristic roots of the drift-flux model are also always real. Thus, we can conclude that the drift-flux model is also unconditionally well-posed.

The next set of equations that we investigate is the characteristic roots of the two-fluid model. To simplify our analysis, we assume only incompressible fluids and stratified flow regime in this model. In fact, in the stratified flow regime we have the full terms of the momentum equations. The system of equations in the stratified two-fluid model can be written as

$$\frac{\partial\left(\alpha_g\right)}{\partial t} + \frac{\partial\left(\alpha_g u_g\right)}{\partial x} = \dot{\psi}_g + \Gamma_g, \tag{3.57}$$
$$\frac{\partial\left(\alpha_l\right)}{\partial t} + \frac{\partial\left(\alpha_l u_l\right)}{\partial x} = \dot{\psi}_l - \Gamma_g, \tag{3.58}$$

$$
\begin{aligned}
&\frac{\partial \alpha_g u_g}{\partial t}+\frac{\partial \alpha_g u_g^2}{\partial x}+\frac{\alpha_g}{\rho_g}\frac{\partial P_I}{\partial x}-\left(\frac{\alpha_g}{\alpha_g'}\right)B_y\frac{\partial \alpha_g}{\partial x}= \\
&-\alpha_g B_x-\alpha_g u_g FWG-\frac{\Gamma_g}{\rho_g}(u_g-u_{gi})-\frac{\dot{\psi}_g}{\rho_g}u_g-\alpha_g\left(u_g-u_l\right)FIG,
\end{aligned}
\tag{3.59}
$$

$$
\begin{aligned}
&\frac{\partial \alpha_l u_l}{\partial t}+\frac{\partial \alpha_l u_l^2}{\partial x}+\frac{\alpha_l}{\rho_l}\frac{\partial P}{\partial x}+\left(\frac{\alpha_l}{\alpha_l'}\right)B_y\frac{\partial \alpha_l}{\partial x}= \\
&-\alpha_l B_x-\alpha_l u_l FWL+\frac{\Gamma_g}{\rho_l}(u_l-u_{li})-\frac{\dot{\psi}_l}{\rho_l}u_l-\alpha_l\left(u_l-u_g\right)FIL,
\end{aligned}
\tag{3.60}
$$

where $\alpha_g' = \dfrac{\partial \alpha_g}{\partial h_g}$ and $\alpha_l' = \dfrac{\partial \alpha_l}{\partial h_l}$.

Using Equations (3.57) through (3.60), the variables vector and the matrix coefficients of the two-fluid model are

$$
U=\left[\alpha_l, u_l, u_g, P_I\right]^T, \tag{3.61}
$$

$$
A=\begin{bmatrix}
-1 & 0 & 0 & 0\\
1 & 0 & 0 & 0\\
-u_g & 0 & \alpha_g & 0\\
u_l & \alpha_l & 0 & 0
\end{bmatrix}, \tag{3.62}
$$

$$
B=\begin{bmatrix}
-u_g & 0 & \alpha_g & 0\\
u_l & \alpha_l & 0 & 0\\
-u_g^2+\left(\dfrac{\alpha_g}{\alpha_g'}\right)B_y & 0 & 2\alpha_g u_g & \dfrac{\alpha_g}{\rho_g}\\
u_l^2+\left(\dfrac{\alpha_l}{\alpha_l'}\right)B_y & 2\alpha_l u_l & 0 & \dfrac{\alpha_l}{\rho_l}
\end{bmatrix}. \tag{3.63}
$$

Accordingly, the characteristic equation of the system becomes

$$\begin{vmatrix} -\lambda+u_g & 0 & -\alpha_g & 0 \\ \lambda-u_l & -\alpha_l & 0 & 0 \\ -\lambda u_g+u_g^2-\left(\dfrac{\alpha_g}{\alpha_g'}\right)B_y & 0 & \lambda\alpha_g-2\alpha_g u_g & -\dfrac{\alpha_g}{\rho_g} \\ \lambda u_l-u_l^2-\left(\dfrac{\alpha_l}{\alpha_l'}\right)B_y & \lambda\alpha_l-2\alpha_l u_l & 0 & -\dfrac{\alpha_l}{\rho_l} \end{vmatrix}=0. \tag{3.64}$$

The solution of Equation (3.64) yields the Eigenvalues of the two-fluid model as follows:

$$\lambda=\frac{\left(\dfrac{\rho_l u_l}{\alpha_l}+\dfrac{\rho_g u_g}{\alpha_g}\right)\pm\sqrt{\left(\dfrac{\rho_l}{\alpha_l}+\dfrac{\rho_g}{\alpha_g}\right)\left(\dfrac{\rho_l-\rho_g}{\alpha_l'}\right)B_y-\dfrac{\rho_l\rho_g}{\alpha_l\alpha_g}\left(u_g-u_l\right)^2}}{\left(\dfrac{\rho_l}{\alpha_l}+\dfrac{\rho_g}{\alpha_g}\right)} \tag{3.65}$$

As Equation (3.65) shows, the two-fluid model has real eigenvalues if

$$\left(\frac{\rho_l}{\alpha_l}+\frac{\rho_g}{\alpha_g}\right)\left(\frac{\rho_l-\rho_g}{\alpha_l'}\right)B_y-\frac{\rho_l\rho_g}{\alpha_l\alpha_g}\left(u_g-u_l\right)^2>0 \tag{3.66}$$

If $\left(u_g-u_l\right)$ exceeds $\sqrt{\left(\dfrac{\rho_m}{\rho_l\rho_g}\right)\left(\dfrac{\rho_l-\rho_g}{\alpha_l'}\right)g\sin\theta}$, the two-fluid system will have complex eigenvalues and the stratified flow model will be unstable. This condition is in correspondence to the Kelvin-Helmholtz condition that verifies the flow regime transition from stratified to non-stratified flow.

In addition, if we neglect the gravity effect due to liquid level gradient, the only condition to have real eigenvalues in the two-fluid model is when actually both liquid and gas velocities are equal. Since this condition is not necessarily met in the physical models, there is high chance to obtain complex eigenvalues in two-fluid models. Complex eigenvalues mean loss of hyperbolicity and well-posedness of the equations. Thus, two-fluid models in general need regularization to avoid instability issues (Dinh et al., 2003).

3.4 REGULARIZATION OF NON-HYPERBOLIC EQUATIONS

There are several different approaches for regularization of non-hyperbolic equations which have complex characteristics. In this section, we briefly explain these methods and the application of them in the stabilization of numerical solutions for two-fluid models.

The first approach for mathematical regularization is hyperbolization of the model by adding some *ad hoc* terms to the momentum equations. In this method, some physical phenomena (i.e. surface tension, viscosity effect, interfacial pressure) can be considered in the model to move the characteristic roots from complex zone to real zone. For example, Drew and Lahey (1979) added virtual mass terms to the right hand side of the momentum equations which had time and space derivatives of the variables. Furthermore, No and Kazimi (1981) discussed this model to characterize the virtual mass coefficient range to obtain real roots for the characteristic equation and reasonable error growth amplitude.

Song and Ishii (2000) used some empirical parameters as momentum flux parameters to avoid the non-hyperbolic condition of two-fluid model. Some other researchers also added two-pressure model for gas and liquid (Banerjee and Chan, 1980; Ransom and Hicks, 1984).

The second idea for regularization is parabolization. In this approach, diffusion terms such as numerical diffusion or viscose-like diffusion terms are imposed in the system of the equation to convert the system to parabolic system. Considering coarse gridblocks can cause numerical diffusion and consequently stability of the two-fluid models. However, this larger coarse grid also reduces the accuracy of the solution. Thus, an optimum size should always be chosen in this approach.

In addition to mathematical regularization, there are some complex numerical approaches that also can leverage the properties of the discrete model to avoid the ill-posedness of the mathematical equations.

In the current development of UTWELL, we follow the approach proposed by No and Kazimi (1981) and the model developed in RELAP5 to regulate our two-fluid model. In fact, we consider the virtual mass Equation (3.67) in the right hand side of the momentum equation and we add the viscose-like diffusion terms in the discretized form of the model (Section 5.1.1).

$$F^V = -C^{vm}\alpha_l\alpha_g\rho_m\left[\frac{\partial\left(u_l-u_g\right)}{\partial t}+u_g\frac{\partial u_l}{\partial x}-u_l\frac{\partial u_g}{\partial x}\right]. \tag{3.67}$$

It is also valid to use the simplified version of the virtual mass force per volume as follows:

$$F^V = -C^{vm}\alpha_l\alpha_g\rho_m\left[\frac{\partial\left(u_l-u_g\right)}{\partial t}\right]. \tag{3.68}$$

In Equations (3.67) and (3.68) the virtual mass coefficient C^{vm} is

$$C^{vm} = \frac{1}{2}\frac{\left(1+2\alpha_g\right)}{\left(1-\alpha_g\right)}, \quad \text{for} \quad 0 \le \alpha_g \le 0.5 \tag{3.69}$$

$$C^{vm} = \frac{1}{2}\frac{\left(3-2\alpha_g\right)}{\alpha_g}, \quad \text{for} \quad 0.5 \le \alpha_g \le 1.0 \tag{3.70}$$

3.5 FLOW REGIME DETECTION

One of the most important steps in the multiphase flow modeling is correct flow pattern determination. Since the dominant flow regime characterizes the flow equation, the accuracy of the simulation results is very much affected by the flow pattern detection algorithms. In addition, since the momentum equations are changed for the force balance terms in different flow regimes, the transition of the flow patterns can also add a source of discontinuity and numerical convergence issues in the equations. In this section, we are going to discuss on some robust algorithms for flow regime detection and flow transition smoothing that we have adopted for our model development.

In general, different parameters such as liquid and gas velocity, flow line inclination and fluid density, and viscosity establish the dominant flow pattern during multiphase flow. To determine these flow patterns and the criteria that drive the transition among them, a set of experimental tests should be performed. Since these experiments are sensitive to flow conditions and are recognized by visual means, different flow regimes and transition maps might be observed and reported in the literature. Thus, the flow regime transition maps might not be universal and it is recommended to test the experiment for particular fluids and conditions to ensure correct flow patterns selections. However, there are general definitions for flow patterns that have been accepted by many researchers. These flow pattern definitions can mainly be classified for horizontal, deviated, and vertical inclinations.

3.5.1 Flow Patterns in Vertical and Deviated Wells

Kaya et al. (1999) presented comprehensive mechanistic models for flow pattern detection, and pressure and holdup calculations in deviated and vertical wells. They considered five different flow regimes such as bubbly, dispersed bubbly, slug, churn, and annular flows (Figure 3.2). Kaya et al. (1999) tested their models against a handful of experimental and field data and showed reasonably good agreement with the data. They also evaluated their model against other existing models developed by other researchers (Aziz et al. (1972), Hasan and Kabir (1988), Chokshi (1994), and Hagadorn and Brown (1965)) and showed acceptable results.

In this section, we briefly review those models proposed by Kaya et al. (1999) for each flow regime and clarify the flow regime algorithms used in the UTWELL development. Furthermore, we regenerated the flow map model for deviated and vertical wells similar to Kaya et al.'s (1999).

Bubbly Flow Transition. Bubbly flow occurs in relatively low velocities of gas and liquid and low gas volume fractions in vertical inclination. This flow regime is characterized by small bubbles in the continuous liquid phase. Increasing the gas flow rate, bubbly flow can be changed into slug flow (Line A in Figure 3.3). Increasing the liquid velocity also breaks down the bubbles and changes the bubbly flow to dispersed bubbly flow (Line B in Figure 3.3). Taitel et al. (1980) proposed the packing volume fraction of 0.25 and the minimum pipe diameter of D_{mn} as the criteria for existence of bubbly flow.

$$D_{mn} = 19.01\left(\frac{\sigma\left(\rho_l-\rho_g\right)}{\rho_l^2 g}\right) \tag{3.71}$$

Kaya et al. (1999) reformulated the packing volume fraction as the superficial gas velocity for the transition of bubbly flow to

$$u_{sg} = 0.333u_{sl} + 0.25\frac{v_{bs}}{\sqrt{sin\theta\alpha_l}}, \tag{3.72}$$

where v_{bs} is the gas rise velocity which is defined as follows:

$$v_{bs} = 1.53\left(\frac{g\sigma\left(\rho_l-\rho_g\right)}{\rho_l^2}\right)^{0.25}, \tag{3.73}$$

α_l is also liquid holdup in Equation (3.72) which is a function of liquid and gas superficial velocities. To obtain Line A in Figure 3.3, we need to calculate liquid volume fraction (holdup) iteratively in order to compute Equation (3.72).

In the bubbly flow regime, drift-flux approach is used to calculate holdup and pressure loss. Using the mixture average velocity and the gas superficial velocity, the implicit equation to obtain holdup in the bubbly flow is

$$1.53\left(\frac{g\sigma\left(\rho_l-\rho_g\right)}{\rho_l^2}\right)^{0.25}\sqrt{sin\theta\alpha_l} = \frac{u_{sg}}{1-\alpha_l} - 1.2u_m. \tag{3.74}$$

Using average mixture properties the pressure loss in bubbly flow is also

$$\left(\frac{\partial P}{\partial l}\right) = \rho_m g sin\theta + \frac{f_m \rho_m u_m^2}{2D}. \tag{3.75}$$

Dispersed Bubbly Flow Transition. Dispersed bubbly flow can exist in high flow rates, where a strong turbulent force can break large bubbles into small ones. This mechanism is maintained until the volume fraction of gas is below a certain limit. Once the gas volume fraction increases, the turbulent force cannot prevent bubble agglomeration and cannot break the bubbles to small ones. At this condition a chaotic slug flow is observed.

The maximum diameter of stable dispersed bubble (Barnea et al. (1982)) is

$$D_{mx} = \left(4.15\left(\frac{u_{sg}}{u_{sg}+u_{sl}}\right)^{0.5} + 0.725\right)\left(\frac{\sigma}{\rho_l}\right)^{0.6}\left(\frac{f_m}{2D}\right)^{-0.4} u_m^{-1.2}. \tag{3.76}$$

Dispersed bubbly flow exists if the maximum stable bubble size is smaller than the critical bubble size (Line B Figure 3.3).The critical bubble size proposed by Taitel et al. (1980) is

$$D_{CD} = 2.0\left(\frac{0.4\sigma}{g\left(\rho_l - \rho_g\right)}\right)^{0.5}. \tag{3.77}$$

Barnea modified the Tatiel model to D_{CB} and considered the inclination effect for critical bubble size,

$$D_{CB} = \frac{3.0}{8.0}\left(\frac{\rho_l}{\rho_l - \rho_g}\right)\left(\frac{f_m u_m^2}{g sin\theta}\right). \tag{3.78}$$

The transition of dispersed bubbly flow to slug (Line C in Figure 3.3) is also obtained from maximum gas volume fraction of 0.52. This criterion in terms of superficial gas and liquid velocities becomes

$$u_{sg} = 1.083 u_{sl}. \tag{3.79}$$

In dispersed bubbly flow the holdup is calculated from no slip holdup

$$\alpha_l = \frac{u_{sl}}{u_{sl} + u_{sg}}. \tag{3.80}$$

and similar to bubbly flow, Equation (3.75) is used for the total pressure loss.

Slug Flow Transition. Increasing the gas superficial velocity can change slug flow to a more chaotic flow, churn or annular flow. Kaya et al. (1999) showed that the transition of the slug to churn flow (Line D in Figure 3.3) can occur at

$$u_{sg} = 12.19\left(1.2 u_{sg} + v_o\right), \tag{3.81}$$

where v_o is Taylor bubble rise velocity

$$v_o = \left(0.35 sin\theta + 0.54 cos\theta\right)\left(\frac{gD\left(\rho_l - \rho_g\right)}{\rho_l}\right)^{0.5}. \tag{3.82}$$

In the slug flow condition, since we have elongated bubbles and liquids (Figure 3.3), the method of holdup and pressure loss calculation is more complicated than that of bubbly and dispersed bubbly flow. In this flow regime, we calculate holdup and pressure loss by the following procedure. Assuming

$$v_{\infty} = 1.53\left(\frac{g\sigma\left(\rho_l - \rho_g\right)}{\rho_l^2}\right)^{0.25}, \tag{3.83}$$

$$v_{TB} = 1.25u_m + 0.35\left(\frac{gD\left(\rho_l - \rho_g\right)}{\rho_l}\right)^{0.5}, \tag{3.84}$$

the variables in the liquid slug unit are calculated as

$$H_{GLS} = \frac{u_{sg}}{\left(1.208u_m + 0.921v_{\infty}\right)}, \tag{3.85}$$

$$H_{LLS} = 1 - H_{GLS}, \tag{3.86}$$

$$v_{GLS} = 1.08u_m + 0.921v_{\infty}, \tag{3.87}$$

$$v_{LLS} = \frac{\left(u_m - H_{GLS}v_{GLS}\right)}{H_{LLS}}, \tag{3.88}$$

where, H_{GLS} is the gas volume fraction, H_{LLS} is the liquid volume fraction, v_{GLS} is gas velocity and v_{LLS} is the liquid velocity in the liquid slug unit.

The variables in Taylor bubble also can be calculated iteratively as

$$v_{LTB} = -9.916\left(gD\left(1 - \sqrt{H_{GTB}}\right)\right)^{0.5}, \tag{3.89}$$

$$H_{GTB} = 1 - \frac{\left(v_{TB} - v_{LLS}\right)H_{LLS}}{\left(v_{TB} - v_{LTB}\right)}, \tag{3.90}$$

$$H_{LTB} = 1 - H_{GTB}. \tag{3.91}$$

Using the liquid slug and the Taylor bubble variables, the ratio of Taylor bubble length to slug unit is obtained

$$\xi = 1 - \frac{\left(u_{sl} + (v_{TB} - v_{LLS})H_{LLS} - v_{TB}H_{LTB}\right)}{v_{TB}\left(H_{GTB} - H_{GLS}\right)}. \tag{3.92}$$

In addition, the liquid slug density and viscosity are updated as follows:

$$\rho_{ls} = \rho_l H_{LLS} + \rho_g H_{GLS}, \tag{3.93}$$

$$\mu_{ls} = \mu_l H_{LLS} + \mu_g H_{GLS}. \tag{3.94}$$

Furhtermore, the liquid holdup and the pressure loss in fully developed slug flow are calcualted as follows:

$$\alpha_l = H_{LLS}(1-\xi) + H_{LTB}\xi, \tag{3.95}$$

$$\left(\frac{\partial P}{\partial l}\right) = \rho_{ls} g sin\theta + \frac{f_{ls}\rho_{ls}u_m^2}{2D}(1-\xi). \tag{3.96}$$

For churn flow, pressure loss and holdup calculation, similar to the approach pursued for slug flow, is applied.

Annular Flow Transition. In annular flow regime, a gas core is observed that is surrounded by a thin liquid film. Taitel et al. (1980) showed that the annular flow regime occurs when the gas superficial velocity exceeds a critical value v_{gc}

$$v_{gc} = 3.1\left(\frac{g\sigma\left(\rho_l - \rho_g\right)}{\rho_g^2}\right)^{0.25}. \tag{3.97}$$

In addition to critical gas velocity, Hasan et al. (2007) added a minimum gas volume fraction of 0.7 to the criteria of existing annular flow. Line E in Figure 3.3 represents the Taitel et al. (1980) and the Hasan et al. (2007) annular flow transition border.

Kaya et al. (1999), following the approach by Ansari et al. (1994), slightly modified the annular flow transition criterion. In this approach, the annular flow is changed to slug flow when the liquid film becomes unstable. From mathematical point of view, this condition is satisfied when

$$Y_M \geq \frac{2-1.5H_{LF}}{H_{LF}^3(1-1.5H_{LF})} X_M^2, \tag{3.98}$$

$$\left(H_{LF} + \lambda_{LC}\frac{A_C}{A}\right) \geq 0.12. \tag{3.99}$$

H_{LF} is the liquid film holdup, a function of dimensionless liquid film thickness ($\underline{\delta}$). Y_M and X_M are modified Lockhart-Martinelli (1949) parameters which are functions of liquid entrainment fraction in the gas core (FE) and superficial frictional pressure gradients for liquid and gas core.

$$H_{LF} = 4\underline{\delta}(1-\underline{\delta}), \tag{3.100}$$

$$Y_M - \frac{Z}{4\underline{\delta}(1-\underline{\delta})\left[1-4\underline{\delta}(1-\underline{\delta})\right]^{2.5}} + \frac{X_M^2}{\left[4\underline{\delta}(1-\underline{\delta})\right]^3} = 0, \tag{3.101}$$

$$Y_M = \frac{g sin\theta \left(\rho_l - \rho_c\right)}{\left(dP/dL\right)_{SC}}, \tag{3.102}$$

$$X_M = \sqrt{\left(1-FE\right)^2 \frac{f_F}{f_{SL}} \frac{\left(dP/dL\right)_{SL}}{\left(dP/dL\right)_{SC}}}, \tag{3.103}$$

$$FE=1-exp\left[-0.125\left(1000\frac{u_{sg}\mu_g}{\sigma}\sqrt{\frac{\rho_g}{\rho_l}}\right)-1.5\right], \tag{3.104}$$

$$Z=1+300\underline{\delta} \qquad \text{for} \qquad FE>0.9, \tag{3.105}$$

$$Z=1+\left(\frac{\rho_l}{\rho_c}\right)^{1/3}\underline{\delta} \qquad \text{for} \qquad FE \le 0.9,$$

$$\lambda_{LC} = \frac{FE \times u_{sl}}{FE \times u_{sl} + u_{sg}}. \tag{3.106}$$

In Equations (3.98) through (3.106), the gas core properties are calculated by volumetric averaging of entrained liquid and gas properties. Details of the other related parameters can be found in Kaya et al. (1999) and Ansari et al. (1994).

Finally, to compute the pressure loss and holdup in annular flow, we use the following equations

$$\alpha_l = \left(H_{LF} + \lambda_{LC}\frac{A_C}{A}\right), \tag{3.107}$$

$$\left(\frac{\partial P}{\partial l}\right) = \rho_c g sin\theta + \frac{Z}{\left(1-2\underline{\delta}\right)^5}\left(\frac{dP}{dL}\right)_{SC}. \tag{3.108}$$

The annular flow transition proposed by Ansari et al. (1994) and Kaya et al. (1999) predicts the annular flow regime in higher gas superficial velocity than the Taitel et al .(1980) and the Hasan et al. (2007) approaches. For this reason, to mitigate this discrepancy in UTWELL, both options have been considered in the vertical annular flow detection.

3.5.2 Flow Patterns in Horizontal Wells

For horizontal or near-horizontal wells, four flow patterns have generally been introduced (Shoham, 2005). Although, these flow patterns can be sub-divided into slightly different flow regimes, in order to avoid situations that are more complex we only consider them as main flow configurations. Stratified, bubbly, intermittent, and annular flows as shown in Figure 3.4 are the main flow regimes researchers have agreed upon for the horizontal flow (Shoham, 2005).

For horizontal flow pattern detection, we follow a procedure similar to Shoham's (2005). The first step in flow pattern detection in horizontal inclinations is recognizing the stratified flow regime. For this purpose, the Kelvin-Helmholtz constraint is verified to check whether the stratified flow can exist or not. With this constraint, when the gas actual velocity exceeds a critical velocity, the flow regime can no longer be stratified.

$$u_g \geq \left(1-\frac{h}{D}\right)\left(\frac{g cos\theta\left(\rho_l-\rho_g\right)A_g}{\rho_g\left(dA_l/dh\right)}\right)^{0.5}. \tag{3.109}$$

Assuming non-dimensional form of the variables in the expression (3.109), we obtain the stratified flow transition when

$$F_0 \geq F, \tag{3.110}$$

where

$$F=\left(\frac{\left(1-\tilde{h}_l\right)^2\tilde{A}_g}{\tilde{u}_g^2\tilde{S}_i}\right)^{0.5}, \tag{3.111}$$

$$F_0 = u_{sg}\left(\frac{\rho_g}{Dg\cos\theta\left(\rho_l-\rho_g\right)}\right)^{0.5}. \tag{3.112}$$

The key parameter in Equation (3.111) is $\tilde{h}_l = \frac{h}{D}$. All the other parameters (i.e. $\tilde{S}_i$, $\tilde{A}_g$) can be calculated as a function of $\tilde{h}_l$ (Shoham (2005), page 67).

$\tilde{h}_l$ can be obtained from momentum equations of liquid and gas in stratified flow condition. Assuming separate flows for gas and liquid and neglecting the axial holdup gradient and momentum acceleration terms, we have

$$\frac{\partial P}{\partial x} + \frac{\tau_{wg}S_g}{A_g} + \frac{\tau_i S_i}{A_g} + \rho_g g\sin\theta = 0, \tag{3.113}$$

$$\frac{\partial P}{\partial x} + \frac{\tau_{wl}S_l}{A_l} - \frac{\tau_i S_i}{A_l} + \rho_l g\sin\theta = 0. \tag{3.114}$$

Subtracting (3.113) from (3.114) we obtain

$$\frac{\tau_{wg}S_g}{A_g} - \frac{\tau_{wl}S_l}{A_l} + \tau_i S_i\left(\frac{1}{A_g} + \frac{1}{A_l}\right) - \left(\rho_l-\rho_g\right)g\sin\theta = 0. \tag{3.115}$$

In Equation (3.115), S_l is the wetted perimeter by liquid phase, S_g is the wetted perimeter by gas phase and S_i is the interphase perimeter. A_g and A_l are gas and liquid phase cross-sectional areas. All the parameters in Equation (3.115) can be written as a function of liquid level, velocities and fluid properties. In addition, Equation (3.115) can be transformed to non-dimensional form as in

$$X^2\left[\left(\tilde{u}_l\tilde{d}_l\right)^{-n}\frac{\tilde{u}_l^2\tilde{S}_l}{\tilde{A}_l}\right]-\left[\left(\tilde{u}_g\tilde{d}_g\right)^{-m}\tilde{u}_g^2\left(\frac{\tilde{S}_g}{\tilde{A}_g}+\frac{\tilde{S}_i}{\tilde{A}_g}+\frac{\tilde{S}_i}{\tilde{A}_l}\right)\right]+4Y=0, \tag{3.116}$$

$$X^2=\frac{\left(dP/dl\right)_{SL}}{\left(dP/dl\right)_{SG}}, \tag{3.117}$$

$$Y=\frac{\left(\rho_l-\rho_g\right)gsin\theta}{-\left(dP/dl\right)_{SG}}. \tag{3.118}$$

Solution of the equation (3.116) yields $\tilde{h}_l$. For flow regime detection, if the calculated $\tilde{h}_l$ satisfies condition in (3.110), the system has non-stratified flow; otherwise, the system has stratified flow. If system became non-stratified and the non-dimensional liquid level turned out to be less than 0.35, system would be assumed to have bubbly flow; otherwise, constraint (3.119) would be verified:

$$T_0<T, \tag{3.119}$$

$$T=\left(\frac{8\tilde{A}_g}{\tilde{u}_l^2\tilde{S}_i\left(\tilde{u}_l\tilde{d}_l\right)^{-0.2}}\right)^{0.5}, \tag{3.120}$$

$$T_0=\left(\frac{-\left(dP/dl\right)_{SL}}{gcos\theta\left(\rho_l-\rho_g\right)}\right)^{0.5}. \tag{3.121}$$

If constraint (3.119) is satisfied, the dominant flow regime is intermittent flow; otherwise, it is annular flow.

Once we define the system's dominant flow pattern, the holdup and the pressure loss can be calculated accordingly. The pressure loss and the holdup for bubbly, intermittent, and annular flow are calculated in a fashion similar to deviated wells' except with some corrections for the inclination angle. However, for the stratified flow, the holdup and the pressure loss are computed as follows:

$$\alpha_l = D\tilde{h}_l, \tag{3.122}$$

$$\left(\frac{\partial P}{\partial l}\right) = \rho_l g sin\theta + \frac{\tau_{wl} S_l}{A_l} - \frac{\tau_i S_i}{A_l}. \tag{3.123}$$

Closing the section on flow pattern detection, we also pay attention to few convergence issues related to flow regime transitions. Since flow pattern transitions introduce discontinuities in the two-fluid models, the transitions criteria should be smoothened. In the UTWELL development for steady-state flow models, the flow regimes are selected based on the same approaches given in Sections 3.5.1 and 3.5.2. However, for transient models, since discontinuities can cause severe problems, the transition criteria are slightly modified for using RELAP5 (2012) to avoid stability problems.

3.6 CONSTITUTIVE RELATIONS

The constitutive models referred to in this section are the equations we apply for correlations of phasic velocities in the drift-flux models and for interphase drag forces in the two-fluid models. These relations are required in the momentum equations to grant a closure to the system of equations.

3.6.1 Drift-flux Model

The slippage between two fluids results from the non-uniform profile of velocity and buoyancy forces between the phases. This phenomenon can be modeled for a mixture of gas and liquid by a mathematical equation (Shi et al., 2005) as follows:

$$u_g = C_{0gl} u_m + Vd_{gl}, \tag{3.124}$$

$$u_l = \left(\frac{1-\alpha_g C_{0gl}}{1-\alpha_g} \right) u_m - \left(\frac{\alpha_g}{1-\alpha_g} \right) Vd_{gl}. \tag{3.125}$$

C_{0gl} is a profile parameter, u_m is volumetric average mixture velocity, and Vd_{gl} is drift velocity. Hasan and Kabir (1999) applied a similar model for the mixture of water and oil as in

$$u_o = C_{0ow} u_l + Vd_{ow}, \tag{3.126}$$

$$u_w = \frac{\alpha_l - \alpha_o C_{0ow}}{\alpha_w} u_l - \frac{\alpha_o}{\alpha_w} Vd_{ow}. \tag{3.127}$$

Substituting liquid velocity u_l from Equation (3.125) to Equations (3.126) and (3.127), oil and water velocities can eventually become a function of mixture velocity as well:

$$u_o = C_{0ow} \left(\frac{1-\alpha_g C_{0gl}}{1-\alpha_g} \right) u_m - C_{0ow} \left(\frac{\alpha_g}{1-\alpha_g} \right) Vd_{gl} + Vd_{ow}, \tag{3.128}$$

$$u_w = \frac{\alpha_l\left(\frac{1-\alpha_g C_{0gl}}{1-\alpha_g}\right) - \alpha_o C_{0ow}\left(\frac{1-\alpha_g C_{0gl}}{1-\alpha_g}\right)}{\alpha_w} u_m - \frac{\alpha_l}{\alpha_w}\left(\frac{\alpha_g}{1-\alpha_g}\right) Vd_{gl} \tag{3.129}$$

$$+\frac{\alpha_o}{\alpha_w} C_{0ow}\left(\frac{\alpha_g}{1-\alpha_g}\right) Vd_{gl} - \frac{\alpha_o}{\alpha_w} Vd_{ow}.$$

The key parameters in the drift flux models are the profile parameters and the drift velocities for liquid/gas and oil/water systems. These variables are dependent on the flow regime condition and the spatial distribution of the fluids as well. Shi et al. (2005) and Hasan and Kabir (2007) proposed general algorithms to define the drift-flux parameters. They showed that by using some interpolation rules, the drift-flux parameters can also become continuous in the entire range of solutions.

Figure 3.6 shows the drift flux parameters that we have calculated for a typical oil ($\rho_o = 58\frac{lb}{ft^3}, \mu_o = 1.0Cp, \sigma_{ow} = 10\frac{dyne}{cm}$), gas ($\rho_g = 0.077\frac{lb}{ft^3}, \mu_g = 0.018Cp, \sigma_{gl} = 36\frac{dyne}{cm}$) and water ($\rho_w = 63.4\frac{lb}{ft^3}, \mu_w = 1.0Cp$) mixture in a pipe with 0.498 ft diameter from drift-flux model in UTWELL. The trends of curves that we obtained are similar to Shi et al. (2005) solutions for default drift-flux coefficients.

Furthermore, if the mixture velocity in the drift-flux model is obtained as mass average velocity, the drift-flux equations should be modified accordingly. Using Equations (3.130) and (3.131), the new drift-flux model for mass average mixture velocity is obtained as follows:

$$u_g = C_{0gl}\left(\alpha_g u_g + \alpha_l u_l\right) + Vd_{gl}, \tag{3.130}$$

$$\alpha_g \rho_g u_g + \alpha_l \rho_l u_l = \rho_m u_m, \tag{3.131}$$

$$u_g = \left[1 + \frac{\left(\frac{\rho_l}{\rho_m}\right)\left(C_{0gl}-1\right)}{\left(1-\left(C_{0gl}-1\right)\alpha_g \frac{\left(\rho_l-\rho_g\right)}{\rho_m}\right)} \right] u_m + \frac{\left(\frac{\rho_l}{\rho_m}\right)}{\left(1-\left(C_{0gl}-1\right)\alpha_g \frac{\left(\rho_l-\rho_g\right)}{\rho_m}\right)} Vd_{gl}, \tag{3.132}$$

$$u_l = \left[1 - \frac{\left(\frac{\alpha_g \rho_g}{\alpha_l \rho_m}\right)\left(C_{0gl}-1\right)}{\left(1-\left(C_{0gl}-1\right)\alpha_g \frac{\left(\rho_l-\rho_g\right)}{\rho_m}\right)} \right] u_m + \frac{-\left(\frac{\alpha_g \rho_g}{\alpha_l \rho_m}\right)}{\left(1-\left(C_{0gl}-1\right)\alpha_g \frac{\left(\rho_l-\rho_g\right)}{\rho_m}\right)} Vd_{gl}. \tag{3.133}$$

3.6.2 Two-fluid Model

The interphase velocity (u_i) and the interphase friction force (FI) as shown in Equations (3.25) and (3.26) are the two main parameters in the momentum equation calculations that have been left undetermined so far. In this section, we introduce few constitutive relations used for calculating these parameters.

First, the undetermined terms, u_i, can be correlated to the velocities of gas and liquid using a weighting factor λ as follows:

$$u_i = \lambda u_g + (1-\lambda) u_l, \tag{3.134}$$

where, λ can be defined with a constant value (0.5) to yield the average velocities of liquid and gas or can be defined as $\lambda = 0$, when $\Gamma_g > 0$; and $\lambda = 1$, when $\Gamma_g < 0$. In UTWELL development, we used $\lambda = 0.5$ for the entire solution.

The second undetermined term in momentum equations is the interphase shear force coefficient (FI). This term is flow regime-dependent, which can be related to shear force per unit volume of gas and liquid phases (F_{ig} and F_{il}) in the momentum equations.

$$F_{ig} = FIG\alpha_g \rho_g \left(u_g - u_l\right) \tag{3.135}$$

$$F_{il} = FIL\alpha_l \, \rho_l \, \left(u_g - u_l\right) \tag{3.136}$$

Manipulation of Equations (3.135) and (3.136), in consideration of Equation (3.26), can yield a new formulation for FI

$$FI = \frac{\dfrac{F_{ig}}{\alpha_g \rho_g} + \dfrac{F_{il}}{\alpha_l \rho_l}}{\rho_m \left(u_g - u_l\right)}. \tag{3.137}$$

Assuming $F_{ig} = F_{il} = F_i$, Equation (3.137) becomes a function of global interphase friction force F_i. Consequently, if we define a constitutive relation for F_i, we can define the constitutive relations for FI. Since FI is related to FIG and FIL via Equation (3.26), defining a constitutive relation for FI can yield a constitutive relation for FIG and FIL as well. F_i is a flow-regime dependent parameter, which can be obtained for two category of flow regimes: dispersed flow and separated flow. In dispersed flows (such as bubbly, slug, churn, intermittent), the interphase friction force per unit volume can be correlated as

$$F_i = C_i \left|V_r\right| V_r, \tag{3.138}$$

using drift velocity of the gas phase where,

$$V_r = \left(\frac{1 - \alpha_g C_{0gl}}{1 - \alpha_g}\right) u_g - C_{0gl} u_l, \tag{3.139}$$

$$C_i = \frac{\alpha_g \alpha_l^3 \left(\rho_l - \rho_g\right) g sin\theta}{V d_{gl}^2}. \tag{3.140}$$

In separated flows (such as stratified and annular), the interphase friction force per unit volume can be correlated as

$$F_i = \frac{1}{8}\rho_c \left|u_g - u_l\right| \left(u_g - u_l\right) C_D S_F a_{gl}, \tag{3.141}$$

using the drag force effect, where ρ_c is the continuous phase density, C_D is drag coefficient, S_F is shape factor, and a_{gl} is interfacial area per unit volume.

Equations (3.138) and (3.141) can be computed for whole range of conditions using appropriate drift-flux parameters from Section 3.6.1 and appropriate correlations for drag force parameters from RELAP5 (2012). Figure 3.7 shows an example of FI calculation for different liquid and gas velocities and gas volume fractions. In this example, the flow regimes are only bubbly and slug. As can be seen, when the liquid and gas velocity difference becomes larger, the drag force coefficient FI becomes larger as well. In addition, when one of the phases disappears or its volume fraction decreases, the interphase coefficient decreases too. The absolute value of interphase friction coefficient can be an order of magnitude different for various flow conditions. The largest values are usually obtained in bubbly flows, where the liquid and gas contact area is the largest.

3.7 PHASIC WALL FRICTION

In the momentum equations, there are wall friction terms (FWL and FWG) that contribute the interaction of wall with the fluids. Defining a correct mathematical model for these terms is crucial since they significantly contribute to pressure drop at high flow rates. Wall friction terms are function of wall roughness, velocity of phases, and surface contact of fluids with wall. To calculate wall friction terms, first we define a two-phase wall friction term. Afterward, we split it to friction forces of liquid and gas phases by a partitioning factor. Equation (3.142) shows the two-phase wall friction term, where f_l is the liquid phase friction factor, f_g is the gas phase friction factor and C is the correlation coefficient. These parameters have been discussed in (RELAP, 2012) with all details of calculation.

$$\left(\frac{dP}{dl}\right)_{2\Phi} = \frac{1}{2D}\left(f_l \rho_l \left(\alpha_l u_l\right)^2 + C\left[f_l \rho_l \left(\alpha_l u_l\right)^2 f_g \rho_g \left(\alpha_g u_g\right)^2 \right]^{0.5} + f_g \rho_g \left(\alpha_g u_g\right)^2 \right) \tag{3.142}$$

The partitioning factor is calculated as

$$Z^2 = \frac{f_l \rho_l u_l^2 \dfrac{\alpha_{lw}}{\alpha_l}}{f_g \rho_g u_g^2 \dfrac{\alpha_{gw}}{\alpha_g}}, \tag{3.143}$$

where α_{lw} and α_{lw} are liquid and gas fractions on the wall. These fractions are defined for each flow regime. Using Equations (3.142) and (3.143) FWL and FWG become

$$FWL = \frac{1}{\rho_l u_l}\left(\frac{dP}{dl}\right)_{2\Phi}\left(\frac{Z^2}{\alpha_g + \alpha_l Z^2}\right), \tag{3.144}$$

$$FWG = \frac{1}{\rho_g u_g}\left(\frac{dP}{dl}\right)_{2\Phi}\left(\frac{1}{\alpha_g + \alpha_l Z^2}\right). \tag{3.145}$$

Figure 3.8 shows an example of results for the wall friction force coefficients, FWG and FWL, as a function of liquid and gas velocities. As can be seen, for bubbly and slug flows, the liquid wall friction is an order of magnitude larger than the gas wall friction since gas does not contact with wall as much as liquid does.

3.8 INTERPHASE MASS TRANSFER

Interphase mass transfer Γ_g is another undetermined term in mass conservation equations. This parameter defines the amount of gas that can evaporate or condensate between hydrocarbon gas and liquid system. Figure 3.9 shows control volume of a liquid and gas system that can exchange mass. Since the amount of gas that is exchanged between the phases depends on pressure and temperature variations in the control volume, Γ_g is computed as a function of pressure and temperature. Equation (3.146) illustrates the magnitude of gas mass transfer between oil and gas.

$$\Gamma_g = -\frac{\rho_{gsc}}{5.615B_o}\begin{bmatrix}\left(\frac{\partial R_s}{\partial P}\right)\frac{\partial P}{\partial t}\alpha_o + \left(\frac{\partial R_s}{\partial P}\right)\frac{\partial P}{\partial x}(u_o\alpha_o) + \\ \left(\frac{\partial R_s}{\partial T}\right)\frac{\partial T}{\partial t}\alpha_o + \left(\frac{\partial R_s}{\partial T}\right)\frac{\partial T}{\partial x}(u_o\alpha_o)\end{bmatrix}, \tag{3.146}$$

where R_s is solution gas oil ratio, B_o is oil formation volume factor, and ρ_{gsc} is gas standard density. These parameters can be calculated using either blackoil correlations or compositional models of hydrocarbon phases.

3.9 STATE RELATIONS

The primary variables that are calculated from the system of mass conservation and momentum conservation equations in multiphase flow models are pressure, liquid and gas volume fractions, and liquid and gas velocities. Other variables that appeared in the equations are dependent variables and are calculated as functions of the primary variables. Among the dependent variables, the ones that are related to fluid properties (density, viscosity, interfacial tensions, solution gas oil ratio, and oil formation volume factor) are state variables calculated from state relations.

In the development of UTWELL, there are two approaches to calculate state relations. One approach is based on empirical correlations, called blackoil models. The other approach is based on equation-of-state compositional models. These models have been developed under the phase behavior modules, where all the properties of the fluids (such as density, viscosity, enthalpy, compositions, and interfacial tensions) and the derivatives of properties with respect to pressure and temperature are computed.

Appendices B and C show the details of property calculations in UTWELL. We use Equation-of-State compositional approach and blackoil correlations, respectively.

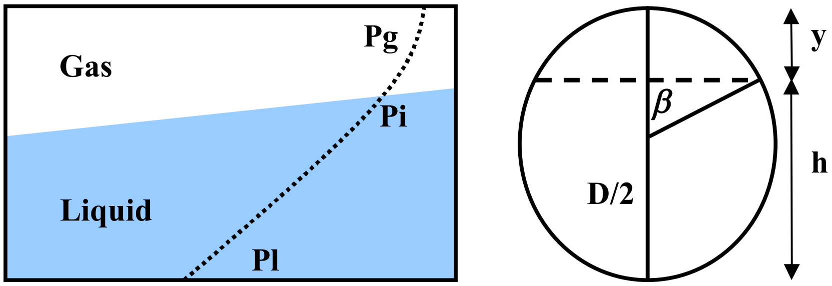

Figure 3.1 Schematic view of stratified flow in horizontal wells.

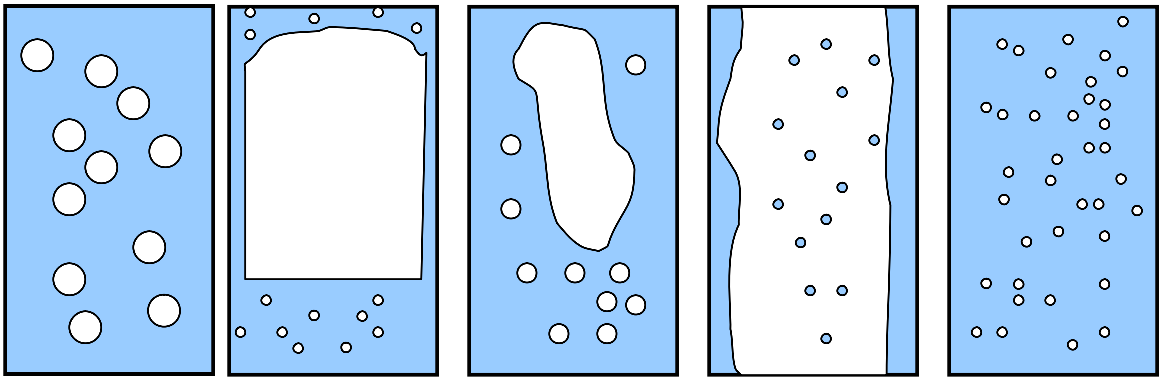
(a) (b) (c) (d) (e)

Figure 3.2 Schematic views of flow regimes in vertical wells, (a) bubbly flow, (b) slug flow, (c) churn flow, (d) annular flow (e) disperse bubbly flow.

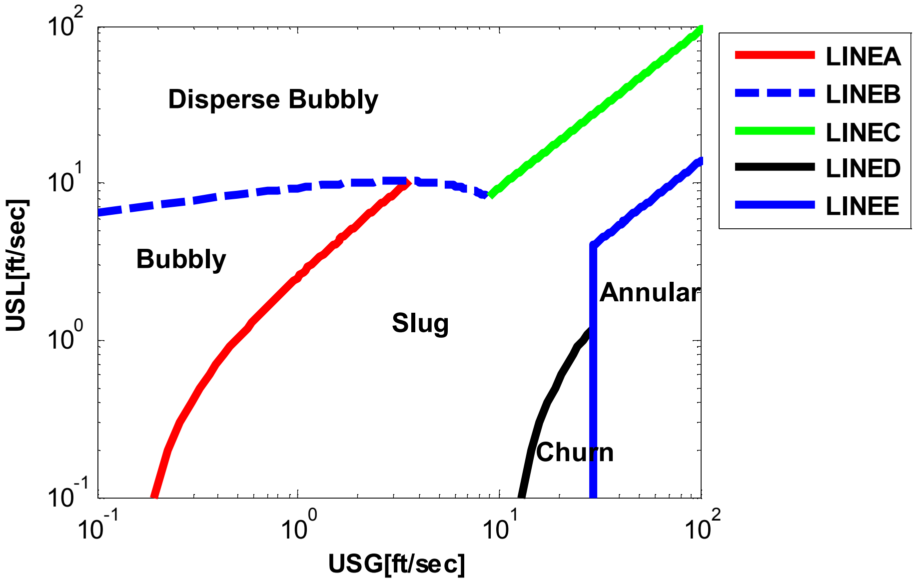

Figure 3.3 Flow pattern map detection for vertical and deviated wells, reproduced from Kaya et al. (1999), Ansari et al. (1994) and Hasan and Kabir (2007).

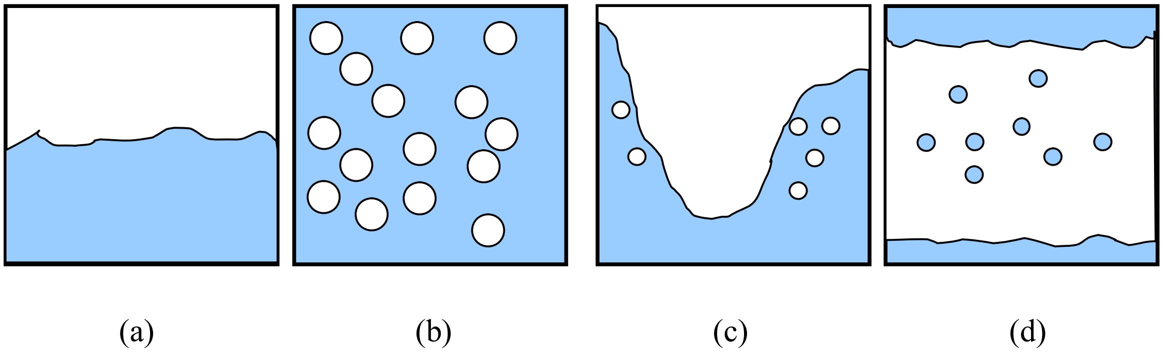

Figure 3.4 Schematic views of flow regimes in horizontal wells, (a) stratified flow, (b) bubbly flow, (c) intermittent flow, (d) annular flow.

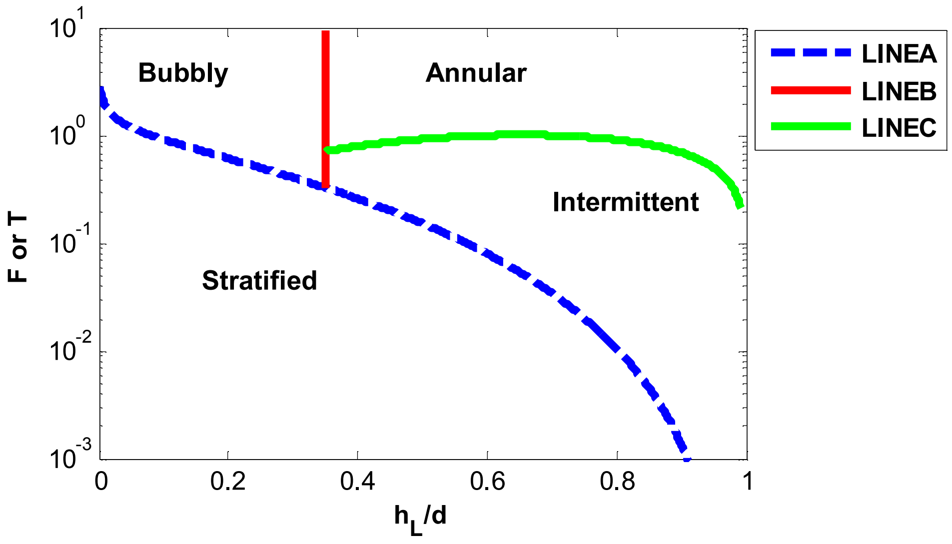

Figure 3.5 Flow pattern map for horizontal well, reproduced from Taitel and Dukler (1976) and Shoham (2005).

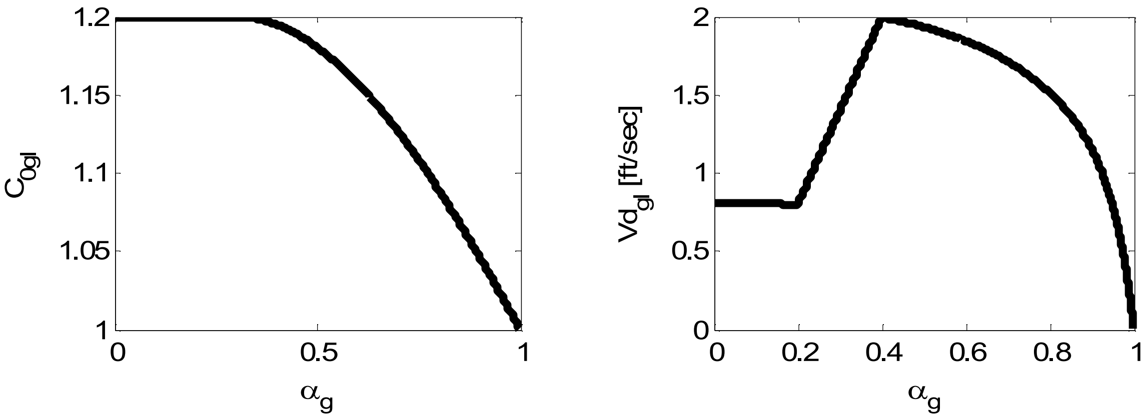

(a) (b)

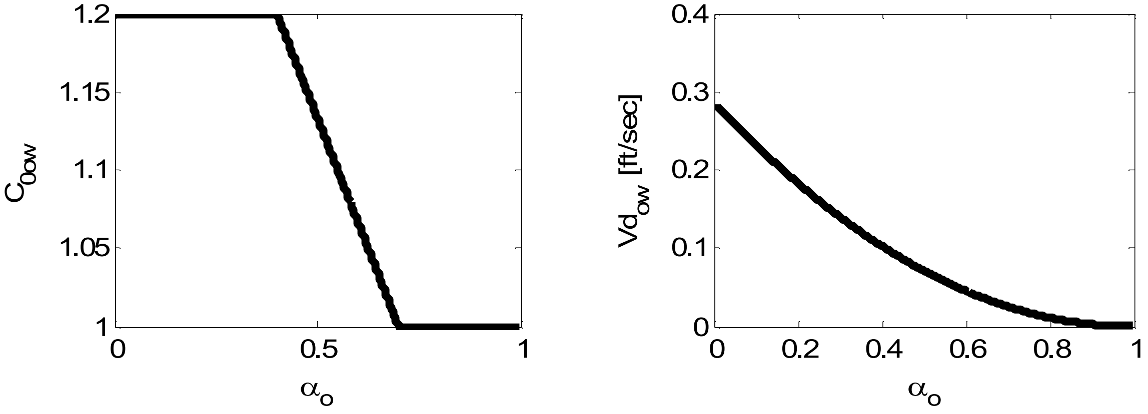

(c) (d)

Figure 3.6 Drift-flux models (a) gas-liquid profile coefficient (C0gl), gas-liquid drift velocity (Vdgl), oil-water profile parameter (C0ow), oil-water drift velocity (Vdow).

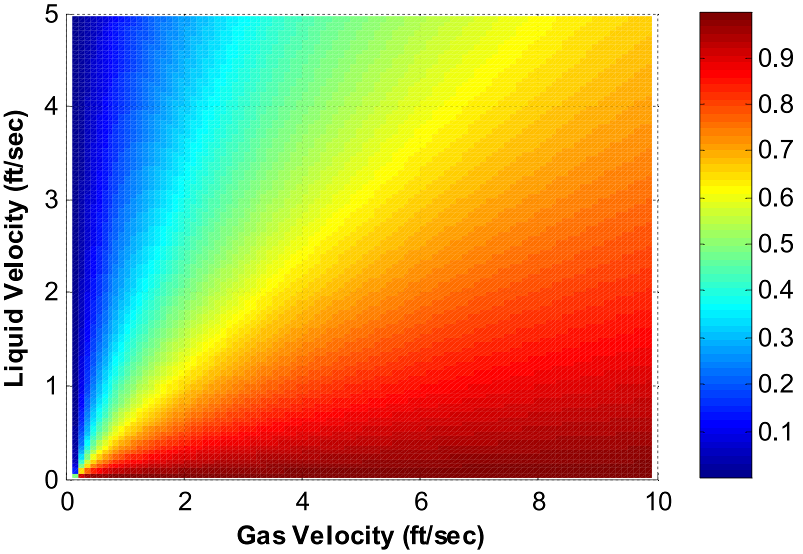

(a)

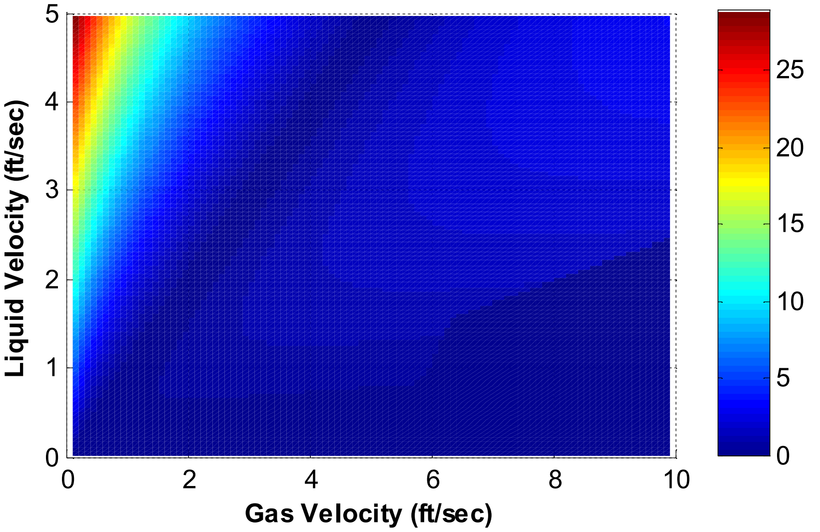

(b)

Figure 3.7 An example of interphase friction force coefficient calculation for various liquid and gas velocities, (a) gas volume fraction (b) FI

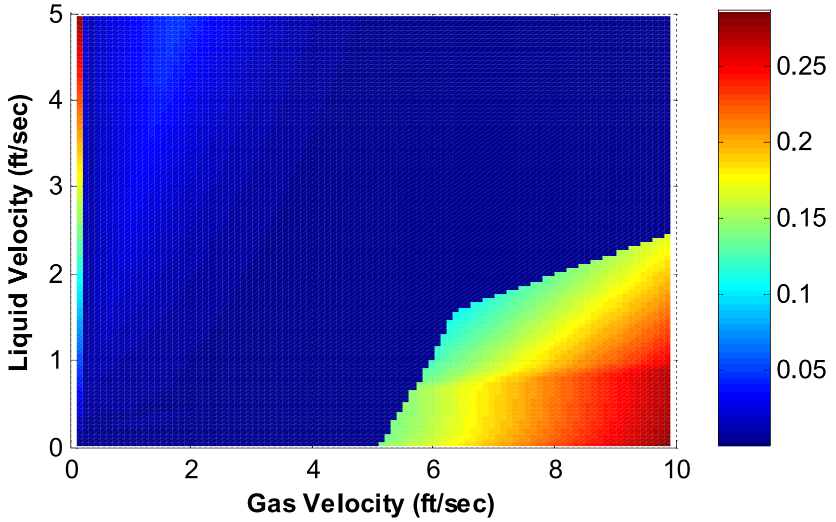

(a)

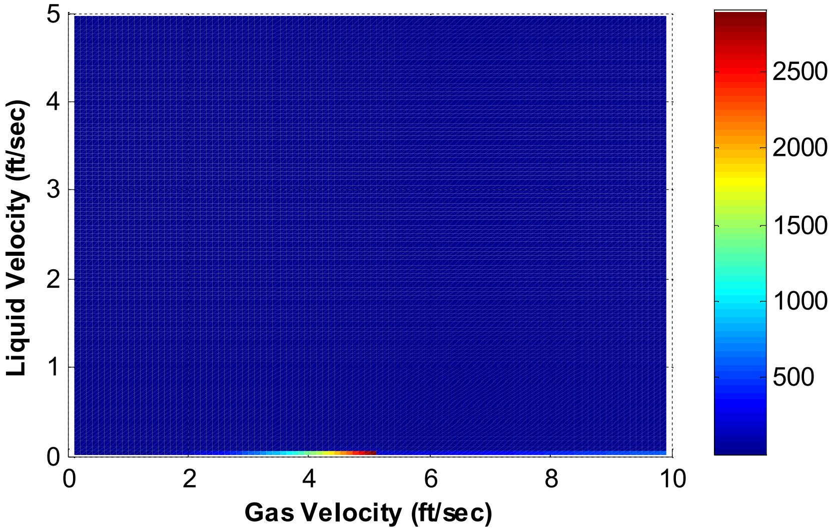

(b)

Figure 3.8 An example of phasic wall friction calculation for various liquid and gas velocities, (a) FWG, (b) FWL.

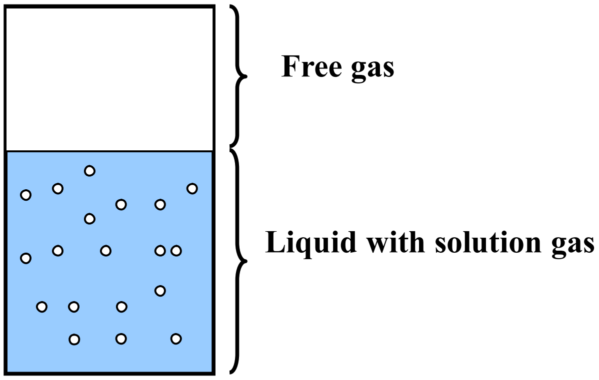

Figure 3.9 Schematic view of liquid gas equilibrium and interphase mass transfers.

Chapter 4: Wellbore Heat Transfer Models

Transportation of fluids in the wellbore always involves heat transfer between the fluid and its surrounding during production or injection processes. Most of the time, controlling the amount of heat exchange between these two systems is important in field operations. For example, in hot fluid injection heat-loss management is one of the crucial tasks to target the desired temperature of the injection process. In production systems, also monitoring the temperature of the fluid is important to control the route the fluid moves in its phase envelope. In fact, some hydrocarbon fluids can create precipitates and flow assurance problems at certain temperatures.

In this chapter, we study the process of heat transfer between wellbore and the surrounding (ambience), solving the coupled wellbore/surrounding energy equations. With the energy equation for the ambient and the wellbore taken into account, more accurate results are obtained for fluid temperature. In addition, since temperature affects the fluids' properties, a better approximation of temperature can yield a better approximation of flow rates and pressure.

4.1 ENERGY EQUATION IN THE WELLBORE

Although in reality the flowing liquid and gas temperatures are not equal, for the sake of simplicity we assume they are identical in our application. Accordingly, the energy equation that we solve to obtain fluid temperature in wellbore is the total energy conservation:

$$
\frac{\partial\left[\alpha_o\rho_o\left(\overline{h}_o+\frac{u_o^2}{2g_cJ_c}\right)\right]}{\partial t}+\frac{\partial\left[\alpha_g\rho_g\left(\overline{h}_g+\frac{u_g^2}{2g_cJ_c}\right)\right]}{\partial t}+\frac{\partial\left[\alpha_w\rho_w\left(\overline{h}_w+\frac{u_w^2}{2g_cJ_c}\right)\right]}{\partial t}+
$$

$$
\frac{1}{A}\frac{\partial\left[A\alpha_o\rho_ou_o\left(\overline{h}_o+\frac{u_o^2}{2g_cJ_c}\right)\right]}{\partial x}+\frac{1}{A}\frac{\partial\left[A\alpha_g\rho_gu_g\left(\overline{h}_g+\frac{u_g^2}{2g_cJ_c}\right)\right]}{\partial x}+\frac{1}{A}\frac{\partial\left[A\alpha_w\rho_wu_w\left(\overline{h}_w+\frac{u_w^2}{2g_cJ_c}\right)\right]}{\partial x}-
$$

$$
\dot{H}_w-\dot{H}_o-\dot{H}_g+\alpha_w\rho_w\frac{u_w}{g_cJ_c}gsin\theta+\alpha_o\rho_o\frac{u_o}{g_cJ_c}gsin\theta+\alpha_g\rho_g\frac{u_g}{g_cJ_c}gsin\theta+
$$

$$
\frac{\dot{Q}_{loss}}{A}=0. \tag{4.1}
$$

In the above equation, $\overline{h}_o$, $\overline{h}_g$, $\overline{h}_w$ are oil, gas and water enthalpies per unit mass, g_cJ_c are the unit conversion factors, $\dot{H}_o$, $\dot{H}_g$ and $\dot{H}_w$ are the oil, gas and water enthalpy influxes per unit well gridblock volume.

The enthalpy can be related to the pressure and temperature via the heat capacity ($C_p\left(\frac{Btu}{{}^\circ F-lbm}\right)$) and Joule Thomson coefficient, ($\eta\left(\frac{{}^\circ F}{Btu-ft^{-2}}\right)$):

$$
d\overline{h}_j=C_{pj}dT-\left(\frac{144}{J_c}\right)\eta_jC_{pj}dP,\quad j=o,g,w \tag{4.2}
$$

Hence, for any specific pressure and temperature, the liquid and gas enthalpies can be calculated with respect to a reference pressure and temperature. The enthalpy calculation is explained in detail in Appendices B and C for compositional and blackoil models.

4.2 WELLBORE HEAT LOSS MODEL

In Equation (4.1), $\dot{Q}_{loss}$ is the heat exchange, per unit length, between the fluid and the surrounding formation. This term is defined as

$$\dot{Q}_{loss} = 2\pi r_{to} U_{to} (T_f - T_{wb}), \tag{4.3}$$

where U_{to} is the overall heat transfer coefficient, T_f is the fluid temperature, r_{to} is the tubing outer radius and T_{wb} is the formation temperature at the vicinity of the wellbore.

Overall heat transfer coefficient is defined on the basis of composite layer geometry around the wellbore (Figure 4.1) and the heat transfer coefficient of each layer. Equation (4.4) shows the final expression for U_{to} as function of radius and heat transfer coefficient of composite layers

$$\frac{1}{U_{to}} = \frac{r_{to}}{r_{ti} h_{to}} + \frac{r_{to} \ln(r_{to}/r_{ti})}{k_t} + \frac{r_{to} \ln(r_{ins}/r_{to})}{k_{ins}} + \frac{r_{to}}{r_{ins}(h_c + h_r)} + \frac{r_{to} \ln(r_{co}/r_{ci})}{k_{cas}} + \frac{r_{to} \ln(r_{wb}/r_{co})}{k_{cem}}. \tag{4.4}$$

In Equation (4.4), the conduction heat transfer coefficients are user input values and the convection heat transfer coefficients are calculated using appropriate correlations (PIPESIM user manual, 2011).

4.3 AMBIENT TEMPERATURE MODEL

Heat transfer between the wellbore and the surrounding formation (ambient) causes temperature change not only in the wellbore fluid but also in the ambient formation. In Equation (4.3) T_{wb} is the temperature of the ambient fluid at the contact point of composite layer of wellbore and formation. Depending on the magnitude of the heat transfer between wellbore and ambience, T_{wb} can be significantly different than formation temperature far from wellbore. At a distance far from wellbore (~100ft), a constant geothermal temperature gradient can be maintained from top to the bottom of formation. However, getting closer to the wellbore this gradient is no longer constant.

Since ambient temperature is integrated with the heat loss calculation, an accurate estimation of this variable is crucial. In this section, we introduce robust numerical and analytical models for ambient temperature calculation that can be applied in the heat loss equation. Our analytical model is similar to Ramey's (1962) model with some modifications to include the superposition effect. In fact, Ramey's model is not sufficiently correct for wellbore temperature calculation during wellbore shutdown and startup conditions.

Assuming a cylindrical geometry around the wellbore, an axisymmetric two-dimensional model can be considered for heat transfer into the formation domain (Figure 4.2). Considering Fourier heat conduction in two-dimensional cylindrical geometry, the mathematical formulation of ambient temperature becomes

$$\frac{1}{r}\frac{\partial}{\partial r}\left(r\frac{\partial T}{\partial r}\right)+\frac{\partial}{\partial z}\left(\frac{\partial T}{\partial z}\right)=\frac{1}{\alpha_e}\frac{\partial T}{\partial t}, \tag{4.5}$$

where α_e is heat diffusivity coefficient

$$\alpha_e=\frac{\rho_e Cp_e}{K_e}. \tag{4.6}$$

To solve Equation (4.5) appropriate initial condition and boundary conditions should be applied. Equation (4.7) shows the initial distribution of ambient temperature and Equations (4.8) through (4.11) show the boundary conditions.

$$T(r,z,0)=T_{bh}-\left(\frac{T_{bh}-T_{surf}}{l_z}\right)\left(l_z-z\right), \tag{4.7}$$

$$\left.\frac{\partial T}{\partial r}\right|_{r_{wb}}=\frac{-Q_z}{2\pi r_{wb}K_e}, \tag{4.8}$$

$$\left.\frac{\partial T}{\partial r}\right|_{r\to\infty}=0, \tag{4.9}$$

$$T(r,0,t)=T_{surf}, \tag{4.10}$$

$$T(r,l_z,t)=T_{bh}. \tag{4.11}$$

One approach to obtain the ambient temperature from Equation (4.5) is discretizing the equation with finite difference schemes and solving it numerically (Erickson and Mai, 1992). Since in the discretization of Equation (4.5), logarithmic distances are used in the radial direction, we substitute r with a new variable $r^*=ln(r)$ in order to be able to discretize the equation linearly in the r-direction. Hence, we obtain

$$e^{-2r^*}\frac{\partial}{\partial r^*}\left(r^*\frac{\partial T}{\partial r^*}\right)+\frac{\partial}{\partial z}\left(\frac{\partial T}{\partial z}\right)=\frac{1}{\alpha_e}\frac{\partial T}{\partial t}. \tag{4.12}$$

The discretized form of Equation (4.12) yields a system of linear equations as

$$\left(a_{i-1,k}\right)T_{i-1,k}^{n+1}+\left(a_{i,k}\right)T_{i,k}^{n+1}+\left(a_{i+1,k}\right)T_{i+1,k}^{n+1}+\left(a_{i,k-1}\right)T_{i,k-1}^{n+1}+\left(a_{i,k+1}\right)T_{i,k+1}^{n+1}=-T_{i,k}^{n}, \tag{4.13}$$

where

$$a_{i-1,k} = a_{i+1,k} = \alpha_e e^{-2r_i^*} \left(\frac{\Delta t}{\Delta r_i^{*2}} \right), \tag{4.14}$$

$$a_{i,k} = -(2\alpha_e e^{-2r_i^*} \left(\frac{\Delta t}{\Delta r_i^{*2}} \right) + 2\alpha_e \left(\frac{\Delta t}{\Delta z_k^2} \right) + 1), \tag{4.15}$$

$$a_{i,k-1} = a_{i,k+1} = \alpha_e \left(\frac{\Delta t}{\Delta z_k^2} \right). \tag{4.16}$$

Using N_R grids in the *r*-direction and N_Z grids in the *z*-direction the gridblock dimension sizes are obtained as

$$\Delta r^* = \frac{ln\left(\frac{r_e}{r_{wb}} \right)}{N_R}, \tag{4.17}$$

$$\Delta z = \frac{l_z}{N_Z}. \tag{4.18}$$

The discretized form of the boundary conditions for Equation (4.13) is also defined as

$$T_{i,k}^{n=0} = T_{bh} - \left(\frac{T_{bh} - T_{surf}}{l_z} \right) \left(l_z - z(i) \right), \tag{4.19}$$

$$T_{i,1}^n = T_{surf}, \tag{4.20}$$

$$T_{i,n_z}^n = T_{bh}, \tag{4.21}$$

$$T_{1,k}^n = T_{2,k}^n + \frac{\Delta r}{2\pi r_{wb}} \frac{Q_z}{K_e}, \tag{4.22}$$

$$T_{n_r,k}^n = T_{n_r-1,k}^n. \tag{4.23}$$

Combining Equations (4.13) through (4.16) with Equations (4.19) through (4.23), we obtain a system of linear equation that can be solved using a linear solver.

Another approach to solve Equation (4.5) is using analytical solutions for radial geometry. If we assume that at $r \to \infty$, the ambient temperature is found from a constant geothermal gradient, we can only solve the Fourier heat conduction equation in the *r*-direction. With this assumption, we actually neglect the heat transfer in the *z*-direction. This assumption is reasonable at near wellbore since the temperature gradient in the *z*-direction is much smaller than the *r*-direction. Hence, Equation (4.5) can be simplified to

$$\frac{1}{r}\frac{\partial}{\partial r}\left(r\frac{\partial T}{\partial r}\right)=\frac{1}{\alpha_e}\frac{\partial T}{\partial t}. \tag{4.24}$$

Considering

$$r_D=\frac{r}{r_{wb}}, \tag{4.25}$$

$$t_D=\frac{t}{\alpha_e r_{wb}^2}, \tag{4.26}$$

$$T_D=2\pi K_e\left(\frac{T_0-T}{Q_z}\right), \tag{4.27}$$

Equation (4.24) can be written in non-dimensional form as

$$\frac{1}{r_D}\frac{\partial}{\partial r_D}\left(r_D\frac{\partial T_D}{\partial r_D}\right)=\frac{\partial T_D}{\partial t_D}. \tag{4.28}$$

The initial condition and boundary conditions for Equation (4.28) are also defined in non-dimensional form as in

$$T_D(r_D,0)=0, \tag{4.29}$$

$$r_D \left.\frac{\partial T_D}{\partial r_D}\right|_{r_D=1} = -1, \tag{4.30}$$

$$T_D(r_D \to \infty, t_D)=0, \tag{4.31}$$

$$\left.\frac{\partial T_D}{\partial r_D}\right|_{r_D \to \infty} = 0. \tag{4.32}$$

The analytical solution for Equation (3.28) can be divided into three regions, the early transient, later transient, and pseudo-steady state. When $t_{DE} = \frac{t}{\alpha_e r_{wb}^2} \le 0.1$ the solution is early transient as

$$T_D(r_D,t_D) = -0.5E_i\left(\frac{r_D^2}{4t_D}\right), \tag{4.33}$$

when $0.1 < t_{DE} \le \pi$ the solution is later transient as

$$T_D(r_D=1,t_D) = \frac{2t_D}{R^2} + lnR - \frac{3}{4} - 0.84e^{-\left(\frac{14.6819t_D}{R^2}\right)}, \tag{4.34}$$

where $R = \frac{r_e}{r_{wb}}$. Finally, when $\pi < t_{DE}$ the solution is pseudo-steady state as

$$T_D(r_D=1,t_D) = \frac{2t_D}{R^2} + lnR - \frac{3}{4}. \tag{4.35}$$

Converting the non-dimensional temperature to actual temperature the final solution for the ambient temperature becomes

$$T(r,t)=T(r,t_0)-Q_z\frac{I(r,t)}{2\pi K_e}, \tag{4.36}$$

where $I(t)$ is one of the solutions in early transient or later transient or pseudo-steady state. Equations (4.36) is valid only if a constant heat exchange rate between well and the formation is maintained. If the heat exchange rate becomes variable with time, the solution for the ambient temperature is modified based on the superposition principle. In variable heat flux condition, the ambient temperature solution becomes

$$T(r,t)=T(r,t_0)-Q_z(t_0)\frac{I(r,t_0)}{2\pi K_e}-\sum_{t_i=t_1}^{t_{n-1}=t-\delta t}\left(Q_z(t_i)-Q_z(t_{i-1})\right)\frac{I(r,(t-t_i))}{2\pi K_e}. \tag{4.37}$$

To evaluate the numerical and the analytical results, we made a comparison of ambient temperature calculation for a cyclic hot fluid injection. Table 1 shows the pertinent data for the well geometry. In this case, we injected hot fluid for three weeks and then shut down the well. To avoid full simulation of the fluid temperature in the wellbore, we assumed that the heat flux to the formation follows the curve shown in Figure 4.3. With this example, we only want to test the solution results for ambient temperature warm-up and cool-down processes.

Figure 4.4 shows the ambient temperature (T_{wb}) at the vicinity of the wellbore at a depth ($Z=2500ft$). As can be seen, the analytical solution with superposition (Equation 4.37) perfectly matches the numerical solution (Equation 4.13). However, the analytical solution without superposition effect (Equation 4.36) over estimates the ambient temperature during the warm-up period and underestimates the ambient temperature during the cool-down period. Since in this case we had variable heat exchange between wellbore and the formation, the analytical model without superposition is unable to accurately predict the ambient temperature. However, at constant heat-loss between wellbore and formation, the results for all methods are similar. Figure 4.5 illustrates same results for both analytical and numerical calculation of the ambient temperature versus time for a constant heat exchange of $20\left(\frac{Btu}{hr.ft}\right)$.

From the final results of numerical and analytical methods, we conclude that analytical models inclusive of superposition effects can reasonably achieve the same solution by numerical simulation. Since analytical methods are an order of magnitude faster than numerical simulations, the application of those models is more desirable for comprehensive wellbore modeling. Finally, since in reality the heat exchange between wellbore and formation varies with time, the analytical models with superposition effect is necessary for ambient temperature calculation.

Table 4.1 Wellbore and formation geometry

Inside diameter of well (ft)	0.4
Well length (ft)	5000
Surface temperature (^{o}F)	60
Bottom-hole temperature (^{o}F)	220
Formation radius (ft)	50
Number of gridblocks	50×50
Earth density (lb/ft^3)	132.0
Earth heat capacity (Btu/hr-ft)	0.252
Earth heat conductivity (Btu/hr-^{o}F-ft)	1.0

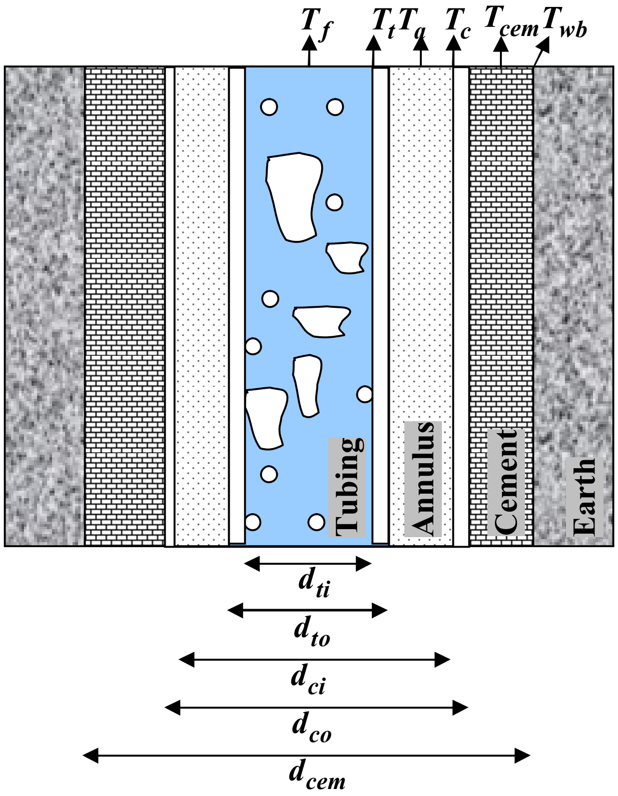

Figure 4.1 Schematic view of the composite layer geometry around the wellbore.

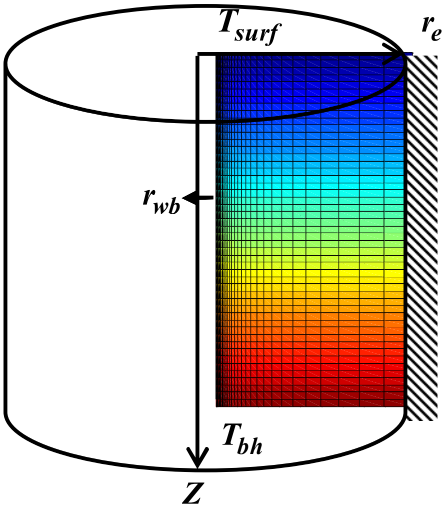

Figure 4.2 Two-dimensional axisymmetric models for surrounding formation with initial temperature distribution.

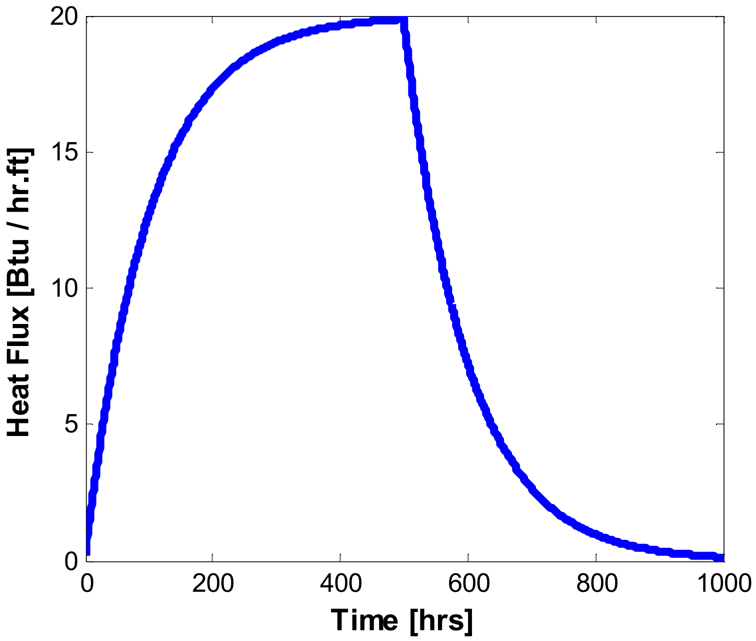

Figure 4.3 Heat rate per unit length adsorption to the formation versus time.

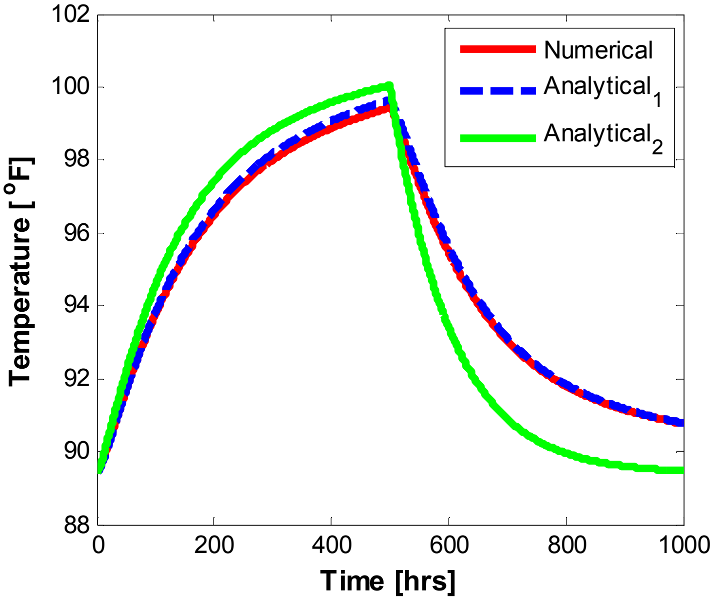

Figure 4.4 Comparison of numerical and analytical models (1 = with superposition, 2 = without superposition) results for ambient temperature calculation with variable heat exchange.

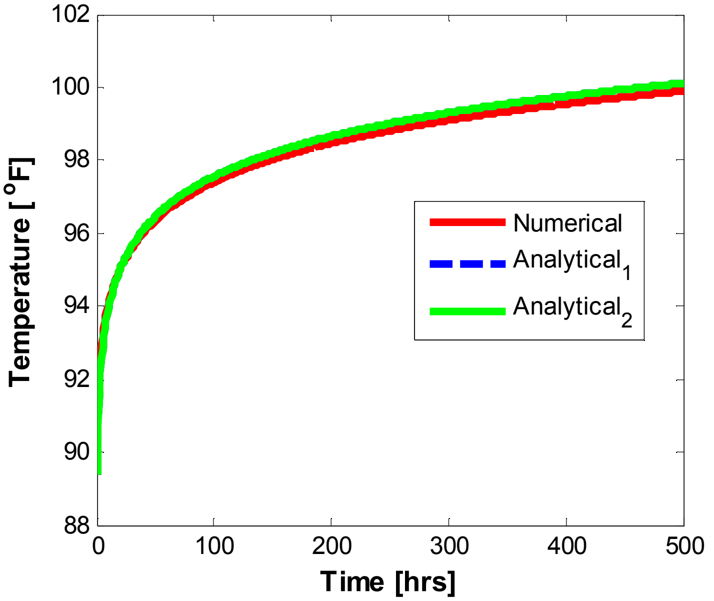

Figure 4.5 Comparison of numerical and analytical models (1= with superposition, 2 = without superposition) results for ambient temperature calculation with constant heat exchange.

Chapter 5: Wellbore Models Numerical Solutions

The UTWELL multiphase flow simulator solves six field equations to obtain six primary variables defining the state of fluids in the wellbore. The primary variables solved in UTWELL consist of volume fraction of water (α_w), volume fraction of gas (α_g), pressure (P), velocity of gas (u_g), velocity of liquid (u_l) and temperature (T). These variables are used to update the secondary variables from state relations, constitutive relations, and the phasic wall frictions.

In Chapters 3 and 4, we derived the basic differential equations that form mathematical models of the field equations. We obtained one-dimensional multiphase flow model along the well trajectory that includes mass conservation, momentum conservation and energy conservation equations.

In this chapter, we introduce different numerical algorithms that can be used to solve the field equations. We consider finite-difference methods to discretize the system of equations. We also investigate various numerical methods, such as semi-implicit, nearly implicit and fully implicit methods, to approximate the linearization of the equations. Furthermore, in the following sections, we verify the solution results of discretized equation for convergence, robustness, and accuracy against several test cases.

5.1 DISCRETIZATION OF FIELD EQUATIONS

One of the first steps in numerically solving a Partial Differential Equation (PDE) is approximating the time and spatial derivatives and linearizing the equations. In this section, we introduce the discretization of field equations with regard to flow models as in two-fluid and drift-flux. Since two-fluid models are subjected to the ill-posedness problem, employment of stabilizing techniques is necessary in the discretized equations. However, since drift-flux models are always well-posed, they do not need extra care in the discretization schemes.

Addition of second-order differential terms, such as viscous diffusivity terms, and the virtual mass term in the phasic momentum equations proffers well-posedness to the two-fluid model. Furthermore, selective implicit evaluation of spatial gradient terms at the new time and donor based parameters for flux terms yields numerical stability of the two-fluid models as well as faster computation time.

5.1.1 Discretization Method for Two-fluid Models

The guideline for discretization of the two-fluid model is listed as follows:

- A staggered gridding is considered as shown in Figure 5.1. Junctions of the gridblocks (vector nodes) are labeled with j index and the centers of gridblocks (scalar nodes) are labeled with K, L, and M.
- Pressure, temperature, and phase volume fractions are calculated in the center of the gridblocks and the phase velocity vectors are calculated at the junction.
- Liquid is the mixture of oil and water. The liquid phase properties are obtained from volumetric or mass averaging. The velocity of oil and water can be attributed to the velocity of liquid either using drift-flux approach or assuming no slip condition.
- A selective implicit evaluation is used for spatial gradient terms. Implicit terms are used only for velocities in mass and energy convection terms, pressure gradient in the momentum equation and interface mass and momentum transfer in mass and momentum equations.
- A donor-like formulation is used for the flux terms.

- Equations are reformulated in a way that can be degraded to single phase smoothly when some phases are disappeared.

The final form of reformulated equations used in two-fluid model consists of water mass conservation, liquid and gas mass conservation difference, liquid and gas mass conservation summation, liquid and gas momentum conservation difference, liquid and gas momentum conservation summation, and liquid and gas energy conservation summation as

$$\frac{\partial(\rho_w\alpha_w)}{\partial t}+\frac{1}{A}\frac{\partial A(\rho_w\alpha_w u_w)}{\partial x}=\dot{\psi}_w, \tag{5.1}$$

$$\frac{\partial\left(\rho_g\alpha_g-\rho_o\alpha_o-\rho_w\alpha_w\right)}{\partial t}+\frac{1}{A}\frac{\partial A\left(\rho_g\alpha_g u_g-\rho_o\alpha_o u_o-\rho_w\alpha_w u_w\right)}{\partial x}=2\Gamma_g+\dot{\psi}_g-\dot{\psi}_o-\dot{\psi}_w, \tag{5.2}$$

$$\frac{\partial\left(\rho_g\alpha_g+\rho_o\alpha_o+\rho_w\alpha_w\right)}{\partial t}+\frac{1}{A}\frac{\partial A\left(\rho_g\alpha_g u_g+\rho_o\alpha_o u_o+\rho_w\alpha_w u_w\right)}{\partial x}=\dot{\psi}_g+\dot{\psi}_o+\dot{\psi}_w, \tag{5.3}$$

$$\begin{aligned}&\frac{\partial u_g}{\partial t}-\frac{\partial u_l}{\partial t}+\frac{\partial u_g^2}{2\partial x}-\frac{\partial u_l^2}{2\partial x}=-\left(144.0g_c\right)\left(\frac{1}{\rho_g}-\frac{1}{\rho_l}\right)\frac{\partial P}{\partial x}-\frac{\rho_m}{\rho_g\rho_l}\left(\rho_l-\rho_g\right)B_y\frac{\partial y}{\partial x}-u_g FWG+\\&u_l FWL-\Gamma_g\left(\frac{\alpha_l\rho_l u_g+\alpha_g\rho_g u_l-\rho_m u_i}{\alpha_g\rho_g\alpha_l\rho_l}\right)-\left(\frac{\dot{\psi}_g u_g}{\alpha_g\rho_g}-\frac{\dot{\psi}_l u_l}{\alpha_l\rho_l}\right)-\rho_m(u_g-u_l)FI-\\&\frac{C^{vm}\rho_m}{\rho_g\rho_l}\frac{\partial\left(u_g-u_l\right)}{\partial t},\end{aligned} \tag{5.4}$$

$$\begin{aligned}&\alpha_g\rho_g\frac{\partial u_g}{\partial t}+\alpha_l\rho_l\frac{\partial u_l}{\partial t}+\alpha_g\rho_g\frac{\partial u_g^2}{2\partial x}+\alpha_l\rho_l\frac{\partial u_l^2}{2\partial x}=-\left(144.0g_c\right)\frac{\partial P}{\partial x}-\rho_m B_x-\\&\alpha_g\rho_g u_g FWG-\alpha_l\rho_l u_l FWL-\Gamma_g(u_g-u_l)-\dot{\psi}_g u_g-\dot{\psi}_l u_l,\end{aligned} \tag{5.5}$$

$$\frac{\partial\left[\alpha_g\rho_g\left(\bar{h}_g+\frac{u_g^2}{2g_cJ_c}\right)\right]}{\partial t}+\frac{\partial\left[\alpha_o\rho_o\left(\bar{h}_o+\frac{u_o^2}{2g_cJ_c}\right)\right]}{\partial t}+\frac{\partial\left[\alpha_w\rho_w\left(\bar{h}_w+\frac{u_w^2}{2g_cJ_c}\right)\right]}{\partial t}+$$

$$\frac{1}{A}\frac{\partial\left[A\alpha_g\rho_g u_g\left(\bar{h}_g+\frac{u_g^2}{2g_cJ_c}\right)\right]}{\partial x}+\frac{1}{A}\frac{\partial\left[A\alpha_o\rho_o u_o\left(\bar{h}_o+\frac{u_o^2}{2g_cJ_c}\right)\right]}{\partial x}+\frac{1}{A}\frac{\partial\left[A\alpha_w\rho_w u_w\left(\bar{h}_w+\frac{u_w^2}{2g_cJ_c}\right)\right]}{\partial x}=$$

$$\dot{H}_w+\dot{H}_o+\dot{H}_g-\alpha_g\rho_g\frac{u_g}{g_cJ_c}gsin\theta-\alpha_o\rho_o\frac{u_o}{g_cJ_c}gsin\theta-\alpha_w\rho_w\frac{u_w}{g_cJ_c}gsin\theta-$$

$$\frac{\dot{Q}_{loss}}{A}. \tag{5.6}$$

Equations (5.1) through (5.6) can be discretized to

Water Mass Conservation

$$V_b\left[\rho_{w,L}^n\left(\tilde{\alpha}_{w,L}^{n+1}-\alpha_{w,L}^n\right)+\alpha_{w,L}^n\left(\tilde{\rho}_{w,L}^{n+1}-\rho_{w,L}^n\right)\right]+$$

$$\Delta t\left[\dot{\alpha}_{w,j+1}^n\dot{\rho}_{w,j+1}^n A_{j+1}^n u_{w,j+1}^{n+1}-\dot{\alpha}_{w,j}^n\dot{\rho}_{w,j}^n A_j^n u_{w,j}^{n+1}\right]=V_b\Delta t\dot{\psi}_{w,L}^n, \tag{5.7}$$

Gas and Liquid Mass Conservation Difference

$$V_b\left[\rho_{g,L}^n\left(\tilde{\alpha}_{g,L}^{n+1}-\alpha_{g,L}^n\right)-\rho_{o,L}^n\left(\tilde{\alpha}_{o,L}^{n+1}-\alpha_{o,L}^n\right)-\rho_{w,L}^n\left(\tilde{\alpha}_{w,L}^{n+1}-\alpha_{w,L}^n\right)\right]+$$

$$V_b\left[\alpha_{g,L}^n\left(\tilde{\rho}_{g,L}^{n+1}-\rho_{g,L}^n\right)-\alpha_{o,L}^n\left(\tilde{\rho}_{o,L}^{n+1}-\rho_{o,L}^n\right)-\alpha_{w,L}^n\left(\tilde{\rho}_{w,L}^{n+1}-\rho_{w,L}^n\right)\right]+$$

$$\Delta t\left[\dot{\alpha}_{g,j+1}^n\dot{\rho}_{g,j+1}^n A_{j+1}^n u_{g,j+1}^{n+1}-\dot{\alpha}_{g,j}^n\dot{\rho}_{g,j}^n A_j^n u_{g,j}^{n+1}\right]-$$

$$\Delta t\left[\dot{\alpha}_{o,j+1}^n\dot{\rho}_{o,j+1}^n A_{j+1}^n u_{o,j+1}^{n+1}-\dot{\alpha}_{o,j}^n\dot{\rho}_{o,j}^n A_j^n u_{o,j}^{n+1}\right]-$$

$$\Delta t\left[\dot{\alpha}_{w,j+1}^n\dot{\rho}_{w,j+1}^n A_{j+1}^n u_{w,j+1}^{n+1}-\dot{\alpha}_{w,j}^n\dot{\rho}_{w,j}^n A_j^n u_{w,j}^{n+1}\right]=$$

$$V_b\Delta t\left(2\tilde{\Gamma}_g^{n+1}+\dot{\psi}_{g,L}^n-\dot{\psi}_{o,L}^n-\dot{\psi}_{w,L}^n\right), \tag{5.8}$$

Gas and Liquid Mass Conservation Summation

$$
\begin{aligned}
&V_b\left[\rho_{g,L}^{n}\left(\tilde{\alpha}_{g,L}^{n+1}-\alpha_{g,L}^{n}\right)+\rho_{o,L}^{n}\left(\tilde{\alpha}_{o,L}^{n+1}-\alpha_{o,L}^{n}\right)+\rho_{w,L}^{n}\left(\tilde{\alpha}_{w,L}^{n+1}-\alpha_{w,L}^{n}\right)\right]+\\
&V_b\left[\alpha_{g,L}^{n}\left(\tilde{\rho}_{g,L}^{n+1}-\rho_{g,L}^{n}\right)+\alpha_{o,L}^{n}\left(\tilde{\rho}_{o,L}^{n+1}-\rho_{o,L}^{n}\right)+\alpha_{w,L}^{n}\left(\tilde{\rho}_{w,L}^{n+1}-\rho_{w,L}^{n}\right)\right]+\\
&\Delta t\left[\dot{\alpha}_{g,j+1}^{n}\dot{\rho}_{g,j+1}^{n}A_{j+1}^{n}u_{g,j+1}^{n+1}-\dot{\alpha}_{g,j}^{n}\dot{\rho}_{g,j}^{n}A_{j}^{n}u_{g,j}^{n+1}\right]+\\
&\Delta t\left[\dot{\alpha}_{o,j+1}^{n}\dot{\rho}_{o,j+1}^{n}A_{j+1}^{n}u_{o,j+1}^{n+1}-\dot{\alpha}_{o,j}^{n}\dot{\rho}_{o,j}^{n}A_{j}^{n}u_{o,j}^{n+1}\right]+\\
&\Delta t\left[\dot{\alpha}_{w,j+1}^{n}\dot{\rho}_{w,j+1}^{n}A_{j+1}^{n}u_{w,j+1}^{n+1}-\dot{\alpha}_{w,j}^{n}\dot{\rho}_{w,j}^{n}A_{j}^{n}u_{w,j}^{n+1}\right]=\\
&V_b\Delta t\left(\dot{\psi}_{g,L}^{n}+\dot{\psi}_{o,L}^{n}+\dot{\psi}_{w,L}^{n}\right),
\end{aligned}
\tag{5.9}
$$

Gas and Liquid Momentum Conservation Difference

$$
\begin{aligned}
&\Delta x_j\left(1+\frac{C^{vm}\rho_m^2}{\rho_g\rho_l}\right)_j^n\left[\left(u_{g,j}^{n+1}-u_{g,j}^{n}\right)-\left(u_{l,j}^{n+1}-u_{l,j}^{n}\right)\right]+\\
&\frac{\Delta t}{2}\left[\left(\frac{\dot{\alpha}_g\dot{\rho}_g}{\alpha_g\rho_g}\right)_j^n\left((u_g^2)_L^n-(u_g^2)_K^n\right)-\left(\frac{\dot{\alpha}_l\dot{\rho}_l}{\alpha_l\rho_l}\right)_j^n\left((u_l^2)_L^n-(u_l^2)_K^n\right)\right]-\\
&\frac{\Delta t}{2}\left[\left(\frac{\dot{\alpha}_g\dot{\rho}_g}{\alpha_g\rho_g}\right)_j^n VISG_j^n-\left(\frac{\dot{\alpha}_l\dot{\rho}_l}{\alpha_l\rho_l}\right)_j^n VISL_j^n\right]=\\
&-\Delta t\left(144.0g_c\right)\left(\frac{\rho_l-\rho_g}{\rho_l\rho_g}\right)_j^n\left(P_L^{n+1}-P_K^{n+1}\right)-\Delta t\Delta x_j FWG_j^n u_{g,j}^{n+1}+\Delta t\Delta x_j FWL_j^n u_{l,j}^{n+1}\\
&+\Delta t\Delta x_j\left(\frac{\Gamma_g}{\alpha_g\rho_g\alpha_l\rho_l}\right)_j^n\left(\rho_{m,j}^{n}u_{i,j}^{n+1}-\alpha_{l,j}^{n}\rho_{l,j}^{n}u_{g,j}^{n+1}-\alpha_{g,j}^{n}\rho_{g,j}^{n}u_{l,j}^{n+1}\right)\\
&+\Delta t\Delta x_j f_{x,j}^n\left(\frac{1}{\alpha_g\rho_g}+\frac{1}{\alpha_l\rho_l}\right)_j^n\left(fwg_j^n u_{g,j}^{n+1}-fwl_j^n u_{l,j}^{n+1}\right)\\
&-\Delta t\Delta x_j\left(\rho_m FI\right)_j^n\left[(1+f_x(C_{1gl}-1))_j^n u_{g,j}^{n+1}-(1+f_x(C_{0gl}-1))_j^n u_{l,j}^{n+1}\right]\\
&-\Delta t\left(\frac{\rho_m}{\rho_g\rho_l}\right)_j^n\left(\rho_l-\rho_g\right)_j^n B_y\left(y_L^n-y_K^n\right)
\end{aligned}
$$

$$-\Delta t \Delta x_j \left[\left(\frac{\dot{\alpha}_g \dot{\rho}_g}{\alpha_g \rho_g} \right)_j^n \left(\frac{\dot{\psi}_g}{\alpha_g \rho_g} \right)_j^n u_{g,j}^{n+1} - \left(\frac{\dot{\alpha}_l \dot{\rho}_l}{\alpha_l \rho_l} \right)_j^n \left(\frac{\dot{\psi}_l}{\alpha_l \rho_l} \right)_j^n u_{l,j}^{n+1} \right]. \tag{5.10}$$

VISG and VISL in Equation (5.10) are the viscous-like terms for gas and liquid phase that are added for the stability and well-posedness of the phasic momentum equations. These terms are defined as

$$VISG_j^n = \frac{1}{2} \left[\left| u_{g,L}^n \right| \left(u_{g,j+1}^n \frac{A_{j+1}}{A_j} - u_{g,j}^n \right) - \left| u_{g,K}^n \right| \left(u_{g,j}^n - u_{g,j-1}^n \frac{A_{j-1}}{A_j} \right) \right], \tag{5.11}$$

$$VISL_j^n = \frac{1}{2} \left[\left| u_{l,L}^n \right| \left(u_{l,j+1}^n \frac{A_{j+1}}{A_j} - u_{l,j}^n \right) - \left| u_{l,K}^n \right| \left(u_{l,j}^n - u_{l,j-1}^n \frac{A_{j-1}}{A_j} \right) \right]. \tag{5.12}$$

f_x in Equation (5.10) is also the coefficient with the value of zero or one that incorporates the extra terms for the dispersed drag model. When the flow regime is bubbly, slug or churn, f_x is one; otherwise, it is zero. In dispersed flow, f_{wg} and f_{wl} are added using the following equations to incorporate the surface drag forces of dispersed phase and continuous phase.

$$f_{wl} = \alpha_l \alpha_g \rho_l FWL, \tag{5.13}$$

$$f_{wg} = \alpha_l \alpha_g \rho_g FWG. \tag{5.14}$$

The liquid and gas profile parameters C_{0gl} and C_{1gl} also appear in the dispersed flow regimes, where C_{0gl} is obtained from Chapter 3 and C_{1gl} is defined as follows:

$$C_{1gl} = \left(\frac{1 - \alpha_g C_{0gl}}{1 - \alpha_g} \right). \tag{5.15}$$

Moreover, in the momentum difference equation for stratified flows, the gravity term for liquid height gradient in the axial direction is incorporated as $\Delta t\left(\frac{\rho_m}{\rho_g \rho_l}\right)_j^n \left(\rho_l - \rho_g\right)_j^n B_y \left(y_L^n - y_K^n\right)$ where

$$y_L = \frac{D}{2}\left(1 + cos\beta\right), \tag{5.16}$$

$$\pi\alpha_g = D - cos\beta sin\beta, \tag{5.17}$$

$$B_y = gsin\theta. \tag{5.18}$$

Gas and Liquid Momentum Conservation Summation

$$\begin{aligned}
&\Delta x_j \left[\left(\alpha_g \rho_g\right)_j^n \left(u_{g,j}^{n+1} - u_{g,j}^n\right) + \left(\alpha_l \rho_l\right)_j^n \left(u_{l,j}^{n+1} - u_{l,j}^n\right)\right] + \\
&\frac{\Delta t}{2}\left[\left(\dot{\alpha}_g \dot{\rho}_g\right)_j^n \left((u_g^2)_L^n - (u_g^2)_K^n\right) + \left(\dot{\alpha}_l \dot{\rho}_l\right)_j^n \left((u_l^2)_L^n - (u_l^2)_K^n\right)\right] - \\
&\frac{\Delta t}{2}\left[\left(\dot{\alpha}_g \dot{\rho}_g\right)_j^n VISG_j^n + \left(\dot{\alpha}_l \dot{\rho}_l\right)_j^n VISL_j^n\right] = \\
&-\Delta t\left(144.0 g_c\right)\left(P_L^{n+1} - P_K^{n+1}\right) - \Delta t \Delta x_j (\rho_m)_j^n B_x - \Delta t \Delta x_j (\alpha_g \rho_g)_j^n FWG_j^n u_{g,j}^{n+1} \\
&-\Delta t \Delta x_j (\alpha_l \rho_l)_j^n FWL_j^n u_{l,j}^{n+1} - \Delta t \Delta x_j (\varGamma_g)_j^n \left(u_g - u_l\right)_j^{n+1} \\
&-\Delta t \Delta x_j (\dot{\psi}_g)_j^n u_{g,j}^{n+1} - \Delta t \Delta x_j (\dot{\psi}_l)_j^n u_{l,j}^{n+1}.
\end{aligned} \tag{5.19}$$

Gas and Liquid Energy Conservation Summation

$$\begin{aligned}
&V_b\left[\alpha_{o,L}^{n+1} \rho_{o,L}^{n+1}\left(\bar{h}_{o,L}^{n+1} + \frac{(u_o^2)_L^{n+1}}{2 g_c J_c}\right) - \alpha_{o,L}^n \rho_{o,L}^n \left(\bar{h}_{o,L}^n + \frac{(u_o^2)_L^n}{2 g_c J_c}\right)\right] + \\
&V_b\left[\alpha_{g,L}^{n+1} \rho_{g,L}^{n+1}\left(\bar{h}_{g,L}^{n+1} + \frac{(u_g^2)_L^{n+1}}{2 g_c J_c}\right) - \alpha_{g,L}^n \rho_{g,L}^n \left(\bar{h}_{g,L}^n + \frac{(u_g^2)_L^n}{2 g_c J_c}\right)\right] + \\
&V_b\left[\alpha_{w,L}^{n+1} \rho_{w,L}^{n+1}\left(\bar{h}_{w,L}^{n+1} + \frac{(u_w^2)_L^{n+1}}{2 g_c J_c}\right) - \alpha_{w,L}^n \rho_{w,L}^n \left(\bar{h}_{w,L}^n + \frac{(u_w^2)_L^n}{2 g_c J_c}\right)\right] +
\end{aligned}$$

$$\Delta t\left[A_{j+1}^{n}\dot{\alpha}_{o,j+1}^{n+1}\dot{\rho}_{o,j+1}^{n+1}u_{o,j+1}^{n+1}\left(\dot{\bar{h}}_{o,j+1}^{n+1}+\frac{(u_o^2)_{j+1}^{n+1}}{2g_cJ_c}\right)-A_{j}^{n}\dot{\alpha}_{o,j}^{n+1}\dot{\rho}_{o,j}^{n+1}u_{o,j}^{n+1}\left(\dot{\bar{h}}_{o,j}^{n+1}+\frac{(u_o^2)_{j}^{n+1}}{2g_cJ_c}\right)\right]$$

$$\Delta t\left[A_{j+1}^{n}\dot{\alpha}_{g,j+1}^{n+1}\dot{\rho}_{g,j+1}^{n+1}u_{g,j+1}^{n+1}\left(\dot{\bar{h}}_{g,j+1}^{n+1}+\frac{(u_g^2)_{j+1}^{n+1}}{2g_cJ_c}\right)-A_{j}^{n}\dot{\alpha}_{g,j}^{n+1}\dot{\rho}_{g,j}^{n+1}u_{g,j}^{n+1}\left(\dot{\bar{h}}_{g,j}^{n+1}+\frac{(u_g^2)_{j}^{n+1}}{2g_cJ_c}\right)\right]$$

$$\Delta t\left[A_{j+1}^{n}\dot{\alpha}_{w,j+1}^{n+1}\dot{\rho}_{w,j+1}^{n+1}u_{w,j+1}^{n+1}\left(\dot{\bar{h}}_{w,j+1}^{n+1}+\frac{(u_w^2)_{j+1}^{n+1}}{2g_cJ_c}\right)-A_{j}^{n}\dot{\alpha}_{w,j}^{n+1}\dot{\rho}_{w,j}^{n+1}u_{w,j}^{n+1}\left(\dot{\bar{h}}_{w,j}^{n+1}+\frac{(u_w^2)_{j}^{n+1}}{2g_cJ_c}\right)\right]=$$

$$V_b\Delta t\left[\dot{H}_{o,L}^{n+1}+\dot{H}_{g,L}^{n+1}+\dot{H}_{w,L}^{n+1}\right]-$$

$$V_b\Delta t\left[\alpha_{o,L}^{n+1}\rho_{o,L}^{n+1}\frac{u_{o,L}^{n+1}}{g_cJ_c}g\sin\theta+\alpha_{g,L}^{n+1}\rho_{g,L}^{n+1}\frac{u_{g,L}^{n+1}}{g_cJ_c}g\sin\theta+\alpha_{w,L}^{n+1}\rho_{w,L}^{n+1}\frac{u_{w,L}^{n+1}}{g_cJ_c}g\sin\theta\right]-$$

$$V_b\Delta t\left[\frac{\dot{Q}_{loss,L}^{n}}{A_j^n}\right]. \tag{5.20}$$

In discretized equations, V_b is the bulk volume of the gridblock, Δx_j is the grid size length, Δt is the time step size, n is time index, L is the gridblock center index, j is gridblock junction index. In addition, parameters with dot (.) over-score correspond to donor-like parameters or influx rate terms; parameters with tilde ($\sim$) are provisional advanced time variables with intermediate value before the final update.

Since the primary variables in our linearized equations are only $\alpha_w^{n+1},\alpha_g^{n+1},u_l^{n+1},u_g^{n+1},T^{n+1},P^{n+1}$; the secondary variables that appeared in advanced time ($n+1$) are written as a function of primary variables. Hence, the following auxiliary equations are combined with discretized equations to solve the system of equations:

$$\alpha_w^{n+1}+\alpha_o^{n+1}=\alpha_l^{n+1}, \tag{5.21}$$

$$\alpha_w^{n+1} + \alpha_o^{n+1} + \alpha_g^{n+1} = 1, \tag{5.22}$$

$$u_o^{n+1} = C_{0ow} u_l^{n+1} + Vd_{ow}, \tag{5.23}$$

$$u_w^{n+1} = C_{0ow} u_l^{n+1} + Vd_{ow}, \tag{5.24}$$

$$\tilde{\Gamma}_g^{n+1} = -\left(\frac{\alpha_{o,L}^n \rho_{gsc}}{5.615 B_{o,L}^n} \right) \begin{bmatrix} \left(\frac{\partial R_s}{\partial P} \right)_L^n \left(P_L^{n+1} - P_L^n \right) + \left(\frac{\partial R_s}{\partial T} \right)_L^n \left(T_L^{n+1} - T_L^n \right) + \\ \left(\frac{\partial R_s}{\partial P} \right)_L^n \left(\frac{P_K^n - P_L^n}{\Delta x_j} \right) \left(\alpha_{o,L}^n u_{o,L}^n \right) + \\ \left(\frac{\partial R_s}{\partial T} \right)_L^n \left(\frac{T_K^n - T_L^n}{\Delta x_j} \right) \left(\alpha_{o,L}^n u_{o,L}^n \right) \end{bmatrix}, \tag{5.25}$$

$$\tilde{\rho}_{w,L}^{n+1} = \rho_{w,L}^n + \left(\frac{\partial \rho_w}{\partial P} \right)_L^n \left(P_L^{n+1} - P_L^n \right) + \left(\frac{\partial \rho_w}{\partial T} \right)_L^n \left(T_L^{n+1} - T_L^n \right), \tag{5.26}$$

$$\tilde{\rho}_{o,L}^{n+1} = \rho_{o,L}^n + \left(\frac{\partial \rho_o}{\partial P} \right)_L^n \left(P_L^{n+1} - P_L^n \right) + \left(\frac{\partial \rho_o}{\partial T} \right)_L^n \left(T_L^{n+1} - T_L^n \right), \tag{5.27}$$

$$\tilde{\rho}_{g,L}^{n+1} = \rho_{g,L}^n + \left(\frac{\partial \rho_g}{\partial P} \right)_L^n \left(P_L^{n+1} - P_L^n \right) + \left(\frac{\partial \rho_g}{\partial T} \right)_L^n \left(T_L^{n+1} - T_L^n \right). \tag{5.28}$$

Furthermore, the junction parameters (parameters defined at the junction without the over-score dot) are calculated from the linear interpolation of neighboring cells and donor-like parameters (Φ) are defined as follows:

if $u_j \neq 0$,

$$\dot{\Phi}_j = \frac{1}{2}\left(\Phi_K + \Phi_L \right) + \frac{1}{2} \frac{|u_j|}{u_j} \left(\Phi_K - \Phi_L \right), \tag{5.29}$$

if $u_j = 0$ and $P_K > P_L$,

$$\dot{\Phi}_j = \Phi_K, \tag{5.30}$$

if $u_j = 0$ and $P_K < P_L$,

$$\dot{\Phi}_j = \Phi_L, \tag{5.31}$$

if $u_j = 0$ and $P_K = P_L$,

$$\dot{\Phi}_j = \frac{\rho_K \Phi_K + \rho_L \Phi_L}{\rho_K + \rho_L}, \tag{5.32}$$

where u_j is the junction velocity for specific phase, K and L are the mass control volume indices in the neighboring of junction and $\dot{\Phi}$ is the donor parameter (i.e. density).

5.1.2 Discretization Method for Drift-flux Model

Similar to two-fluid model, a staggered gridding is used for discretization of drift-flux model. The mixture velocity vector is calculated at the junction and the pressure, temperature, and phasic volume fractions are calculated in the center of the gridblock.

The discretized equations in the drift-flux model consist of water mass conservation, liquid mass conservation, mixture mass conservation, mixture momentum conservation and mixture energy conservation. The final forms of those equations are

$$\frac{\partial(\rho_w \alpha_w)}{\partial t} + \frac{1}{A}\frac{\partial A(\rho_w \alpha_w u_w)}{\partial x} = \dot{\psi}_w, \tag{5.33}$$

$$\frac{\partial(\rho_o \alpha_o + \rho_w \alpha_w)}{\partial t} + \frac{1}{A}\frac{\partial A(\rho_o \alpha_o u_o + \rho_w \alpha_w u_w)}{\partial x} = -\Gamma_g + \dot{\psi}_o + \dot{\psi}_w, \tag{5.34}$$

$$\frac{\partial\left(\rho_g \alpha_g + \rho_o \alpha_o + \rho_w \alpha_w\right)}{\partial t} + \frac{1}{A}\frac{\partial A\left(\rho_g \alpha_g u_g + \rho_o \alpha_o u_o + \rho_w \alpha_w u_w\right)}{\partial x} = \dot{\psi}_g + \dot{\psi}_o + \dot{\psi}_w, \tag{5.35}$$

$$\frac{\partial(\rho_m u_m)}{\partial t} + \frac{\partial\left(\rho_g \alpha_g u_g^2 + \rho_o \alpha_o u_o^2 + \rho_w \alpha_w u_w^2\right)}{\partial x} = -(144.0 g_c)\frac{\partial P}{\partial x} - \rho_m g sin\theta - \frac{\tau_m \pi D}{A}, \tag{5.36}$$

$$\frac{\partial\left[\alpha_g\rho_g\left(\overline{h}_g+\frac{u_g^2}{2g_cJ_c}\right)\right]}{\partial t}+\frac{\partial\left[\alpha_o\rho_o\left(\overline{h}_o+\frac{u_o^2}{2g_cJ_c}\right)\right]}{\partial t}+\frac{\partial\left[\alpha_w\rho_w\left(\overline{h}_w+\frac{u_w^2}{2g_cJ_c}\right)\right]}{\partial t}+$$

$$\frac{1}{A}\frac{\partial\left[A\alpha_g\rho_g u_g\left(\overline{h}_g+\frac{u_g^2}{2g_cJ_c}\right)\right]}{\partial x}+\frac{1}{A}\frac{\partial\left[A\alpha_o\rho_o u_o\left(\overline{h}_o+\frac{u_o^2}{2g_cJ_c}\right)\right]}{\partial x}+\frac{1}{A}\frac{\partial\left[A\alpha_w\rho_w u_w\left(\overline{h}_w+\frac{u_w^2}{2g_cJ_c}\right)\right]}{\partial x}=$$

$$\dot{H}_w+\dot{H}_o+\dot{H}_g-\alpha_g\rho_g\frac{u_g}{g_cJ_c}gsin\theta-\alpha_o\rho_o\frac{u_o}{g_cJ_c}gsin\theta-\alpha_w\rho_w\frac{u_w}{g_cJ_c}gsin\theta-\frac{\dot{Q}_{loss}}{A}. \qquad (5.37)$$

Using a first-order upwind scheme, the discretized form of Equations (5.33) through (5.37) becomes

Water Mass Conservation

$$V_b\left[\rho_{w,L}^{n+1}\alpha_{w,L}^{n+1}-\rho_{w,L}^{n}\alpha_{w,L}^{n}\right]+$$
$$\Delta t\left[\alpha_{w,j}^{n+1}\rho_{w,j}^{n+1}A_j^n u_{w,j}^{n+1}-\alpha_{w,j-1}^{n+1}\rho_{w,j-1}^{n+1}A_{j-1}^{n}u_{w,j-1}^{n+1}\right]=V_b\Delta t\dot{\psi}_{w,L}^{n+1}. \qquad (5.38)$$

Liquid Mass Conservation

$$V_b\left[\left(\rho_{o,L}^{n+1}\alpha_{o,L}^{n+1}-\rho_{o,L}^{n}\alpha_{o,L}^{n}\right)+\left(\rho_{w,L}^{n+1}\alpha_{w,L}^{n+1}-\rho_{w,L}^{n}\alpha_{w,L}^{n}\right)\right]+$$
$$\Delta t\left[\alpha_{o,j}^{n+1}\rho_{o,j}^{n+1}A_j^n u_{o,j}^{n+1}-\alpha_{o,j-1}^{n+1}\rho_{o,j-1}^{n+1}A_{j-1}^{n}u_{o,j-1}^{n+1}\right]+$$
$$\Delta t\left[\alpha_{w,j}^{n+1}\rho_{w,j}^{n+1}A_j^n u_{w,j}^{n+1}-\alpha_{w,j-1}^{n+1}\rho_{w,j-1}^{n+1}A_{j-1}^{n}u_{w,j-1}^{n+1}\right]=$$
$$V_b\Delta t\left(-\Gamma_g^{n+1}+\dot{\psi}_{o,L}^{n+1}+\dot{\psi}_{w,L}^{n+1}\right). \qquad (5.39)$$

Mixture Mass Conservation

$$V_b\left[\left(\rho_{g,L}^{n+1}\alpha_{g,L}^{n+1}-\rho_{g,L}^{n}\alpha_{g,L}^{n}\right)+\left(\rho_{o,L}^{n+1}\alpha_{o,L}^{n+1}-\rho_{o,L}^{n}\alpha_{o,L}^{n}\right)+\left(\rho_{w,L}^{n+1}\alpha_{w,L}^{n+1}-\rho_{w,L}^{n}\alpha_{w,L}^{n}\right)\right]+$$
$$\Delta t\left[\alpha_{g,j}^{n+1}\rho_{g,j}^{n+1}A_j^n u_{g,j}^{n+1}-\alpha_{g,j-1}^{n+1}\rho_{g,j-1}^{n+1}A_{j-1}^{n}u_{g,j-1}^{n+1}\right]+$$

$$\begin{aligned}
&\Delta t\left[\alpha_{o,j}^{n+1}\rho_{o,j}^{n+1}A_j^n u_{o,j}^{n+1}-\alpha_{o,j-1}^{n+1}\rho_{o,j-1}^{n+1}A_{j-1}^n u_{o,j-1}^{n+1}\right]+\\
&\Delta t\left[\alpha_{w,j}^{n+1}\rho_{w,j}^{n+1}A_j^n u_{w,j}^{n+1}-\alpha_{w,j-1}^{n+1}\rho_{w,j-1}^{n+1}A_{j-1}^n u_{w,j-1}^{n+1}\right]=\\
&V_b\Delta t\left(\dot{\psi}_{g,L}^{n}+\dot{\psi}_{o,L}^{n}+\dot{\psi}_{w,L}^{n}\right).
\end{aligned} \tag{5.40}$$

<u>Mixture Momentum Conservation</u>

$$\begin{aligned}
&\Delta x_j\left[\rho_{m,j}^{n+1}u_{m,j}^{n+1}-\rho_{m,j}^{n}u_{m,j}^{n}\right]+\\
&\Delta t\left[\rho_{m,L}^{n+1}(u_m^2)_L^{n+1}-\rho_{m,L}^{n+1}(u_m^2)_L^{n+1}\right]=\\
&-\Delta t\left(144.0g_c\right)\left(P_L^{n+1}-P_K^{n+1}\right)-\Delta t\Delta x_j\rho_{m,j}^{n+1}gsin\theta-\Delta t\Delta x_j\tau_{m,j}^{n+1}\frac{\pi D}{A_j^n}.
\end{aligned} \tag{5.41}$$

<u>Mixture Energy Conservation</u>

$$\begin{aligned}
&V_b\left[\alpha_{g,L}^{n+1}\rho_{g,L}^{n+1}\left(\bar{h}_{g,L}^{n+1}+\frac{(u_g^2)_L^{n+1}}{2g_cJ_c}\right)-\alpha_{g,L}^{n}\rho_{g,L}^{n}\left(\bar{h}_{g,L}^{n}+\frac{(u_g^2)_L^{n}}{2g_cJ_c}\right)\right]+\\
&V_b\left[\alpha_{o,L}^{n+1}\rho_{o,L}^{n+1}\left(\bar{h}_{o,L}^{n+1}+\frac{(u_o^2)_L^{n+1}}{2g_cJ_c}\right)-\alpha_{o,L}^{n}\rho_{o,L}^{n}\left(\bar{h}_{o,L}^{n}+\frac{(u_o^2)_L^{n}}{2g_cJ_c}\right)\right]+\\
&V_b\left[\alpha_{w,L}^{n+1}\rho_{w,L}^{n+1}\left(\bar{h}_{w,L}^{n+1}+\frac{(u_w^2)_L^{n+1}}{2g_cJ_c}\right)-\alpha_{w,L}^{n}\rho_{w,L}^{n}\left(\bar{h}_{w,L}^{n}+\frac{(u_w^2)_L^{n}}{2g_cJ_c}\right)\right]+\\
&\Delta t\left[A_j^{n+1}\alpha_{g,L}^{n+1}\rho_{g,L}^{n+1}u_{g,j}^{n+1}\left(\bar{h}_{g,L}^{n+1}+\frac{(u_g^2)_j^{n+1}}{2g_cJ_c}\right)-A_{j-1}^{n+1}\alpha_{g,K}^{n+1}\rho_{g,K}^{n+1}u_{g,K}^{n+1}\left(\bar{h}_{g,K}^{n+1}+\frac{(u_g^2)_{j-1}^{n+1}}{2g_cJ_c}\right)\right]\\
&\Delta t\left[A_j^{n+1}\alpha_{o,L}^{n+1}\rho_{o,L}^{n+1}u_{o,j}^{n+1}\left(\bar{h}_{o,L}^{n+1}+\frac{(u_o^2)_j^{n+1}}{2g_cJ_c}\right)-A_{j-1}^{n+1}\alpha_{o,K}^{n+1}\rho_{o,K}^{n+1}u_{o,j-1}^{n+1}\left(\bar{h}_{o,K}^{n+1}+\frac{(u_o^2)_{j-1}^{n+1}}{2g_cJ_c}\right)\right]\\
&\Delta t\left[A_j^{n+1}\alpha_{w,L}^{n+1}\rho_{w,L}^{n+1}u_{w,j}^{n+1}\left(\bar{h}_{w,L}^{n+1}+\frac{(u_w^2)_j^{n+1}}{2g_cJ_c}\right)-A_{j-1}^{n+1}\alpha_{w,K}^{n+1}\rho_{w,K}^{n+1}u_{w,j-1}^{n+1}\left(\bar{h}_{w,K}^{n+1}+\frac{(u_w^2)_{j-1}^{n+1}}{2g_cJ_c}\right)\right]=\\
&V_b\Delta t\left[\dot{H}_{o,L}^{n+1}+\dot{H}_{g,L}^{n+1}+\dot{H}_{w,L}^{n+1}\right]-
\end{aligned}$$

$$V_b \Delta t \left[\alpha_{g,L}^{n+1} \rho_{g,L}^{n+1} \frac{u_{g,L}^{n+1}}{g_c J_c} gsin\theta + \alpha_{o,L}^{n+1} \rho_{o,L}^{n+1} \frac{u_{o,L}^{n+1}}{g_c J_c} gsin\theta + \alpha_{w,L}^{n+1} \rho_{w,L}^{n+1} \frac{u_{w,L}^{n+1}}{g_c J_c} gsin\theta \right] -$$

$$V_b \Delta t \left[\frac{\dot{Q}_{loss,L}^{n+1}}{A_j^n} \right]. \tag{5.42}$$

5.2 WELLBORE BOUNDARY CONDITIONS

In UTWELL, we can assign different types of boundary conditions for the wellbore. Figure 5.2 shows the arrangement of typical boundary conditions that can be used for the transient multiphase flow in the wellbores or pipelines. As can be seen the boundary nodes can be defined as

1) Pressure Node
2) Mass Flow Node
3) Mass Source Node
4) Closed Node

All of these boundary conditions are assigned to the junction of nodes at the inlet or outlet except Mass Flow Node. For the inlet node, temperature, gas oil ratio, and water cut; or the mass flow rate of gas, oil, and water are also defined.

To effectively implement the boundary conditions in our numerical calculation, we consider imaginary nodes with zero volume ($\Delta x_j = 0$) at inlet and outlet and assign the given boundary values to these nodes. In Section 5.3, the boundary node equations are discussed in detail.

In addition to the boundary conditions defined in Figure 5.2, for the single-phase flow and steady state multiphase flow, additional types of boundary conditions have been considered in UTWELL. These boundary conditions are used for coupled wellbore/reservoir models where we have

1) Constant Wellhead Flow Rate
2) Constant Bottom-hole Pressure

For Constant Wellhead Flow Rate, the well is operated at a pressure condition that can honor the flow rate of liquid or oil, which is required at the wellhead. For Constant Bottom-hole Pressure, the wellbore pressure in the zone connecting with the reservoir is maintained constant at the given value and all the flow rates are calculated.

5.3 SOLUTION METHODS

The discretized equations in Section 5.1 are linearized into a system of equations to solve for the primary variables. In this section, we introduce different algorithms to construct the linear system of equations for various flow models (i.e. homogenous, drift flux, two-fluid). First, we present semi-implicit and nearly-implicit algorithms to solve the two-fluid models. These methods are armed with some numerical techniques to decrease the computation time for such sophisticated models. Secondly, we discuss a fully-implicit algorithm to linearize the discretized equations for the drift-flux model. Since we obtained a non-linear system of equations in the discretized form of drift-flux model, we use the Newton method for the linearization of the equations. The simplification of two-fluid and drift flux models, with consideration of no slip condition, also yields homogenous model.

Finally, we discuss the solution methods for steady-state multiphase flow models. We use a marching algorithm to solve steady-state model.

5.3.1 Semi-Implicit Approach

Many multiphase flow simulators (such as OLGA, RELAP5, and CATHARE) use semi-implicit methods to solve the field equations. These methods have shown a lot of promise in regards to stability and robustness of multiphase flow model solutions. In the UTWELL development, we chose this method to solve the transport equations in the two-fluid model. Hence, we used the semi-implicit approach to obtain α_w^{n+1}, α_g^{n+1}, u_l^{n+1}, u_g^{n+1}, and P^{n+1} from mass and momentum conservation equations. We decouple the energy equation from the former equations and solve it separately to obtain temperature, T^{n+1}.

Using the method explained in Section 5.2.1, the discretized equations are already obtained as a linear function of primary variables. The discretized equations are partially as function of advanced time and partially old time. The implicit variables are selected in a way that gives better numerical stability. Once we generated the semi-implicit discretized equations, we follow the following procedure to decouple the variables and construct final shape of algebraic equations.

First, we setup the water mass conservation, difference of gas and liquid mass conservation, and summation of liquid and gas mass conservation as functions of liquid and gas velocities.

$$\begin{aligned} &A(I,1)\left(\tilde{\alpha}_{w,L}^{n+1}-\alpha_{w,L}^{n}\right)+A(I,2)\left(\tilde{\alpha}_{g,L}^{n+1}-\alpha_{g,L}^{n}\right)+A(I,3)\left(P_L^{n+1}-P_L^{n}\right)= \\ &B(I)+G_1(I)(u_g)_{j+1}^{n+1}+G_0(I)(u_g)_j^{n+1}+L_1(I)(u_l)_{j+1}^{n+1}+L_0(I)(u_l)_j^{n+1}. \end{aligned} \tag{5.43}$$

$I=1$ corresponds to water mass conservation equation, $I=2$ corresponds to difference between gas and liquid mass conservation equation and $I=3$ corresponds to summation of gas and liquid mass conservation equation. Matrix A and vectors B, G and L are obtained from Equations (5.7), (5.8) and (5.9).

Decoupling Equation (5.43) for primary variable $\left(P_L^{n+1}\text{-}P_L^n\right)$ can be obtained as

$$\begin{aligned}\left(P_L^{n+1}\text{-}P_L^n\right) = A^{-1}B(3) + A^{-1}G_1(3)(u_g)_{j+1}^{n+1} + A^{-1}G_0(3)(u_g)_j^{n+1} + \\ A^{-1}L_1(3)(u_l)_{j+1}^{n+1} + A^{-1}L_0(3)(u_l)_j^{n+1}.\end{aligned} \tag{5.44}$$

We also setup the difference gas and liquid momentum equation and summation of liquid and gas momentum equation to obtain liquid and gas velocities as a function of pressure.

$$X(I,1)(u_g)_j^{n+1} + X(I,2)(u_l)_j^{n+1} = Y(I) + Z(I)\left(P_L^{n+1} - P_K^{n+1}\right), \tag{5.45}$$

$I = 1$ corresponds to the difference of gas and liquid momentum equations and $I = 2$ corresponds to summation of liquid and gas momentum equations. Matrix X and vectors Y and Z are obtained from rearranging Equations (5.10) and (5.19). Solutions of Equation (5.45) for liquid and gas velocities are

$$(u_g)_j^{n+1} = X^{-1}Y(1) + X^{-1}Z(1)\left(P_L^{n+1} - P_K^{n+1}\right), \tag{5.46}$$

$$(u_l)_j^{n+1} = X^{-1}Y(2) + X^{-1}Z(2)\left(P_L^{n+1} - P_K^{n+1}\right). \tag{5.47}$$

If we plug the velocity of gas and liquid in Equation (5.44), we obtain the final formula for the pressure equation as follows:

$$\begin{aligned}\left(P_L^{n+1}\text{-}P_L^{n}\right) = A^{-1}B(3) + A^{-1}G_1(3)&\left[X^{-1}Y(1) + X^{-1}Z(1)\left(P_M^{n+1} - P_L^{n+1}\right)\right] + \\ A^{-1}G_0(3)&\left[X^{-1}Y(1) + X^{-1}Z(1)\left(P_L^{n+1} - P_K^{n+1}\right)\right] + \\ A^{-1}L_1(3)&\left[X^{-1}Y(2) + X^{-1}Z(2)\left(P_M^{n+1} - P_L^{n+1}\right)\right] + \\ A^{-1}L_0(3)&\left[X^{-1}Y(2) + X^{-1}Z(2)\left(P_L^{n+1} - P_K^{n+1}\right)\right].\end{aligned} \tag{5.48}$$

Equation (5.48) can be written for all the nodes from *L=1* to *L=N*. This equation is modified for the boundary nodes (*L=1* and *L=N)* at inlet and outlet.

If the inlet boundary condition is Pressure Node then the pressure equation at first node becomes

$$\begin{aligned}\left(P_1^{n+1}\text{-}P_1^{n}\right) = A^{-1}B(3) + A^{-1}G_1(3)&\left[X^{-1}Y(1) + X^{-1}Z(1)\left(P_2^{n+1} - P_1^{n+1}\right)\right] + \\ A^{-1}G_0(3)&\left[X^{-1}Y(1) + X^{-1}Z(1)\left(P_1^{n+1} - P_{inlet}\right)\right] + \\ A^{-1}L_1(3)&\left[X^{-1}Y(2) + X^{-1}Z(2)\left(P_2^{n+1} - P_1^{n+1}\right)\right] + \\ A^{-1}L_0(3)&\left[X^{-1}Y(2) + X^{-1}Z(2)\left(P_1^{n+1} - P_{inlet}\right)\right].\end{aligned} \tag{5.49}$$

If the inlet boundary condition is Mass Flow Node then we have

$$\begin{aligned}\left(P_1^{n+1}\text{-}P_1^{n}\right) = A^{-1}B(3) + A^{-1}G_1(3)&\left[X^{-1}Y(1) + X^{-1}Z(1)\left(P_2^{n+1} - P_1^{n+1}\right)\right] + \\ A^{-1}G_0(3)&\left[u_{g,inlet}\right] + \\ A^{-1}L_1(3)&\left[X^{-1}Y(2) + X^{-1}Z(2)\left(P_2^{n+1} - P_1^{n+1}\right)\right] + \\ A^{-1}L_0(3)&\left[u_{l,inlet}\right].\end{aligned} \tag{5.50}$$

Similarly, Equation (5.48) is modified for the outlet boundary condition at node $L=N$. For Closed Node boundary condition, we use Mass Flow Node with zero value. Considering Equation (5.48) with boundary node effects, a linear system of equations as function of pressure is obtained. This equation can be solved by a tri-diagonal solver to obtain pressure.

Next step in semi-implicit algorithm is updating the other primary variables after calculating the pressure equation. Once we obtain the pressure, we can use Equations (5.46) and (5.47) to calculate the velocity of gas and liquid, respectively. Afterward, we update the provisional advanced time water and gas volume fractions ($\tilde{\alpha}_{w,L}^{n+1}$ and $\tilde{\alpha}_{g,L}^{n+1}$) using Equation (5.43). Other provisional advanced time variables can be updated accordingly.

Finally, we update the actual phasic volume fractions and the mixture density using the unexpanded version of mass conservation of each phase as follows:

$$(\rho_w \alpha_w)_L^{n+1} =$$

$$\rho_{w,L}^n \alpha_{w,L}^n + \frac{\Delta t}{V_b}\left[\dot{\alpha}_{w,j-1}^n \dot{\rho}_{w,j-1}^n A_{j-1}^n u_{w,j-1}^{n+1} - \dot{\alpha}_{w,j}^n \dot{\rho}_{w,j}^n A_j^n u_{w,j}^{n+1}\right] + \Delta t \dot{\psi}_{w,L}^n, \tag{5.51}$$

$$(\rho_o \alpha_o)_L^{n+1} =$$

$$\rho_{o,L}^n \alpha_{o,L}^n + \frac{\Delta t}{V_b}\left[\dot{\alpha}_{o,j-1}^n \dot{\rho}_{o,j-1}^n A_{j-1}^n u_{o,j-1}^{n+1} - \dot{\alpha}_{o,j}^n \dot{\rho}_{o,j}^n A_j^n u_{o,j}^{n+1}\right] + \Delta t\left(-\tilde{\Gamma}_g^{n+1} + \dot{\psi}_{o,L}^{n+1}\right), \tag{5.52}$$

$$(\rho_g \alpha_g)_L^{n+1} =$$

$$\rho_{g,L}^n \alpha_{g,L}^n + \frac{\Delta t}{V_b}\left[\dot{\alpha}_{g,j-1}^n \dot{\rho}_{g,j-1}^n A_{j-1}^n u_{g,j-1}^{n+1} - \dot{\alpha}_{g,j}^n \dot{\rho}_{g,j}^n A_j^n u_{g,j}^{n+1}\right] + \Delta t\left(\tilde{\Gamma}_g^{n+1} + \dot{\psi}_{g,L}^{n+1}\right), \tag{5.53}$$

$$(\alpha_w)_L^{n+1} = \frac{(\rho_w \alpha_w)_L^{n+1}}{\tilde{\rho}_{w,L}^{n+1}}, \tag{5.54}$$

$$(\alpha_o)_L^{n+1} = \frac{(\rho_o \alpha_o)_L^{n+1}}{\tilde{\rho}_{o,L}^{n+1}}, \tag{5.55}$$

$$(\alpha_g)_L^{n+1} = 1 - (\alpha_o)_L^{n+1} - (\alpha_w)_L^{n+1}. \tag{5.56}$$

Phasic volume fractions are always checked to be less than one, or larger than zero. At this point, having the new pressure values and phasic volume fractions the state relations are also used to update the fluid properties.

In case the process we simulate in the wellbore is thermal and involves a great amount of heat exchange, energy equation should be solved to update the temperature in the wellbore. For this purpose, Equation (5.20) is solved using all the other primary variables ($\alpha_w^{n+1}, \alpha_g^{n+1}, u_l^{n+1}$, u_g^{n+1}, and P^{n+1}) obtained from the semi-implicit approach. Newton-Raphson method is used to solve the energy equation. Hence, a residual vector (R_T) is calculated as shown in Equation (5.57) and a Jacobian matrix (J_T) is constructed, which is the derivative of energy equation respect to temperature.

$$
\begin{aligned}
&R_T = V_b\left[\alpha_{o,L}^{n+1}\rho_{o,L}^{n+1}\left(\bar{h}_{o,L}^{n+1}+\frac{(u_o^2)_L^{n+1}}{2g_cJ_c}\right)-\alpha_{o,L}^{n}\rho_{o,L}^{n}\left(\bar{h}_{o,L}^{n}+\frac{(u_o^2)_L^{n}}{2g_cJ_c}\right)\right]+\\
&V_b\left[\alpha_{g,L}^{n+1}\rho_{g,L}^{n+1}\left(\bar{h}_{g,L}^{n+1}+\frac{(u_g^2)_L^{n+1}}{2g_cJ_c}\right)-\alpha_{g,L}^{n}\rho_{g,L}^{n}\left(\bar{h}_{g,L}^{n}+\frac{(u_g^2)_L^{n}}{2g_cJ_c}\right)\right]+\\
&V_b\left[\alpha_{w,L}^{n+1}\rho_{w,L}^{n+1}\left(\bar{h}_{w,L}^{n+1}+\frac{(u_w^2)_L^{n+1}}{2g_cJ_c}\right)-\alpha_{w,L}^{n}\rho_{w,L}^{n}\left(\bar{h}_{w,L}^{n}+\frac{(u_w^2)_L^{n}}{2g_cJ_c}\right)\right]+\\
&\Delta t\left[A_{j+1}^{n}\dot{\alpha}_{o,j+1}^{n+1}\dot{\rho}_{o,j+1}^{n+1}u_{o,j+1}^{n+1}\left(\dot{\bar{h}}_{o,j+1}^{n+1}+\frac{(u_o^2)_{j+1}^{n+1}}{2g_cJ_c}\right)-A_{j}^{n}\dot{\alpha}_{o,j}^{n+1}\dot{\rho}_{o,j}^{n+1}u_{o,j}^{n+1}\left(\dot{\bar{h}}_{o,j}^{n+1}+\frac{(u_o^2)_{j}^{n+1}}{2g_cJ_c}\right)\right]\\
&\Delta t\left[A_{j+1}^{n}\dot{\alpha}_{g,j+1}^{n+1}\dot{\rho}_{g,j+1}^{n+1}u_{g,j+1}^{n+1}\left(\dot{\bar{h}}_{g,j+1}^{n+1}+\frac{(u_g^2)_{j+1}^{n+1}}{2g_cJ_c}\right)-A_{j}^{n}\dot{\alpha}_{g,j}^{n+1}\dot{\rho}_{g,j}^{n+1}u_{g,j}^{n+1}\left(\dot{\bar{h}}_{g,j}^{n+1}+\frac{(u_g^2)_{j}^{n+1}}{2g_cJ_c}\right)\right]\\
&\Delta t\left[A_{j+1}^{n}\dot{\alpha}_{w,j+1}^{n+1}\dot{\rho}_{w,j+1}^{n+1}u_{w,j+1}^{n+1}\left(\dot{\bar{h}}_{w,j+1}^{n+1}+\frac{(u_w^2)_{j+1}^{n+1}}{2g_cJ_c}\right)-A_{j}^{n}\dot{\alpha}_{w,j}^{n+1}\dot{\rho}_{w,j}^{n+1}u_{w,j}^{n+1}\left(\dot{\bar{h}}_{w,j}^{n+1}+\frac{(u_w^2)_{j}^{n+1}}{2g_cJ_c}\right)\right]-\\
&V_b\Delta t\left[\dot{H}_{o,L}^{n+1}+\dot{H}_{g,L}^{n+1}+\dot{H}_{w,L}^{n+1}\right]+
\end{aligned}
$$

$$V_b\Delta t\left[\alpha_{o,L}^{n+1}\rho_{o,L}^{n+1}\frac{u_{o,L}^{n+1}}{g_cJ_c}gsin\theta+\alpha_{g,L}^{n+1}\rho_{g,L}^{n+1}\frac{u_{g,L}^{n+1}}{g_cJ_c}gsin\theta+\alpha_{w,L}^{n+1}\rho_{w,L}^{n+1}\frac{u_{w,L}^{n+1}}{g_cJ_c}gsin\theta\right]+$$

$$V_b\Delta t\left[\frac{\dot{Q}_{loss,L}^{n}}{A_j^n}\right], \tag{5.57}$$

$$J_T=\begin{bmatrix}\frac{\partial R_{T,1}}{\partial T_1} & \frac{\partial R_{T,1}}{\partial T_2} & \dots & \dots & 0\\ \frac{\partial R_{T,2}}{\partial T_1} & \frac{\partial R_{T,2}}{\partial T_2} & \frac{\partial R_{T,2}}{\partial T_3} & \dots & 0\\ 0 & \frac{\partial R_{T,i}}{\partial T_{i-1}} & \frac{\partial R_{T,i}}{\partial T_i} & \frac{\partial R_{T,i}}{\partial T_{i+1}} & 0\\ 0 & \dots. & \frac{\partial R_{T,N-1}}{\partial T_{N-2}} & \frac{\partial R_{T,N-1}}{\partial T_{N-1}} & \frac{\partial R_{T,N-1}}{\partial T_N}\\ 0 & \dots & \dots & \frac{\partial R_{T,N}}{\partial T_{N-1}} & \frac{\partial R_{T,N}}{\partial T_N}\end{bmatrix}. \tag{5.58}$$

Finally the new temperature is obtained as

$$\vec{T}^{n+1}=\vec{T}^{n}-J_T^{-1}R_T. \tag{5.59}$$

The Jacobian of energy equation, Equation (5.58), the derivatives of densities and enthalpies respect to temperature are all calculated from state relations, Appendices B and C.

5.3.2 Nearly-Implicit Approach

Nearly-implicit is similar to semi-implicit approach with only few modifications in the flux gradient term and the axial liquid height term in the momentum equations. In semi-implicit approach, the momentum flux gradient was considered in an explicit format. However, in the nearly-implicit method, this term is linearized into both implicit and explicit terms. Recalling from Equations (5.10) and (5.19), the flux term derivatives were calculated as

$$\Delta_1 = \frac{\Delta t}{2}\left[\left(\frac{\dot{\alpha}_g\dot{\rho}_g}{\alpha_g\rho_g}\right)_j^n\left((u_g^2)_L^n-(u_g^2)_K^n\right)-\left(\frac{\dot{\alpha}_l\dot{\rho}_l}{\alpha_l\rho_l}\right)_j^n\left((u_l^2)_L^n-(u_l^2)_K^n\right)\right],$$
$$\Delta_2 = \frac{\Delta t}{2}\left[\left(\dot{\alpha}_g\dot{\rho}_g\right)_j^n\left((u_g^2)_L^n-(u_g^2)_K^n\right)+\left(\dot{\alpha}_l\dot{\rho}_l\right)_j^n\left((u_l^2)_L^n-(u_l^2)_K^n\right)\right].$$

In nearly-implicit method, those terms are replaced with the following equations for momentum difference and momentum summation equations, respectively.

$$\Delta_1 = \frac{\Delta t}{2}\left(\frac{\dot{\alpha}_g\dot{\rho}_g}{\alpha_g\rho_g}\right)_j^n\left[2(u_g)_L^n\left((u_g)_L^{n+1}-(u_g)_L^n\right)-2(u_g)_K^n\left((u_g)_K^{n+1}-(u_g)_K^n\right)+(u_g^2)_L^n-(u_g^2)_K^n\right]-$$
$$\frac{\Delta t}{2}\left(\frac{\dot{\alpha}_l\dot{\rho}_l}{\alpha_l\rho_l}\right)_j^n\left[2(u_l)_L^n\left((u_l)_L^{n+1}-(u_l)_L^n\right)-2(u_l)_K^n\left((u_l)_K^{n+1}-(u_l)_K^n\right)+(u_l^2)_L^n-(u_l^2)_K^n\right]$$
$$\Delta_2 = \frac{\Delta t}{2}\left(\dot{\alpha}_g\dot{\rho}_g\right)_j^n\left[2(u_g)_L^n\left((u_g)_L^{n+1}-(u_g)_L^n\right)-2(u_g)_K^n\left((u_g)_K^{n+1}-(u_g)_K^n\right)+(u_g^2)_L^n-(u_g^2)_K^n\right]+$$
$$\frac{\Delta t}{2}\left(\dot{\alpha}_l\dot{\rho}_l\right)_j^n\left[2(u_l)_L^n\left((u_l)_L^{n+1}-(u_l)_L^n\right)-2(u_l)_K^n\left((u_l)_K^{n+1}-(u_l)_K^n\right)+(u_l^2)_L^n-(u_l^2)_K^n\right]$$

In addition, the axial liquid height gradient term $\Delta t\left(\frac{\rho_m}{\rho_g\rho_l}\right)_j^n\left(\rho_l-\rho_g\right)_j^n B_y\left(y_L^n-y_K^n\right)$ in Equation (5.10) is converted to the implicit term as $\Delta t\left(\frac{\rho_m}{\rho_g\rho_l}\right)_j^n\left(\rho_l-\rho_g\right)_j^n B_y$ $\left(y_L^{n+1}-y_K^{n+1}\right)$. Consequently, this term is changed to a function of gas volume fraction

$$\Delta t\left(\frac{\rho_m}{\rho_g \rho_l}\right)_j^n \left(\rho_l - \rho_g\right)_j^n B_y \left(\frac{\partial y}{\partial \alpha_g}\right)_j^n \left(\tilde{\alpha}_{g,L}^{n+1} - \tilde{\alpha}_{g,K}^{n+1}\right).$$

Considering the changes made in the momentum equations, the pressure equation is not obtained as straightforwardly as in the semi-implicit method. Instead, in nearly-implicit approach, the velocity equation is constructed first.

From Equation (5.43), we can obtain pressure and gas volume fractions as functions of liquid and gas velocities as given below

$$\begin{aligned}\left(P_L^{n+1} - P_L^n\right) = A^{-1}B(3) + A^{-1}G_1(3)(u_g)_{j+1}^{n+1} + A^{-1}G_0(3)(u_g)_j^{n+1} + \\ A^{-1}L_1(3)(u_l)_{j+1}^{n+1} + A^{-1}L_0(3)(u_l)_j^{n+1},\end{aligned} \tag{5.60}$$

$$\begin{aligned}\left(\tilde{\alpha}_{g,L}^{n+1} - \alpha_{g,L}^n\right) = A^{-1}B(2) + A^{-1}G_1(2)(u_g)_{j+1}^{n+1} + A^{-1}G_0(2)(u_g)_j^{n+1} + \\ A^{-1}L_1(2)(u_l)_{j+1}^{n+1} + A^{-1}L_0(2)(u_l)_j^{n+1}.\end{aligned} \tag{5.61}$$

From momentum equations, after substitution of implicit terms, we also have

$$\begin{aligned}&X(1,1)(u_g)_{j-1}^{n+1} + X(1,2)(u_g)_j^{n+1} + X(1,3)(u_g)_{j+1}^{n+1} + \\ &X(1,4)(u_l)_{j-1}^{n+1} + X(1,5)(u_l)_j^{n+1} + X(1,6)(u_l)_{j+1}^{n+1} = \\ &Y(1) + Z(1)\left(P_L^{n+1} - P_K^{n+1}\right) + V(1)\left(\tilde{\alpha}_{g,L}^{n+1} - \tilde{\alpha}_{g,K}^{n+1}\right),\end{aligned} \tag{5.62}$$

$$\begin{aligned}&X(2,1)(u_g)_{j-1}^{n+1}+X(2,2)(u_g)_{j}^{n+1}+X(2,3)(u_g)_{j+1}^{n+1}+\\&X(2,4)(u_l)_{j-1}^{n+1}+X(2,5)(u_l)_{j}^{n+1}+X(2,6)(u_l)_{j+1}^{n+1}=\\&Y(2)+Z(2)\left(P_L^{n+1}-P_K^{n+1}\right)+V(2)\left(\tilde{\alpha}_{g,L}^{n+1}-\tilde{\alpha}_{g,K}^{n+1}\right).\end{aligned}\tag{5.63}$$

Substituting P_L^{n+1} and $\tilde{\alpha}_{g,L}^{n+1}$ from Equations (5.60) and (5.61) into Equations (5.62) and (5.63), the system of equations is decoupled and becomes only functions of liquid and gas velocities at advanced time. In this fashion, the velocities of liquid and gas can be found from the final rearrangements in Equations (5.62) and (5.63). After solving the velocities, pressure is updated from Equation (5.60) and the provisional gas and water volume fractions are updated from Equation (5.43). Continuing the same approach, as done for the semi-implicit method, we can also calculate the final values of primary variables, using unexpanded phasic mass conservation equations.

Although in the nearly-implicit method we only made a small change in the momentum equations, it caused much more complications in the calculation of primary variables. Our experience shows that this small change also adds significant stability to the two-fluid model, especially for the phase redistribution problems.

5.3.3 Fully-Implicit Approach

Fully implicit approach has been used to solve the drift-flux flow model in UTWELL. Since the discretized equations for drift flux model are still non-linear with fully implicit approach, we used Newton method to linearize the equations and solve for primary variables. We decouple the energy equation from the mass and momentum conservation equations similar to the semi-implicit and nearly-implicit methods. Hence, we first solve the transport equation and then update the temperature, if thermal modeling was involved.

In the Newton method, we solved the mass balance and momentum balance equations by constructing a Jacobian matrix, J, and a residual vector, R, with primary variables: mixture average velocity, pressure, liquid volume fraction, and water volume fraction. As explained in Section 5.1.2, the equations we solve are f_1 as mixture momentum balance; f_2 as mixture mass balance; f_3 as liquid mass balance; f_4 as water mass balance.

$$J=\begin{bmatrix}
\frac{\partial f_{1,1}}{\partial u_{m,1}} & \frac{\partial f_{1,1}}{\partial P_1} & \frac{\partial f_{1,1}}{\partial \alpha_{l,1}} & \frac{\partial f_{1,1}}{\partial \alpha_{w,1}} & \cdots & \frac{\partial f_{1,1}}{\partial u_{m,N}} & \frac{\partial f_{1,1}}{\partial P_N} & \frac{\partial f_{1,1}}{\partial \alpha_{l,N}} & \frac{\partial f_{1,1}}{\partial \alpha_{w,N}} \\
\frac{\partial f_{2,1}}{\partial u_{m,1}} & \frac{\partial f_{2,1}}{\partial P_1} & \frac{\partial f_{2,1}}{\partial \alpha_{l,1}} & \frac{\partial f_{2,1}}{\partial \alpha_{w,1}} & \cdots & \frac{\partial f_{2,1}}{\partial u_{m,N}} & \frac{\partial f_{2,1}}{\partial P_N} & \frac{\partial f_{2,1}}{\partial \alpha_{l,N}} & \frac{\partial f_{2,1}}{\partial \alpha_{w,N}} \\
\frac{\partial f_{3,1}}{\partial u_{m,1}} & \frac{\partial f_{3,1}}{\partial P_1} & \frac{\partial f_{3,1}}{\partial \alpha_{l,1}} & \frac{\partial f_{3,1}}{\partial \alpha_{w,1}} & \cdots & \frac{\partial f_{3,1}}{\partial u_{m,N}} & \frac{\partial f_{3,1}}{\partial P_N} & \frac{\partial f_{3,1}}{\partial \alpha_{l,N}} & \frac{\partial f_{3,1}}{\partial \alpha_{w,N}} \\
\frac{\partial f_{4,1}}{\partial u_{m,1}} & \frac{\partial f_{4,1}}{\partial P_1} & \frac{\partial f_{4,1}}{\partial \alpha_{l,1}} & \frac{\partial f_{4,1}}{\partial \alpha_{w,1}} & \cdots & \frac{\partial f_{4,1}}{\partial u_{m,N}} & \frac{\partial f_{4,1}}{\partial P_N} & \frac{\partial f_{4,1}}{\partial \alpha_{l,N}} & \frac{\partial f_{4,1}}{\partial \alpha_{w,N}} \\
\cdots & \cdots & \cdots & \cdots & \cdots & \cdots & \cdots & \cdots & \cdots \\
\frac{\partial f_{1,N}}{\partial u_{m,1}} & \frac{\partial f_{1,N}}{\partial P_1} & \frac{\partial f_{1,N}}{\partial \alpha_{l,1}} & \frac{\partial f_{1,N}}{\partial \alpha_{w,1}} & \cdots & \frac{\partial f_{1,N}}{\partial u_{m,N}} & \frac{\partial f_{1,N}}{\partial P_N} & \frac{\partial f_{1,N}}{\partial \alpha_{l,N}} & \frac{\partial f_{1,1}}{\partial \alpha_{w,N}} \\
\frac{\partial f_{2,N}}{\partial u_{m,1}} & \frac{\partial f_{2,N}}{\partial P_1} & \frac{\partial f_{2,N}}{\partial \alpha_{l,1}} & \frac{\partial f_{2,N}}{\partial \alpha_{w,1}} & \cdots & \frac{\partial f_{2,N}}{\partial u_{m,N}} & \frac{\partial f_{2,N}}{\partial P_N} & \frac{\partial f_{2,N}}{\partial \alpha_{l,N}} & \frac{\partial f_{2,1}}{\partial \alpha_{w,N}} \\
\frac{\partial f_{3,N}}{\partial u_{m,1}} & \frac{\partial f_{3,N}}{\partial P_1} & \frac{\partial f_{3,N}}{\partial \alpha_{l,1}} & \frac{\partial f_{3,N}}{\partial \alpha_{w,1}} & \cdots & \frac{\partial f_{3,N}}{\partial u_{m,N}} & \frac{\partial f_{3,N}}{\partial P_N} & \frac{\partial f_{3,N}}{\partial \alpha_{l,N}} & \frac{\partial f_{3,1}}{\partial \alpha_{w,N}} \\
\frac{\partial f_{4,N}}{\partial u_{m,1}} & \frac{\partial f_{4,N}}{\partial P_1} & \frac{\partial f_{4,N}}{\partial \alpha_{l,1}} & \frac{\partial f_{4,N}}{\partial \alpha_{w,1}} & \cdots & \frac{\partial f_{4,N}}{\partial u_{m,N}} & \frac{\partial f_{4,N}}{\partial P_N} & \frac{\partial f_{4,N}}{\partial \alpha_{l,N}} & \frac{\partial f_{4,1}}{\partial \alpha_{w,N}}
\end{bmatrix},$$

$$R = \begin{bmatrix} f_{1,1} \\ f_{2,1} \\ f_{3,1} \\ f_{4,1} \\ \dots \\ f_{1,N} \\ f_{2,N} \\ f_{3,N} \\ f_{4,N} \end{bmatrix}. \tag{5.64}$$

The updated primary variable at advance time is

$$\Delta\vec{X} = J^{-1}R. \tag{5.65}$$

After solving for mixture velocity, pressure, liquid volume fraction and water volume fraction, velocities of the gas and liquid are updated by drift-flux correlations and the energy equation is solved as in the semi-implicit method to obtain temperature.

5.3.4 Steady State Model

Steady-state condition is obtained when the flow parameters remain constant with time elapsed. In the transient simulation, total enthalpy of the fluids can be a good indicator to verify whether or not steady state condition has been reached. In fact, this parameter is a function of all the other primary variables, which can represent variations of them with time. When the total enthalpy variation over time becomes zero, the transient solution converges to the steady-state solution.

Usually, steady-state solution is desirable for simulations where early transient results are not needed or where only the final condition of the system is important. In this situation, fully transient modeling is not performed and steady state modules are used.

In UTWELL, we have developed steady-state modules using a marching algorithm. In this approach, all the flow parameters are calculated iteratively from the inlet boundary to the outlet boundary until convergence is observed for all the nodes. The discretized forms of equations solved in the steady-state model are listed as follows:

$$\rho_{o,L}\alpha_{o,L}u_{o,j}-\rho_{o,K}\alpha_{o,K}u_{o,j-1}=\frac{V_b}{A_j}\left(\dot{\psi}_{o,L}-\Gamma_{g,L}\right), \tag{5.66}$$

$$\rho_{g,L}\alpha_{g,L}u_{g,j}-\rho_{g,K}\alpha_{g,K}u_{g,j-1}=\frac{V_b}{A_j}\left(\dot{\psi}_{g,L}+\Gamma_{g,L}\right), \tag{5.67}$$

$$\rho_{w,L}\alpha_{w,L}u_{w,j}-\rho_{w,K}\alpha_{w,K}u_{w,j-1}=\frac{V_b}{A_j}\left(\dot{\psi}_{w,L}\right), \tag{5.68}$$

$$P_L=P_K-\Delta x_j\frac{\rho_j g sin\theta}{\left(144.0g_c\right)}-\Delta x_j\frac{\pi D\tau_j}{\left(144.0g_c\right)A_j^n}+\frac{\rho_L(u_L^2)-\rho_K(u_K^2)}{\left(144.0g_c\right)}, \tag{5.69}$$

$$\alpha_w=\frac{u_{sw}}{u_{sl}}\alpha_l, \tag{5.70}$$

$$\left[A_j\alpha_{g,L}\rho_{g,L}u_{g,j}\left(\bar{h}_{g,L}+\frac{(u_g^2)_j}{2g_cJ_c}\right)-A_{j-1}\alpha_{g,K}\rho_{g,K}u_{g,j-1}\left(\bar{h}_{g,K}+\frac{(u_g^2)_{j-1}}{2g_cJ_c}\right)\right]$$
$$\left[A_j\alpha_{g,L}\rho_{g,L}u_{g,j}\left(\bar{h}_{g,L}+\frac{(u_g^2)_j}{2g_cJ_c}\right)-A_{j-1}\alpha_{g,K}\rho_{g,K}u_{g,j-1}\left(\bar{h}_{g,K}+\frac{(u_g^2)_{j-1}}{2g_cJ_c}\right)\right]$$
$$\left[A_j\alpha_{o,L}\rho_{o,L}u_{o,j}\left(\bar{h}_{o,L}+\frac{(u_o^2)_j}{2g_cJ_c}\right)-A_{j-1}\alpha_{o,K}\rho_{o,K}u_{o,j-1}\left(\bar{h}_{o,K}+\frac{(u_o^2)_{j-1}}{2g_cJ_c}\right)\right]$$
$$\left[A_j\alpha_{g,L}\rho_{g,L}u_{g,j}\left(\bar{h}_{g,L}+\frac{(u_o^2)_j}{2g_cJ_c}\right)-A_{j-1}\alpha_{g,K}\rho_{g,K}u_{g,j-1}\left(\bar{h}_{g,K}+\frac{(u_g^2)_{j-1}}{2g_cJ_c}\right)\right]=$$

$$V_b\left[\dot{H}_{o,L}+\dot{H}_{g,L}+\dot{H}_{w,L}\right]-$$

$$V_b\left[\alpha_{g,L}\rho_{g,L}\frac{u_{g,L}}{g_cJ_c}gsin\theta+\alpha_{o,L}\rho_{o,L}\frac{u_{o,L}}{g_cJ_c}gsin\theta+\alpha_{w,L}\rho_{w,L}\frac{u_{w,L}}{g_cJ_c}gsin\theta\right]-$$

$$V_b\left[\frac{\dot{Q}_{loss,L}}{A_j}\right]. \tag{5.71}$$

In the marching algorithm, we have two convergence criteria. The first criterion is the convergence of each individual node for the equations solved. The second criterion is the convergence of overall system for boundary conditions imposed. In this numerical method, first we solve the mass conservation equations in the inlet (bottom-hole) node. These equations are solved to obtain the phase velocities. If the boundary condition in the inlet is not pressure, a pressure is guessed for this node for calculating the fluids properties. The guess pressure can be a pressure close to the reservoir's or the initial pressure. Afterward, using Equation (5.69) and the constitutive relations explained in Section 3.5, flow regimes, pressure drop and holdup (liquid volume fraction) are calculated for the inlet node junction. After updating the velocities at the inlet, the energy equation (5.71) is solved iteratively to obtain temperature of the inlet node. Once convergence is achieved in the first node, the pressure gradient at the junction is used to update the pressure of the next node. Having the pressure of the next node, mass conservation equations (5.66), (5.67) and (5.68) are solved to obtain the phase velocity at this node. Again, pressure, holdup, and temperature are calculated and the steps are repeated at this node until convergence. These steps are repeated until we march all the nodes and reach the outlet boundary node. If a boundary condition, such as constant wellhead pressure or constant wellhead flow rate, were imposed to the outlet node, the calculated flow materials at outlet should be compared with the boundary values. If the calculated value for the outlet node is not close to the boundary value, all the calculations from inlet to outlet should be repeated with a new pressure guess at the inlet. For a shorter computation time, the inlet pressure is guessed using the Bisection algorithm. With the Bisection algorithm, we first give two initial guesses for the inlet (bottom-hole) pressure that yields larger and smaller values than the boundary values. These two pressures are the upper and lower bounds of the searching interval for the correct pressure. Thus, the Bisection algorithm searches this interval until it reaches inlet pressure that maintains the closest value of outlet flow to the boundary value.

Since the Bisection algorithm works only for monotonic functions, the pressure interval given for root searching should have this feature. In multiphase flow models due to non-linearity of the equations, pressure-flow relation may deviate from monotonic functionality. Hence, depending on the flow conditions, multiple solutions may exist for the inlet pressure that can satisfy the outlet boundary condition. Finding the correct pressure depends on the selection of correct interval for the bisection algorithm.

5.3.5 Updating the State Relations

Once the field equations are solved from the discretized equations the fluids state can be calculated using the state relations. In Appendix (B) and (C) the main formulations for compositional and blackoil models are discussed in detail.

Since in compositional modeling approach the overall mole composition of crude oil is needed as the feed to the flash calculation following equations from components mass conservation are used to update the molar compositions.

$$
\begin{aligned}
N_{k,i}^{n+1} = N_{k,i}^{n} + \\
&\frac{\Delta t}{V_b^n} A_{i-1}^n \left[\left(\hat{\rho}_o \alpha_o u_o \right)_{i-1}^{n+1} x_{k,i-1}^n + \left(\hat{\rho}_g \alpha_g u_g \right)_{i-1}^{n+1} y_{k,i-1}^n \right] - \\
&\frac{\Delta t}{V_b^n} A_i^n \left[\left(\hat{\rho}_o \alpha_o u_o \right)_i^{n+1} x_{k,i}^n + \left(\hat{\rho}_g \alpha_g u_g \right)_i^{n+1} y_{k,i}^n \right] + \\
&\Delta t \left[\dot{\psi}_{ok} + \dot{\psi}_{gk} \right]_i^{n+1}, \qquad k = 1, \ldots, nc
\end{aligned}
\tag{5.72}
$$

$$
z_{k,i}^{n+1} = \frac{N_{k,i}^{n+1}}{\sum_{k=1}^{nc} N_{k,i}^{n+1}}, \tag{5.73}
$$

where, $N_{k,i}$ is the mole per bulk volume of component *k* at node *i*, $x_{k,i}$ is the composition of component *k* in oil phase, $y_{k,i}$ is the composition of component *k* in gas phase, $z_{k,i}$ is the overall molar composition of component *k* in the hydrocarbon phases.

5.4 TIME-STEP CONTROL

The last step in multiphase flow calculation is time-step controlling, which dictates the size of the time-step in the simulation. In UTWELL we have used two different time-step controlling techniques for semi-implicit and fully-implicit numerical methods.

Since in the semi-implicit method, solutions are obtained with no iterations, the size of the time-step is crucial for linear convergence of the model. The criterion for time step-size in semi-implicit method is the total mass error in the gridblocks. From Equations (5.51), (5.52) and (5.53), the total in-situ mass calculated from mass conservation equations is obtained

$$
(\rho_{mt})_L^{n+1} = (\rho_w \alpha_w)_L^{n+1} + (\rho_g \alpha_g)_L^{n+1} + (\rho_o \alpha_o)_L^{n+1}. \tag{5.74}
$$

Using the state relations, the total in-situ mass should be

$$(\rho_{ms})_L^{n+1} = (\rho_{w,L}^{n+1}\alpha_{w,L}^{n+1}) + (\rho_{o,L}^{n+1}\alpha_{o,L}^{n+1}) + (\rho_{g,L}^{n+1}\alpha_{g,L}^{n+1}). \tag{5.75}$$

The difference between these two average mixture densities reflects on the calculated mass error in each gridblock. Accordingly, we define the relative mass error and root mean square of mass error as the indices for time-step controlling as follows:

$$\varepsilon_m = \frac{max\left(\left|(\rho_{ms})_L^{n+1} - (\rho_{mt})_L^{n+1}\right|\right)}{(\rho_{ms})_L^{n+1}}, \tag{5.76}$$

$$\varepsilon_{rms} = \frac{2\sum_{L=1}^{N}\left[V_{b,L}\left((\rho_{ms})_L^{n+1} - (\rho_{mt})_L^{n+1}\right)\right]^2}{\sum_{L=1}^{N}\left(V_{b,L}(\rho_{ms})_L^{n+1}\right)^2}. \tag{5.77}$$

We define the time-step size based on the magnitude of relative error as

$URME < \varepsilon_m, \varepsilon_{rms}$, $\quad \Delta t^{new} = \frac{1}{2}\Delta t^{old}$, repeat the calculation

$LRME < \varepsilon_m, \varepsilon_{rms} < URME \quad \Delta t^{new} = \Delta t^{old}$

$\varepsilon_m, \varepsilon_{rms} < LRME \quad \Delta t^{new} = 2\Delta t^{old}$

where $URME$ and $LRME$ are the upper and the lower residual mass error parameters. We typically choose 8×10^{-3} and 8×10^{-4} for these parameters, respectively.

In addition, the time-step size is limited to phasic CFL numbers which are defined as

$$(\Delta t_c)_j = \Delta x_j \times \frac{max(\alpha_{o,j}, \alpha_{g,j}, \alpha_{w,j})}{max(\left|\alpha_{o,j} u_{o,j}\right|, \left|\alpha_{g,j} u_{g,j}\right|, \left|\alpha_{w,j} u_{w,j}\right|)}. \tag{5.80}$$

So Δt should always be smaller than $min(\Delta t_{c,j})$.

For the fully implicit method we used for the drift-flux model, the time-step control does not need the CFL number check. In this technique, we also define the time-step size with the total mass error index. Hence, the new time-step for the fully implicit method is obtained

$$\Delta t^{new} = \frac{RME}{\left(\frac{(\rho_{ms})_L^{n+1} - (\rho_{ms})_L^n}{(\rho_{ms})_L^n} \right)} \Delta t^{old}, \tag{5.81}$$

where RME is the defined residual mass error.

5.5 NUMERICAL CONVERGENCE AND ROBUSTNESS OF SOLUTIONS

In the following sections, we perform several validation tests on our multiphase flow models against analytical solutions and available multiphase flow programs.

5.5.1 Water Faucet Problem

Water faucet problem is a famous problem introduced by Ransom (1987) for testing correctness of conservation equations and the numerical solution scheme of multiphase flow models. Nevertheless, this test cannot verify the flow regimes and the drag forces correlations between the phases and the wall.

When we open a water faucet, we always observe that water falls down with a varying cross section. It becomes narrower in the bottom than top of the flow path. The reason for this phenomenon is the gravity acceleration that changes the velocity of water and consequently the shape of water cross section .Assuming a negligible pressure gradient in the flow, using equations of motion, or macroscopic energy, we can derive the following expression for the velocity of water:

$$u_w = \sqrt{u_{w0}^2 + 2gz}, \tag{5.82}$$

where z is distance from inlet and u_{w0} is the velocity of water at inlet.

Combing the velocity equation with continuity, we can also find the cross section of the water along its path as

$$\alpha_w u_w = \left(\alpha_w u_w\right)_0 . \tag{5.84}$$

The water faucet problem can also be modeled in multiphase flow simulators. We can build an equivalent imaginary discretized pipe with zero roughness that is filled with air, and water is injected from top of this pipe. The cross section of this pipe is assumed to be an arbitrary constant value (i.e. 0.229 ft) and the length of the pipe is assumed 100 ft. The boundary conditions that we assign are Mass Flow Node at inlet with an arbitrary value (i.e. 10 lb/sec) and Pressure Node at the outlet (i.e. 15 psi). The amount of inlet mass flow rate of water prescribes the volume fraction of the water in the pipe. The higher the flow rate is the higher the volume fraction of water is in the pipe.

We discretize the pipe to 21 gridblocks. We run the simulation for about 100 sec to make sure that we reach to steady state condition. Moreover, we turn off the interphase drag force, virtual mass, and wall drag forces calculations to have a similar condition with analytical model.

Figure 5.3 shows the comparison of velocity profiles between analytical and numerical simulation and Figure 5.4 shows the comparison of water volume fraction obtained from numerical simulation and the analytical model. As can be seen, we achieved perfect match between these two models. These comparisons endorse the validity of our numerical model for consistency and convergence.

5.5.2 Phase Redistribution Problem

One of the challenging problems that are tested for the numerical convergence of multiphase flow simulators is the phase redistribution problem. In this case we start from an unphysical initial condition and let the system to reach to the equilibrium condition and separate the light and heavy phases. In this section, we assume a 1600 ft column of liquid and gas mixture with 50 percent of gas volume fraction is equilibrated to separate the gas liquid phases. The liquid is assumed to be water and the gas to be air at initial condition of hydrostatic pressure with 2500 psi at bottom and constant temperature of 85 ^{o}F. We assign Closed Node boundary conditions in the inlet an outlet to make sure that mass does not flow in the column. We perform the simulation for 2500 sec using the nearly-implicit approach for two-fluid model.

Figure 5.5 through 5.8 show the liquid volume fraction, pressure, velocity of gas and velocity of liquid profiles with time elapsed. As can be seen the simulator is capable to robustly separate the fluids after 1900 sec. The interface reaches to the middle of the column (800 ft) where were expecting. The velocity profiles in the graphs also show a jump at the interface due to the saturation shock. In addition, the velocities profiles shrinkage around the interface point and vanish with time progression.

In Figure 5.9 we also plotted the bottom-hole pressure versus time. As can be seen the bottom-hole pressure increases with time until it reaches to a final value at equilibrium. Fair (1981) performed similar calculation for the effect of phase redistribution on pressure buildup analysis. He introduced an analytical model for the bottom-hole pressure as function of time as follow:

$$\Delta P_{bh} = C_{\varphi}\left(1 - e^{-\xi t}\right). \tag{5.85}$$

Considering ξ = 0.0035 and C_{φ} = 133.2 psi in Equation (5.85), we plotted this equation in Figure 5.9 as well. As can be seen the trend of our numerical simulation results fairly match with the Fair (1981) analytical model. The discrepancy between analytical and numerical model at initial time is due to drag forces that is accounted in the numerical model and the initial condition of the system. Since at initial time the phase velocities are not negligible, the drag forces affect the bottom-hole pressure. This behavior confirms our physical intuition from phase separation process where a column of liquid is added to the initial pressure after complete separation in a closed system.

5.6 SIMULATION RESULTS

In this section, comparison of different numerical models that we previously discussed, such as semi-implicit two-fluid model (SIMPTF), nearly-implicit two-fluid model (NIMPTF), semi-implicit homogenous model (SIMPH), fully implicit drift-flux model (FIMPDF), fully implicit homogenous model (FIMPHM) and steady state two-fluid model (SS) are performed to investigate the efficiency and accuracy of the models against each other. In addition, validation tests are performed against commercial simulators such as OLGA and PIPESIM to verify the numerical consistency of UTWELL for multiphase flow simulation.

Moreover, several other test cases of original version of UTWELL have been verified against field and experimental data in Shirdel (2010) and Shirdel and Sepehrnoori (2012).

5.6.1 Comparison of Different Numerical Methods

We consider two sets of simulations to compare our different numerical methods results for multiphase flow simulation. First, we perform a three phase (gas, oil, water) flow simulation in the wellbore until we reach to steady state solution. Second, we only produce gas after reaching to the steady state condition to deplete all the liquid phases in the wellbore. With these simulations we desire to verify the solution results for two-fluid model, drift-flux model and homogenous model, the consistency of the numerical approaches (NIMPTF, SIMPTF) for two-fluid model and the computation time for each methods. We use only default values of all the constitutive relations and the correlations in the drift-flux slippage ratio and the interphase drag forces.

5.6.1.1 Three-phase Flow Simulation

Table 5.1 shows the main input parameters for the simulation of three-phase flow in the wellbore. The detail of the input data for this simulation is also in Appendix (E.1). In this simulation, we have a 2000 ft well initially filled with 0.1 volume fraction of water, 0.1 volume fraction of oil and 0.8 volume fraction of gas. We produce from this well with constant wellhead pressure of 1000 psi for about 2 hours until well reaches to the steady state condition. In this simulation, we are interested to compare the performance of different models that we have developed in UTWELL. Thus, we perform the simulations using different methods such as two-fluid model, drift-flux model and homogenous model, and different numerical approaches.

Table 5.5 shows the computation time for each method. As can be seen, the simulation times for semi-implicit and nearly implicit models are very close to each other, the fully implicit methods are about two times slower than semi-implicit models and the steady state method is about 10 times faster. The computation time reported in Table 5.5 is very case dependent. We do not necessarily have this order in all the simulations. In fact, SS simulation is always the fastest method since it does not march in the time. The fully implicit method depending on the solver algorithm and the size of gridblocks and maximum allowable time step can become faster than semi-implicit models too.

Figures 5.10 (a) through 5.10 (h) shows the profiles of all the main variables (pressure, temperature, water velocity, oil velocity, gas velocity, water volume fraction, oil volume fraction, gas volume fraction) that are calculated in UTWELL. As we observe the trend of each flow model regardless of the numerical approach that is used, are similar. For instance, the Semi-implicit Two-fluid Model (SIMPTF) and Nearly-implicit Two-fluid Model (NIMPTF) show very close results to Steady-state model with marching algorithm (SS). The drift-flux model has also similar trend to two-fluid models however it has some discrepancies in its results. The homogenous models developed in fully-implicit and semi-implicit numerical methods also show similar trends in the profiles. In fact, the discrepancies in the simulation results are inherent in the assumptions of each model and more importantly the assumptions for modeling slippage between oil, water and gas. Since our steady-state model is based on two-fluid approach it shows similar results to our transient two-fluid models .However, since the constitutive relations in SS and TF models are not quit the same we do not achieve exactly the same solutions for all of the profiles.

Moreover, from these simulation we conclude that slippage between the phases plays an important role in the profiles of pressure, velocities and volume fractions. In fact, this parameter is non-linearly coupled to all the field equations and estimating the slippage between the phases (or the constitutive relations for interphase forces) wrongly can yield completely wrong solutions.

5.6.1.2 Gas Production Simulation

The next simulations that we performed after three-phase flow in the wellbore was producing only gas from bottom of the well. This is a hypothetic case that we just want to observe the behavior of the models when they are turned from multiphase flow to single-phase flow. Therefore, in this set of simulation we changed the oil and water productivity indices to zero and increased the productivity index of gas to10 ft^3/D-ft-psi. We performed the simulation until new steady state solution is observed.

Figures 5.11 (a) through 5.11 (d) show the pressure, temperature, gas velocity and gas volume fractions at the end of steady state solution, respectively. As we can see, the results for all numerical models and the calculations methods are very close. In fact, since we obtain single-phase flow in our system, we were expecting that all the models converge to the same solutions. This simulation validates different important terms such as phasic wall friction, drag forces and also it can validates the accuracy and convergence of the models where we know the results of single phase flow conditions.

5.6.2 Validation of Transient Models

We chose a water and gas two-phase flow problem to compare our results against a commercial transient simulator OLGA (Bendiksen et al., 1991). To avoid the complexity of the interphase mass transfer and the PVT calculation we considered water/gas two-phase flow. We compared the simulation results for pressure, temperature, phase velocities and the volume fraction results at the end of simulation time when we obtain steady state solutions.

The input parameter setup for this case has been shown in Table 5.2. Figures 5.12 (a) through 5.12 (f) show the simulation results for pressure, temperature, gas volume fraction, water volume fraction, gas velocity and water velocity , respectively. As can be seen our results have very good agreement with OLGA results.

5.6.3 Validation of Steady State Models

A gas-lift simulation plus a case study for wellbore temperature calculation from Hasan and Kabir (1996) are used for verification of our steady-state model.

5.6.3.1 Gas-lift Simulation

Table 5.3 shows the pertinent data for the gas-lift simulation case. In this case, we have dead oil filling a 7000 ft well and we want to inject gas at the depth about 4100 ft to assist the well to flow. Initially, due to hydrostatic pressure the well was killed and flow was zero. Injecting the gas in the wellbore reduces the density of the well and causes flow. Gas injection flow rate should not exceed a certain value since the larger flow can also cause larger friction loss effect.

Similar models are built in PIPESIM and UTWELL to compare the results. In fact, we chose this simulation to be able to test the gas injection process along with flow regimes changes, and test more complicated flow regimes like slug flow in UTWELL. We chose Ansari et al. (1994) model in PIPESIM for the entire simulations.

When we inject gas into the wellbore the pressure profile changes and causes a drawdown pressure between wellbore and the reservoir through the perforations. This pressure gradient can cause flow. The greater draw-down pressure we obtain the greater oil flow. A bunch of simulations is designed to obtain the effect of gas injection rate on the oil flow rate. Depending on the flow rate of injected gas, a series of different flow regimes from bubbly flow to annular flow is observed in our simulation. These simulations are performed in both PIPESIM and UTWELL.

Figure 5.13 shows the oil flow results against gas flow rate for UTWELL and PIPESIM. Figures 5.14 and 5.15 also show the pressure profiles in the tubing for two of the simulations that gas injection rates are 0.2 and 0.5 MMSCF/D respectively. As can be seen there are good agreements between our model results and PIPESIM. In addition, as we were expecting, the oil flow rate reaches a maximum value in a specific gas injection rate, which beyond that oil flow rate declines due to friction forces.

5.6.3.2 Wellbore Temperature Model

A numerical approach with consideration of enthalpy change is used for UTWELL steady state model. In this model the energy equation is solved using Newton-Raphson method after obtaining momentum and mass conservation results. A similar approach is also used in PIPESIM for temperature calculation. In this section, we compare our results with PIPESIM plus the analytical results from Hasan and Kabir

(1996). Table 5.4 shows the pertinent data for the simulation setup, wellbore, reservoir and fluid data.

Figure 5.16 also shows the temperature profile results. UTWELL results are reasonable against the other models. The existing discrepancy can be related the annulus heat transfer model. In fact, in this case gas is injected through annulus that can affect the heat transfer between wellbore and the surrounding formation.

Table 5.1 Input parameters for gas/oil/ water three-phase flow simulation in UTWELL with different numerical schemes

Well Data		**Reservoir and Fluid Data**	
Well MD	2000 ft	Net pay zone	150 ft
Well TVD	2000 ft	Reservoir pressure	2000 psi
Max grid size	50.0 ft	Reservoir temperature	180 °F
Ambient temperature at top	60 °F	Oil API	30
Ambient temperature at bottom	180 °F	Oil bubble point pressure	2000 psi
Total heat transfer coefficient	1.0 Btu/ft^2-hr-°F	Gas specific gravity	0.6
Tubing ID	0.229 ft	Water specific gravity	1.0
Oil productivity index	0.1 ft^3/psi-ft-day	Gas heat capacity	0.55 Btu/lbm-°F
Water productivity index	0.1 ft^3/psi-ft-day	Oil heat capacity	0.45 Btu/lbm-°F
Gas productivity index	1.0 ft^3/psi-ft-day	Water heat capacity	1.0 Btu/lbm-°F
Wellhead pressure	1000 psi		

Table 5.2 Input parameters for gas/water two-phase flow simulation in UTWELL and OLGA

Well Data		**Fluid Data**	
Well MD	5000 ft	Gas specific gravity	0.7
Well TVD	5000 ft	Water specific gravity	0.98
Max grid size	50 ft	Gas heat capacity	0.55 Btu/lbm-°F
Ambient temperature at top	71 °F	Water heat capacity	1.0 Btu/lbm-°F
Ambient temperature at bottom	141 °F		
Total heat transfer coefficient	0.5 Btu/ft^2-hr-°F		
Tubing ID	0.25 ft		
Water mass injection	1 lb/sec		
Gas mass injection	1 lb/sec		
Wellhead pressure	500 psi		

Table 5.3 Input parameters for the gas-lift simulation in UTWELL and PIPESIM

Well Data		**Reservoir and Fluid Data**	
Well MD	7000 ft	Net pay zone	100 ft
Well TVD	7000 ft	Reservoir pressure	2350 psi
Tubing ID	0.229 ft	Reservoir temperature	155.9 F
Tubing OD	0.29166 ft	Oil API	35.072
Casing ID	1.56 ft	Oil bubble point pressure	14.696 psi
Casing OD	1.66 ft	Gas specific gravity	0.55
Wellbore hole size	1.7498 ft	Oil heat capacity	0.45 Btu/lbm-^{o}F
Well productivity index	0.02 STB/ psi-ft-day	Gas heat capacity	0.40 Btu/lbm-^{o}F
Wellhead pressure	150 psi	Oil thermal conductivity	0.45 Btu/hr-ft-^{o}F
Gas injection depth	4100 ft	Gas thermal conductivity	0.55 Btu/hr-ft-^{o}F

Table 5.4 Input parameters for comparison of wellbore temperature calculation between UTWELL, PIPESIM and analytical model from Hasan and Kabir (1996)

Well and Reservoir Data		**Fluid Data**	
Well MD	15000 ft	Net pay zone	100 ft
Well TVD	15000 ft	Reservoir pressure	5000 psi
Tubing ID	0.46 ft	Reservoir temperature	250 F
Tubing OD	0.56 ft	Oil API	20.661
Casing ID	0.7 ft	Oil bubble point pressure	14.696 psi
Casing OD	0.8 ft	Gas specific gravity	0.6
Wellbore hole size	1.0 ft	Oil heat capacity	0.40 Btu/lbm-^{o}F
Well productivity index	0.1 STB/ psi-ft-day	Gas heat capacity	0.25 Btu/lbm-^{o}F
Bottom-hole pressure	4071 psi	Oil thermal conductivity	0.45 Btu/hr-ft-^{o}F
Gas injection depth	14900 ft	Gas thermal conductivity	0.55 Btu/hr-ft-^{o}F
Casing head pressure	3500 psi		
Casing head temperature	75 ^{o}F		

Table 5.5 Comparison of computation times for different numerical models on a windows platform with 2.17 GB usable RAM and 2.30 GHz CPU

SIMPTF	45 sec
NIMPTF	49 sec
SIMPHM	49 sec
FIMPDF	101 sec
FIMPHM	98 sec
SS	4 sec

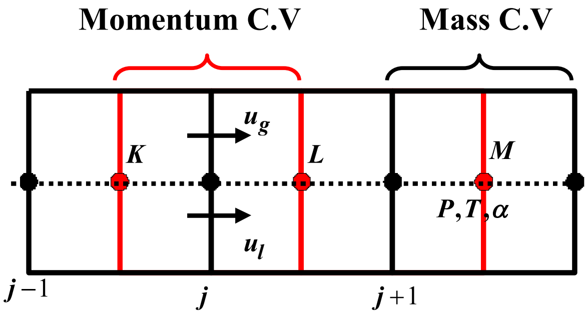

Figure 5.1 Schematic view of the staggered gridding.

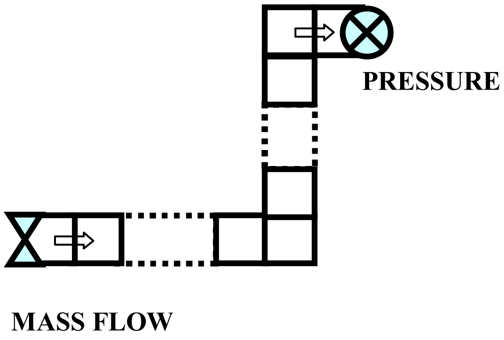

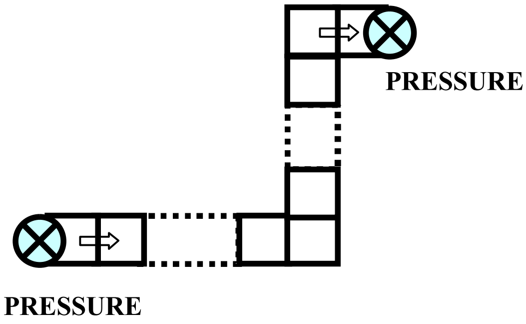

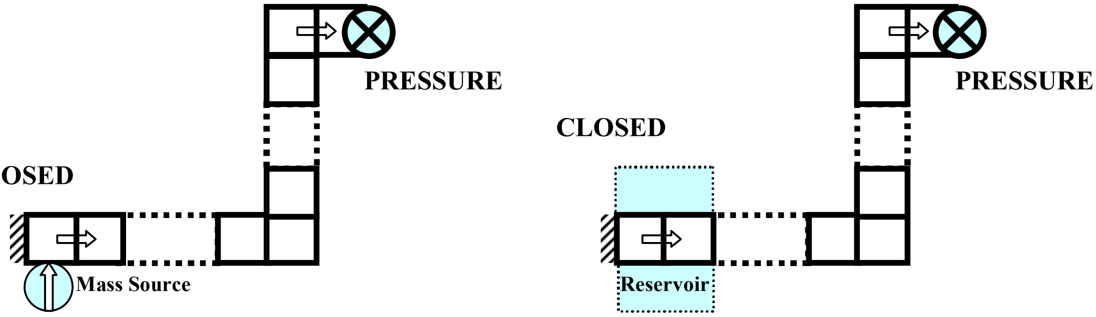

Figure 5.2 Schematic view of boundary conditions setup in UTWELL.

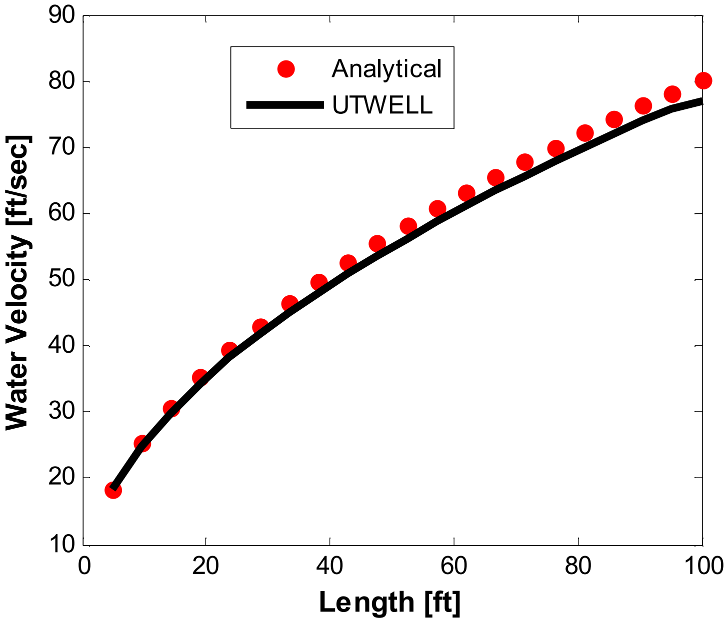

Figure 5.3 Comparison of numerical and analytical solutions for water velocity profiles in water faucet problem.

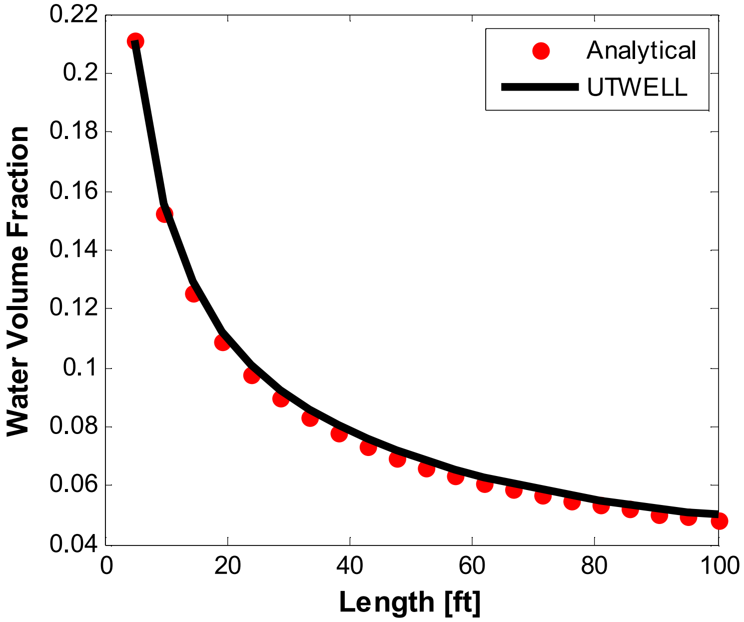

Figure 5.4 Comparison of numerical and analytical solutions for water volume fraction profiles in water faucet problem.

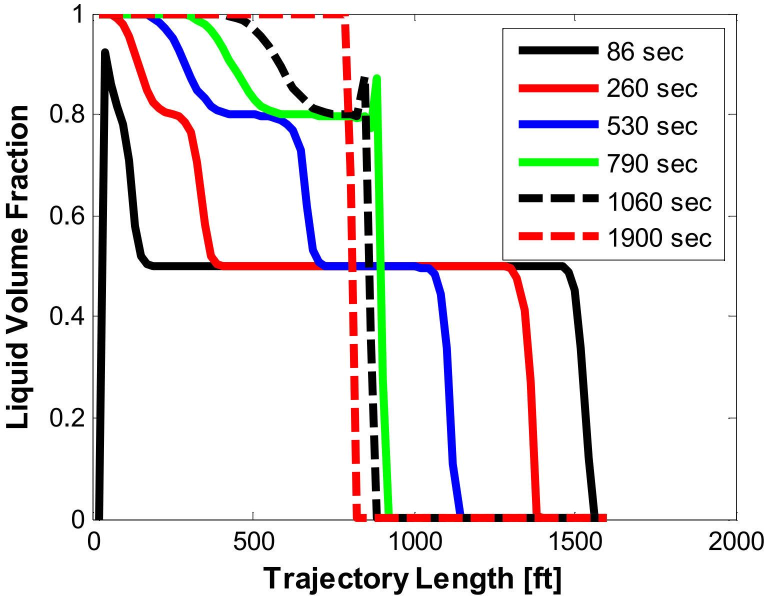

Figure 5.5 Pressure profile results for phase redistribution of a gas liquid mixture column.

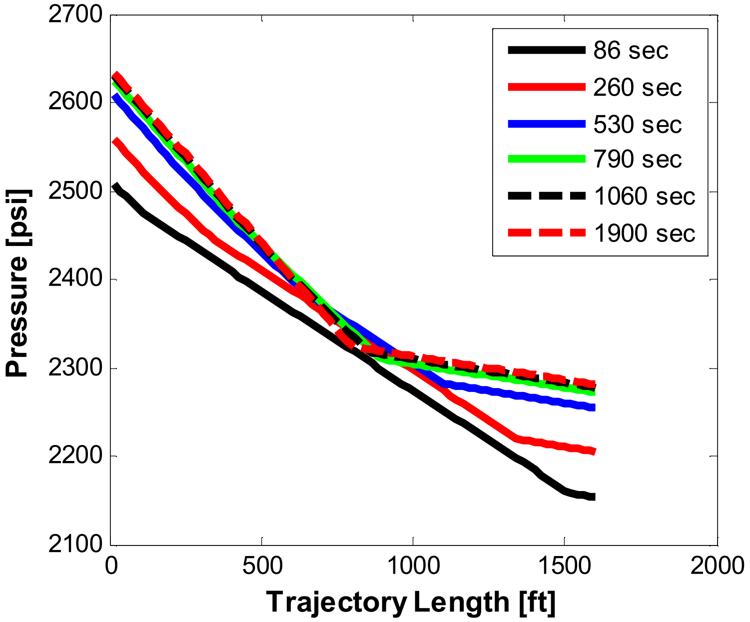

Figure 5.6 Pressure profile results for phase redistribution of a gas liquid mixture column.

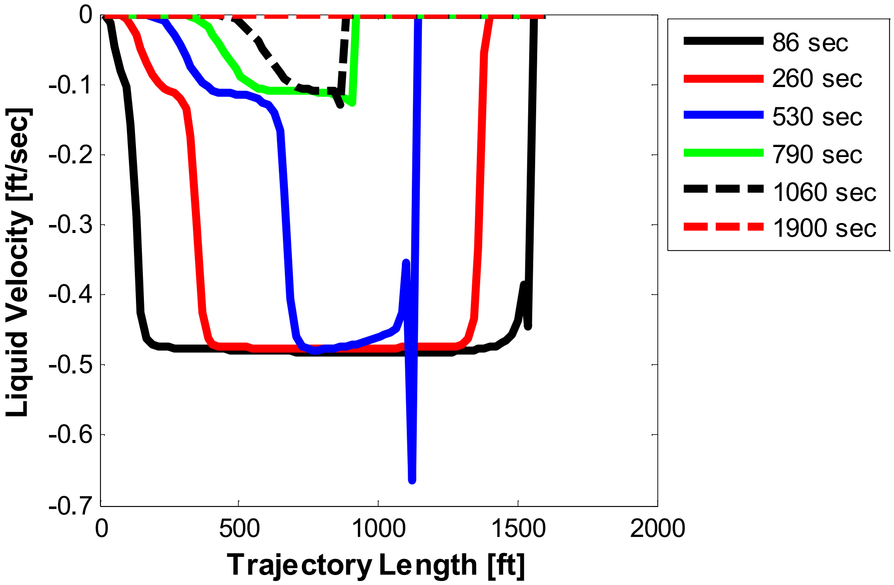

Figure 5.7 Pressure profile results for phase redistribution of a gas liquid mixture column.

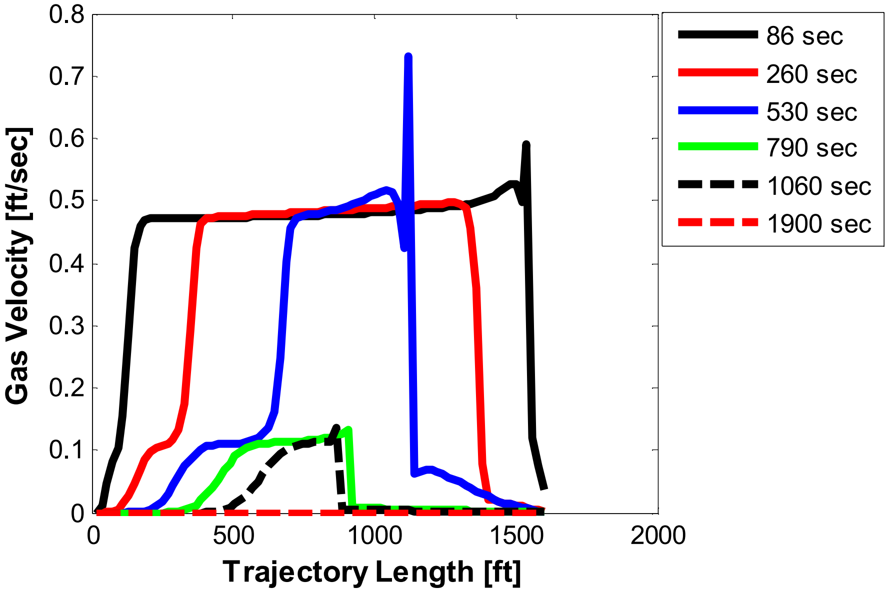

Figure 5.8 Pressure profile results for phase redistribution of a gas liquid mixture column.

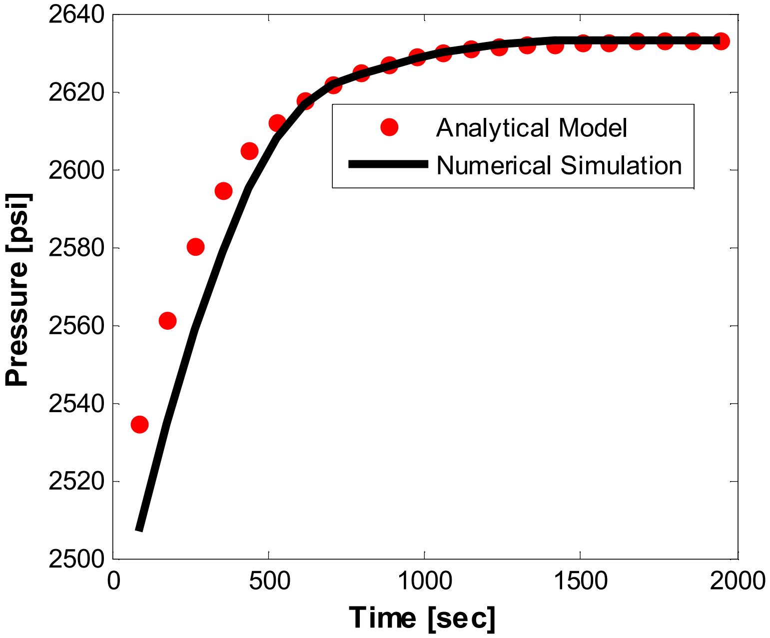

Figure 5.9 Variation of bottom of column pressure versus time for phase redistribution process of a gas liquid mixture.

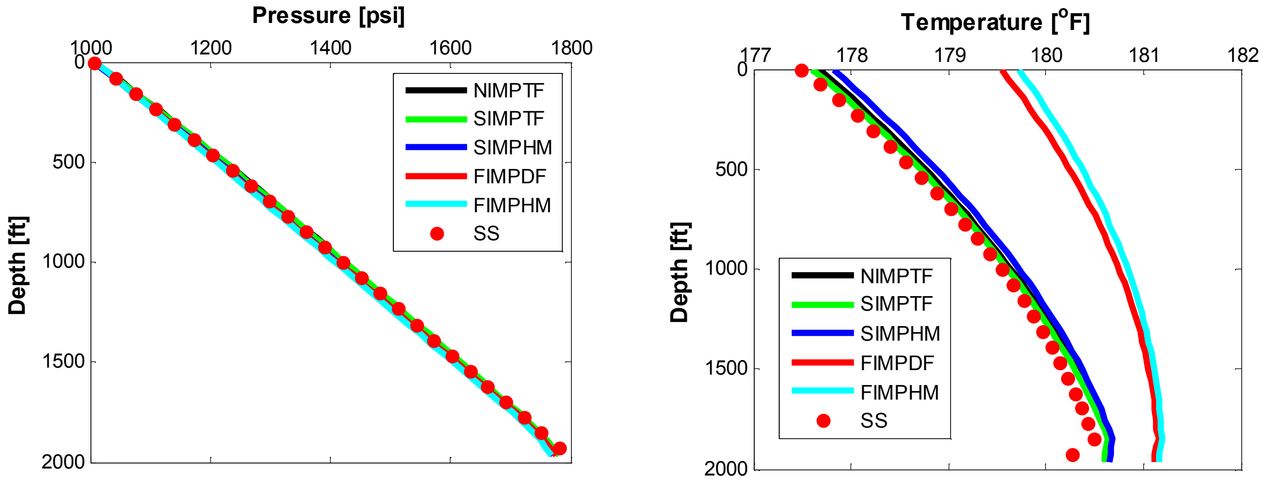

(a) pressure profiles

(b) temperature profiles

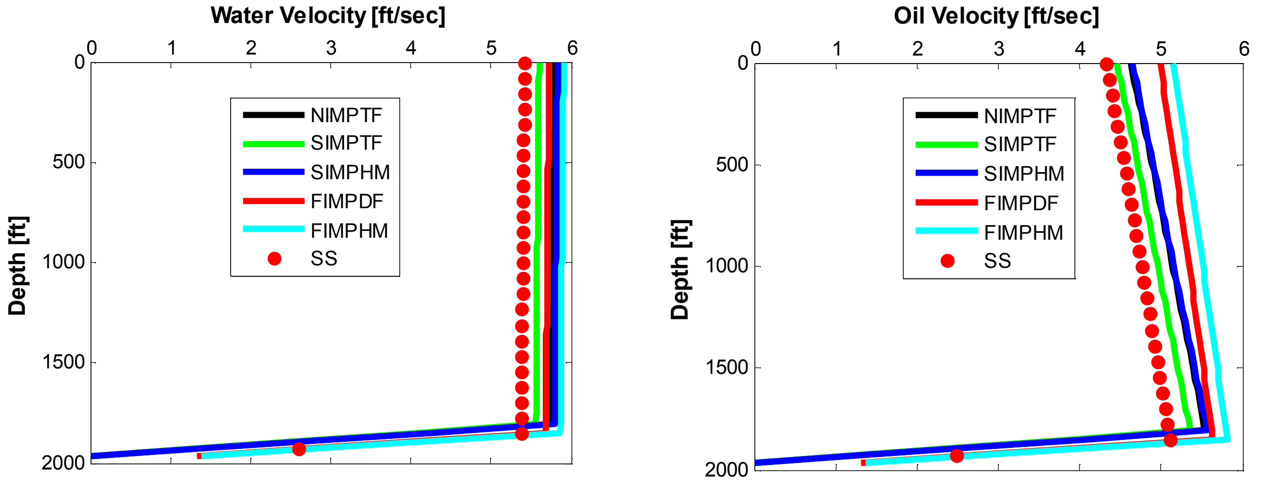

(c) water velocity profile

(d) oil velocity profile

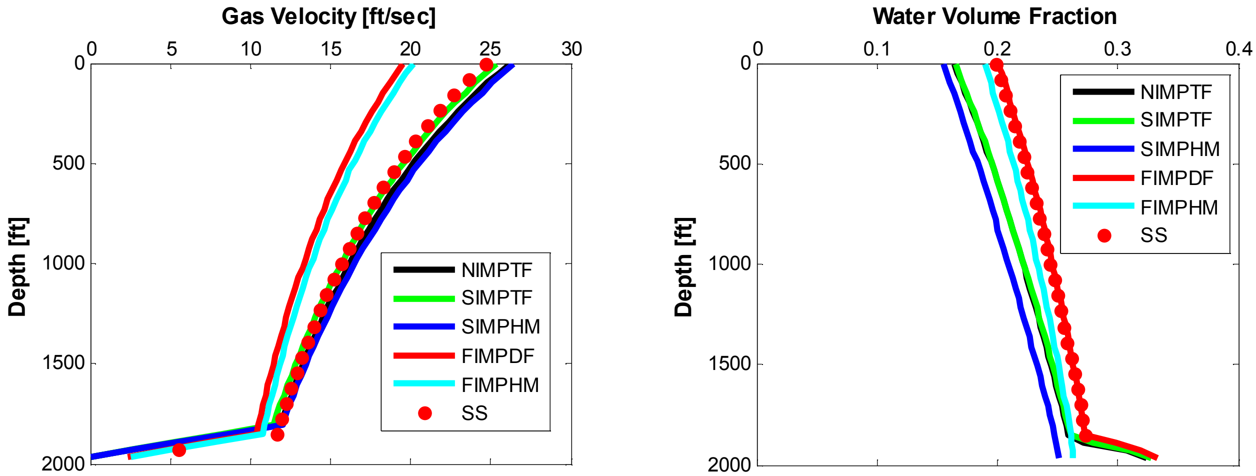

(e) gas velocity profile

(f) water holdup profile

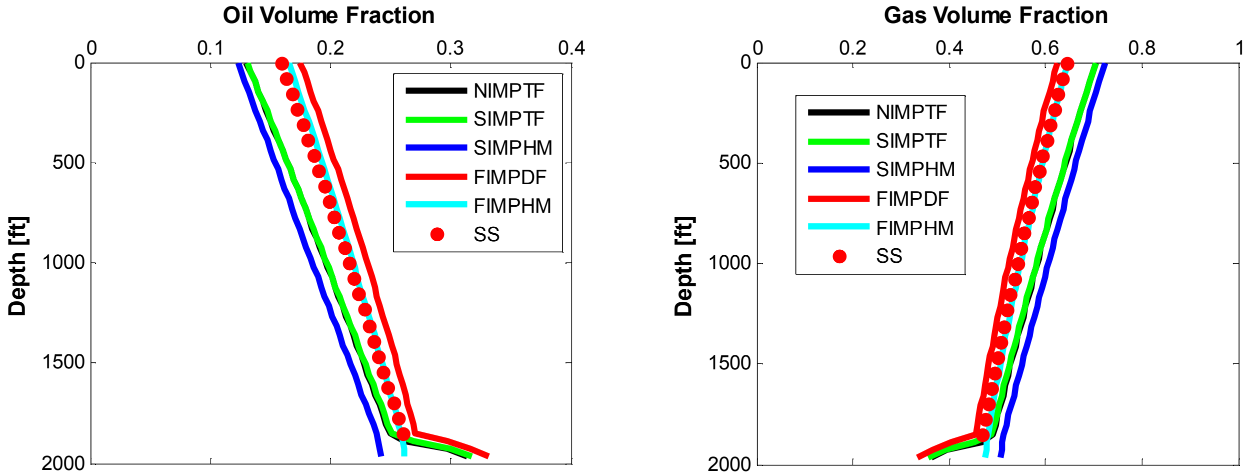

(g) oil holdup profile

(h) gas holdup profile

Figure 5.10 Comparison of primary variables profiles along the well for different multiphase flow models (two-fluid, drift-flux, homogenous) and different numerical methods (Semi-implicit, Nearly-implicit, Fully-implicit, Steady State Marching Method) at the end of steady state solution.

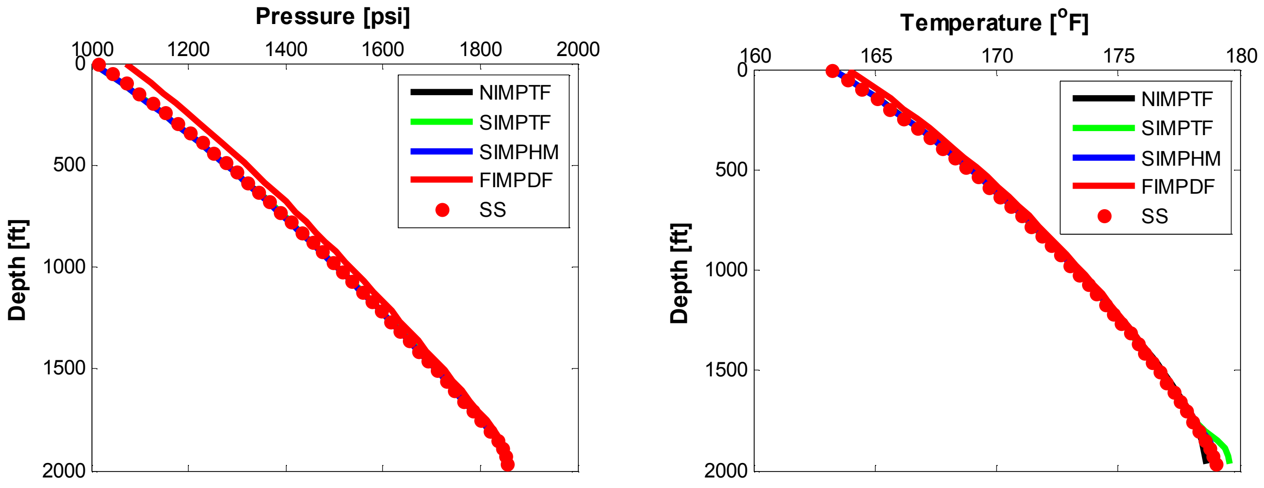

(a) pressure profiles

(b) temperature profiles

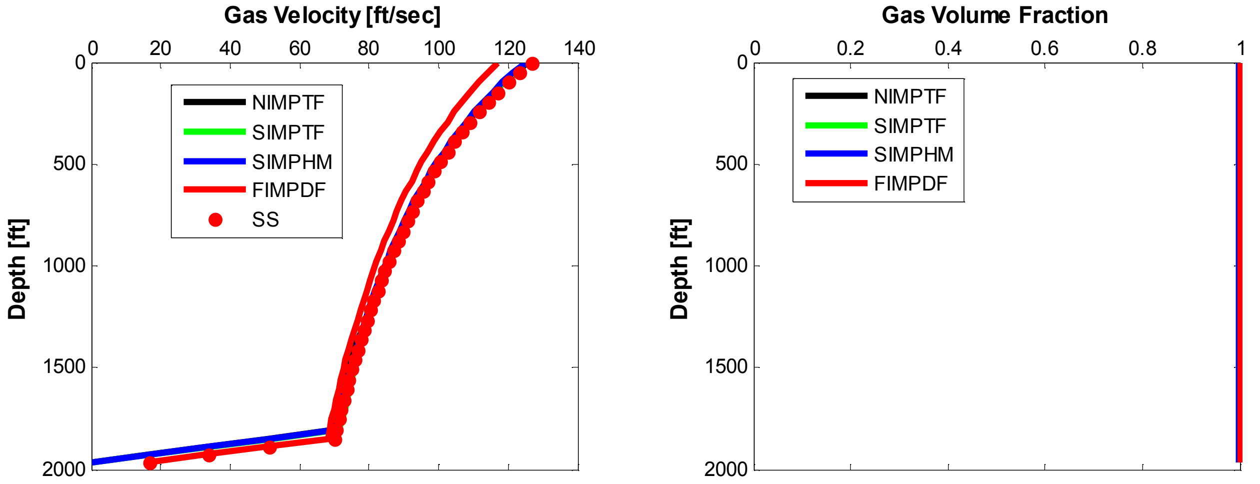

(c) gas velocity profiles

(d) gas volume fraction profiles

Figure 5.11 Comparison of main variables profiles along the well for different multiphase flow models and numerical methods for gas production at the end of steady state solution.

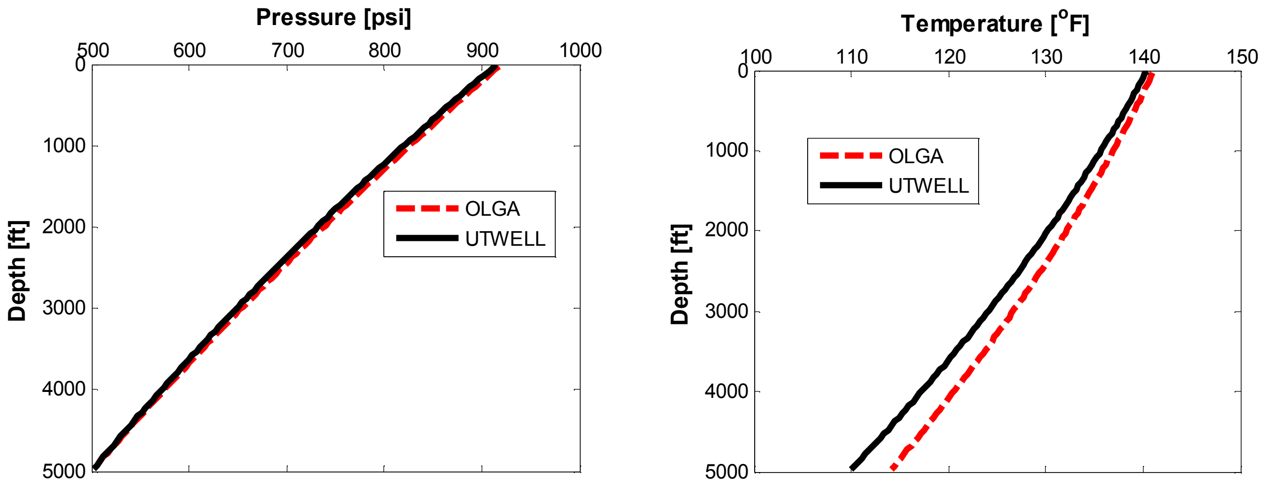

(a) pressure profiles

(b) temperature profiles

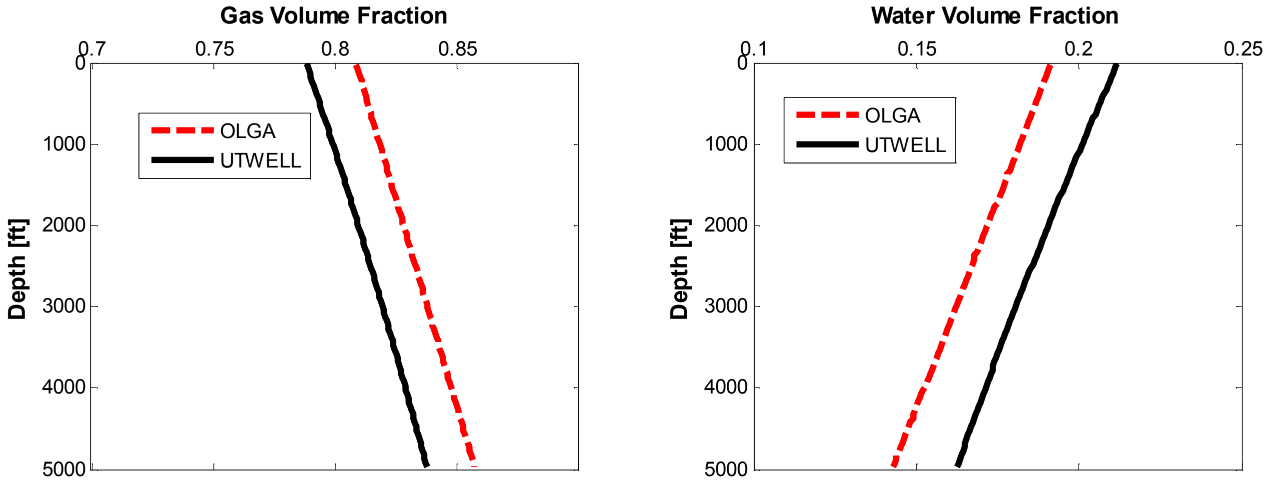

(c) gas volume fraction profiles

(d) water volume fraction profiles

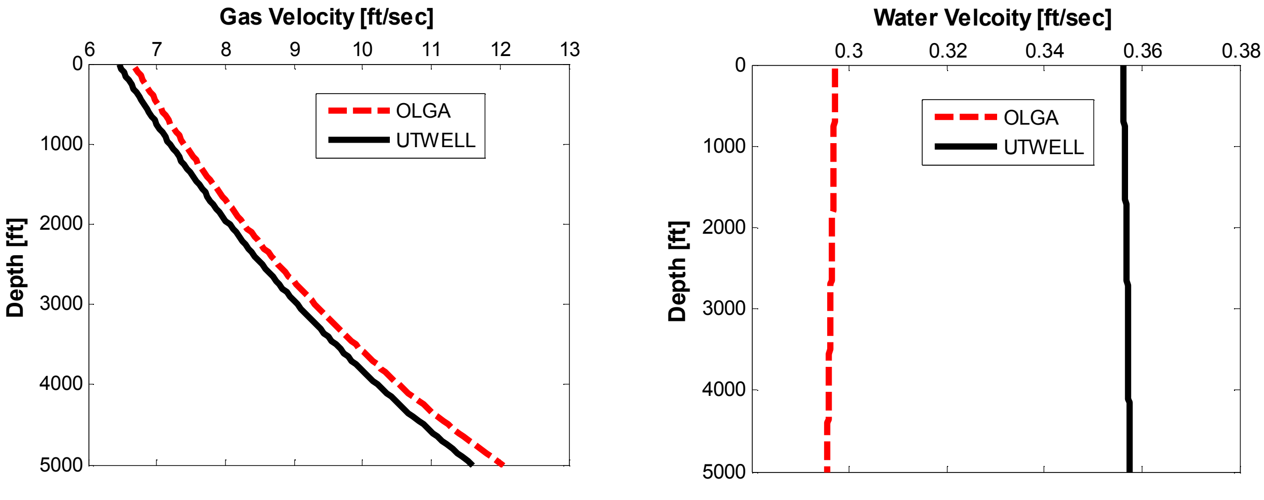

(e) gas velocity profile

(f) water velocity profile

Figure 5.12 Comparison of main variables profiles between OLGA and UTWELL for transient two-phase flow simulation.

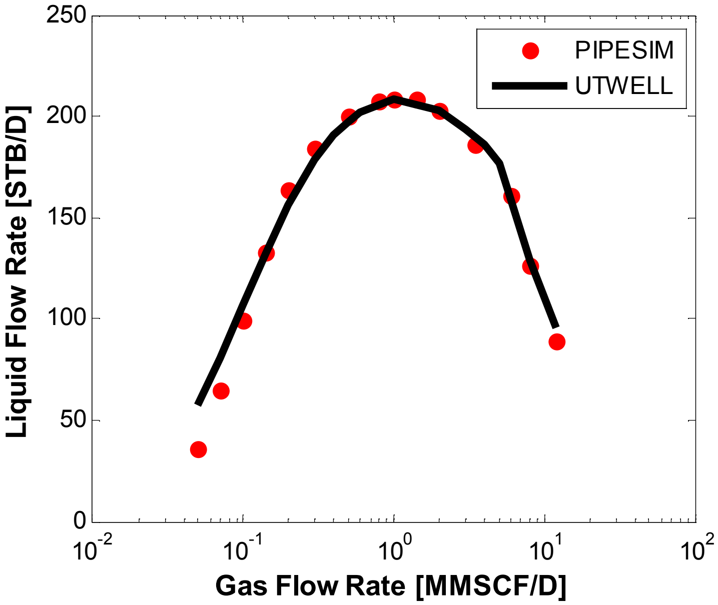

Figure 5.13 Liquid flow rate versus gas injection rate for gas-lift optimization curve. Comparison between PIPESIM and UTWELL results.

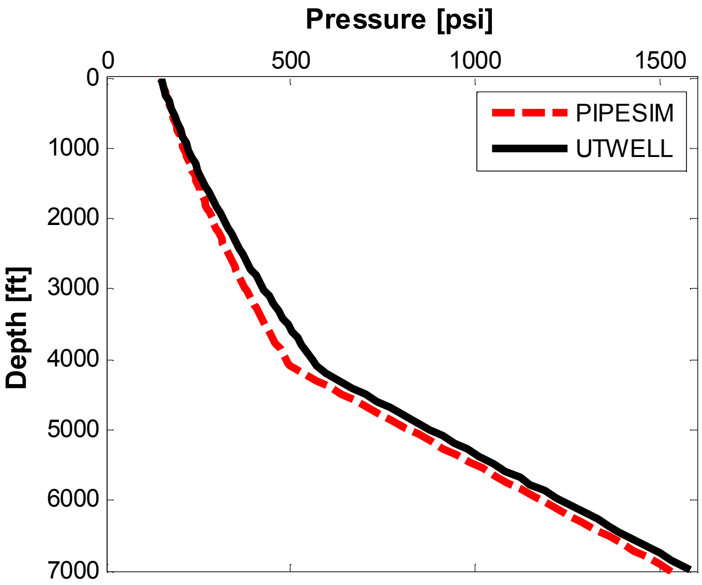

Figure 5.14 Pressure profiles along the well after 0.2 MMSCF/D gas injection at depth 4100 ft. Comparison of results between PIPESIM and UTWELL.

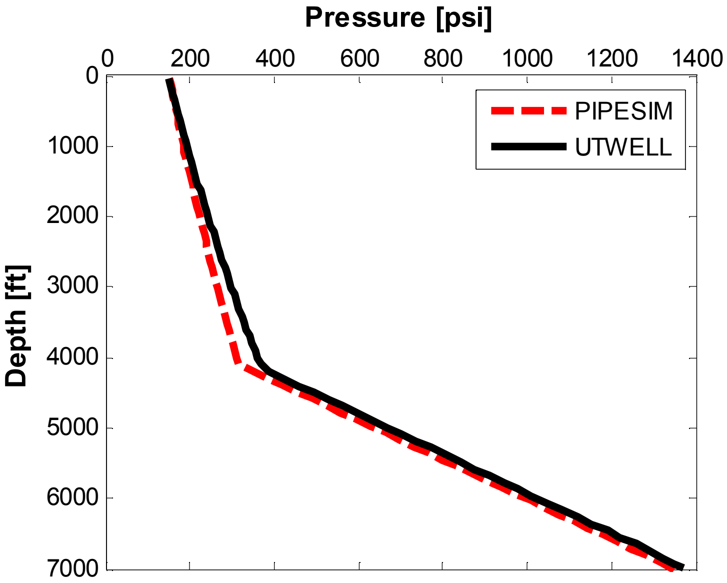

Figure 5.15 Pressure profiles along the well after 0.5 MMSCF/D gas injection at the depth 4100 ft. Comparison of results between PIPESIM and UTWELL.

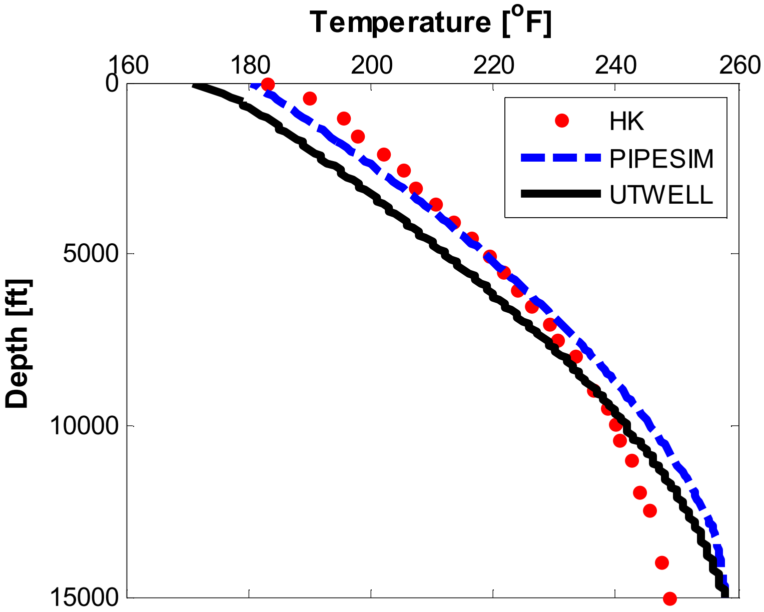

Figure 5.16 Comparison of temperature profiles along the well between PIPESIM, UTWELL and Hasan and Kabir (1996) analytical model.

Chapter 6: Flow Assurance Issues in the Wellbore

The major flow assurance problems that occur in the fields concern with asphaltene, wax, and scale deposition. Wax and asphaltene deposition are mostly addressed in deep-water environments, where fluid flows through a long path with a wide range of pressure and temperature variations. In fact, a significant change in the thermodynamic condition of the fluid yields phase instability and solid deposit formation. Recently, application of light hydrocarbon injection also has increased the chance for aspahtlene deposition and asphaltene flow assurance in the fields. In contrast to wax and asphaltene, scales are geochemical solid particles formed in aqueous phase when incompatible ions are mixed.

In this chapter, we discuss asphaltene, wax and scale formation in the wellbore and probe the thermodynamic equilibrium condition whether the fluids containing these particles are stable or unstable. Understanding the phase behavior of these complex fluids is crucial for detecting flow assurance problems in fields.

6.1 ASPHALTENE

The name asphaltene is attributed to the most polar and heaviest components of the crude oil with an average carbon number of 40 to 80 and H/C ratio of 1.1 to 1.2. These components are insoluble in low molecular weight alkanes, like n-heptanes, and soluble in aromatic hydrocarbons like benzene (Carnahan, 2000). Asphaltene is composed of a polydisperse mixture of molecules containing oxygen, sulfur, nitrogen, certain metals (Iron, Nickel, and Vanadium) and polynuclear aromatic components (Scotti and Montanari, 1998).

During field operations, hydrocarbon fluid properties can drastically change from the reservoir condition to the surface. In some extent, the variation of fluid condition can cause instabilities in complex hydrocarbon fluids. Hydrocarbon fluids that contain asphaltene without enough support to stabilize these components are subjected to flow assurance problems. Various scenarios such as pressure, temperature change, presence of light hydrocarbon components, and comingling of incompatible fluids could be a potential reason for the asphaltene instability problem. Asphaltene problem is not only endemic to heavy oils, whereas these types of oils have handful of other stabilizing components such as resin that prevents insatiability of asphaltene. However, in some conventional oils where asphaltene is not readily dissolved, this issue, even with a few percent of mass content of asphaltene, is more pronounced.

6.1.1 Asphaltene Precipitation Model

For predicting asphaltene precipitation, most of the models are based on the classical Flory Huggins polymer solution theory. Leontaritis and Mansoori (1987) proposed a colloidal model which assumed that asphaltene particles were suspended solids in crude oil. Nghiem et al. (1993) also used an EOS-based approach for asphaltene precipitation. Victorov and Firoozabadi (1996) discussed the micellization of asphaltene and proposed the thermodynamic micellization models. However, recently Gonzalez et al. (2007) and Li and Firoozabadi (2009) have proposed modified Equation-of-States with association terms, which appropriately consider the asphaltene polarity effect in the hydrocarbon mixtures for asphaltene precipitation.

Recently, new equations of state have been developed to deal with asymmetric mixtures (i.e., mixtures containing molecules with large size differences) and associating molecules such as polar components. Chapman et al. (1990) developed a new Equation-of-State based on Statistical Associating Fluid Theory (SAFT). Later Gross and Sadowski (2001) modified the SAFT Equation-of-State to the Perturbed-Chain SAFT Equation-of-State (PC-SAFT EOS). PC-SAFT and SAFT EOS have shown promising results in modeling the phase equilibrium of systems containing heavy hydrocarbons such as asphaltene (Gonzalez et al., 2005; Gonzalez et al., 2007). Since these Equation-of-States consider the interaction of molecules correctly, they have better potential for addressing asphaltene precipitation. However, these models are not fully developed for fluid characterization yet.

In our study, for the sake of simplicity, we use an approach similar to Nghiem et al.'s (1993). In this model, a cubic Equation-of-State (such as Peng-Robinson) is combined with a solid model for the fugacity of the heaviest component in solid phase to solve the equilibrium condition. We assume a portion of the heaviest components creates asphaltene component in crude oil that can precipitate and generate asphaltene solid phase. Thus, in our model we have a single pseudo-component solid phase.

To account for the polarity effect of the asphaltene component, we also tune the Binary Interaction Coefficients (BIC) between other hydrocarbon components and asphaltene. BICs are tuned to better predict the amount of asphaltene precipitation for the existing precipitation data.

Once we completed the characterization of fluids using different regression parameters and experimental data. We apply the components data to UTWELL phase behavior modules to solve the thermodynamic equilibrium condition. The fluid characterization can be performed in commercial PVT software like WINPROP, PVTSIM, etc.

In our phase behavior modules, we essentially solve Equation (6.1) as the thermodynamic equilibrium condition, which corresponds to equality of component fugacities.

$$f_i^V = f_i^L = f_i^S, \qquad i = 1,....n_c. \tag{6.1}$$

In Equation (6.1) the liquid and the gas phase component fugacities are calculated from a cubic Equation-of-State (i.e. Peng-Robinson). However, the fugacity of the solid phase component is calculated from the pure solid component.

$$f_i^S = f_i^{oS}. \tag{6.2}$$

One method to calculate the fugacity of pure solid component is calculating the fugacity of pure liquid phase component from the cubic Equation-of-State and then converting it to the fugacity of solid by the amount of Gibbs free energy change from pure liquid to pure solid. This method requires some correlations for enthalpy change and volume change for solid/liquid conversion. In the next section, we discuss this method for the wax precipitation model.

Since we assume that our asphaltene phase is made from only one pseudo-component, there is a simpler method to calculate the fugacity of solid phase at a given pressure and temperature. If we assume that at temperature T^* the pressure at which asphaltene starts to flash out from crude oil, Asphaltene Onset Pressure (AOP), is P^*, referring to Equation (6.1), the solid phase fugacity becomes

$$f_{nc}^S\Big|_{T^*,P^*} = f_{nc}^{L^*}. \tag{6.3}$$

Equation (6.3) gives us a clue that we can always relate the fugacity of solid component to the same component in the liquid mixture. Hence, the solid phase fugacity at the onset pressure is equal to the fugacity of component *nc* in the liquid mixture. Now, if the pressure goes below or above the onset pressure at constant temperature, we can calculate the solid phase fugacity using Gibbs free energy relation as follows:

$$RT^{*} ln\left(\frac{f_{nc}^{S}\Big|_{T^{*},P}}{f_{nc}^{S}\Big|_{T^{*},P^{*}}}\right) = \int_{P^{*}}^{P} vdP. \tag{6.4}$$

Assuming constant molar volume for the solid phase (v_{bs}) we obtain

$$ln(f_{nc}^{S}\Big|_{T^{*},P}) = ln(f_{nc}^{S}\Big|_{T^{*},P^{*}}) + v_{bs}\frac{\left(P-P^{*}\right)}{RT^{*}}, \tag{6.5}$$

$$ln(f_{nc}^{S}\Big|_{T^{*},P}) = ln(f_{nc}^{L*}) + v_{bs}\frac{\left(P-P^{*}\right)}{RT^{*}}. \tag{6.6}$$

Having the onset pressure for a given temperature, we can use Equation (6.6) to calculate the fugacity of asphaltene in solid phase. However, if the onset pressure data was not given, Kohse et al. (2000) suggested using the following equation for the solid phase fugacity:

$$\begin{aligned} ln(f_{nc}^{S}) = ln(f_{nc}^{L*}) + \frac{v_{bs}}{R}\left[\frac{P-P_{tp}}{T} - \frac{P^{*}-P_{tp}}{T^{*}}\right] - \frac{\Delta H_{tp}}{R}\left(\frac{1}{T}-\frac{1}{T^{*}}\right) \\ -\frac{\Delta C_{p}}{R}\left(\ln\frac{T^{*}}{T} - T_{tp}(\frac{1}{T}-\frac{1}{T^{*}})\right). \end{aligned} \tag{6.7}$$

In Equation (6.7), ΔH_{tp}, ΔC_p, P_{tp}, and T_{tp} are the triple point parameters that can be calculated from correlation, Won (1986), or from user input. Equation (6.7) can also be reduced to Equation (6.6) if we substitute T by T^*.

Finally, to perform the three-phase flash calculation with asphaltene precipitation, we use the following procedure. First, we calculate the flash routine for vapor/liquid system at the asphaltene onset pressure (P^* corresponding to the given temperature) with no solid phase. From this flash, the fugacity of component *nc* in liquid phase is obtained at the onset pressure. Consequently, using Equation (6.6) the fugacity of solid phase is calculated at the given pressure. Next we perform another vapor/liquid flash routine at the given pressure (P) to calculate the fugacity of component *nc* in liquid phase. If the fugacity of component *nc* in liquid phase becomes larger than fugacity of solid phase, precipitation occurs. If solid precipitation occurs in the system, a flash routine with Rachford-Rice mass balance equation is used for only liquid/solid system to obtain the amount of precipitation. A Newton-Raphson algorithm is used for liquid/solid flash. After liquid/solid flash the composition of liquid is updated and a routine flash for vapor/liquid only is performed to obtain the vapor/liquid ratio. This procedure is continued until convergence is achieved in vapor, liquid and solid systems. Once the convergence is reached, the mole fraction of each phase and the compositions of vapor and liquid phases are also calculated.

Asphaltene precipitate not only changes the composition of the crude oil and causes flow assurance problems but also affects the rheology of the fluid mixture. Pedersen and Rønningsen (2000) proposed the following model for modifying the viscosity of oil due to solid suspends (wax):

$$\mu = \mu^* \left(\exp\left(D\varphi_{solid} \right) + \frac{E\varphi_{solid}}{\sqrt{\gamma}} + \frac{F\varphi_{solid}^4}{\gamma} \right). \tag{6.8}$$

In Equation (6.8), γ is shear rate (sec^{-1}), $\gamma = \frac{\tau_w}{\mu}$, μ^* is the pure oil viscosity (mPa/sec), and φ_{solid} is the volume fraction of solid. D, E, F in the Equation (6.8) are the constant coefficients that can be tuned for the fluid mixture viscosity. The default values are $D = 18.12$, $E = 405.1$, $F = 7.876 \times 10^6$. Likewise, we use the same model to update the viscosity of the oil due to asphaltene particle suspension in the oil.

6.1.2 Asphaltene Aggregation

Fresh asphaltene molecules that are stripped out from crude oil are individual molecules with the size of less than one nanometer. These small particles are stable in the crude oil and do not precipitate until they become larger by aggregation process. With time elapsing, asphaltene molecules can aggregate with each other and create larger size asphaltene clusters and flocculate. Once these clusters are generated asphaltene precipitation starts.

The process of asphaltene aggregation is a function of two main parameters. First parameter is the concentration of asphaltene. As a matter of fact, any other parameters that can affect the asphaltene concentration, such as pressure, temperature and composition, also indirectly affect the asphaltene aggregation. Second parameter is time allowance. If asphaltene particles have enough time to collide and form clusters, aggregation is more extensive and vigorous.

An experimental result reported by Akbarzadeh et al. (2007) shows that at very low concentrations, below 10^{-4} mass fraction, asphaltene molecules in toluene are in dispersed solution. At higher concentrations, on the order of 10^{-4} mass fraction, asphaltene molecules stick together to form nanoaggregates or nanometer-sized particles. The nanoaggregates are stably suspended in liquid phase. As concentration of asphaltene increases to mass fraction of 5×10^{-3}, the nanoaggregates start forming clusters. The clusters can stay in stable colloidal suspension until asphaltene concentration reaches a mass fraction of roughly 10^{-2}. At higher concentrations, the asphaltene clusters flocculate and precipitate in the crude oil. Figure 6.1 shows the evolution of asphaltene particles by concentration. Similar features are seen in crosslinked polymer blends and this is explained via fractal dimension arguments by Mamun (2005a and 2005b)).

Eskin et al. (2011) also show the distribution of asphaltene particle size with time. They argued that asphaltene particles are distributed in normal Gaussian trend with their mean value increasing as time progresses (Figure 6.2). Their experiments show that particle size can change from few nanometers to hundreds of nanometers in about 10 hours. Notwithstanding, in flow through pipe that happens very fast (few minutes); this change might not be considerable. However, in flow through porous media in the reservoir, this effect should be considered. Particle size variation can drastically change the deposition rate.

In our modeling for asphaltene precipitation, we assume two critical sizes for asphaltene particles. These particle sizes can be obtained from experimental probes. We assume the first size to be about 10 nm, which is attributed to the first-aggregated asphaltene particles and the second size to be around 300 nm, which is the well-developed critical particle size. Afterward, we use a first-order kinetic model as shown in Equations (6.9) and (6.10) for the conversion of the first population of asphaltene particles to the second population. This way we can address the two main sizes of asphaltene particles appearing in the flow line. However, since the flow in pipeline is fast enough (less than one hour) we will not see much difference in the particles size variation in the flow.

$$\frac{d[C_{s2}]}{dt} = k_{s1s2}[C_{s1}], \tag{6.9}$$

$$[C_{s1}] = [C_{s1}]_0 e^{-k_{s1s2}t}. \tag{6.10}$$

Moreover, we can treat S_2 as the asphaltene particles that cannot dissolve back in the crude oil and S_1 as the particles that can reversibly dissolve in crude oil. k_{s1s2} can also control the conversion of S_1 to S_2. Zero k_{s1s2} means all the particles can reversibly dissolve and precipitate in the crude oil.

6.1.3 Verification of Asphaltene Precipitation Model

We compared our asphaltene precipitation model against Burke et al. (1990) experimental data and CMG Winprop (Computer Modeling Group) on a live oil mixture at reservoir temperature. Fluid characterization and components' properties are presented in Tables 6.1 and 6.2. Asphaltene onset pressure is considered about 4600 psi at reservoir temperature (212 °F).

Figure 6.3 shows the batch calculation results for asphaltene precipitation versus pressure against experimental data. As can be seen, the precipitation model (explained in the model development section) can capture the behavior of asphaltene precipitation fairly well. Depleting the pressure from above the onset pressure value to below bubble point pressure, we see that the maximum precipitation amount is reached and then it decreases. However, both CMG and UTWELL calculation cannot completely match the below bubble-point pressure perfectly. The discrepancy between CMG and UTWELL results might be ascribed to the different fluid characterization.

Figure 6.4 also shows the vapor liquid equilibrium calculation and the onset pressure of asphaltene at lower and upper range. The maximum asphaltene precipitation occurs at the saturation point between upper and lower onset pressures.

6.2 WAX

Wax flow assurance problem more likely occurs in the wellbores and surface facilities with low temperatures. Like other flow assurance problems, wax deposition in the pipelines and wellbore can significantly influence the economy of field development and the remediation jobs. Usually in the deep-water fields, where temperature and pressure can go below the stability condition of wax, deposition can be observed. With elapse of time, the evolution of wax deposition in the flow lines can plug the system and cause low productivity of the wells. At this situation, a remediation process (i.e., pigging) is required to scrap the flow path and to reestablish the well for production.

Wax deposition not only causes detrimental effect in the flow path but also increases the viscosity of flowing hydrocarbon fluid due to suspended particles. Increasing the viscosity of the hydrocarbon fluid can also potentially decrease the productivity of the well.

Hence, there are several advantages to study the risk of wax deposition before developing a reservoir. A wax prediction tool not only can alarm the possibility of wax formation but also can determine the location and chronological frequency of the problem. In addition, having this tool we can define the shape of the wax deposition in the flow path for an effective remediation process.

The nature of wax phase comes from paraffinic components of the oil that can be crystallized and precipitate at cooler temperature. At such conditions, precipitated wax is partially deposited and partially flocculated in the flowing fluid. As a matter of fact, the deposited wax plugs the flow line and the flocculated wax changes the rheology of the oil toward more viscous fluid.

In contrast to the components that reside in asphaltene solid, wax solid has paraffinic non-polar components with different distribution of molar fractions. This discrepancy completely affects the phase behavior of wax and asphaltene. Although in some literature these two are treated with similar set of thermodynamic equations (such as cubic Equation-of-Sates), they are distinguished properly in the properties of components characteristic.

The method we use for the phase behavior of wax formation is according to the correlations in Pederson and Christensen (2007). We combine the wax thermodynamic phase behavior with the multiphase flow equations and the wax deposition rate equations in the wellbore to close our system of equations.

6.2.1 Wax Precipitation Model

There are plenty of models in the literature to study the phase behavior of wax. In this study, we use Ideal Solution Wax model plus we distinguish the wax forming components and non-wax forming components based on the idea of Erickson et al. (1993). The modifications proposed by Pederson (1995) and Rønningsen et al. (1997) are also applied in our calculation. In our wax model, we assume only C_{7+} components contribute to the wax formation. Hence, after splitting C_{7+} to single carbon fraction and then lumping them to several pseudo-components, the details of wax forming components are defined. Wax forming components are taken from compounds below C_{50}.

As Pederson (1995) and Rønningsen et al. (1997) introduced the mole fraction of pseudo-components that potentially forms wax, is divided to waxing and non-waxing compounds mole fractions as follows:

$$z_i^S = z_i^{tot}\left[1-(A+B\times M)\left(\frac{\rho_i-\rho_i^P}{\rho_i^P}\right)^C\right]. \tag{6.11}$$

z_i^{tot} is the total mole fraction of the pseudo-component *i*, z_i^s is the mole fraction of pseudo-component that can form wax, and *A, B , C* are empirical constants determined from wax experimental data. In this equation, ρ_i is the density of component *i* and ρ_i^P is the density of normal paraffin with the same molecular weight of M_i

$$\rho_i^P = 0.3915 + 0.0675\ lnM_i. \tag{6.12}$$

Our default values for *A, B, C* are1.074, $6.584\times10^{-4}$and 0.1915, respectively. In Equation (6.11) if z_i^s becomes negative or zero we assume no wax-forming fraction exists in that pseudo-component. In addition, we assume that the equation of state parameters (Tc, Pc, etc.) of the wax forming components up to C_{20+} are equal to that of the non-wax forming component, and for C_{20+} the critical pressure of wax forming and non-wax forming component are distinguished as follows:

$$P_{ci}^S = P_{ci}\left(\frac{\rho_i^P}{\rho_i}\right)^{3.46}, \tag{6.13}$$

$$\frac{1}{P_{ci}} = \frac{\left(\frac{z_i^{tot} - z_i^s}{z_i^{tot}}\right)^2}{P_{ci}^{no-S}} + \frac{\left(\frac{z_i^s}{z_i^{tot}}\right)^2}{P_{ci}^S} + \frac{2\left(\frac{z_i^{tot} - z_i^s}{z_i^{tot}}\right)\left(\frac{z_i^s}{z_i^{tot}}\right)}{\sqrt{P_{ci}^{no-S}}\sqrt{P_{ci}^S}}. \tag{6.14}$$

After characterizing the system of complex fluid with wax, we solve the fugacity equilibrium for the gas, liquid and solid system to obtain the composition of each phase at equilibrium. Essentially Equation (6.15) should be honored to achieve equilibrium condition.

$$f_i^V = f_i^L = f_i^S, \qquad i = 1, \ldots, n_c. \tag{6.15}$$

In Equation (6.15) the components fugacity of the liquid and gas phases are calculated from Cubic Equation-of-State (i.e. Peng-Robinson). However, the components fugacity of solid phase is calculated by the following expression:

$$f_i^S = X_i^S f_i^{oS}. \tag{6.16}$$

f_i^{oS} is the fugacity of pure solid component i and X_i^S is the mole fraction of this component in the solid phase. Assuming a thermodynamic path to convert a pure component i from liquid phase to solid phase, we can calculate the fugacity of pure component in solid phase as follows:

$$f_i^{oS} = \phi_i^{oL}(P) P \exp\left(-\frac{\Delta H_i^f}{RT}\left(1 - \frac{T}{T_i^f}\right) + \frac{\Delta V_i^f \left(P - P_{ref}\right)}{RT}\right). \tag{6.17}$$

As can be seen, the fugacity of pure component in the solid phase is related to fugacity coefficient of pure liquid phase plus the energy Gibbs change due to melting and volume shrinkage in the conversion process. In Equation (6.17) ΔH_i^f and ΔV_i^f can be calculated by the correlations proposed by Won (1986) or can be defined from wax formation experiments.

Wons (1986) correlated the melting enthalpy (Cal/mole) of component *i* as

$$\Delta H_i^f = 0.1426 M_i T_i^f , \tag{6.18}$$

and the melting temperature (*K*) as

$$T_i^f = 374.5 + 0.02617 M_i - \frac{20172}{M_i} . \tag{6.19}$$

From the definition of fugacity of each component at each phase ($f_i^L = X_i^L \phi_i^L P , f_i^V = X_i^V \phi_i^V P , f_i^S = X_i^S \phi_i^S P$) we realize that the components partitioning K-factor between the solid and the liquid phase at equilibrium condition can be obtained as follows:

$$K_i^{SL} = \frac{X_i^S}{X_i^L} = \frac{\phi_i^L}{\phi_i^S} , \tag{6.20}$$

where $\phi_i^S = \frac{f_i^{oS}}{P}$. Accordingly, the new estimates of solid and liquid phase compositions can be obtained as follows:

$$X_i^S = \frac{X_i K_i^{SL}}{1+\beta(K_i^{SL}-1)}, \quad (6.21)$$

$$X_i^L = \frac{X_i}{1+\beta(K_i^{SL}-1)}. \quad (6.22)$$

β is the mole fraction of liquid phase that is converted to solid and X_i is the normalized total mole fraction of component i in the liquid/solid binary system. Once the composition of liquid and solid phases are updated the equilibrium condition between liquid and vapor is also checked. This system is updated iteratively until the condition of equilibrium in the entire system is met by the equal fugacity of all components in all phases.

6.2.2 Verification of Wax Precipitation Model

Six fluid samples (Oil 11a- Oil 11f) from the experimental data performed by Rønningsen et al. (1997) are used in this section to evaluate the validity of our wax precipitation model. These fluid samples have also been reported in Pederson and Christensen (2007) for studying the effect of C1 component on the Wax Appearance Temperature (WAT) at constant pressure.

Table 6.3 shows the composition of the fluids as Oil 11a to Oil 11f, respectively. After characterizing the fluids and calculating the wax forming components and their fraction, we use UWELL wax forming module to calculate WAT for each sample. Figure 6.5 shows the results we obtained compared with the values that were reported by Rønningsen et al (1997). We obtained fairly good agreement between UTWELL and experimental results.

In Figure 6.5, WAT versus the mole fraction of component C1 is plotted. As can be seen, increasing the mole fraction of light component (C1) in the mixture reduces the wax appearance temperature. This behavior means higher the C1 concentration, higher the stability of wax in the mixture and greater the tolerance of oil to temperature without any wax problem. Referring to asphaltene phase behavior, this observation is in contrary with asphaltene.

6.3 GEOCHEMICAL SCALE

Scale precipitation is a challenging flow assurance issue that may occur in different stages of production. Several types of scales according to the specific condition of the formation have been introduced in the literature. For instance, sulfate scales like barite ($BaSO_4$) are formed by the mixing of sulfate-rich seawater injection and the formation brine, which originally has high metal ion content (e.g., *Ca, Ba*, and *Sr*). The same mechanism can generate carbonate scales like calcite ($CaCO_3$) but to a lesser extent. Carbonate scales' main deriving mechanism is related more to changes in pressure (because of reservoir depletion) or changes in temperature. The depletion in pressure allows release of CO_2 gases out of solution which leads to increasing latter's pH. Increasing the solution pH (basic state) will reduce the solubility of the calcite. The third mechanism involves the corrosion of iron-based metals dissolved in solutions containing oxygen or H_2S to produce typical scales, such as iron oxides or iron sulfides.

Hydrochloric acid has been widely used in treating calcium carbonate scales remediation, but calcite may re-precipitate prematurely right after the dissolution in the acid. Following the dissolution of metal ions, the natural tendency of calcium to bond again with carbonate is high and tends to increase as the acid is spent. Adding chelating solutions to the acid treatment can offset this tendency (Frenier and Ziauddin, 2008). A classic example of chelatants is the Na_2H_2Y form of EDTA.

To model the scale generation process in the fields, different researchers have developed various simulators. For instance, Yuan and Todd (1991) successfully predicted the tendency of sulfate scaling in oilfield operations. Their simulator predicts the solubility for a wide range of sulfate salts such as *BaSO4, CaSO4*, and *SrSO4* at different compositions, temperatures, and pressures by using Pitzer's equation.

Rocha et al. (2001) developed a geochemical model with the necessary transport equations to accurately simulate the flow and diffusion of ions, but only for a single-phase flow. Delshad and Pope (2003) have also simulated the precipitation of barium sulfate and focused their study on the effect of seawater desulfurization on sulfate deposition prevention in the reservoir.

In our study, for scale equilibrium calculation and transportation we used a powerful tool PHREEQC (USDI, USGS 2013) which is explicitly coupled to UTWELL. Once the flow fields are calculated in UTWELL, PHREEQC is called to update the equilibrium condition in aqueous phase. With this process, the amount of solid precipitate is calculated and fed to the transport models.

PHREEQC version 3 is a computer program in C++ language that was developed by U.S. Department of Interior and U.S. Geological Survey (Parkhurst and Appelo 2013) for simulating chemical reactions and transport processes in aqueous phase. The older version of this program is PHREEQE in FORTRAN language. The PHREEQC program is based on equilibrium chemistry of aqueous solutions interacting with minerals, gases, solid solutions, exchangers, adsorption surfaces, which accounts for the original acronym—pH-Redox-Equilibrium. The program has evolved to include the capability to model kinetic reactions and one-dimensional transport in dual continuum media as well.

PHREEQC considers different aqueous models for solute activities such as two ion-association aqueous models, Pitzer specific-ion-interaction aqueous model, and the SIT (Specific Interaction Theory) aqueous model. In addition, the Peng-Robinson equation of state has been implemented in PHREEQC for calculating the solubility of gases at high pressure.

There are a variety of capabilities in PHREEQC to calculate saturation indices, the distribution of aqueous species, the density and specific conductance of a specified solution composition, and many more that can be found in the program user's manual.

PHREEQC has been developed in a way that can be executed by a binary application file or a user interface program. Additionally, the program can be executed in different platforms in Linux and Windows. In our application, we used binary executable file of PHREEQC for batch calculation in Windows. To do this, we wrote a script to execute PHREEQC in UTWELL program should we need to update the aqueous phase equilibrium. To avoid the complexity of considering all possible reactions in PHREEQC, we create the input data that considers only the acid-base and solid precipitation reactions.

The coupling method we used for UTWELL/PHREEAC is a traditional approach for which we write the PHREEQC input file in a folder and use Call System to run PHREEQC from the main program. However, a new feature has been developed as PHREEQCi, which makes PHREEQC to be interactive to other programs. In the interactive version of PHREEQC there is no need to write/read input/output files. Hence in this version, the computation time becomes much faster. In the current version of UTWELL/PHREEQC, we use Call System approach to run PHREEQC which is less complicated to implement.

Since for executing PHREEQC, in addition to input files, we need a database that defines the reaction, a suitable database is included in our simulation. In PHREEQC user's manual there is a comprehensive database file (*Phreeqc.dat*) that considers all the reactions data. For our application, we can use this file with some simplifications. Appendix (E.6) shows an example of a simplified database file for PHREEQC. We keep PHREEQC database under the name GEOCHEM.DAT in the UTWELL library.

Once input file (i.e. GEOCHEM.INPUT) is written and assigned to PHREEQC along with a database file (i.e. GEOCHEM.DAT), PHREEQC is executed. PHREEQC reports the results to GEOCHEM.OUT in Output folder and "select.out" to ObjFile folder. The updated equilibrium concentrations for selected fluid species are written to "select.out". Thus, by reading this file we can access the calculated values of concentration for each fluid species.

6.3.1 Scale Precipitation Model

The theoretical model of scale perception, in PHREEQC, is summarized here. To determine the equilibrium state of aqueous phase, the independent elements are distributed between the fluid species with defined reaction stoichiometry. Thus, the mass balance of the independent element, the electrical neutrality of the aqueous phase, and the equilibrium constant relations are solved in Equations (6.23), (6.24) and (6.25), respectively.

$$C_n^{total} = \sum_{i=1}^{n_{aq}} h_{ni} C_i + \sum_{k=1}^{n_{sld}} g_{nk} C_k \tag{6.23}$$

$$\sum_{i=1}^{n_{aq}} Z_i C_i = 0 \tag{6.24}$$

$$K_i = a_i \prod_{j=1}^{n_{aq}} a_j^{-w_{ji}}, \qquad j = 1,\ldots,n_{aq}. \tag{6.25}$$

In the above equations C_n^{total} is the total element initial concentration in the solution, C_i is the concentration of fluid species and C_k is the concentration of suspended solid precipitates. In addition, h_{ni} in Equation (6.23) is the stoichiometric coefficient of the element *n* in aqueous species *i*, g_{ni} is the stoichiometric coefficient of element *n* in precipitated solid *k* and Z_i is the ionic charge of the species *i.*

In Equation (6.25) K_i is the temperature-dependent equilibrium constant for reaction producing master species *i*. In the equilibrium equation, species activities are used instead of concentrations. In fact, this parameter shows the real mixture ionic activities which is obtained from multiplication of ion activity coefficient and ion concentration. Ion activity coefficient is calculated based on the ionic strength of the solution. One method to obtain this coefficient is using the Debye and Huckel model (details given in PHREEQC user's manual) as

$$log\gamma_i = -\frac{Az_i^2\sqrt{\mu}}{1 + Ba_i^0\sqrt{\mu}} + b_i\mu. \tag{6.26}$$

Furthermore, to check whether or not the solid phase is present in equilibrium, the solubility product parameter is used. For each type of solid, the expression (6.27) is verified to see whether or not solid can precipitate. If solid can precipitate, Equation (6.27) is combined with Equations (6.23) through (6.26) to solve the system of equations at equilibrium.

$$\prod_{j=1}^{n_{aq}} a_j^{w_{jk}} \le KSP_k \,, \qquad k = 1,\ldots,n_{sld}\,. \tag{6.27}$$

To model the chemical reactions in PHREEQC, the reacting elements along with the existing fluid species in the reactions should be introduced by the user. For instance, in theory, the dilution of Na_2SO_4, $CaCl_2$, Na_2CO_3 and $BaCl_2$ in the water will yield a variety of fluid species. Below is a list of reactions defined in the geochemical model and used in our study:

$Na_2SO_4(aq) \rightarrow 2Na^+(aq) + SO_4^{2-}(aq)$

$Na_2CO_3(aq) \rightarrow 2Na^+(aq) + CO_3^{2-}(aq)$

$CaCl_2(aq) \rightarrow Ca^{2+}(aq) + 2Cl^-(aq)$

$BaCl_2(aq) \rightarrow Ba^{2+}(aq) + 2Cl^-(aq)$

$H_2O(l) \rightleftharpoons H^+(aq) + OH^-(aq)$ $\qquad K_1 = Kw$

$CO_3^{2-}(aq) + H_2O \rightleftharpoons HCO_3^-(aq) + OH^-(aq)$ $\qquad K_2 = Kb_1$

$HCO_3^-(aq) + H_2O \rightleftharpoons CO_2(aq) + OH^-(aq)$ $\qquad K_3 = Kb_2$

$CaSO_4(aq) \rightleftharpoons Ca^{2+}(aq) + SO_4^{2-}(aq)$ $\qquad K_4 = Keq_1$

$BaSO_4(aq) \rightleftharpoons Ba^{2+}(aq) + SO_4^{2-}(aq)$ $\qquad K_5 = Keq_2$

$CaCO_3(aq) \rightleftharpoons Ca^{2+}(aq) + CO_3^{2-}(aq)$ $\qquad K_6 = Keq_3$

$BaCO_3(aq) \rightleftharpoons Ba^{2+}(aq) + CO_3^{2-}(aq)$ $\qquad K_7 = Keq_4$

$CaSO_4(s) \rightleftharpoons Ca^{2+}(aq) + SO_4^{2-}(aq)$ $\qquad K_8 = Ksp_1$

$BaSO_4(s) \rightleftharpoons Ba^{2+}(aq) + SO_4^{2-}(aq)$ $\qquad K_9 = Ksp_2$

$CaCO_3(s) \rightleftharpoons Ca^{2+}(aq) + CO_3^{2-}(aq)$ $\qquad K_{10} = Ksp_3$

$BaCO_3(s) \rightleftharpoons Ba^{2+}(aq) + CO_3^{2-}(aq)$ $\qquad K_{11} = Ksp_4$

The main pseudo-elements in this case would be Ca, Ba, Na, SO_4, CO_3,, H, and Cl, while the fluid species including independent species are Ca^{2+}, Ba^{2+}, H^+, Na^+, CO_3^{2-}, SO_4^{2-}, and H_2O and dependent ones are HCO_3^-, OH^-, $CaSO_4$, $BaSO_4$, $CaCO_3$, and $BaCO_3$.

Table 6.4 shows the summary of reactive species equilibrium data used in PHREEQC. Appendix (E.7) also shows the sample input file that is generated by UTWELL to be used in PHREEQC calculation. In the example file, we assume 0.05 mole of Na_2SO_4, $CaCl_2$, Na_2CO_3 and $BaCl_2$ are dissolved in 1*kg* of water at room temperature and pressure. If we let the system to reach to equilibrium, we observe the concentration of each species in (*mole / kg*) as shown in Tables 6.5 through 6.8. As can be seen among different scales, the tendency toward Barite ($BaSO_4$) and Calcite ($CaCO_3$) formation is most prevalent. However, the calcite formation can be manipulated by changing the pH of the solution.

Finally, to account for the kinetics of scale precipitation from individual solid particles, a similar first-order kinetic model for asphaltene particles is used for the scale. This model is simple to implement and control the precipitation rate with time.

Table 6.1 Fluid characterization and composition for comparing the model against Burke, et al. (1990)

Component	**Pc (psi)**	**Tc (R)**	**VC (ft^3/lbmol)**	**Mw (lb/lbmol)**	**Acentric Factor**	**Parachor**	**Volume Shift**	**Primary Composition**
CO_2	1070.09	547.56	1.5071	44.01	0.225	168.17	0	0.0246
C1-C2	668.51	360.61	1.6431	17.417	0.015127	92.19	0	0.4041
C3-C5	573.15	732.89	3.8098	53.516	0.179313	195.33	0	0.0755
C6-C19	291.41	1135.31	13.7197	164.423	0.655007	512.21	0	0.2719
C20-C30	175.41	1419.29	29.033	340.927	1.064023	1016.51	0	0.1064
C31+	143.17	1682.93	56.5489	665.624	1.371778	1944.21	0	0.0774
Asphaltene	143.17	1682.93	56.5489	665.624	1.371778	1944.21	0	0.0401

Table 6.2 Binary interaction coefficients used for modeling Burke et al. (1990) fluid

	CO_2	**C1-C2**	**C3-C5**	**C6-C19**	**C20-C30**	**C31+**	**Asphaltene**
CO_2	0						
C1-C2	0.0001	0					
C3-C5	0.0068	0.0056	0				
C6-C19	0.0375	0.0347	0.013	0			
C20-C30	0.0651	0.0616	0.0319	0.0045	0		
C31+	0.0945	0.0905	0.0548	0.0158	0.0035	0	
Asphaltene	0.22	0.22	0.22	0	0	0	0

Table 6.3 Molar composition of Oil 11a – Oil 11f from Rønningsen et al. (1997) experimental data for waxy crude oil

Component	Oil 11a	Oil 11b	Oil 11c	Oil 11d	Oil 11e	Oil 11f	Mole Weight	Denisty (g/cm^3)
N2	0.29	0.13	0.04	0.01	0.02	0.0		
CO_2	5.57	4.92	3.89	2.76	1.77	0.04		
C1	55.62	38.23	21.97	10.99	4.81	0.06		
C2	9.06	9.00	8.38	7.17	5.65	0.26		
C3	5.08	6.03	6.82	7.06	6.81	0.81		
iC4	0.91	1.18	1.45	1.61	1.67	0.37		
nC4	1.87	2.53	3.21	3.65	3.87	1.09		
iC5	0.70	1.02	1.35	1.59	1.74	0.84		
nC5	0.8	1.18	1.58	1.88	2.07	1.14		
C6	1.07	1.68	2.33	2.83	3.16	2.74		
C7	1.95	3.26	4.60	5.64	6.35	6.90	90.5	0.746
C8	2.27	3.89	5.55	6.82	7.71	9.52	102.6	0.773
C9	1.39	2.42	3.47	4.28	4.84	6.43	116.7	0.793
C10+	13.4	24.53	35.38	43.72	49.56	69.80	290.0	0.876

Table 6.4 Input parameters for geochemical scale batch reaction in PHREEQC

Water disassociation constant	K_1	1.00×10^{-14}
Carbonate hydrolysis constant	K_2	2.13×10^{-4}
Bicarbonate hydrolysis constant	K_3	2.25×10^{-8}
Anhydride disassociation constant	K_4	5.00×10^{-3}
Barite disassociation constant	K_5	2.00×10^{-3}
Calcite disassociation constant	K_6	5.97×10^{-4}
Witherite disassociation constant	K_7	1.90×10^{-3}
Anhydride solubility product constant	K_8	3.31×10^{-15}
Barite solubility product constant	K_9	1.41×10^{-15}
Calcite solubility product constant	K_{10}	3.31×10^{-9}
Witherite solubility product constant	K_{11}	2.74×10^{-9}

Table 6.5 Main elements total concentrations after equilibrium in the solution

Ca (mole / kg)	2.23×10^{-2}
Ba (mole / kg)	9.50×10^{-3}
Na (mole / kg)	2.0×10^{-2}
S(6) (mole / kg)	1.47×10^{-12}
C(4) (mole / kg)	3.18×10^{-2}

Table 6.6 Fluid specious concentrations in the mixture after equilibrium

Ca^{+2} (mole / kg)	2.23×10^{-2}
Ba^{+2} (mole / kg)	9.50×10^{-3}
Na^{+} (mole / kg)	2.0×10^{-1}
SO_4^{-2} (mole / kg)	1.49×10^{-13}
CO_3^{-2} (mole / kg)	4.52×10^{-7}
HCO_3^{-} (mole / kg)	7.81×10^{-3}
CO_2 (mole / kg)	2.40×10^{-2}

Table 6.7 Concentration of dissolved solids in aqueous phase

$CaSO_4$ (mole / kg)	6.36×10^{-13}
$CaCO_3$ (mole / kg)	5.34×10^{-6}
$BaCO_3$ (mole / kg)	6.97×10^{-7}
$BaSO_4$ (mole / kg)	6.81×10^{-13}

Table 6.8 Concentration of precipitate solids as suspension in the solution

Anhydrite (mole / kg)	9.51×10^{-3}
Calcite (mole / kg)	1.82×10^{-2}
Witherite (mole / kg)	0.0
Barite (mole / kg)	4.05×10^{-2}

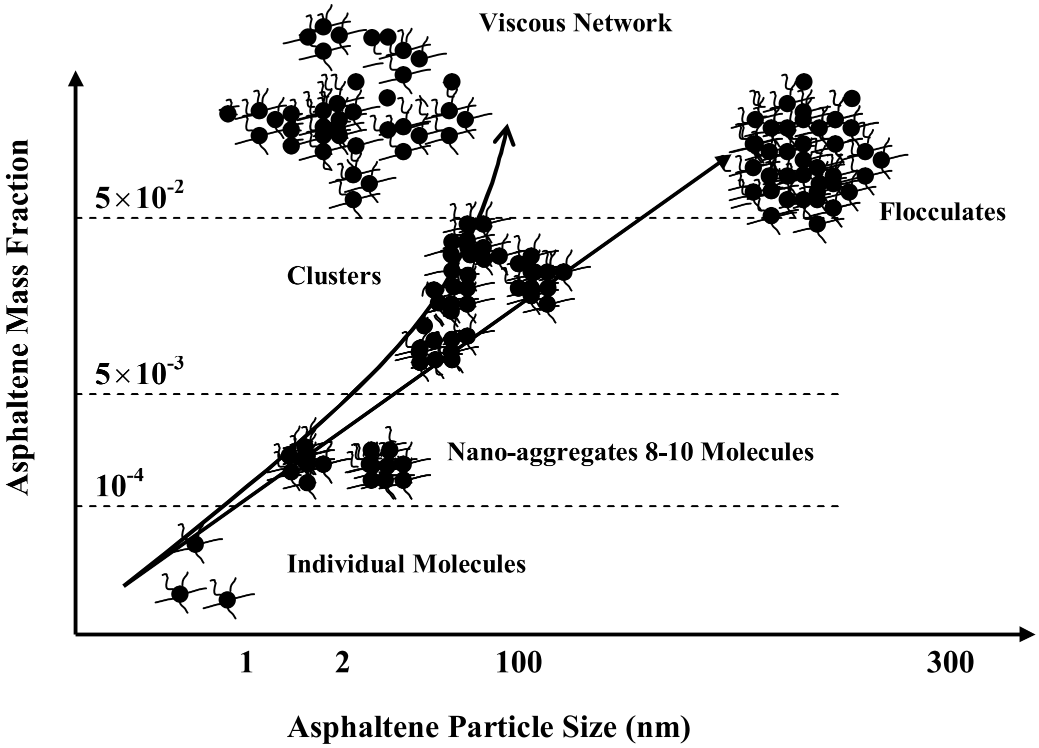

Figure 6.1 Effect of asphaltene concentration on the aggregation process.

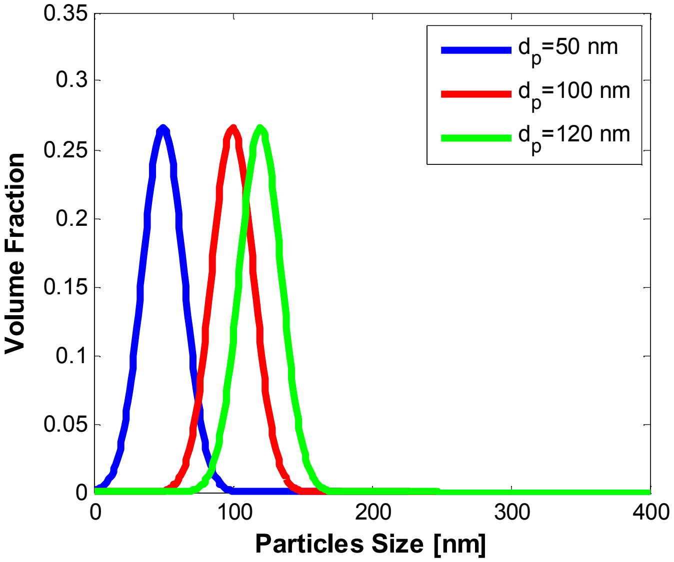

Figure 6.2 Schematic view of asphaltene particles size distribution change with time due to aggregation process.

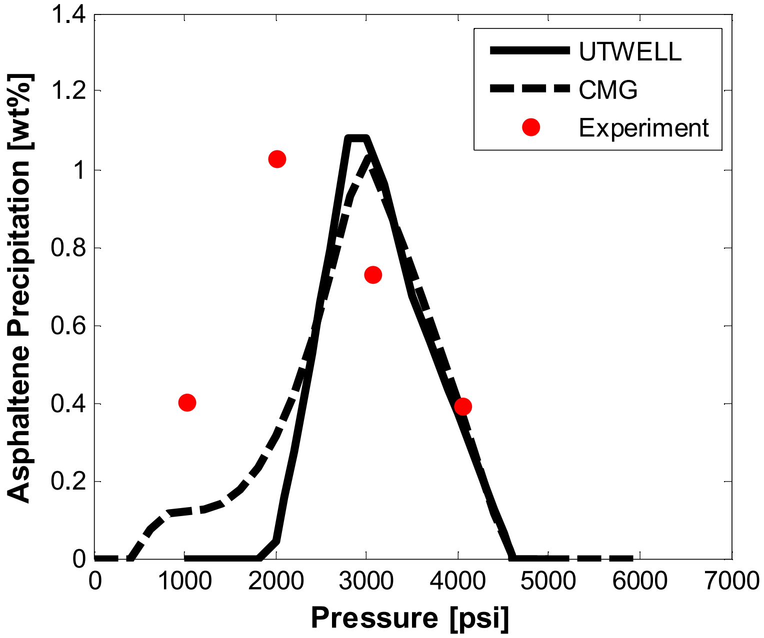

Figure 6.3 Comparison of asphaltene precipitation model calculated in UTWELL, CMG, and experimental data from Burk et al. (1990).

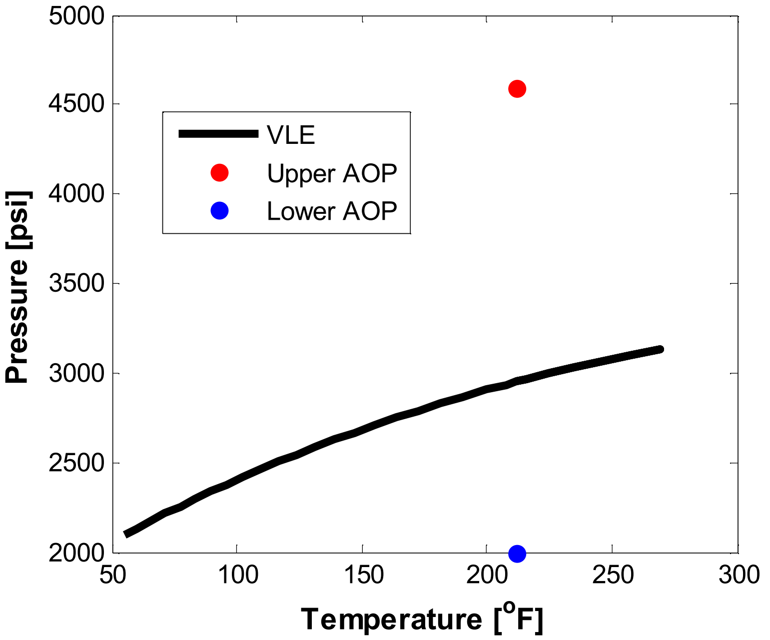

Figure 6.4 The vapor liquid equilibrium line for Burk et al. (1990) fluid with asphaltene onset pressures obtained from UTWELL.

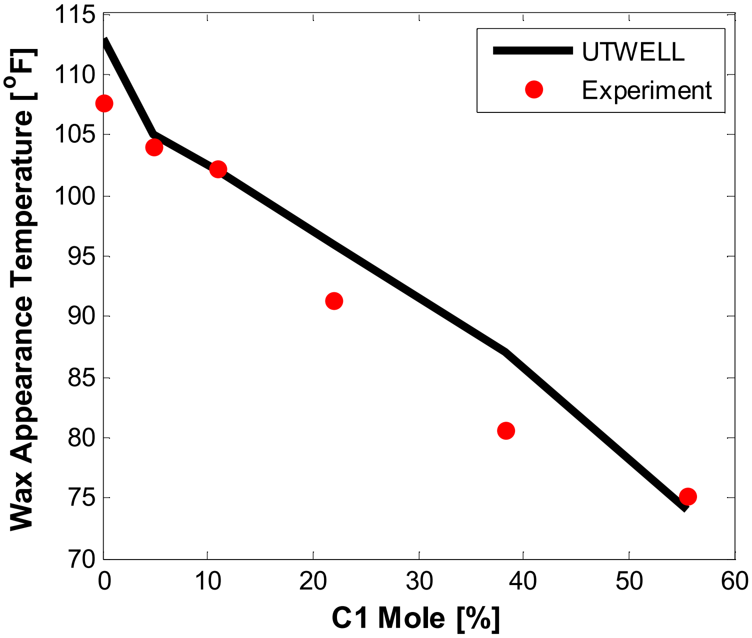

Figure 6.5 Wax precipitation model comparisons with Rønningsen et al. (1997) experiments for wax crude oil. This plot shows the effect of C_1 composition on wax appearance temperature.

Chapter 7: Particle Deposition in the Flow Stream

In this chapter, we primarily present few of the existing models for solid particles deposition in turbulent and laminar flows. Afterward, we apply these models for wax, asphaltene, and scale deposition in the crude oils. In fact, since solid particles are carried in the tubing systems of hydrocarbon reservoirs with large flow rates, we mostly focus on developing deposition models in turbulent flow regimes.

In addition, we characterize the solid particles deposition models in two different sets of correlations. One set of correlation is used for asphaltene and scale deposition and the other set of correlation is used for wax deposition. Since we treat asphaltene and scale as solid spheres and wax as gel-liquid like phase, we distinguish these two particles in our deposition models. We essentially use eddy currents diffusion and Brownian diffusion mechanisms as the dominant process for asphaltene and scale deposition. However, we apply molecular diffusion and shear diffusion as the dominant mechanisms for wax deposition.

7.1 ASPHALTENE AND SCALE DEPOSITION MODELS

Over the past few decades, several researchers have proposed particulate fouling models to study solids deposition (i.e. iron particle) to the pipe walls. Lin et al. (1953) were the first to demonstrate a through classical approach of mass transfer between a turbulent fluid stream and the wall. They explained an analogy with momentum transfer in the turbulent flow to derive the mass transfer of particles. In fact, Lin et al. (1953) used von Karman’s (1935) analysis for the velocity and eddy viscosity distribution in three different flow regions. They introduced mass transfer equation with incorporating the same eddy viscosity distributions found by von Karman’s (1935). Lin et al. (1953) mostly addressed the diffusion mechanism for small particles (< 0.1 m) and calculated the concentration profile in the wall layer and buffer zone. They compared their model deposition rate results with experimental data for turbulent gas stream and showed fairly good agreement.

Friedlander and Johnstone (1957) also presented another aspect of solid particles deposition mechanism in turbulent streams. They addressed the particles momentum effect, which had been neglected by Lin et al. (1953). Friedlander and Johnstone (1957) postulated the free flight velocity of the particles from stopping distance to the wall in the deposition process. In fact, they emphasized this phenomenon for large particles (~ 1 m) where their momentum is not dissipated in viscous sub-layer. Friedlander and Johnstone (1957) also developed an experimental setup for evaluating the rate of solid deposition on the tube wall. They compared their model with their experiments for turbulent gas stream and showed fairly good agreement.

Lin et al. (1953) and Friedlander and Johnstone (1957) models were valid for small (< 0.1 m) and large (~ 1 m) particle sizes, respectively. However, in 1970, Beal combined both approaches and described a method which was valid for small and large particle sizes. Beal (1970) also included a sticking probability effect in his derivation to consider the particles that are carried back into the turbulent core. Beal (1970) compared his model with different published experimental data for gas flow streams as well as liquid flow streams. He showed fairly good agreement between his model and the experiments.

Escobedo (1993) also introduced a classical approach similar to Beal (1970) in order to address asphaltene deposition during turbulent oil production. However, he used the same experimental data as Friedlander and Johnston (1957) to validate his model.

Escobedo and Mansoori (1995) modified their models and implemented new assumptions to better match the experimental data.

In contrast to previous researchers, Cleaver and Yates (1975) followed a different route, applying probabilistic theory, to develop the particles deposition model. They implemented a simple mechanistic model, disregarding the classical flow regions and the artificial boundary conditions, in their calculation. Cleaver and Yates (1975) compared their model with experimental data. They showed that their model had fairly good agreement for small size (<1 m) particles deposition.

Hutchinson et al. (1971) also presented the stochastic theory, implying a random process associated with the turbulence, to address the particles deposition. They introduced a more realistic treatment which was free of limitations and assumptions associated with the classical models. Hutchinson et al. (1971) related the deposition rate of particles to two main fractions: a fraction of particles that approaches the wall and a fraction which penetrates the wall. Afterward they defined a probability density for each fraction using random walk theory and density distribution equations. Hutchinson et al. (1971) compared their model with different experimental data. They showed that their model could satisfactorily predict the deposition rate of particle sizes greater than 10 micron.

In the following sections, we briefly explain the foregoing models, except Hutchinson et al. (1971) which is computationally expensive, and compare their results against two sets of experimental data. One dataset was obtained from the Friedlander and Johnstone (1957) experimental setup, which was obtained for iron and aluminum solid particles deposition in a turbulent airflow. The second dataset was extracted from Jamialahmadi et al. (2009), who conducted experiments for asphaltene deposition in the crude oil flow.

7.1.1 Terminology

In this section, we introduce the basic terminology and equations which are used in the deposition models, presenting the two model approaches.

Usually, the deposition rate is reported by the transport coefficient (K_t), which is analogous to the particle velocity toward the wall. K_t is a global mass transfer coefficient which considers the macroscopic (convective) and microscopic (molecular diffusion) mechanisms:

$$K_t = \frac{N}{C_{avg} - C_s}. \tag{7.1}$$

In Equation (7.1), N is the mass flux and $(C_{avg} - C_s)$ is the concentration difference between the average bulk flow and the surface. K_t can be written in non-dimensional form (K_t^+), dividing by the fluid average friction velocity $(V_{avg}\sqrt{f/2})$ (Epstein, 1988),

$$K_t^+ = \frac{K_t}{V_{avg}\sqrt{f/2}}. \tag{7.2}$$

Another terminology often encountered in the models is concerned with relaxation time. This parameter is related to the particle size and other pertinent data as follows:

$$t_p = \frac{\rho_p d_p^2}{18\mu}, \tag{7.3}$$

t_p in non-dimensional form becomes

$$t_p^+ = \frac{\rho_p d_p^2}{18\mu} \times \frac{f/2.V_{avg}^2}{\nu}. \tag{7.4}$$

The physical meaning for the relaxation time comes from Stokes stopping distance of an immersed particle. If we assume that a spherical particle moves with initial velocity, V_p, in a viscous fluid, the distance that the particle stops due to Stokes drag force is called the Stokes stopping distance (S_p). Hence, we can interpret t_p as a characteristic time required for a particle with initial velocity, V_p, to stop,

$$t_p = \frac{S_p}{V_p}. \tag{7.5}$$

Friedlander and Johnstone (1957) showed that the stopping distance is given by

$$S_p = \frac{\rho_p d_p^2 V_p}{18\mu} \tag{7.6}$$

where V_p is the particle velocity which depends on the particle position in the flow stream. Friedlander and Johnstone (1957), using the data developed by Laufer (1953), showed that the best approximation for V_p to predict the transfer coefficient is

$$V_p = 0.9V_{avg}\sqrt{\frac{f}{2}}. \tag{7.7}$$

Other parameters that are used in the deposition rate equations are the Brownian diffusivity and Schmidt number. Assuming a dilute suspension of spheres and no slip condition on the surface of the spheres, the Brownian diffusivity is obtained from Stokes-Einstein equation (Bird et al. 2002) as follows:

$$D_B = \frac{K_B T}{3\pi\mu d_p}, \tag{7.8}$$

where, K_B is the Boltzman constant, 1.38×10^{-23} (J/K).

By analogy with heat transfer (Prandtl number), Schmidt number can also be defined in mass transfer process,

$$Sc = \frac{\mu}{\rho D_B}. \tag{7.9}$$

Schmidt number represents the ratio of viscous diffusivity to mass diffusivity. Its physical meaning is basically the relative thickness of the hydrodynamic boundary layer and the mass transfer boundary layer. In general, the transport coefficient is inversely related to the Schmidt number.

7.1.2 Deposition Mechanisms

Disregarding the electrostatic forces and the thermophoresis effects between wall and particles, we may have three different mechanisms for particles deposition. Based on particle relaxation time, one of the mechanisms becomes dominant. We define these mechanisms as diffusion ($t_p^+ < 0.1$), inertia ($0.1 < t_p^+ < 10$) and impaction ($10 < t_p^+$).

The diffusion mechanism becomes dominant for small particles (usually, less than 1 m). In this mechanism, the particle stopping distance is small. Hence, particles are carried by Brownian motion of the fluid molecules and transferred to the wall. By increasing particle size, the inertia effect is also incorporated in the deposition process. In this mechanism, particles can obtain sufficient momentum by turbulent eddies to reach to the wall. Finally, for large particles size ($10 < t_p^+$), the impaction mechanism is dominant. In this mechanism, the stopping distance is in the same order of the pipe diameter where we may observe solid slugs flow. In addition, the particles no longer respond to the turbulent flow eddies. Figure 1 shows the schematic view of different deposition mechanisms.

7.1.3 Friedlander and Johnstone Model

Friedlander and Johnstone (1957) applied the classical approach for their deposition model to obtain the transport coefficient (K_t). They formulated the mass transfer flux by analogy to the momentum transfer in turbulent flow. The shear stress, which is a momentum flux measurement, is expressed as

$$\tau = (\mu + \rho\varepsilon)\frac{\partial V}{\partial y}. \tag{7.10}$$

Friedlander and Johnstone (1957) used the molecular diffusivity (Stokes-Einstein) instead of the kinematic viscosity, and eddy diffusivity instead of the eddy viscosity as done by Lin et al. (1953). Hence, they obtained the mass transfer flux as follows:

$$N = (D + \varepsilon)\frac{\partial C}{\partial y}. \tag{7.11}$$

Friedlander and Johnstone (1957) used similar eddy viscosity distributions presented by Lin et al. (1953). As can be seen in Figure 2, Lin et al. (1953) divided the flow regions into three sections where the velocity and eddy viscosity distributions are correlated as follows:

A sub-laminar layer adjacent to the wall $(0 \le y^+ \le 5)$

$$\frac{V}{V_{avg}\sqrt{f/2}} = \frac{14.5}{3}\left[\frac{1}{2}ln\frac{\left(1+\frac{y^+}{14.5}\right)^2}{1-\frac{y^+}{14.5}+\left(\frac{y^+}{14.5}\right)^2}+\sqrt{3}tan^{-1}\frac{\frac{2y^+}{14.5}-1}{\sqrt{3}}+\frac{\pi\sqrt{3}}{6}\right] \approx y^+ \tag{7.12}$$

$$\frac{\varepsilon}{\nu} = \left(\frac{y^+}{14.5}\right)^2, \tag{7.13}$$

A buffer or transition region $(5 \le y^+ \le 30)$

$$\frac{V}{V_{avg}\sqrt{f/2}} = -3.27 + 5ln\left(y^+ + 0.205\right), \tag{7.14}$$

$$\frac{\varepsilon}{\nu} = \frac{y^+}{5} - 0.959. \tag{7.15}$$

A turbulent core $(30 \le y^+)$

$$\frac{V}{V_{avg}\sqrt{f/2}} = 5.5 + 2.5ln\left(y^+\right), \tag{7.16}$$

where y^+ is dimensionless distance from the wall. In order to calculate the total mass flux from the turbulent core to the wall, Friedlander and Johnstone (1957) performed the integration of the concentration differences for the different flow zones in Equation

(7.11). The integration intervals consist of the stopping distance from the wall to the edge of the sub-laminar zone and then, from the sub-laminar layer to the end of buffer zone, and finally, from the buffer zone to the turbulent core. They assumed that the particle concentration is zero at the stopping distance from the wall and assumed a bulk average concentration of C_{avg} in the turbulent core. They also neglected the Stokes-Einstein diffusivity in their models, considering large particles sizes ($t_p^+ > 0.1$).

Since the eddy diffusivity for the turbulent core was not defined, Friedlander and Johnstone (1957) used Reynolds analogy to obtain the concentration difference between turbulent core and buffer zone boundary, Equation (7.17),

$$\frac{N}{\left(\frac{dC}{dy}\right)} = \frac{\tau}{\rho\left(\frac{dU}{dy}\right)}. \tag{7.17}$$

Hence, Friedlander and Johnstone (1957) calculated the transport coefficient in three conditions, depending on the stopping distance value, which can be located inside the sub-laminar layer, buffer zone or turbulent core.

$0<S_p^+\le5$: Stopping distance is located in the sub-laminar layer

$$K_t = \frac{\left(V_{avg} f/2\right)}{\left(1+\sqrt{f/2}\left(\frac{1525}{S_p^{+2}}-50.6\right)\right)}, \tag{7.18}$$

$5<S_p^+\le30$: Stopping distance is located in the buffer zone

$$K_t = \frac{\left(V_{avg} f/2\right)}{\left(1+\sqrt{f/2}\left(5ln\left(\frac{5.04}{\left(S_p^+/5\text{-}0.959\right)}\right)-13.7\right)\right)}, \tag{7.19}$$

$30<S_p^+$: Stopping distance is located in the turbulent core

$$K_t = \left(V_{avg} f/2\right). \tag{7.20}$$

7.1.4 Beal Model

In the previous model, Brownian diffusivity was neglected. However, this is not a reasonable assumption for small particle ($0.1 < t_p^+ < 10$) diffusion in the buffer and the sub-laminar zones. Hence, Beal (1970) developed a model based on both Brownian and eddy diffusion, using similar approach as Friedlander and Johnstone (1957). In addition, Beal (1970) assumed a linear equation for mass and momentum flux.

The following equations present the transport coefficient for the different stopping distances obtained by Beal (1970).

$0<S_p^+\leq 5$: Stopping distance is located in the sub-laminar layer

$$K_t = \frac{V_{avg}\sqrt{f/2}}{\left\{\begin{array}{l} \frac{14.5}{3}Sc^{2/3}F\left(Sc,S_p^+\right)-\frac{14.5^2}{1.5D_0{}^+}Sc^{1/3}G\left(Sc,S_p^+\right) \\ +\left[5+\frac{50}{D_{pipe}^+\nu}\left(D_B-0.959\nu\right)\right]ln\left(\frac{D_B+5.04\nu}{D_B+0.04\nu}\right)-\frac{250}{D_{pipe}^+} \\ +\frac{1-13.73\sqrt{f/2}}{\sqrt{f/2}} \end{array}\right\}}, \tag{7.21}$$

where,

$$KF\left(Sc,S_p^+\right)=\left\{\begin{array}{l} \frac{1}{2}ln\left[\frac{\left(1+\frac{5}{14.5}Sc^{1/3}\right)^2}{1-\frac{5}{14.5}Sc^{1/3}+\left(\frac{5}{14.5}\right)^2 Sc^{2/3}}\right]-\frac{1}{2}ln\left[\frac{\left(1+\frac{S_p^+}{14.5}Sc^{1/3}\right)^2}{1-\frac{S_p^+}{14.5}Sc^{1/3}+\left(\frac{S_p^+}{14.5}\right)^2 Sc^{2/3}}\right] \\ +\sqrt{3}tan^{-1}\left(\frac{\frac{10}{14.5}Sc^{1/3}-1}{\sqrt{3}}\right)-\sqrt{3}tan^{-1}\left(\frac{\frac{2S_p^+}{14.5}Sc^{1/3}-1}{\sqrt{3}}\right) \end{array}\right\},$$

and

$$G\left(Sc,S_p^+\right)=\left\{\begin{array}{l} \frac{1}{2}ln\left[\frac{1-\frac{5}{14.5}Sc^{1/3}+\left(\frac{5}{14.5}\right)^2 Sc^{2/3}}{\left(1+\frac{5}{14.5}Sc^{1/3}\right)^2}\right]-\frac{1}{2}ln\left[\frac{1-\frac{S_p^+}{14.5}Sc^{1/3}+\left(\frac{S_p^+}{14.5}\right)^2 Sc^{2/3}}{\left(1+\frac{S_p^+}{14.5}Sc^{1/3}\right)^2}\right] \\ +\sqrt{3}tan^{-1}\left(\frac{\frac{10}{14.5}Sc^{1/3}-1}{\sqrt{3}}\right)-tan^{-1}\left(\frac{\frac{2S_p^+}{14.5}Sc^{1/3}-1}{\sqrt{3}}\right) \end{array}\right\},$$

$5 < S_p^+ \leq 30$: Stopping distance is located in the buffer zone

$$K_t = \frac{V_{avg}\sqrt{f/2}}{\left[5\left\{ \left[1 + \frac{10}{D_{pipe}^+ \nu}\left(D_B - 0.959\nu\right) \right] ln\left[\frac{D_B + 5.04\nu}{D_B + \left(\frac{s^+}{5} - 0.959 \right)\nu} \right] - \frac{10}{D_{pipe}^+}\left(6 - \frac{S_p^+}{5} \right) \right\} + \frac{1 - 13.73\sqrt{f/2}}{\sqrt{f/2}} \right]}, \tag{7.22}$$

$30 < S_p^+$: Stopping distance is located in the turbulent core

$$K_t = \frac{V_{avg}\left(f/2\right)}{\left(1 - 13.73\sqrt{f/2}\right)}. \tag{7.23}$$

In the above equations, Beal (1970) also performed further refinement on stopping distance definition by adding particles radius $d_p/2$ to S_p.

7.1.5 Escobedo and Mansoori Model

Escobedo (1993) and Escobedo and Mansoori (1995) used Beal's (1970) approach. However, Escobedo and Mansoori (1995) applied slightly different correlations for the eddy diffusion in the sub-laminar and buffer zones (Johansen, 1991). Johansen (1991) introduced the following expressions for turbulent kinematic viscosity distribution:

$$\frac{\varepsilon}{\nu}=\begin{cases}\left(\dfrac{y^{+}}{11.15}\right)^{3} & y^{+}<3.0\\[2ex] \left(\dfrac{y^{+}}{11.4}\right)^{2}-0.049774 & 3.0<y^{+}<52.1\\[2ex] 0.4y^{+} & 52.1<y^{+}\end{cases} \tag{7.24}$$

Since in the Johansen (1991) model, the eddy diffusivity is defined in the turbulent core $(30\leq y^{+})$, Escobedo and Mansoori (1995) did not use the Reynolds analogy for the turbulent core diffusion.

The equations for the transport coefficient calculated by Escobedo and Mansoori (1995) are presented as follows:

$0<S_{p}^{+}\leq 5$: Stopping distance is located in the sub-laminar layer

$$K_{t}=\frac{V_{avg}\sqrt{f/2}}{\left\{\begin{array}{l}\dfrac{11.15Sc^{2/3}}{3}F_{1}\left(Sc,S_{p}^{+}\right)-\dfrac{11.15^{2}Sc^{1/3}}{1.5D_{pipe}^{+}}F_{2}\left(Sc,S_{p}^{+}\right)\\[2ex] +11.4\left[\dfrac{Sc}{(0.049774\cdot Sc-1)}\right]^{1/2}F_{3}(Sc)-\dfrac{11.4^{2}}{D_{pipe}^{+}}ln\left[\dfrac{1-0.049774\cdot Sc+\left(\dfrac{30}{11.4}\right)^{2}Sc}{1-0.049774\cdot Sc+\left(\dfrac{5}{11.4}\right)^{2}Sc}\right]\\[2ex] +\left(2.5+\dfrac{12.5}{D_{pipe}^{+}Sc}\right)ln\left(\dfrac{1+0.4r^{+}{}_{avg}Sc}{1+12Sc}\right)-\dfrac{5r^{+}{}_{avg}}{D_{pipe}^{+}}+\dfrac{150}{D_{pipe}^{+}}\end{array}\right\}}, \tag{7.25}$$

In addition, $F_1\left(Sc, S_p^+\right)$, $F_2\left(Sc, S_p^+\right)$ and $F_3(Sc)$ were calculated as follows:

$$F_1\left(Sc, S_p^+\right)=\left\{\begin{array}{l}\dfrac{1}{2}ln\left[\dfrac{\left(1+\dfrac{5}{11.15}Sc^{1/3}\right)^2}{1-\dfrac{5}{11.15}Sc^{1/3}+\left(\dfrac{5}{11.15}\right)^2 Sc^{2/3}}\right]-\dfrac{1}{2}ln\left[\dfrac{\left(1+\dfrac{S_p^+}{11.15}Sc^{1/3}\right)^2}{1-\dfrac{S_p^+}{11.15}Sc^{1/3}+\left(\dfrac{S_p^+}{11.15}\right)^2 Sc^{2/3}}\right]\\ +\sqrt{3}tan^{-1}\left(\dfrac{\dfrac{10}{11.15}Sc^{1/3}-1}{\sqrt{3}}\right)-\sqrt{3}tan^{-1}\left(\dfrac{\dfrac{2S_p^+}{11.15}Sc^{1/3}-1}{\sqrt{3}}\right)\end{array}\right\},$$

$$F_2\left(Sc, S_p^+\right)=\left\{\begin{array}{l}\dfrac{1}{2}ln\left[\dfrac{1-\dfrac{5}{11.15}Sc^{1/3}+\left(\dfrac{5}{11.15}\right)^2 Sc^{2/3}}{\left(1+\dfrac{5}{11.15}Sc^{1/3}\right)^2}\right]-\dfrac{1}{2}ln\left[\dfrac{1-\dfrac{S_p^+}{11.15}Sc^{1/3}+\left(\dfrac{S_p^+}{11.15}\right)^2 Sc^{2/3}}{\left(1+\dfrac{S_p^+}{11.15}Sc^{1/3}\right)^2}\right]\\ +\sqrt{3}tan^{-1}\left(\dfrac{\dfrac{10}{11.15}Sc^{1/3}-1}{\sqrt{3}}\right)-\sqrt{3}tan^{-1}\left(\dfrac{\dfrac{2S_p^+}{11.15}Sc^{1/3}-1}{\sqrt{3}}\right)\end{array}\right\},$$

and

$$F_3(Sc)=\frac{1}{2}ln\left[\frac{\sqrt{0.049774\,Sc-1}-\dfrac{30}{11.4}Sc^{1/2}}{\dfrac{30}{11.4}Sc^{1/2}+\sqrt{0.049774\,Sc-1}}\right]-\frac{1}{2}ln\left[\frac{\sqrt{0.049774\,Sc-1}-\dfrac{5}{11.4}Sc^{1/2}}{\dfrac{5}{11.4}Sc^{1/2}+\sqrt{0.049774\,Sc-1}}\right],$$

$5 < S_p^+ \le 30$: Stopping distance is located in the buffer zone

$$K_t = \frac{V_{avg}\sqrt{f/2}}{\left\{ \begin{array}{l} 11.4\left[\dfrac{Sc}{(0.049774 \cdot Sc - 1)}\right]^{1/2} F_3(Sc) - \dfrac{11.4^2}{D^+_{pipe}} ln\left[\dfrac{1 - 0.049774 \cdot Sc + \left(\dfrac{30}{11.4}\right)^2 Sc}{1 - 0.049774 \cdot Sc + \left(\dfrac{S^+_p}{11.4}\right)^2 Sc}\right] \\ + \left(2.5 + \dfrac{12.5}{D^+_{pipe} Sc}\right) \ln\left(\dfrac{1 + 0.4 r^+_{avg} Sc}{1 + 12 Sc}\right) - \dfrac{5 r^+_{avg}}{D^+_{pipe}} + \dfrac{150}{D^+_{pipe}} \end{array} \right\}}, \tag{7.26}$$

where r^+_{avg} is the non-dimensional form of the average radial distance from the wall, at which the fluid velocity is equal to the average velocity. This parameter is calculated as follows:

$$r^+_{avg} = \frac{r_{avg} V_{avg} \sqrt{f/2}}{\nu}, \tag{7.27}$$

r_{avg} can be obtained from the turbulent velocity profile, as given by Lin (1953).

$30 < S^+_p$: Stopping distance is located in the turbulent core

$$K_t = \frac{V_{avg}\sqrt{f/2}}{\left[\left(2.5 + \dfrac{12.5}{D^+_{pipe} Sc}\right) ln\left(\dfrac{1 + 0.4 r^+_{avg} Sc}{1 + 0.4 S^+_p Sc}\right) - \dfrac{5 r^+_{avg}}{D^+_{pipe}} + \dfrac{5 S^+_p}{D^+_{pipe}}\right]}. \tag{7.28}$$

7.1.6 Cleaver and Yates Model

Cleaver and Yates (1975) applied a stochastic approach to obtain the transport coefficient, which is presented as follows:

$$K_t = \frac{0.084 V_{avg} \sqrt{f/2}}{Sc^{2/3}}. \tag{7.29}$$

They assumed that the particles are moved to a certain distance from the wall by turbulent diffusion and then entrained in the laminar sub-layer. In the laminar sub-laminar the particles are swept toward the wall by streamline of flow or ejected away from the wall by turbulent burst. Cleaver and Yates (1975) also defined a capture area where the fraction of particles existing in that area impact with the surface. Particles out of the capture area are carried back into the turbulent core. Furthermore, Cleaver and Yates (1975) discussed on small particles diffusion where the Brownian motion is involved. They considered flow fields in laminar sub-layer and derived a diffusion equation to obtain the flux and concentration of particles.

Cleaver and Yates (1975) showed that their model is satisfactorily applicable for small relaxation times where the diffusion mechanism is dominant. However, for most general applications, Epstein (1988) combined Cleaver and Yates (1975) model with Papavergos and Hedly (1984) model, which is also a stochastic approach, for different range of the relaxation times. Papavergos and Hedly (1984) presented the following equations for the transport coefficient when the inertia and impaction mechanisms are dominant ($0.2 < t_p^+$):

$$K_t^+ = 0.00035 (t_p^+)^2, \quad 0.2 < t_p^+ < 10, \tag{7.30}$$

$$K_t^+ = 0.18, \qquad 10 < t_p^+. \tag{7.31}$$

As Equation (7.31) indicates, according to Papavergos and Hedly (1984), the dimensionless transport coefficient is constant for high relaxation times.

7.2 ASPHALTENE AND SCALE DEPOSITION MODEL IN LAMINAR FLOW

We start developing the particles deposition model in laminar flow from Friedlander and Johnstone (1957) classical approach. As shown in Equation (7.11) Friedlander and Johnstone (1957) used the analogy between mass transfer fluxes to the momentum transfer flux in turbulent flow to obtain the particle transport equation in transverse direction. In Equation (7.11) Brownian diffusion and eddy diffusion terms are appeared as the main deposition deriving forces. If we neglect the eddy diffusions in laminar flow, we can find the mass flux equation for particles in laminar flow as

$$N = D_B \frac{\partial C}{\partial y}. \tag{7.32}$$

We follow the same steps in turbulent flow to derive the mass transfer flux term in laminar flow. Using the Beal (1970) approximation for linear mass flux from wall to the center of pipe, we have

$$N = N_0 \left(1 - \frac{2y^+}{D_0^+} \right), \tag{7.33}$$

where N_0 is the particles flux at wall, y^+ is the dimensionless distance from wall and D_0^+ is the dimensionless diameter. All the dimensionless distances are correlated as

$$L^+ = L\frac{V_{avg}\sqrt{f/2}}{v}. \tag{7.34}$$

Combining Equations (7.33) and (7.34) we obtain

$$N_0\left(1-\frac{2y^+}{D_0^+}\right) = D_B\frac{\partial C}{\partial y}, \tag{7.35}$$

$$N_0\left(1-\frac{2y^+}{D_0^+}\right) = D_B\frac{V_{avg}\sqrt{f/2}}{v}\frac{\partial C}{\partial y^+}. \tag{7.36}$$

Assuming C_s solid particle concentration at stopping distance ($y^+ = S_p^+$) and C_{avg} as particle concentration at center of pipe ($y^+ = D_0^+/2$), we can integrate Equation (7.36) to obtain mass flux rate. Since we do not have different regions in laminar flow we can take the integration from stopping distance to the center of the pipe. The mass flux obtained for laminar flow becomes

$$\frac{N_0}{C_{avg}-C_s} = V_{avg}\sqrt{f/2}\frac{4D_0^+\left(\frac{D_B}{v}\right)}{\left(2S_p^+-D_0^+\right)^2}. \tag{7.37}$$

Using the definitions in Section 7.1.1 the transport coefficient in laminar flow also becomes

$$K_t = V_{avg}\sqrt{f/2}\,\frac{4D_0^+\left(\frac{D_B}{\nu}\right)}{\left(2S_p^+ - D_0^+\right)^2}. \tag{7.38}$$

Comparing K_t value for laminar flows with the turbulent flow models shows that it is several orders of magnitude smaller than K_t value in turbulent flows. In fact, the eddy diffusions in the turbulent flow facilitate the movement of particles in radial direction significantly.

7.3 ATTACHMENT PROCESS

Another phenomenon that significantly affects solid deposition is the attachment process. Several active forces between the particles and the fluid, as well as between the particles and the wall influence the deposition process.

The source of those forces can be electrostatic and polar attractions or the shear forces due to high velocity and viscosity of the moving fluids. In gas flow systems, since shear forces are not significant, detachment of the particles is not pronounced. However, for the liquid system, those forces are very important.

One approach to include the attachment process is applying a sticking probability function to the final transport coefficient, where the deposition coefficient could be modified as

$$K_D = SP\,K_t. \tag{7.39}$$

Watkinson and Epstein (1970) defined the sticking probability as follows:

$$SP \propto \frac{\text{Adhesion Force Between Particles and Wall}}{\text{Drag Force on Particles on the Surface}}.$$

Assuming an Arrhenius type expression and using the drag coefficient to calculate the adhesion force and the drag force, respectively, we obtain:

$$SP = S_0 \frac{F_0 e^{\left(-E_a / RT_s\right)}}{\mathrm{C_D A_p} \rho_\mathrm{p} \mathrm{V_{avg}^2}} = k_d \frac{e^{\left(-E_a / RT_s\right)}}{\mathrm{V_{avg}^2}}, \tag{7.40}$$

where k_d and E_a are calculated from experimental results. The material of the wall surface can be related to k_d and E_a parameters. The complete equation for particle deposition flux, considering the attachment process, becomes:

$$\dot{m}_d = SP\ K_t (C_b - C_s). \tag{7.41}$$

Moreover, the deposited solid can also be removed from the surface of the well due to shear forces. For this reason, we define the rate of solid deposit removal as

$$\frac{d\delta}{dt} = k_r \delta \tau^a, \tag{7.42}$$

where δ is the asphaltene deposit thickness, k_r shear removal factor, τ is the shear stress, and a is the shear coefficient. Removed solid thickness can be converted to the removed mass as

$$\dot{m}_r = \pi D \frac{d\delta}{dt} dz \rho_s. \tag{7.43}$$

Attachment and detachment of solid on the surface of the well can also change the roughness of the well surface. Increasing the roughness can contribute on more pressure drop in the wellbore, especially in the turbulent flows. In our models to incorporate the roughness effect, we considered the roughness of contaminated zones by solid deposits as user defined value.

7.4 COMPARISON OF DEPOSITION MODELS WITH EXPERIMENTAL RESULTS

In this section, we present the comparison of the reviewed models for asphaltene deposition with two different sets of experimental results.

7.4.1 Gas/Iron Flow Experiment with no Re-entrainment

Friedlander and Johnstone (1957) designed an experimental setup to evaluate iron and aluminum particles deposition in the turbulent gas flow. In their study, they used two kinds of vertical tubes, one made of brass and other of glass, which eliminated the gravitational force effect in the radial direction and the electrostatic forces effect on deposition process. The experimental setup was also appropriately accommodated with glycerol jelly adhesive and sensors on the tube wall to measure the rate of particle transport to the wall and to prevent deposits re-entrainment. In addition, gas velocity was considered low enough to minimize re-entrainment.

Here we applied Friedlander and Johnstone (1957) data to verify the accuracy of the models described in Section 2: Friedlander and Johnstone (1957), Beal (1970), Escobedo and Mansoori (1995), Epstein (1988), combined Cleaver and Yates (1975) model with Papavergos and Hedly (1984).

Table 7.1 shows the pertinent input data required for calculating the transport coefficient in different models. Tables 7.2 through 7.5 show the average velocities, Reynolds number, relaxation times and transport coefficients obtained for the different models. Figures 7.3 through 7.6 show that the models are in fairly good agreement with the experimental data at the calculated range of relaxation times. It can be observed that the Epstein combined model (which assembles the Cleaver and Yates and the Papavergos and Hedly models) underestimates the measured results. The Escobedo and Mansoori (1995) model overestimates the results. Friedlander and Johnstone (1957) and Beal (1970) models give similar values, which lie in between Escobedo and Mansoori and Epstein combined models. For high Reynolds numbers, the Beal (1970) model deviates from the Friedlander and Johnstone (1957) model.

In general, it can be observed that for small relaxation times, the Epstein combined model offers better predictions. However, for large relaxation times, Beal and Friedlander and Johnstone models predict the transport coefficients better, according to the published experimental data.

7.4.2 Oil/Asphaltene Flow Experiment

Another experimental data set we investigated in this study is asphaltene deposition from crude oil flow. We used the data from the work performed by Jamialahmadi et al. (2009). In this experiment, the apparatus measures the amount of heat transfer during the asphaltene deposition process to calculate the amount of deposited asphaltene. In fact, a heater was accommodated in this system to heat the surface of the pipe, in which the crude oil containing asphaltene flows. By heat flux measurement and temperature difference between bulk flow and pipe surface, the heat transfer coefficient is calculated. The heat transfer coefficient is changed with time when the layers of asphaltene are deposited on the pipe surface. Hence, by calculating the heat transfer coefficient, the thickness of asphaltene layer and the amount of asphaltene deposition are determined.

Table 7.6 shows the range of operating parameters and SARA analysis of the crude oil used in the Jamialahmadi et al. (2009) experiments. Table 7.7 shows the pertinent data we extracted from the Jamialahmadi et al. (2009) paper to assist our calculations. We used d_p=0.5   m for the asphaltene particle diameter size in this study. However, depending on temperature and pressure conditions the aggregated asphaltene particle size can vary. It can reach up to 300   m diameter, when large amount of asphaltene molecules are aggregated (Escobedo and Mansoori, 1995).

In addition, as explained in the modeling section, since we have a liquid flow, both deposition and attachment processes should be considered in the deposition rate equation. Hence, for all of the models, we used the same expression, Equation (7.40), for determining the sticking probability coefficient.

Table 7.8 shows the Reynolds numbers and the corresponding deposition rates. We plotted the deposition rates *versus* Reynolds numbers for the models, comparing to the experimental results. As can be seen in Figure 7.7, except for the Friedlander and Johnstone (1957) model, there is a fairly good agreement between the models results and the experimental data. Particularly, Escobedo and Mansoori's model (1995) presents the most satisfactory match.

Table 7.9 also shows the root mean square of error for different models' deposition rate prediction. We observe that Beal (1970) and Escobedo and Mansoori (1995) models are representative for small and large relaxation times. Cleaver and Yates (1975) model is satisfactorily good for the small relaxation times where the diffusion mechanism is dominant and Friedlander and Johnstone (1957) model is good for large relaxation times where inertia mechanism is dominant.

To better understand the asphaltene deposition behavior, we also investigated the effect of fluid velocity, tubing surface temperature and particles diameter. Figure 7.8 shows the deposition rate versus flow velocity. As can be observed, increasing velocity decreases the deposition rate. In fact, increasing the flow velocity causes more significant shear stress on the wall and, consequently, particle removal.

Figure 7.9 shows the effect of tubing surface temperature. Increasing the surface temperature enhances the deposition rate. In fact, at high temperatures, more asphaltene particles can pass the activation energy barrier (Ea) to stick to the wall.

Figure 7.10 also presents the effect of asphaltene particles size on deposition rate. It can be observed that increasing the particle size reduces the deposition rate. As Table 7.8 shows, the relaxation time (t_p^+) for the asphaltene particles in the oil is very small where diffusion mechanism becomes dominant. Hence, the smaller particle sizes have more diffusivity toward the wall and consequently have greater deposition rate.

7.5 WAX DEPOSITION MODELS

Solid deposition model for wax is slightly different from what we discussed for asphaltene and geochemical scales. Since wax is more like a liquid-gel phase which crystallizes at low temperatures, the mechanism of wax deposition can be different from that of other solid particles. The deriving mechanisms for wax deposition consist of molecular diffusion, shear dispersion, Brownian diffusion, gravity settling, and aging.

Molecular diffusion occurs due to concentration gradient of wax-forming components between the core of the flow and the sub-laminar region. Since in the pipeline, the surface of the wall has a cooler temperature, it can strip out the wax forming components of crude oil in the vicinity of the wall. Higher temperature in the core flow also keeps the concentration of the wax forming components larger in the oil. Thus, the created concentration gradient in the transverse direction of the flow causes a net flux of the dissolved components in the oil to the wall by Fick's law.

$$N = -D_m \left(\frac{dC^{wax}}{dr} \right), \tag{7.44}$$

$$N = -D_m \left(\frac{dC^{wax}}{dT} \right) \left(\frac{dT}{dr} \right), \tag{7.45}$$

where $D_m \left(\frac{m^2}{sec} \right)$ is the molecular diffusivity coefficient, $\left(\frac{dC^{wax}}{dT} \right)$ is the solubility coefficient and $\left(\frac{dT}{dr} \right)$ is the temperature gradient in the *r*-direction . Equation (7.44) can also be written for each individual wax forming components in the crude oil, upon which the summation of fluxes yields the total molar flux of wax to the wall.

The solubility coefficient in Equation (7.44) can be calculated from wax thermodynamic model (Section 6.2.1); the temperature gradient can also be computed from heat transfer models in the wellbore, and the diffusivity coefficient term can be obtained from Hayduk and Minhas (1982) model. Using Hayduk and Minhas (1982) expression the molecular diffusivity coefficient becomes

$$D_m = 13.3 \times 10^{-8} \frac{T^{1.47} \mu^{\left(\frac{10.2}{V_{wax}} - 0.791 \right)}}{V_{wax}^{0.71}}, \tag{7.46}$$

where T is temperature in *Kelvin*, μ is the viscosity of the oil in $mPa.sec$ and the V_{wax} is the wax molar volume (in $\frac{cm^3}{mol}$).

The other mechanism that can possibly occur in wax deposition process is the shear dispersion effect. However, some researchers (Brown et al. (1993) and Hamouda (1995)) neglect this mechanism in comparison to molecular diffusion. Since this mechanism is related to intermolecular interaction, it becomes important when the fluid temperature is already very low and most of the wax-forming components have been stripped out. The main deriving force in the shear dispersion effect is the transverse momentum transfer due to surface shear forces at the wall and the corresponding velocity profile. By shear transfer effect, the solid particles tend to move to the sub-laminar zone and then deposit on the wall surface.

In wax deposition process, similar to asphaltene deposition, Brownian diffusion can also enhance the deposition rate. However, since this mechanism is a random process, it might not be as important as other mechanisms.

In our wax deposition model, we follow the same procedure taken by other researchers (Brown et al., (1993), Singh (2000), Hernandez et al. (2004)) and the PIPESIM 2011 software). In this model, we consider the molecular diffusion mechanism for deposition along with shear removal effects that are calculated using the Venkatesan (2004) correlation. Hence, the overall deposition rate in terms of wax thickness for single-phase flow becomes

$$\left(\frac{d\delta}{dt}\right) = -D_m\left(\frac{1}{1-\varphi}\right)\left(\frac{dC^{wax}}{dT}\right)\left(\frac{dT}{dr}\right) - k\delta\left(\frac{\tau^a}{(1-\varphi)\varphi^b}\right), \tag{7.47}$$

where δ is the wax thickness in m, φ is the porosity of the wax, τ is the shear stress in Pa, k is a user-specified shear reduction multiplier, a is the user-specified shear stress coefficient with default value of 1.9 and b is the user-specified wax porosity coefficient with the default value of 2.3.

In Chapter 8, we will show how the single-phase deposition models can be applied to multiphase flows as well. In addition, we will explain wax deposition model results in the examples given in next chapters.

Table 7.1 Input parameters

Air density (g/cc)	0.001257
Air viscosity(Poise)	0.0001861
Iron particles sizes (m)	0.8,1.32, 1.81, 2.63
Iron particles density (g/cc)	7.8
Pipe diameters (cm)	0.54, 2.5

Table 7.2 Results for 0.8 micron iron particles deposition in 0.54 cm tube diameter A- Friedlander and Johnstone (1957) B- Beal (1970) C- Escobedo and Mansoori (1995) D- Epstein combined (1988)

V_{avg}	**Re**	**tp^+**	**Experiment**	**A**	**B**	**C**	**D**
(cm/s)	**(dimensionless)**	**(dimensionless)**	**(cm/min)**	**(cm/min)**	**(cm/min)**	**(cm/min)**	**(cm/min)**
1,310.64	4,778.78	0.82	0.17	2.11	2.06	4.29	1.28
1,905.00	6,945.91	1.58	2.65	11.03	10.36	20.22	6.59
2,036.06	7,423.78	1.78	1.67	14.91	13.87	26.56	8.82
2,036.06	7,423.78	1.78	2.29	14.91	13.87	26.56	8.82
2,654.81	9,679.82	2.83	6.1	52.24	45.74	77.46	28.15
2,654.81	9,679.82	2.83	6.64	52.24	45.74	77.46	28.15
3,230.88	11,780.26	3.99	23.1	148.24	118.47	167.52	66.47
3,230.88	11,780.26	3.99	50.3	148.24	118.47	167.52	66.47
3,230.88	11,780.26	3.99	59.8	148.24	118.47	167.52	66.47
3,230.88	11,780.26	3.99	34.9	148.24	118.47	167.52	66.47
3,264.41	11,902.51	4.06	44.1	157.46	124.94	174.34	69.54
3,992.88	14,558.62	5.78	69	628.74	385.14	365.42	167.86
3,992.88	14,558.62	5.78	95	628.74	385.14	365.42	167.86
5,486.40	20,004.21	10.07	460	1,532.45	913.44	879.27	3,416.99
5,486.40	20,004.21	10.07	445	1,532.45	913.44	879.27	3,416.99

Table 7.3 Results for 0.8 micron iron particles deposition in 2.5 cm tube diameter A- Friedlander and Johnstone (1957) B- Beal (1970) C- Escobedo and Mansoori (1995) D- Epstein combined (1988)

V_{avg} (cm/s)	Re (dimensionless)	tp^+ (dimensionless)	Experiment (cm/min)	A (cm/min)	B (cm/min)	C (cm/min)	D (cm/min)
837.6628	14140.00	0.2561	0.21980	0.1184	0.1351	0.2733	0.0695
1,012.42	17090.00	0.3568	0.39290	0.2670	0.2794	0.5847	0.1592
1,219.76	20590.00	0.4943	0.74170	0.5959	0.5984	1.2632	0.3596
1,390.37	23470.00	0.6216	0.89480	1.0501	1.0366	2.1806	0.6376
1,553.88	26230.00	0.7551	0.84550	1.7021	1.6611	3.4680	1.0371
1,789.06	30200.00	0.9663	1.30300	3.1496	3.0326	6.2343	1.9214

Table 7.4 Results for 1.81micron iron particles deposition in 2.5 cm tube diameter A- Friedlander and Johnstone (1957) B- Beal (1970) C- Escobedo and Mansoori (1995) D- Epstein combined (1988)

V_{avg} (cm/s)	Re (dimensionless)	tp^+ (dimensionless)	Experiment (cm/min)	A (cm/min)	B (cm/min)	C (cm/min)	D (cm/min)
679.4902	11470.00	0.90886	2.58700	1.19547	1.15435	2.38710	0.72865
859.5818	14510.00	1.37144	4.94500	3.37329	3.18269	6.32598	2.03810
1,277.22	21560.00	2.74249	16.23000	21.00628	18.39024	31.33982	11.52508
1,800.91	30400.00	5.00366	80.19000	144.59372	102.24751	116.74032	51.82061
679.4902	11470.00	0.90886	2.58700	1.19547	1.15435	2.38710	0.72865

Table 7.5 Results for 2.63 micron iron particles deposition in 2.5 cm tube diameter A- Friedlander and Johnstone (1957) B- Beal (1970) C- Escobedo and Mansoori (1995) D- Epstein combined (1988)

V_{avg} (cm/s)	Re (dimensionless)	tp^+ (dimensionless)	Experiment (cm/min)	A (cm/min)	B (cm/min)	C (cm/min)	D (cm/min)
491.2827	8293.00	1.08782	2.60500	1.29230	1.23837	2.52516	0.78596
677.1206	11430.00	1.90719	10.94000	5.44511	5.00929	9.44969	3.19883
856.6198	14460.00	2.87811	31.01000	16.63741	14.46727	24.26899	8.94902
862.5438	14560.00	2.91304	59.55000	17.21801	14.93800	24.93915	9.22296
1,264.78	21350.00	5.69193	118.20000	176.67405	110.15104	105.91761	49.22152

Table 7.6 Input parameters

Inside diameter of pipe (mm)	23.8
Heated length (mm)	160
Flow velocity (m/s)	0.35-2
Heat flux (kW/m^2)	25-86
Asphaltene super-saturation concentration (kg/m^3)	0-5
Saturate Fraction (wt%)	52.49
Aromatic Fraction (wt%)	41.04
Resin Fraction (wt%)	5.48
Asphaltene Fraction (wt%)	0.99

Table 7.7 Input parameters

Oil density (g/cc)	0.866
Oil viscosity (Poise)	0.012
Asphaltene concentration (kg/m^3)	3.5
Asphaltene particles size (m)	0.5
Asphaltene particles density (g/cc)	1.1
Bulk temperature (^oC)	85
Surface temperature (^oC)	120
Pipe diameter (cm)	2.38
Surface adhesions constant (m^2/sec^2)	9.76×10^8
Surface adhesions activation energy (KJ)	65.3

Table 7.8 Results for asphaltene deposition in 2.38 cm diameter tube A- Friedlander and Johnstone (1957) B- Beal (1970) C- Escobedo and Mansoori (1995) D- Cleaver and Yates (1975)

V_{avg} (cm/s)	Re (dimensionless)	tp^+ (dimensionless)	Experiment Jamialahmadi et al (2009) (10^{-6}kg/m^2-s)	A (10^{-6}kg/m^2-s)	B (10^{-6}kg/m^2-s)	C (10^{-6}kg/m^2-s)	D (10^{-6}kg/m^2-s)
35.00	6,011.48	5.10E-06	9.20	0.02	7.73	10.14	11.17
61.00	10,477.16	1.34E-05	5.30	0.03	4.21	5.55	5.98
92.00	15,801.61	2.74E-05	3.20	0.04	2.71	3.59	3.77
125.00	21,469.58	4.69E-05	2.40	0.04	1.96	2.62	2.67
160.00	27,481.07	7.23E-05	1.60	0.05	1.52	2.04	2.02

Table 7.9 Root mean square error of transport coefficient calculated for different models A-Friedlander and Johnstone (1957) B- Beal (1970) C- Escobedo and Mansoori (1995) D- Epstein combined (1988)

Experiment	tp^+ range	A	B	C	D
0.8 micron iron particles deposition in 0.54 cm tube	1-10	446	207.1	202.9	1083
0.8 micron iron particles deposition in 2.5 cm tube	0.1-1	0.838	0.787	2.35	0.343
1.81micron iron particles deposition in 2.5 cm tube	1-10	32.3	11.1	19.8	14.5
2.63 micron iron particles deposition in 2.5 cm tube	1-10	33	21	16.7	39.6
0.5 micron asphaltene deposition in 2.38 cm tube	1e-6-1e-4	5.1	0.87	0.51	0.99

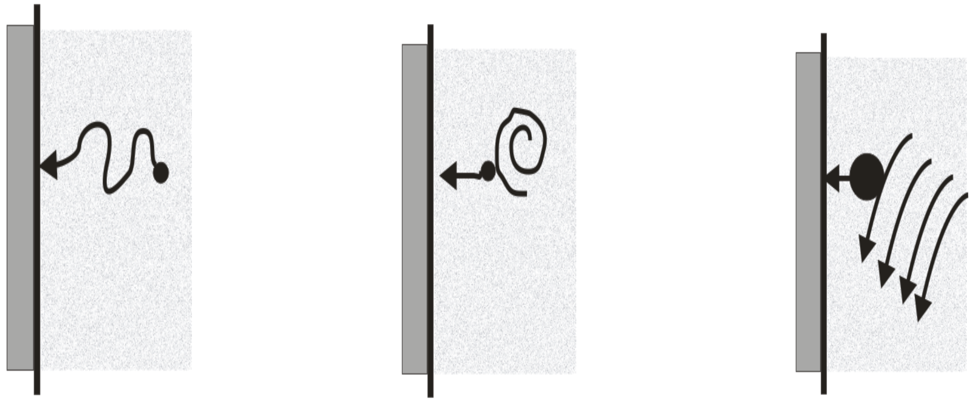

(a) (b) (c)

Figure 7.1 Schematic views of the deposition mechanisms, (a) diffusion, (b) inertia, (c) impaction.

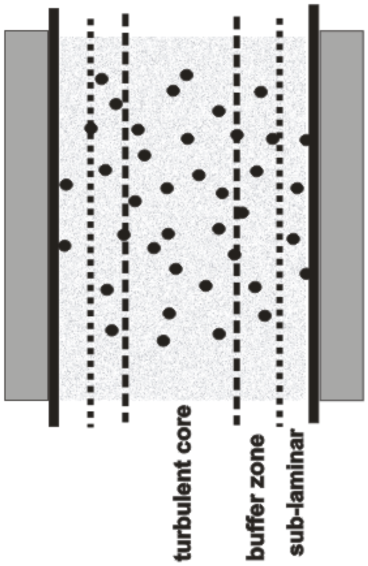

Figure 7.2 The schematic view of three different zones in the turbulent flow.

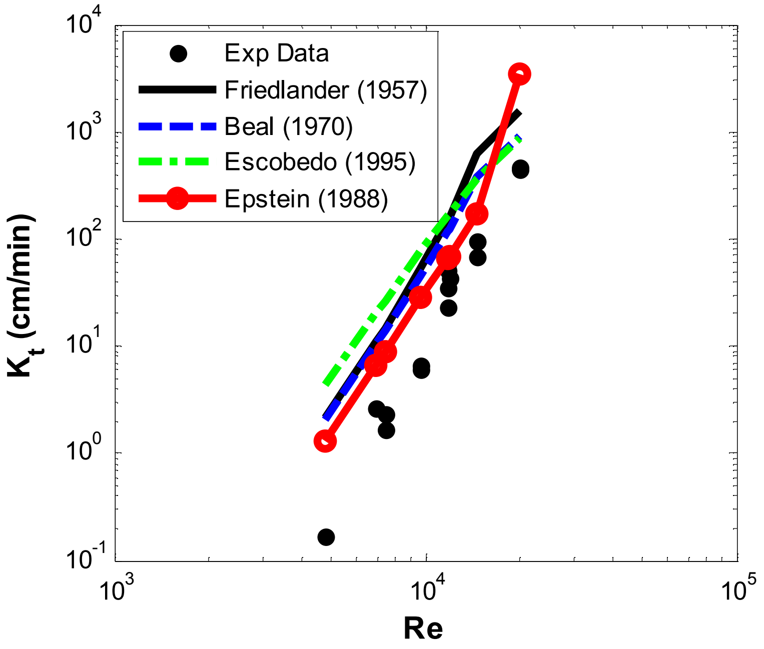

Figure 7.3 Comparison of different models for 0.8 micron iron particles deposition in 0.54 cm diameter glass tube.

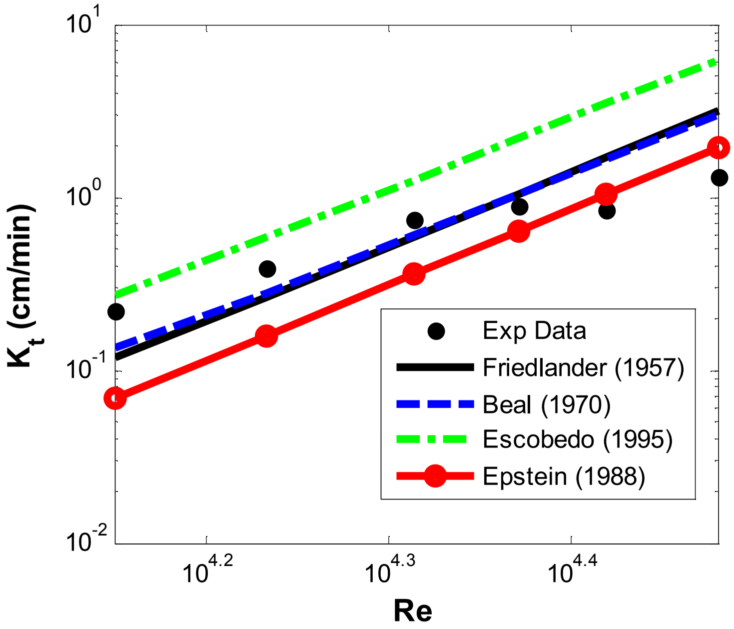

Figure 7.4 Comparison of different models for 1.32 micron iron particles deposition in 2.5 cm diameter glass tube.

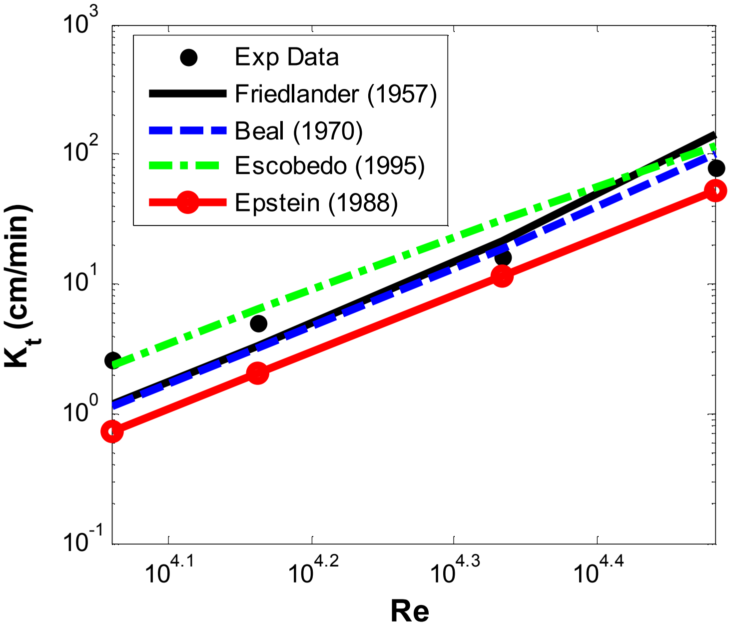

Figure 7.5 Comparison of different models for 1.81 micron iron particles deposition in 2.5 cm diameter glass tube.

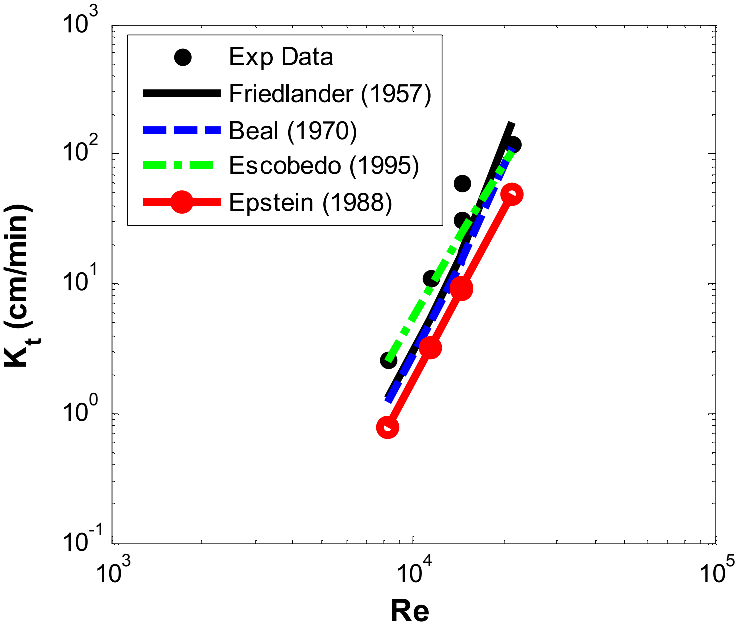

Figure 7.6 Comparison of different models for 2.63 micron iron particles deposition in 2.5 cm diameter glass tube.

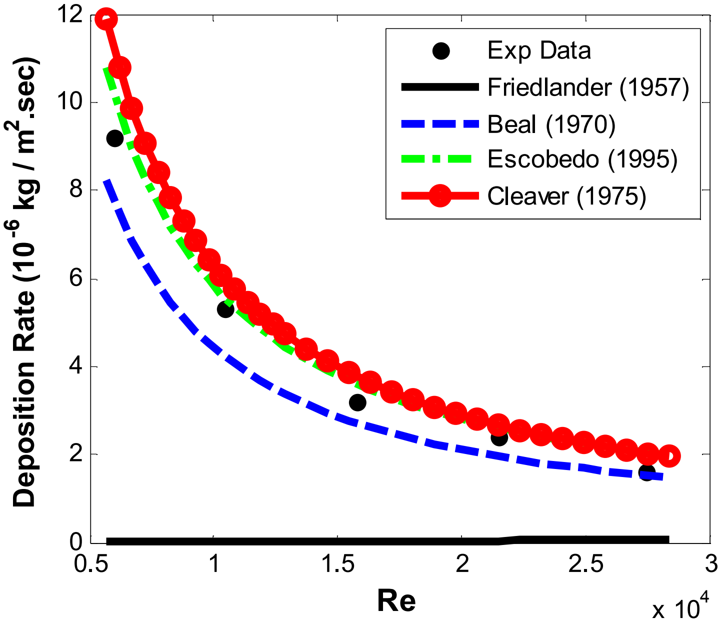

Figure 7.7 Comparison of different models for 0.5 micron asphaltene deposition in 2.38 cm diameter tube.

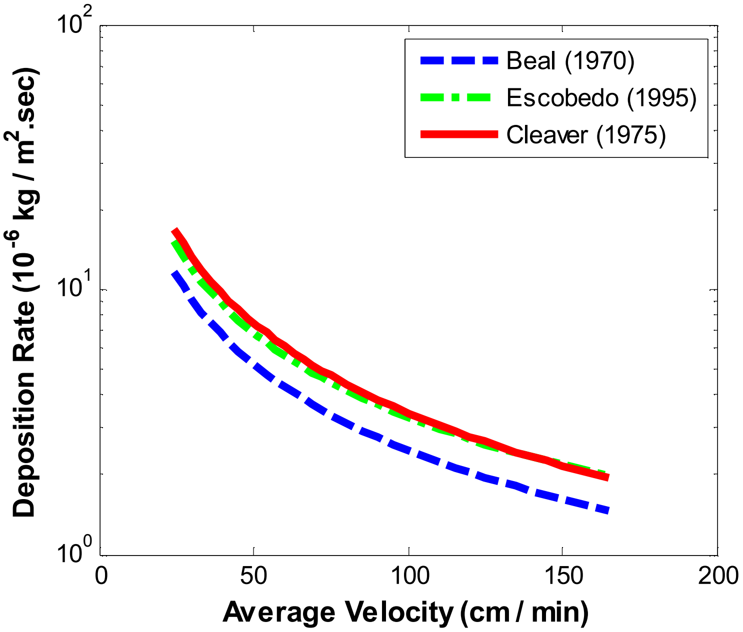

Figure 7.8 Comparison of different models, velocity effect on deposition rate, and 0.5 micron asphaltene deposition in 2.38 cm diameter.

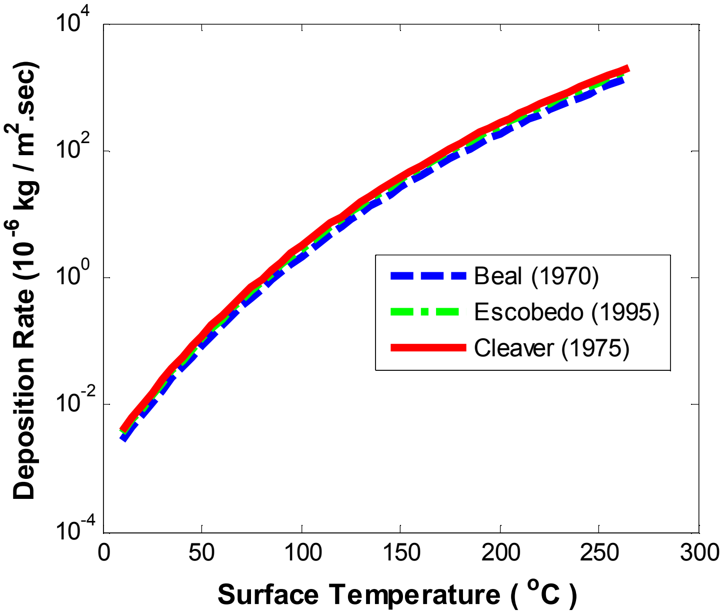

Figure 7.9 Comparison of different models, tubing surface temperature effect on deposition rate, average fluid velocity of 35 (cm/min) and asphaltene particles size of 0.5 micron, in 2.38 cm diameter tube.

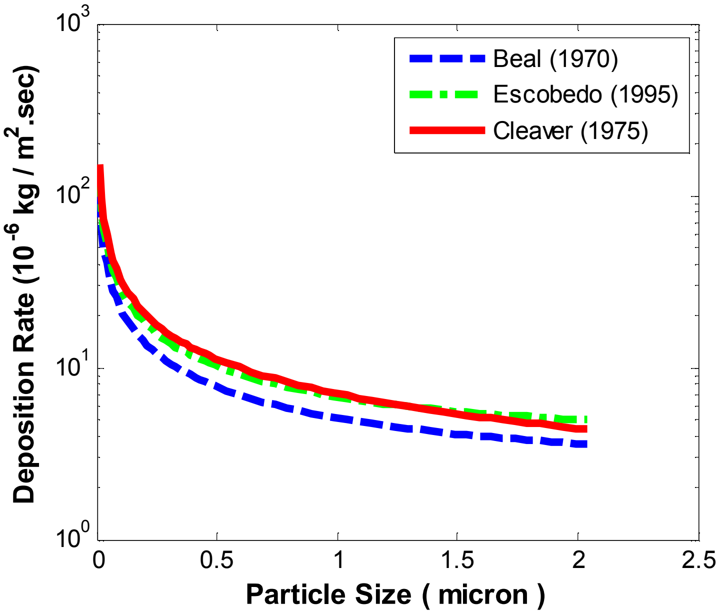

Figure 7.10 Comparison of different models, particles size effect on deposition rate, in average fluid velocity of 35 (cm/min), tubing surface temperature of 124 °C in 2.38 cm diameter tube.

Chapter 8: Particle Transportation in Multiphase Flow

In many hydrocarbon production systems multiphase flow occurs due to pressure depletion or composition change along the flow path. Flow assurance problems can commonly be combined with multiphase flow during the primary production or gas injection processes for enhanced oil recovery.

In previous chapters, we discussed the modeling of multiphase flow and flow assurance problems in the wellbore separately. Here we combine these two phenomena to study the transportation and entrainment of solid particles in the flow line during multiphase flow condition.

8.1 DEPOSITION KINETICS IN MULTIPHASE FLOW SYSTEMS

In multiphase flow systems that involve with gas and liquid phases, we should properly modify deposition equations for solid particles. In fact, we assume that solid particles (asphaltene, wax, scale) only reside as suspended objects in their continuous phases. Hence, the particle concentration is calculated in those phases. In addition, since solid particles can stick on the well surface through the wetted perimeter of the well by the liquid phase (oil or water), we modify deposition equations as a function of these parameters.

To extend the single-phase deposition models to the multiphase flow systems, we use an approach similar to Matzain (2001) empirical correlations for varying flow patterns as follows:

$$\dot{m}_d\Big|_{tp} = S_l^{\omega} \alpha_l^{\upsilon}\, \dot{m}_d\Big|_{sp} . \tag{8.1}$$

In Equation (8.1), $\dot{m}_d\big|_{tp}$ is the deposition rate in the two phase flow system, $\dot{m}_d\big|_{sp}$ is the deposition rate in the single phase flow, S_l is the liquid wetted perimeter to the pipe perimeter ratio, and α_l is the liquid volume fraction. ω and ν are user specified values used as fitting parameters. Default value of ω and ν is 0.5.

8.2 PARTICLE MASS CONSERVATION EQUATION

In Chapter 3, we presented the components mass conservation equations for a multiphase flow system. Addition of solid particles to the fluid flow introduces new sets of mass conservation equations as follows:

$$\frac{\partial\left(A\hat{\rho}_o\alpha_o x_{nc}+Ac_a\alpha_o\right)}{\partial t}+\frac{\partial\left(A\hat{\rho}_o\alpha_o u_o x_{nc}+Au_o c_a\right)}{\partial x}=A\left(\dot{\hat{\psi}}_{o,nc}+\dot{\hat{\Upsilon}}_a-\dot{\hat{m}}_{da}\right), \tag{8.2}$$

$$\frac{\partial\left(\sum\limits_{i=1}^{NWAX} A\hat{\rho}_o\alpha_o x_i+Ac_w\alpha_o\right)}{\partial t}+\frac{\partial\left(\sum\limits_{i=1}^{NWAX} A\hat{\rho}_o\alpha_o u_o x_i+Au_o c_w\right)}{\partial x}= \\ A\left(\sum\limits_{i=1}^{NWAX} \dot{\hat{\psi}}_{o,i}+\dot{\hat{\Upsilon}}_w-\dot{\hat{m}}_{dw}\right), \tag{8.3}$$

$$\frac{\partial\left(Ac_s\alpha_w\right)}{\partial t}+\frac{\partial\left(Au_w c_s\right)}{\partial x}=A\left(\dot{\hat{\Upsilon}}_s-\dot{\hat{m}}_{ds}\right), \tag{8.4}$$

where c_a is the asphaltene concentration in the crude oil, c_w is the wax concentration in the crude oil, c_s is the scale concentration in the aqueous phase, $\dot{\hat{\Upsilon}}$ is the flocculation of solid particles from reservoir (for wax this term may be zero), $\dot{\hat{\psi}}$ is the components molar flux between the wellbore and the reservoir and $\dot{\hat{m}}_d$ is the deposition rate of solid particles.

Equation (8.2) is applied to the fluids that contain asphaltene and cause asphaltene flow assurance problems. Equation (8.3) is used for fluids with wax precipitation potentials and Equation (8.4) is used for the aqueous phase that carries scales. In each specific flow assurance modeling, the corresponding solid mass conservation equations are solved along with the other flow field equations presented in Chapter 5.

To solve Equations (8.2) and (8.3) for asphaltene and wax mass conservation, we can use a similar approach for solution of components mole per volume, at advanced time, Equations (5.72). In fact, for the specific components, *k* (asphaltene or wax forming components), which participates in the flow assurance problem we solve the following equations in gridblock *i*:

$$
\begin{aligned}
N_{k,i}^{n+1} = N_{k,i}^{n} + & \\
& \frac{\Delta t}{V_b^n} A_{i-1}^n \left[\left(\hat{\rho}_o \alpha_o u_o \right)_{i-1}^{n+1} x_{k,i-1}^n + \left(\hat{\rho}_g \alpha_g u_g \right)_{i-1}^{n+1} y_{k,i-1}^n \right] - \\
& \frac{\Delta t}{V_b^n} A_i^n \left[\left(\hat{\rho}_o \alpha_o u_o \right)_i^{n+1} x_{k,i}^n + \left(\hat{\rho}_g \alpha_g u_g \right)_i^{n+1} y_{k,i}^n \right] + \\
& \Delta t \left[\dot{\hat{\psi}}_{ok,i}^{n+1} + \dot{\hat{\psi}}_{gk,i}^{n+1} + \dot{\hat{\Upsilon}}_{a,i}^{n+1} - \dot{\hat{m}}_{da,i}^{n} \right].
\end{aligned}
\tag{8.5}
$$

Once we obtain $N_{k,i}^{n+1}$ (mole of component *k* per bulk volume), we update the overall mole composition of hydrocarbon phases in gridblock *i,* and then perform flash calculation to update the concentration of wax or asphaltene at the new time-step.

In Equation (8.5), the solid deposition rate $\dot{\hat{m}}_{da,i}^{n}$ is used from the old time-step. However, we can update this value after finding the new concentration of wax or asphaltene. We can also reiterate the solution of solid deposition with new deposition rate and solid concentrations until convergence is achieved.

For aqueous phase, Equation (8.6) is solved to obtain the fluid main elements and the solids suspension concentrations ($N_{j,i}^{n+1}$):

$$\begin{aligned} N_{j,i}^{n+1} = N_{j,i}^{n} + & \\ & \frac{\Delta t}{V_b^n} A_{i-1}^n \left[\left(\hat{\rho}_w \alpha_w u_w \right)_{i-1}^{n+1} c_{j,i-1}^n \right] - \\ & \frac{\Delta t}{V_b^n} A_{i}^n \left[\left(\hat{\rho}_w \alpha_w u_w \right)_{i}^{n+1} c_{j,i}^n \right] + \\ & \Delta t \left[\dot{\hat{\psi}}_{wj,i}^{n+1} + \dot{\hat{\Upsilon}}_{s,i}^{n+1} - \dot{\hat{m}}_{ds,i}^{n} \right], \qquad j = 1, \ldots, n_{aq} + n_{sld} . \end{aligned} \tag{8.6}$$

Using the PHREEQC (Parkhurst and Appelo, 2013) module and the new concentrations, again we can update the concentration of the fluid species and the solid in the gridblock *i*.

Another concern in the flow assurance problems is related to the evolution of the particles deposition in the flow path. In fact, when the solid deposition starts at some point in the flow line, it also begins to block the flow path until complete clogging of the wellbore.

Blockage of the flow path causes shrinkage in cross-sectional area and production loss in the wellbore. Depending on the solid deposited volume, the cross- sectional area at new time steps is calculated as

$$A_i^{n+1} = A_i^n - \frac{V_{s,i}^n}{\Delta x_i} . \tag{8.7}$$

Thus, using Equation (8.7), we can follow the progress of solid deposition in each wellbore gridblock. When the cross-sectional area reaches to a point where the wellbore flow starts to decline steeply, a remediation job should be started.

8.3 SIMULATIONS RESULTS IN STAND-ALONE WELLBORE MODEL

In the following sections, we describe the multiphase flow simulations in vertical wells and in a horizontal pipeline to illustrate the implementation of different flow assurance scenarios. The examples show how asphaltene can be generated in the wellbore and be evolved along the well at different conditions, how wax is formed in the horizontal pipelines at low temperatures, and how the geochemical scale reaction with transportation can be coupled in the wells.

Appendices E.2 through E.4 show the sample input data for asphaltene, wax and geochemical scale deposition simulations.

8.4 ASPHALTENE DEPOSITION

We considered three simulation examples in this part. First, we perform simulation of asphaltene deposition in the wellbore with fluid Sample 1. In this case, we reach the bubble point pressure of the fluid in the middle of the wellbore and have concurrent flow of gas and liquid, plus asphaltene deposition. Second, we investigate the effect of CO_2 on asphaltene deposition in fluid Sample 1. This simulation can illustrate the effect of CO_2 on asphaltene deposition in the production well, after breakthrough of CO_2 in enhanced oil recovery.

Finally, we perform similar simulations for fluid Sample 2 which is oil heavier than sample one and does not evaporate gas in the well.

8.4.1 Asphaltene Deposition Case Study with Fluid Sample 1

Table 8.1 shows the input parameters for this case. Tables 8.2 and 8.3 show the composition of the fluid Sample 1, and the characterization of the fluid that are used for our simulation study. The onset pressure and temperature data for the sample fluid one are plotted with the vapor / liquid equilibrium line in Figure 8.1. Since we need to tune the onset pressures and temperatures of asphaltene precipitation in our model, we used those values as input data in our simulation.

In this case study, we have an 8000 ft well which is in primary production stage. This well is in a reservoir with initial pressure of 5200 psi and operates with 1800 psi at wellhead. We will perform multiphase flow simulation for this well to analyze its performance for flow assurance issues. From Figures 8.2 and 8.3, we already know that this well can be subjected to the asphaltene flow assurance problem. PVT analysis can qualitatively show whether the asphaltene precipitation can occur or not. We solve the steady-state solution of the well at initial time, and map it on the vapor/liquid equilibrium and asphaltene onset curve shown in Figure 8.3. As we can see, the pressure-temperature (P-T) path at initial condition (the blue dash line) moves from the asphaltene stable zone to the asphaltene unstable zone and also to the two-phase region zone. Hence, with this analysis, we understand that our well can potentially have asphaltene precipitation.

We proceed with the simulations for predicting the asphaltene deposition rate and quantifying the amount of asphaltene precipitation in the well. Figure 8.4 shows the asphaltene precipitation versus pressure for different temperatures. Since temperature changes drastically in the wellbore, we can expect more asphaltene precipitation in the upper part of the well, where the temperature of the wellbore is lower. As Figure 8.2 shows that the maximum asphaltene precipitation occurs around the bubble point pressure, where the solubility of asphaltene is minimum. As a matter of fact, once gas is relieved from the crude oil, asphaltene components become more stable and more soluble in the oil.

Performing the simulation runs for the wellbore, we can obtain the magnitude of asphaltene deposition and the rate of deposition in the wellbore. Asphaltene deposition in the wellbore changes the wellbore cross-sectional area.

Figure 8.4 shows the profiles of inner radius of the well versus time. As can be seen, the wellbore cross-section starts to shrink from the depth of 6650 ft, all the way to the surface, and reaches the minimum diameter at 2777 ft. The surface of the precipitated asphaltene has small dents due to removal of asphaltene by shear forces. Figure 8.5 shows the profiles of asphaltene flocculates in the wellbore. As we can observe, the concentration of asphaltene reaches the maximum value at 2777 ft. This behavior justifies the maximum deposition at that point.

Accumulation of asphaltene particles in the wellbore can consequently change the pressure, temperature, and velocity fields profiles in the wellbore. Accordingly, it also influences the amount of fluid influx from the reservoir. Asphaltene deposition pressurizes the bottom-hole due to blockage of the wellbore and increment of friction forces between the surfaces of deposited asphaltene and the moving fluid. Consequently, asphaltene deposition reduces the influx from reservoir to the wellbore. Figures 8.6 through 8.9 show the pressure, temperature, oil velocity, and liquid velocity profiles at different times.

Due to asphaltene deposition, velocity fields are drastically changed around the largest deposited area in the wellbore. Velocity change can additionally affect the heat exchange rate between the wellbore fluid and the surrounding. Figure 8.6 shows the temperature of the fluid in the wellbore, which also decreases with progression of time.

Changes in the fluid temperature contradictorily increase the asphaltene precipitation and decrease the asphaltene sticking probability on the well surface.

Moreover, Figure 8.10 shows the variation of pressure at bottom-hole with time. Asphaltene particle blockage in the wellbore increases the pressure of bottom-hole with time elapsed. As a consequence, Figure 8.11 shows that the flow rate of fluid decreases with time due to less fluid influx from the reservoir.

8.4.2 Effect of CO_2 on Asphaltene Deposition

Applications of CO_2 and light hydrocarbon gas injections for enhanced oil recovery process have introduced additional flow assurance issues into the reservoirs and the wellbores (Tuttle, 1983). In several conventional oil fields in the Middle East, asphaltene deposition has been reported as the most problematic issue during the CO_2 flooding process.

In this section, we will simulate the effect of CO_2 on asphaltene precipitation and deposition in the wellbore. In fact, this simulation aims to capture the condition when CO_2 breakthroughs in the production well and mixes with the crude oil.

Vargas (2009) showed that existence of light components or contaminations in crude oil changes the phase behavior of oil drastically. He showed asphaltene becomes more unstable when natural gas or CO_2 is mixed with oil. Figure 8.12 shows his results for the effect of Methane, Nitrogen, and Carbon Dioxide on the P-T phase envelope of crude oil. As we can see, the presence of light components can increase the bubble point pressure and the onset pressure of asphaltene in the crude oil. Vargas (2009) used PC-SAFT EOS to describe the effect of light components on asphaltene phase behavior.

Since in our asphaltene precipitation modeling approach we do not rigorously include the effect of composition on the asphaltene onset pressure, we define those pressures for different temperatures as input variables. In fact, since the cubic Equation-of-State is tuned (for the binary interaction coefficients) to only one set of compositions for the asphaltene precipitation, it might not be correct for the whole range of compositions. However, using experimental values for asphaltene onset pressure can reduce tuning errors for asphaltene precipitation models.

Table 8.4 illustrates the onset pressure of our synthetic fluid (Sample 1) for different molar ratios of CO_2 and oil mixture. The composition of oil after mixing with CO_2 has been shown in Table 8.5. The input onset pressures follow a similar trend as Figure 8.12 (c). With the new compositions of the oil and the input onset pressures of asphaltene, the amount of asphaltene precipitation can be calculated from our asphaltene precipitation module. Figure 8.13 shows the amount of asphaltene precipitation for different molar ratios of CO_2 at 212 ^{o}F. The higher the content of CO_2 the larger asphaltene precipitation is obtained.

We performed multiphase flow simulations in the wellbore for 90 days with the presence of considerable amount of CO_2 in the reservoir fluid. We employed similar input data in Section 8.5.1 for the wellbore and reservoir geometries. Figure 8.14 shows the asphaltene concentration profiles for different compositions of the reservoir oil at the end of 90 days. As we can see, asphaltene concentration is zero in the vicinity of the perforations. Asphaltene starts to flash out from crude oil when pressure and temperature are reduced in the upper parts of the wellbore. Comparing the asphaltene concentration profiles for different compositions of CO_2 in Figure 8.14, we observe that the existence of larger amount of CO_2 lowers the starting point of asphaltene precipitation in the wellbore. Hence, in the cases where more CO_2 reaches the production well, more asphaltene is generated in the bottom of the well. Similarly, we compared the effect of CO_2 on the pressure, temperature, and gas volume fraction profiles in Figures 8.15 through 8.17. CO_2

can indirectly change the pressure and temperature profiles by changing the velocity fields in the wellbore. In addition, the flow regime change can also change the gas volume fraction along the wellbore. As Figure 8.17 shows increment of CO_2 percent in the fluid mixture generally increases the gas volume fraction in the upper part of the wellbore. However, the flow regime change in higher percent of CO_2 can also affect the gas volume fraction change in the wellbore.

Finally, we show the propagation of asphaltene deposition on the surface of the wellbore in Figure 8.18. In the presence of CO_2 wellbore can be plugged several times faster than without CO_2. In addition, the presence of CO_2 lowers the maximum plugged cross-section more toward the bottom of the well.

8.4.3 Asphaltene Deposition Case Study with Fluid Sample 2

In this section, we design another case that studies asphaltene deposition in the wellbore in the absence of gas. Fluid Sample 2 was designed to show the effect of fluid type on the propagation of asphaltene on the surface of the wellbore. In contrast to fluid Sample 1, fluid Sample 2 does not evaporate gas in the wellbore. This fluid is heavier than the previous fluid. Tables 8.6 and 8.7 show the fluid characterization and the compositions, respectively. In comparison to fluid Sample 1, this fluid generates more asphaltene at different temperatures as shown in Figure 8.19. In addition, since the bubble point pressure of this fluid is very low, the trends of asphaltene precipitation curves are different from that of fluid Sample 1.

We set the simulation input parameters of the wellbore and the reservoir, and the operation condition of the well is given in Table 8.8. We perform the simulation for 90 days. Figure 8.20 shows the asphaltene flocculates and the transport coefficient profiles at the end of simulation time. Since the precipitation of asphaltene starts from the bottom of the well, asphaltene deposition covers all the parts in the well. However, since the transport coefficient decreases in the upper part of the well, the deposition rate is smaller in that part. Thus, as Figure 8.21 shows, the asphaltene particles are accumulated in the bottom-hole.

8.5 WAX DEPOSITION

A horizontal pipeline with 1000 ft length as given in Table 8.9 is considered for the simulation of wax deposition. In this case, we inject 0.2335 ft^3/sec oil to the pipeline and maintain the outlet pressure at 1000 psi. We perform the simulation for 10 days to see how wax is generated and deposited in the pipeline.

Table 8.10 shows the injected fluid composition and the properties of the oil mixture components. Using the wax phase behavior module in UTWELL, the calculated Wax Appearance Temperature for this fluid is shown in Figure 8.22. As we can see, wax is formed at very low temperatures in comparison to asphaltene.

Figures 8.23 through 8.25 show the wax deposition thickness, pressure and temperature profile variations in the pipeline. The graphs show that wax is mostly accumulated in the outlet of the pipeline where the temperature is the lowest. In fact, the injected fluid has more time to exchange heat when it reaches the outlet. Recalling from Chapter 7, wax deposition mechanism is highly dependent on the temperature gradient.

8.6 SCALE DEPOSITION

Simulation of scale deposition is considered in the wellbore by coupling multiphase flow calculations in UTWELL and geochemical reactions calculations in

PHREEQC (Parkhurst and Appelo, 2013). Scale is usually formed when two incompatible aqueous phases are mixed or when an ionic reaction happens in the reservoir. In such situations, geochemical scales can flocculate from reservoir and entrain to the wellbore. Like other solid particles, geochemical solid scales can generate a cluster of solids which can deposit in a similar mechanism on the surface of the wellbore.

In this section, we considered a 5000 ft well to simulate scale deposition in the wellbore. We assume that our well produces water and oil with the productivity indices shown in Table 8.11. Other pertinent data also have been shown in Table 8.11. We also presume that the aqueous phase contains 0.1 mole/kg of Anhydrite solid, and 0.1 mole/kg of non-reacted sulfate and calcium ions.

Figure 8.26 shows the transport coefficient and scale flocculate concentration profiles after 90 days. Figure 8.27 shows the scale deposition thickness in the wellbore with elapsed time. As can be seen, from bottom of the well to the top, scale is mostly deposited in the bottom of the well. In contrast to asphaltene and wax depositions, geochemical scale is mostly deposited in the bottom of the well, where the concentration and the transport coefficients are the largest.

Table 8.1 Input parameters for simulation of asphaltene deposition in the wellbore with fluid Sample 1

Well Data		**Reservoir and Fluid Data**	
Well MD	8000 ft	Net pay zone	200 ft
Well TVD	8000 ft	Reservoir pressure	5200 psi
Max grid size	50.0 ft	Reservoir temperature	212 °F
Ambient temperature at top	60 °F		
Ambient temperature at bottom	212 °F		
Total heat transfer coefficient	1.0 Btu/ft^2-hr-°F		
Tubing ID	0.229 ft		
Oil productivity index	0.2 ft^3/psi-ft-day		
Water productivity index	0.0 ft^3/psi-ft-day		
Gas productivity index	0.0 ft^3/psi-ft-day		
Wellhead pressure	1800 psi		

Table 8.2 Fluid characterization and composition for fluid Sample 1

Component	**Pc (psi)**	**Tc (R)**	**VC (ft^3/lbmol)**	**Mw (lb/lbmol)**	**Acentric Factor**	**Parachor**	**Volume Shift**	**Primary Composition**
CO_2	1070.09	547.56	1.5071	44.01	0.225	168.17	0	0.0246
C1-C2	668.51	360.61	1.6431	17.417	0.015127	92.19	0	0.4041
C3-C5	573.15	732.89	3.8098	53.516	0.179313	195.33	0	0.0755
C6-C19	291.41	1135.31	13.7197	164.423	0.655007	512.21	0	0.2719
C20-C30	175.41	1419.29	29.033	340.927	1.064023	1016.51	0	0.1064
C31+	143.17	1682.93	56.5489	665.624	1.371778	1944.21	0	0.0774
Asphaltene	143.17	1682.93	56.5489	665.624	1.371778	1944.21	0	0.0401

Table 8.4 Asphaltene onset pressure and temperature for different mixing ratio of CO_2

Onset Temperature (^oF)	**0% CO_2**	**5% CO_2**	**10% CO_2**	**15% CO_2**
212	4600	4770	4930	5100
200	5045	5165	5285	5400
190	5450	5545	5640	5735
180	5960	6000	6045	6085
170	6660	6625	6590	6560
160	7580	7445	7310	7170
150	8650	8430	8210	7995
145	9545	9175	8810	8440

Table 8.3 Binary interaction coefficients used for modeling fluid Sample 1

	CO_2	**C1-C2**	**C3-C5**	**C6-C19**	**C20-C30**	**C31+**	**Asphaltene**
CO_2	0						
C1-C2	0.0001	0					
C3-C5	0.0068	0.0056	0				
C6-C19	0.0375	0.0347	0.013	0			
C20-C30	0.0651	0.0616	0.0319	0.0045	0		
C31+	0.0945	0.0905	0.0548	0.0158	0.0035	0	
Asphaltene	0.22	0.22	0.22	0	0	0	0

Table 8.5 Reservoir fluid composition for different mixing ratio of CO_2

Component	0% CO_2	5% CO_2	10% CO_2	15% CO_2
CO_2	0.0246	0.07337	0.12214	0.17091
C1-C2	0.4041	0.383895	0.36369	0.343485
C3-C5	0.0755	0.071725	0.06795	0.064175
C6-C19	0.2719	0.258305	0.24471	0.231115
C20-C30	0.1064	0.10108	0.09576	0.09044
C31+	0.0774	0.07353	0.06966	0.06579
Asphaltene	0.0401	0.038095	0.03609	0.034085

Table 8.6 Fluid characterization and composition for fluid Sample 2

Component	Pc (psi)	Tc (R)	VC (ft^3/lbmol)	Mw (lb/lbmol)	Acentric Factor	Parachor	Volume Shift	Primary Composition
N2-C1	640.75	324.04	1.56	17.93	0.01	71.32	0	0.0000321
CO_2	1069.87	547.56	1.51	44.01	0.23	78	0	0.0000409
C2-C3	647.74	630.39	2.94	39.45	0.13	136.05	0	0.0175432
IC4-NC5	519.73	796.06	4.46	64.55	0.21	206.67	0	0.1114261
C6-C9	405.61	1067.24	7.33	124.49	0.33	337.4	0	0.3627861
C10-C19	274.6	1314.89	12.27	217.81	0.57	604.02	0	0.3516170
C20-C29	191.16	1557.76	18.8	364.18	0.89	1022.21	0	0.1154219
C30+	128.27	1859.46	27.68	622.54	1.26	1760.39	0	0.0411327

Table 8.7 Binary interaction coefficients for modeling fluid Sample 2

	N2-C1	**CO_2**	**C2-C3**	**IC4-NC5**	**C6-C9**	**C10-C19**	**C20-C29**	**C30+**
N2-C1	0							
CO_2	0.13000	0						
C2-C3	0.00776	0.13500	0					
IC4-NC5	0.02109	0.12500	0.00336	0				
C6-C9	0.04493	0.10146	0.01600	0.00477	0			
C10-C19	0.07788	0.10146	0.03853	0.01963	0.00515	0		
C20-C29	0.11049	0.10146	0.06372	0.03907	0.01704	0.00353	0	
C30+	0.15119	0.11335	0.09612	0.06530	0.03542	0.01348	0.00308	0

Table 8.8 Input parameters for simulation of asphaltene deposition in the wellbore with fluid Sample 2

Well Data		**Reservoir and Fluid Data**	
Well MD	8000 ft	Net pay zone	100 ft
Well TVD	8000 ft	Reservoir pressure	5000 psi
Max grid size	50.0 ft	Reservoir temperature	220 ^oF
Ambient temperature at top	60 ^oF		
Ambient temperature at bottom	220 ^oF		
Total heat transfer coefficient	1.0 Btu/ft^2-hr-^oF		
Tubing ID	0.229 ft		
Oil productivity index	0.2 ft^3/psi-ft-day		
Water productivity index	0.0 ft^3/psi-ft-day		
Gas productivity index	0.0 ft^3/psi-ft-day		
Wellhead pressure	2000 psi		

Table 8.9 Input parameters for simulation of wax deposition in a pipeline

Pipe Data	
Well MD	1000 ft
Well TVD	0.0 ft
Max grid size	50.0 ft
Surrounding temperature	40 °F
Total heat transfer coefficient	20.0 Btu/ft^2-hr-°F
Pipe inner diameters	0.229 ft
Oil injection rate	0.2335 ft^3/sec
Outlet pressure	1000 psi

Table 8.10 Fluid characterization and composition for wax crude oil sample

Component	**Pc (psi)**	**Tc (R)**	**VC (ft^3/lbmol)**	**Mw (lb/lbmol)**	**Acentric Factor**	**Primary Composition**
C1	667.1961	343.08	1.60823	16.043	8.00E-03	0.6
C2	708.3447	549.72	2.404223	30.07	9.80E-02	0.1
NC4	551.0981	765.36	4.142411	58.124	0.193	0.05
NC5	489.3751	845.28	4.938403	72.151	0.251	0.05
FC6	477.0305	913.5	5.588193	86	0.27504	0.05
FC14	284.0727	1261.26	11.74495	190	0.604823	0.05
FC17	240.2788	1348.56	14.36036	237	0.72857	0.05
FC33	137.5541	1609.02	24.62704	426	1.143446	0.05

Table 8.11 Input parameters for simulation of scale deposition in the wellbore

Well Data		**Reservoir and Fluid Data**	
Well MD	5000 ft	Net pay zone	150 ft
Well TVD	5000 ft	Reservoir pressure	2500 psi
Max grid size	50.0 ft	Reservoir temperature	180 °F
Ambient temperature at top	60 °F	Oil API gravity	30
Ambient temperature at bottom	180 °F	Oil bubble point pressure	500 psi
Total heat transfer coefficient	1.0 Btu/ft^2-hr-°F	Gas specific gravity	0.55
Tubing ID	0.229 ft	Water specific gravity	1.0
Oil productivity index	0.5 ft^3/psi-ft-day	Gas heat capacity	0.55 Btu/lbm-°F
Water productivity index	0.1 ft^3/psi-ft-day	Oil heat capacity	0.45 Btu/lbm-°F
Gas productivity index	0.0 ft^3/psi-ft-day	Water heat capacity	1.0 Btu/lbm-°F
Wellhead pressure	500 psi	Geochemical scale type	Anhydrite

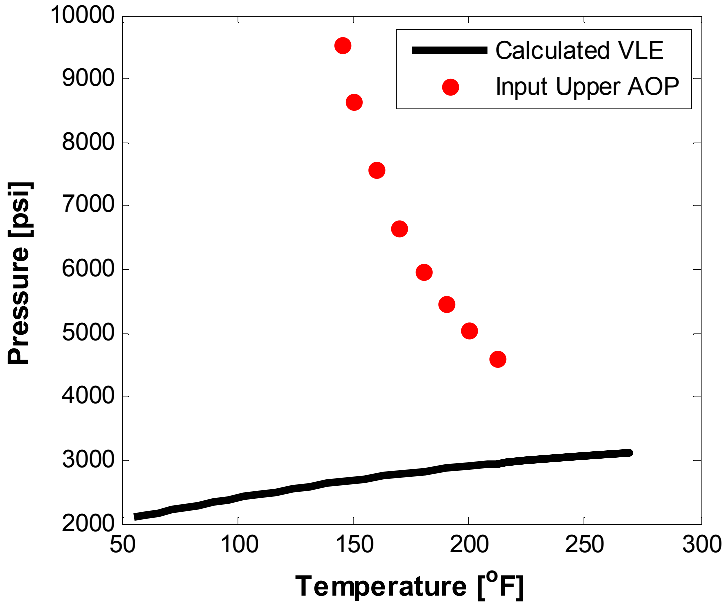

Figure 8.1 Asphaltene vapor / liquid saturation line and asphaltene onset pressure line for fluid Sample 1.

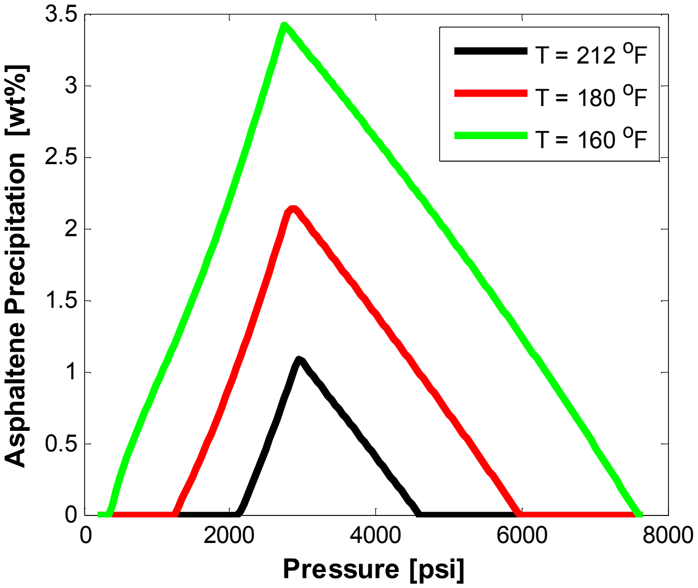

Figure 8.2 Weight percent of asphaltene precipitation as function of pressure in different temperatures.

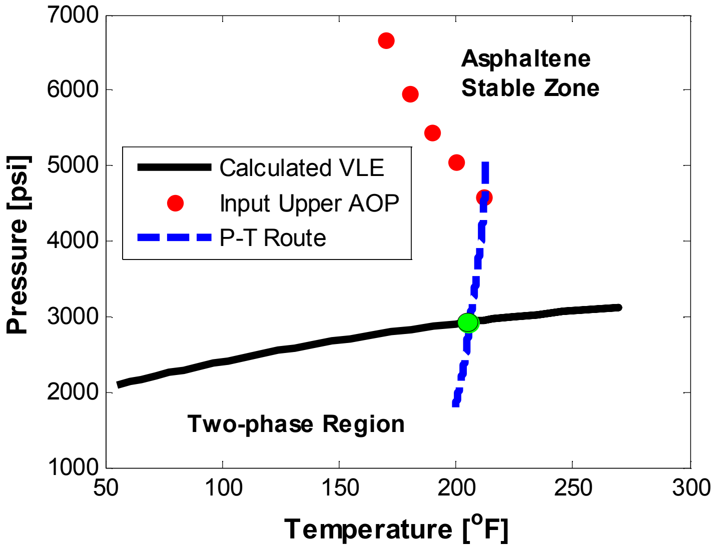

Figure 8.3 Pressure and temperature route from bottom of the well to the surface at time zero (blue dash line), asphaltene onset pressure (red dots) and fluid saturation line (solid line).

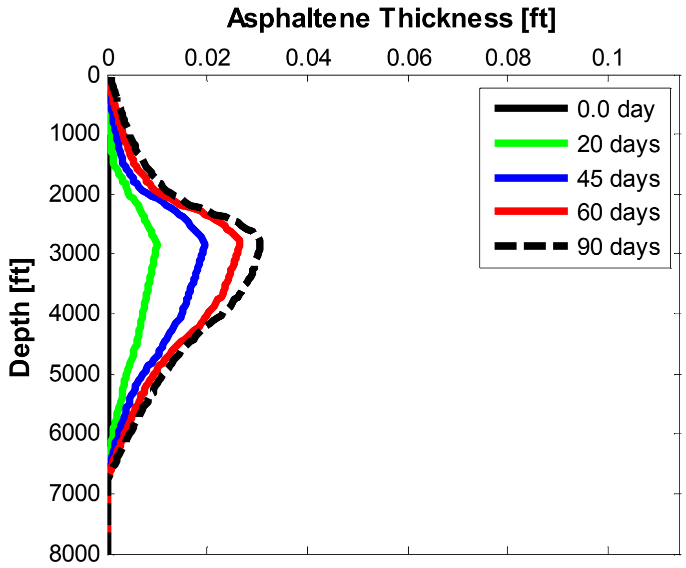

Figure 8.4 Thickness of asphaltene deposit on the inner surface of the wellbore for different times.

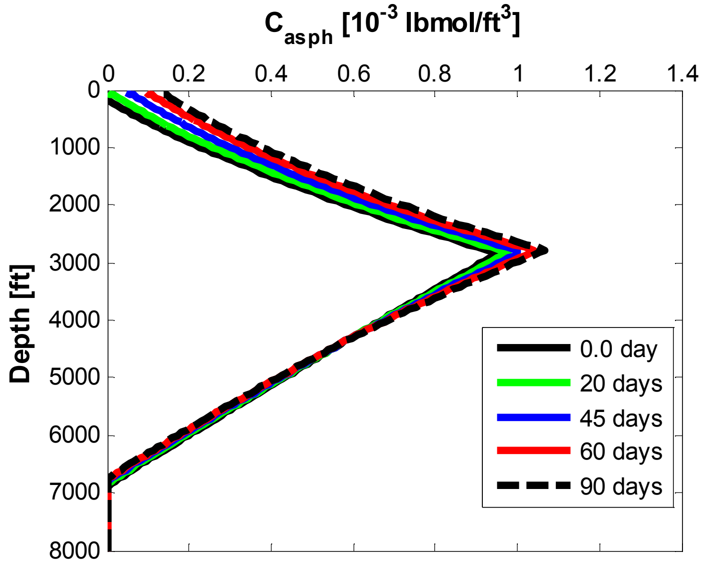

Figure 8.5 Asphaltene flocculate concentration profiles in the wellbore for different times.

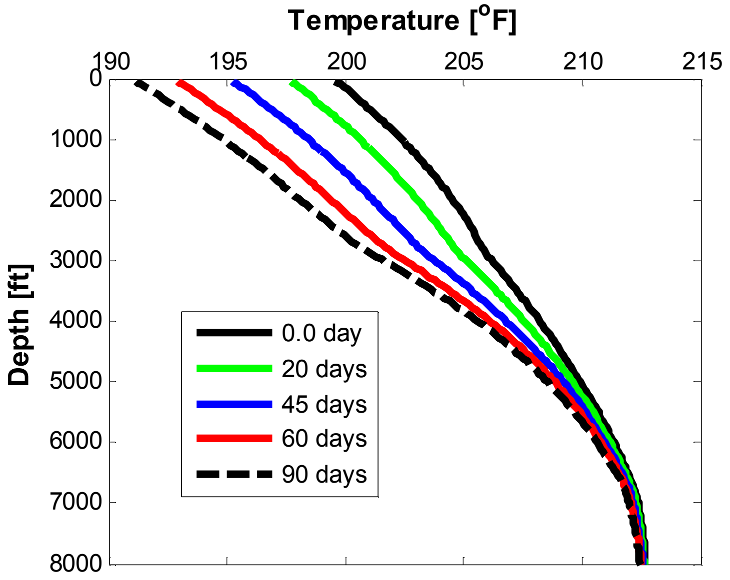

Figure 8.6 Temperature profiles for different times during asphaltene deposition in the wellbore.

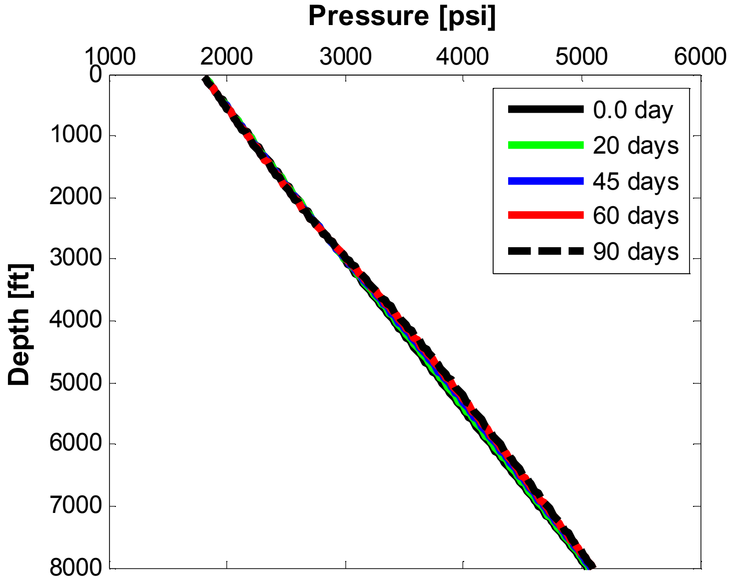

Figure 8.7 Pressure profiles for different times during asphaltene deposition in the wellbore.

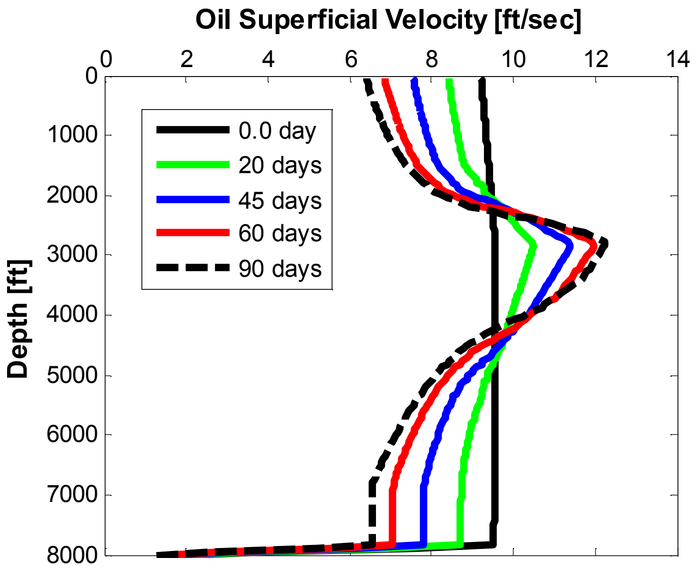

Figure 8.8 Oil superficial velocity profiles for different times in the wellbore during asphaltene deposition in the wellbore.

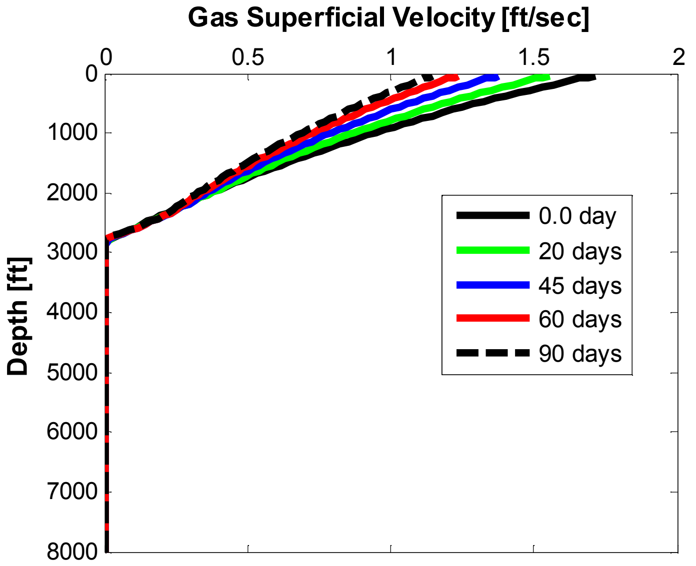

Figure 8.9 Gas superficial velocity profiles for different times in the wellbore during asphaltene deposition in the wellbore.

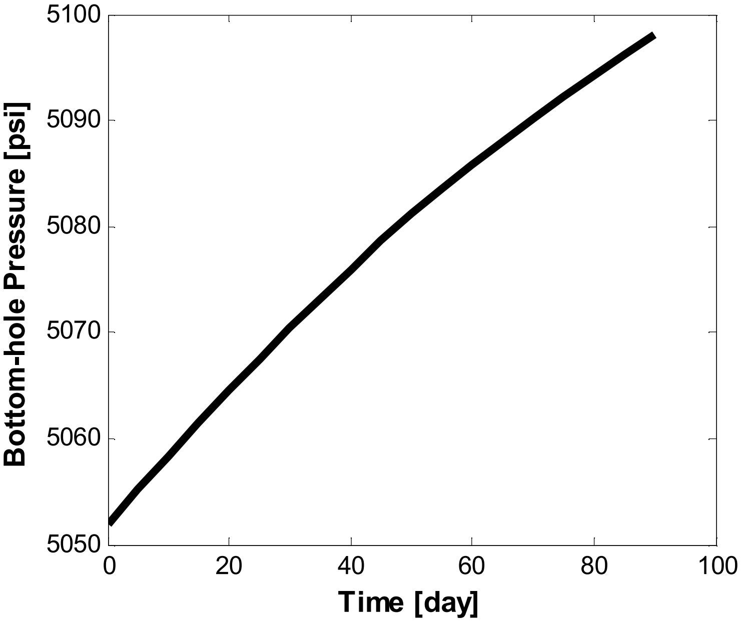

Figure 8.10 Variation of bottom-hole pressure due to asphaltene deposition with time elapsed.

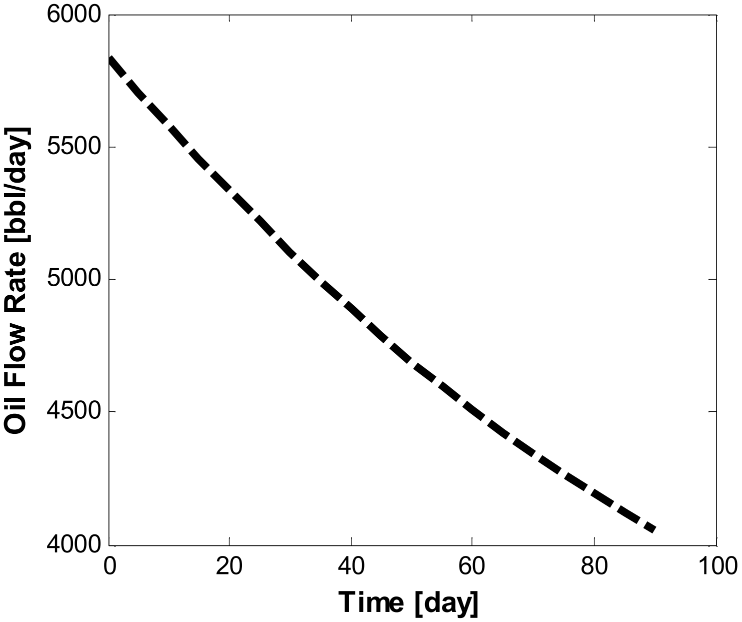

Figure 8.11 Variation of oil flow rate due to asphaltene deposition with time progression.

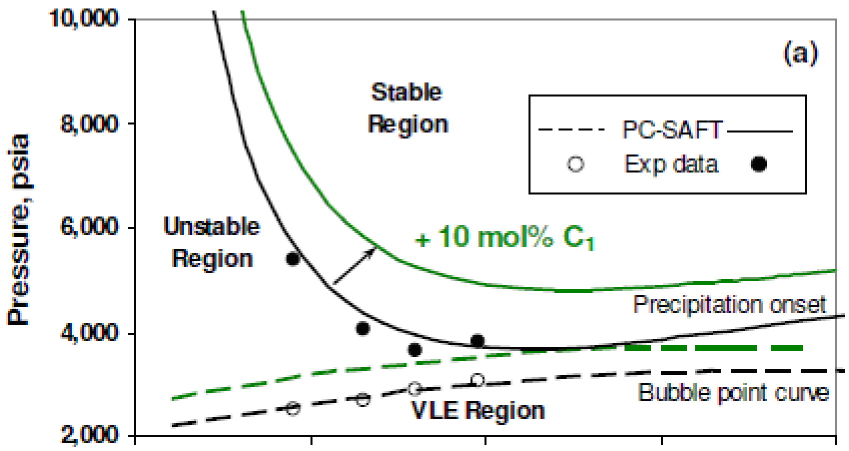
(a)
Pressure, psia
10,000
8,000
6,000
4,000
2,000
Stable Region
Unstable Region
PC-SAFT
Exp data
+ 10 mol% C$_1$
Precipitation onset
Bubble point curve
VLE Region

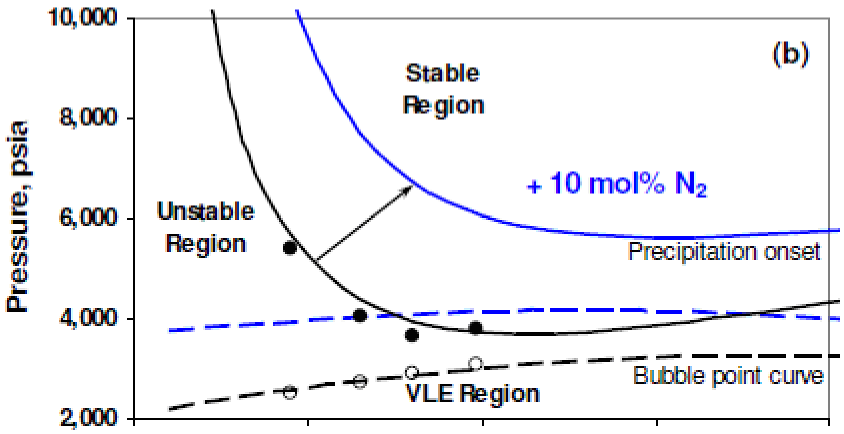
(b)
Pressure, psia
10,000
8,000
6,000
4,000
2,000
Stable Region
Unstable Region
+ 10 mol% N$_2$
Precipitation onset
Bubble point curve
VLE Region

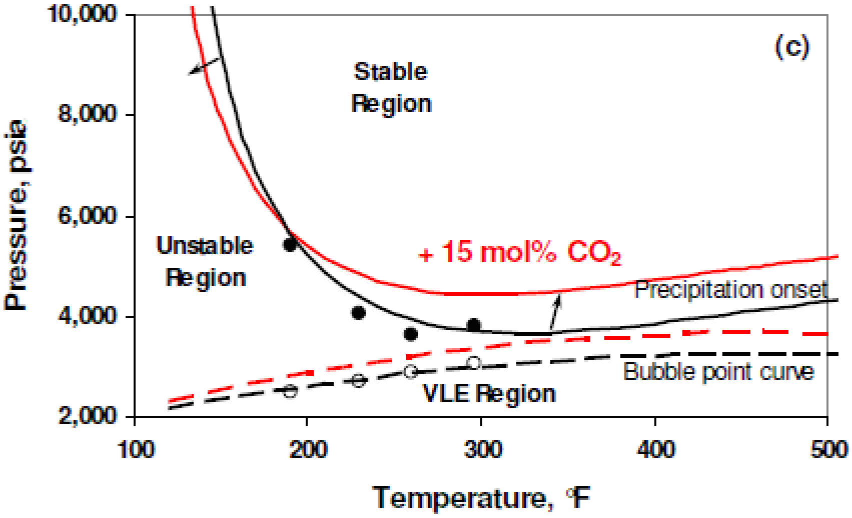

Figure 8.12 Effect of light hydrocarbons mixing on the stability of asphaltene in crude oil. (a) Effect of Methane, (b) effect of Nitrogen (c) effect of CO_2 (from Vargas (2009)).

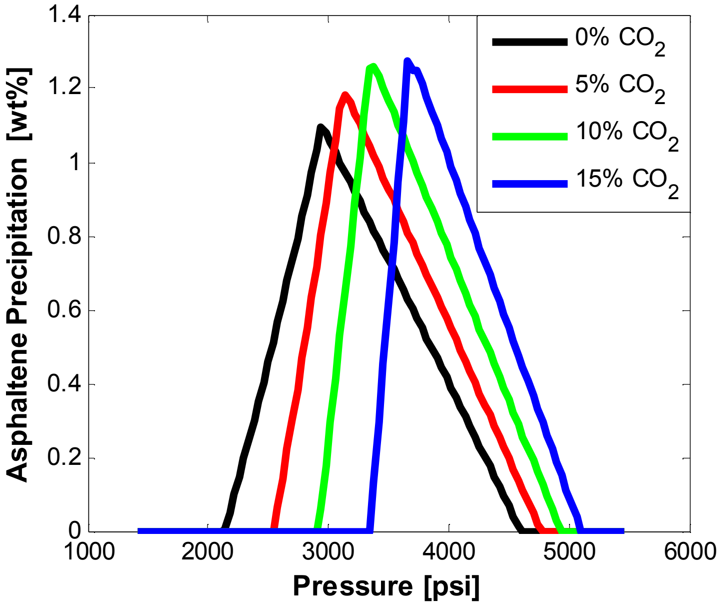

Figure 8.13 Weight percent of asphatlene precipitation in presence of CO_2 with different molar ratios at 212 °F.

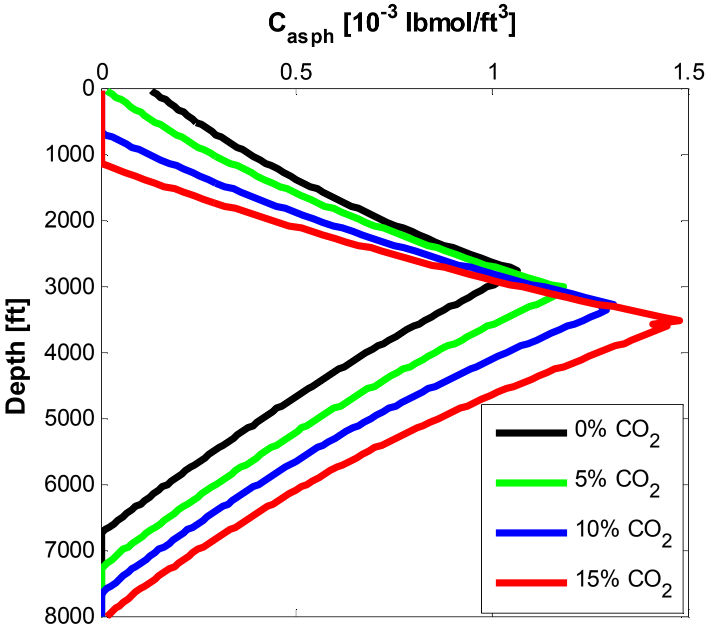

Figure 8.14 Asphaltene concentration profiles at the end of 90 days of production in the wellbore for different fluid compositions.

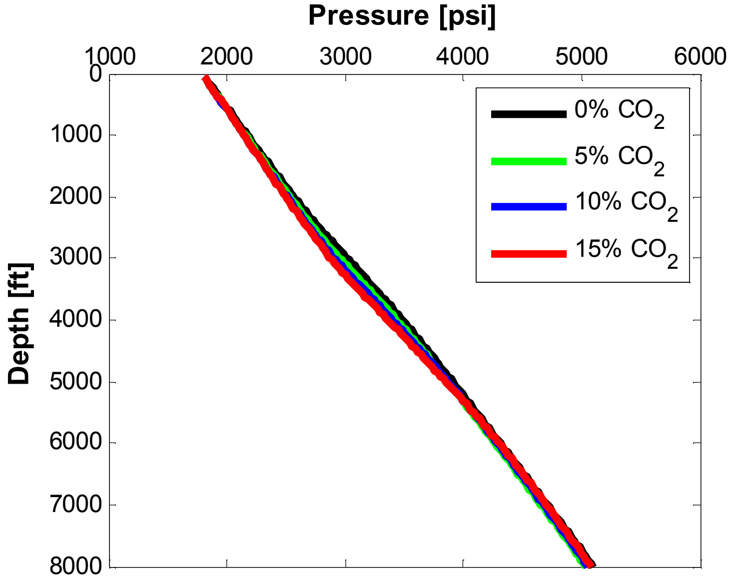

Figure 8.15 Pressure profiles at the end of 90 days of production in the wellbore for different fluid compositions.

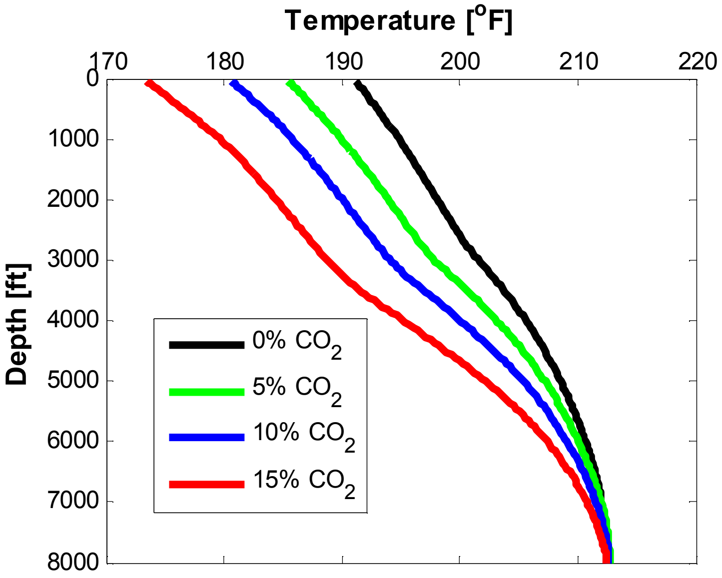

Figure 8.16 Temperature profiles at the end of 90 days of production in the wellbore for different fluid compositions.

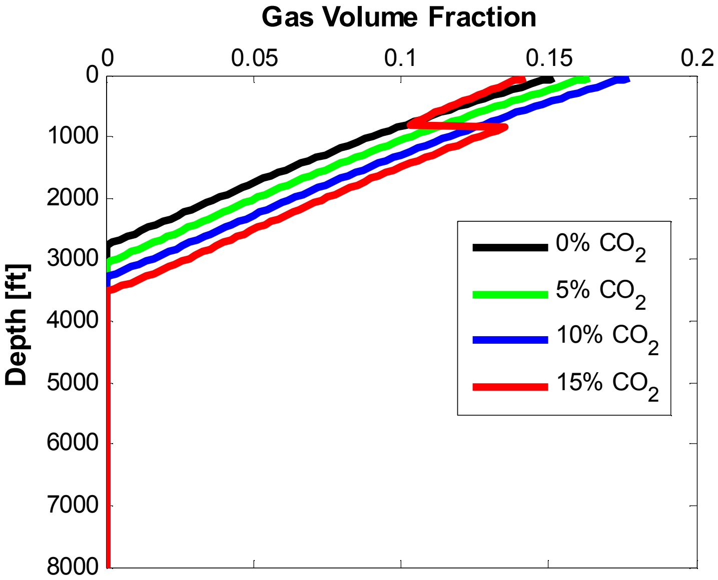

Figure 8.17 Gas volume fraction profiles at the end of 90 days of production in the wellbore for different fluid compositions.

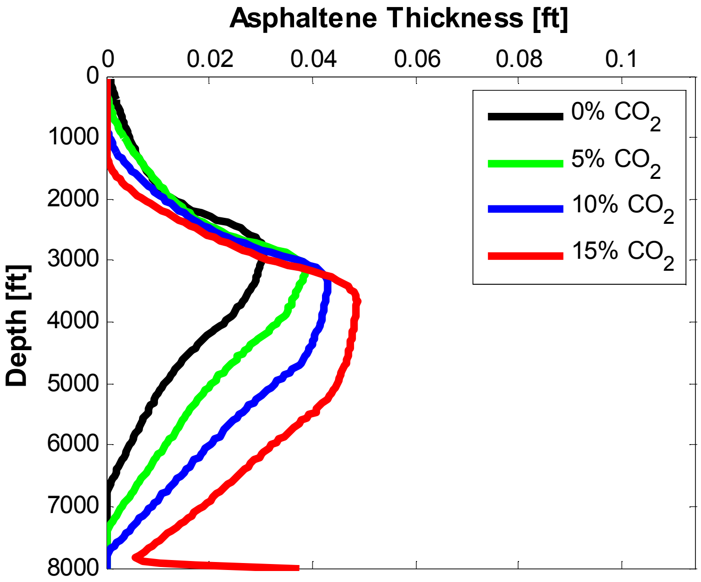

Figure 8.18 Asphaltene deposition thickness profiles at the end of 90 days of production in the wellbore for different fluid compositions.

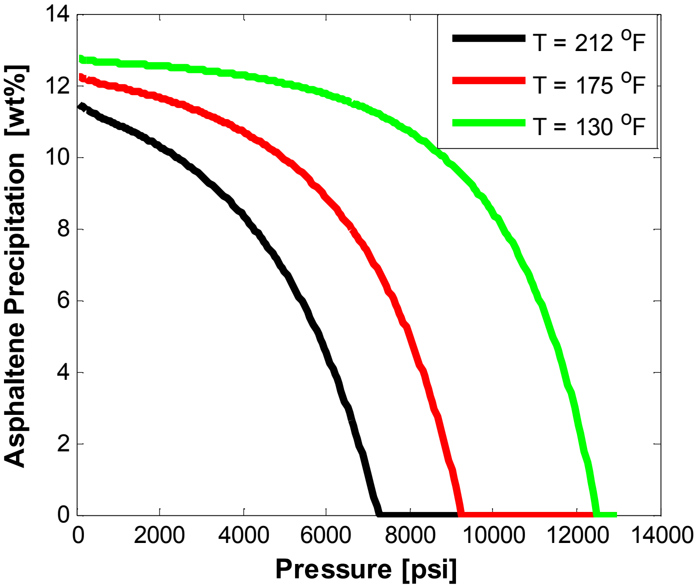

Figure 8.19 Weight percent of asphaltene precipitation as function of pressure at different temperatures.

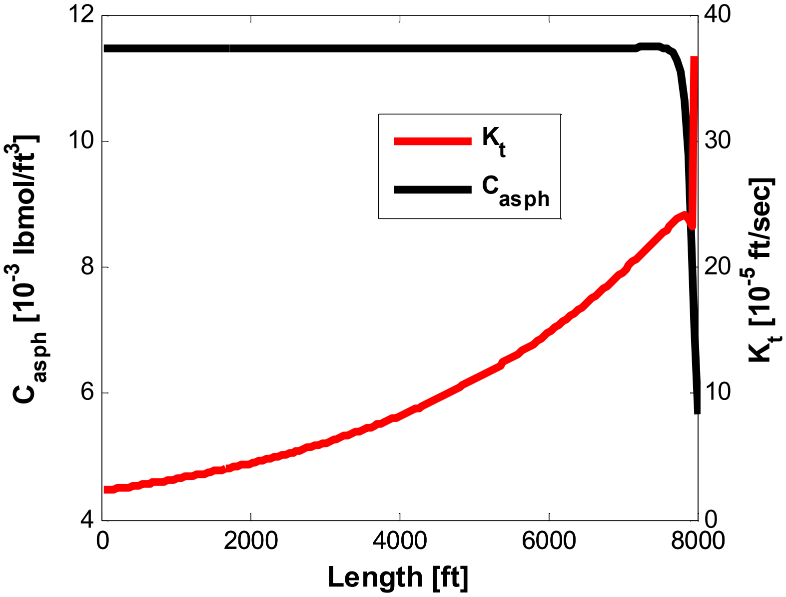

Figure 8.20 Asphaltene flocculate concentration and combined transport coefficient and sticking probability factor (K_t) profiles in the wellbore at the end of simulation time.

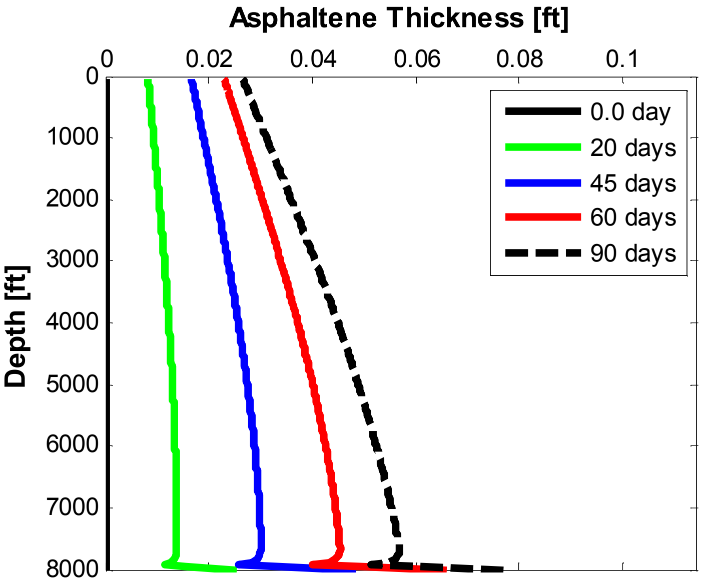

Figure 8.21 Thickness of asphaltene deposit on the inner surface of the wellbore for different times.

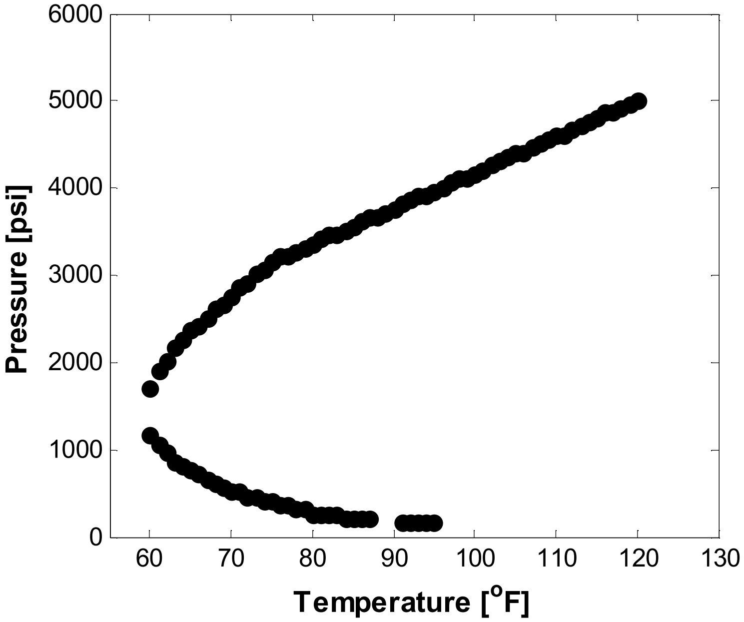

Figure 8.22 Wax appearance temperature (WAT) for different pressures.

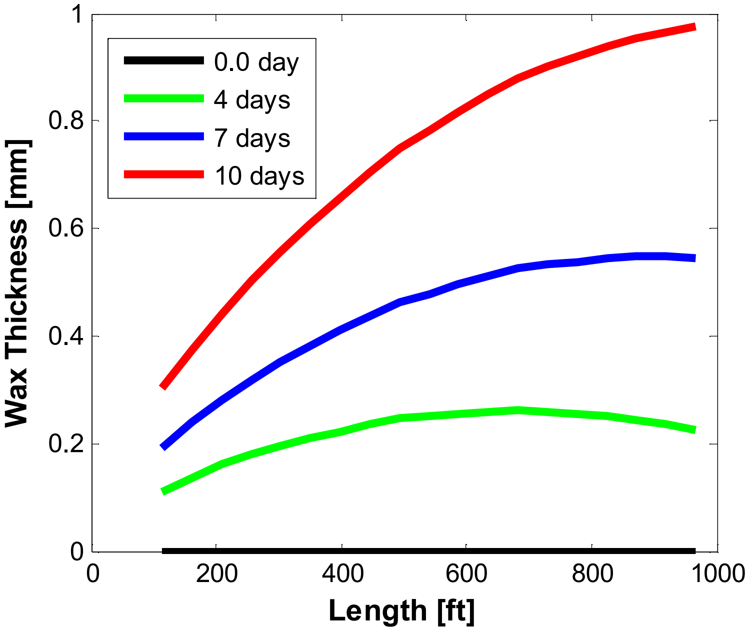

Figure 8.23 Thickness of wax deposit on the inner surface of the pipeline for different times.

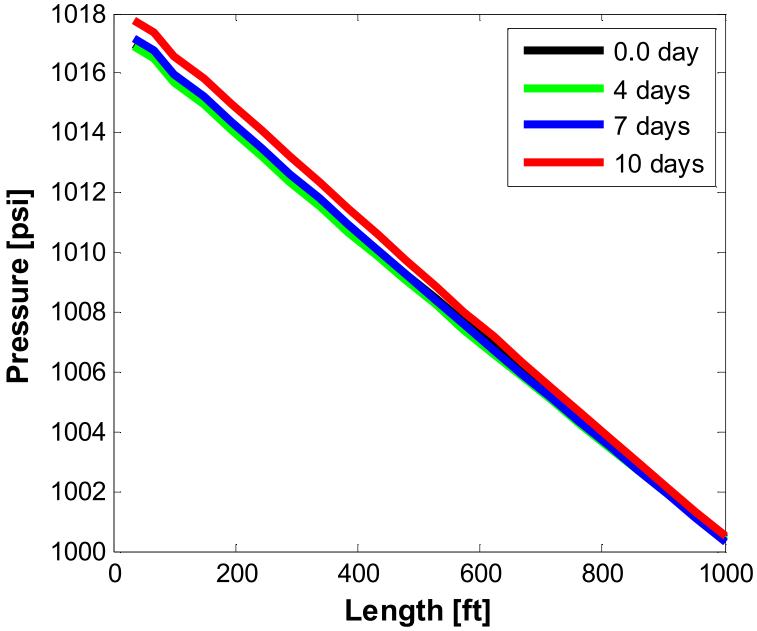

Figure 8.24 Pressure profile in the pipeline for different simulation times.

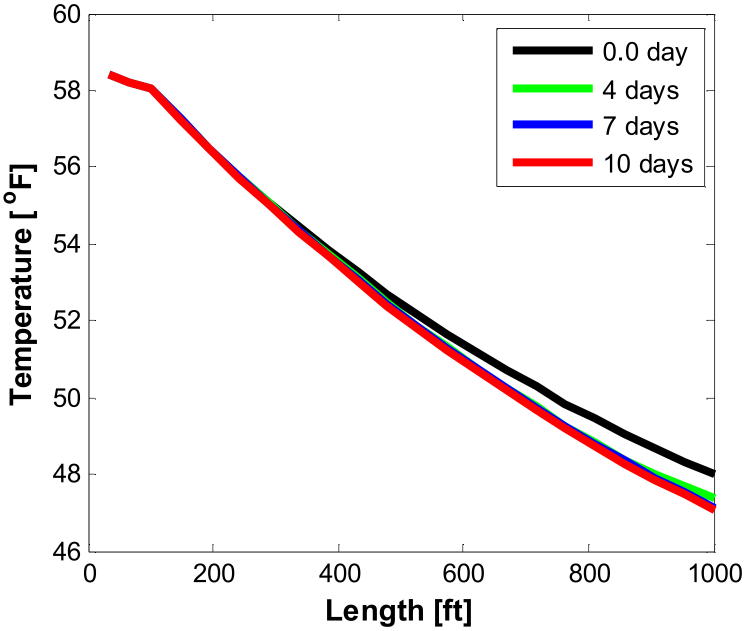

Figure 8.25 Temperature profiles in the pipeline for different simulation times.

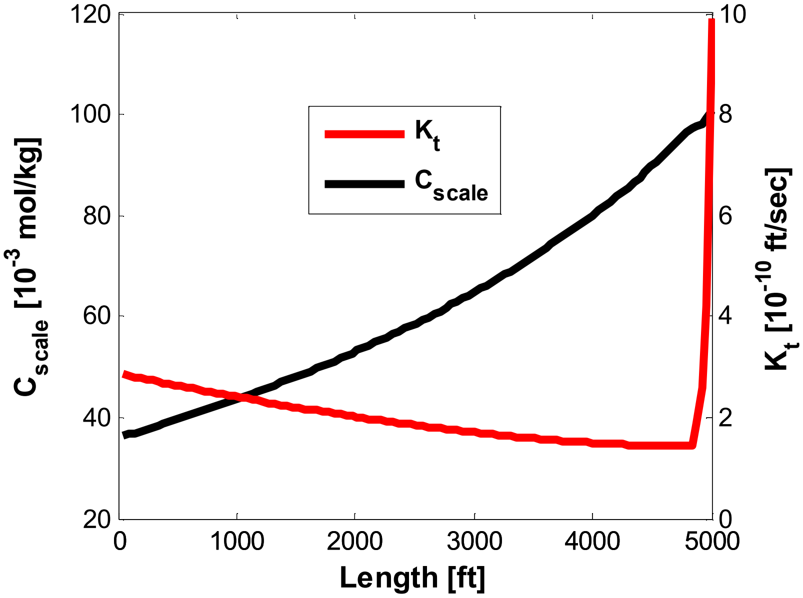

Figure 8.26 Geochemical scales flocculate concentration and combined transport coefficient and sticking probability factor (Kt) profiles in the wellbore at the end of simulation time.

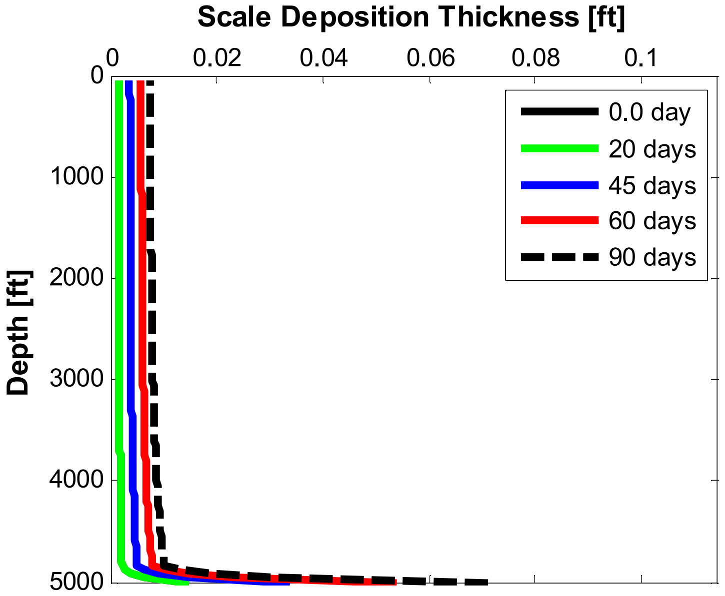

Figure 8.27 Thickness of scale deposit on the inner surface of the wellbore for different times.

Chapter 9: Coupled Wellbore Reservoir Model

In this chapter, we introduce a compositional wellbore model coupled to a compositional reservoir simulator to study the transport phenomena in an entire subsurface system. In previous chapters, we introduced a compositional standalone wellbore model along with flow assurance modules for asphaltene, wax, and geochemical scales.

Since in the reservoir the pressure and temperature do not change significantly, flow assurance problems might not be observed as readily as in a wellbore. However, some field reports have shown that asphaltene deposition and geochemical scales formation can occur at certain conditions in the reservoirs. During miscible gas flooding, such as CO_2 injection for an enhanced oil recovery process, asphaltene precipitation can occur at the reservoir condition. Asphaltene precipitation may plug the pores, change the porosity and the permeability in reservoirs, alter rock wettability and affect all aspects of oil production, processing, and transportation in the reservoir. Incompatible water mixing in the formation, during the secondary recovery, is also believed to be one of the main sources of triggering scale precipitations in the reservoirs. Likewise, geochemical scales can plug the near wellbore regions and reduce the productivity of the wells.

In the following sections, we discuss coupling of UTWELL to UTCOMP (Chang 1990, in house compositional reservoir simulator developed at UT Austin, Appendix A) to solve the wellbore/reservoir model. We also discuss the solution procedures for coupling schemes and present several case studies for asphaltene deposition model in the reservoir and in the wellbore.

9.1 A REVIEW OF COUPLED WELLBORE RESERVOIR MODELS

For a comprehensive reservoir production simulation, the development and application of a coupled wellbore-reservoir simulator is essential. A coupled wellbore-reservoir simulator can be applied to different problems either in the production or in the reservoir engineering areas. For instance, in the well test analysis, wellbore damage simulation (i.e., wellbore plugging by precipitates), well design (i.e., smart wells application), well performance analysis and well control (i.e., kick and blowout situation), a dynamic wellbore-reservoir simulator is required. Several researchers have recently introduced coupled wellbore-reservoir models using different mechanistic approaches. In this section, we review what we consider to be the most important published works.

Stone et al. (1989) presented a fully implicit, blackoil and three-dimensional reservoir simulator coupled to a blackoil and one-dimensional wellbore simulator. They mainly targeted a horizontal well for wellbore-reservoir system in their study. They also used two-fluid model considering different flow regimes for the wellbore model. Stone et al. (1989) solved oil, water and gas mass balance, liquid/gas momentum balance energy equation simultaneously with reservoir equations in their model. They also considered parallel flow in the inner tubing and outer annuli and slant angle effect. Stone et al. (1989) validated their model against field data and showed a good agreement between their model results and field data.

Hasan and Kabir (1996), and Hasan et al. (1997; 1998) presented a blackoil model for single and two-phase flow in wellbores coupled to the reservoir. They applied a hybrid numerical model for the wellbore and an analytical single-phase model for the reservoir. Material balances for each phase, one momentum balance equation for the mixture and energy balance were solved to obtain pressure, velocity, temperature, and fluid density in the wellbore. To calculate the liquid fraction (holdup) at each segment of the wellbore, Hasan et al. (1998) tracked the migration of gas bubbles throughout the wellbore. They used the wellbore-reservoir model for well test analysis application.

Likewise, Fan et al. (2000) developed a semi-analytical wellbore-reservoir simulator in which a single-phase analytical model for the reservoir was coupled to the wellbore. Fan et al. (2000) mainly targeted thermal effects in their study and applied the simulator to a high-temperature gas well pressure buildup test.

Recently, more comprehensive compositional wellbore-reservoir models have been introduced by different researchers. Pourafshary et al. (2009) presented development of a thermal compositional coupled wellbore-reservoir simulator. He performed simulation on producing well with different case studies for crude oil, condensate gas and volatile oil. He demonstrated that the blackoil approach was not accurate for the representation of condensate and volatile oils flow in the wellbore.

Livescu et al. (2009) also developed a fully-coupled thermal compositional wellbore model. Mass conservation for each component, momentum conservation, and energy equation for the mixture of the fluids were solved to obtain pressure, temperature, and holdup profiles in the complete flow line. They used the drift-flux model to consider the slippage between the phases. In their study, different cases for thermal process and different well geometries were presented.

Shirdel (2010) also developed compositional wellbore model for the horizontal, deviated and vertical wells. He showed the effect of pressure and temperature distribution of horizontal wells on the productivity of the well in the reservoir simulators. He also discussed that ignoring the pressure drop in the horizontal wells can cause erroneous results for the production rates at the early stage of production.

9.2 METHODS OF COUPLING WELLBORE TO THE RESERVOIR

In the literature, two different approaches have been introduced for wellbore / reservoir coupling. One method is an iterative explicit coupling, where the wellbore and reservoir systems are solved separately. The other method fully couples the wellbore and reservoir systems.

In the iterative method, the reservoir and wellbore pressure results are iteratively conveyed to each system, along with calculation of productivity indices, to obtain the influx/outflux rates to the wellbore. One of the advantages of the iterative coupling is that the wellbore model can be coupled to any reservoir simulator.

In fully coupled wellbore-reservoir simulations, wellbore and reservoir models are simultaneously solved. Behie et al. (1985) explained a mathematical approach to solve a modified Jacobian matrix in the case where the well crosses multiple blocks of the reservoir grid. They did not present the wellbore model to calculate the perforation pressure. However, they discussed a method to implement a fully coupled wellbore-reservoir system. They claimed that the fully coupled method was more stable than an explicit wellbore pressure coupling.

In our study, since we developed the wellbore model as a standalone simulator, we apply explicit coupling scheme for our wellbore/reservoir model. The flow chart shown in Figure 9.1 shows the subroutines in the main program of UTCOMP (the reservoir simulator) and the inclusion of UTWELL calculations. As can be seen, the communicating parameter between wellbore and the reservoir is the rate for mass influx/out-flux.

In Chapter 3, we defined the influx parameters in mass conservation equations as $\dot{\psi}_{jk}$, which is the component k in phase j mass flux per unit length of the cell. This parameter is calculated as below:

$$\dot{\psi}_{jk} = PI_j \rho_j \frac{Mw_k}{Mw_j} x_{kj} (P_{res} - P). \tag{9.1}$$

PI_j in Equation (9.1) is the productivity index of each phase (water, oil and gas). Appendix A explains the detail of well models and productivity index calculation in UTCOMP. This parameter is obtained from a user specified value in input file in the standalone wellbore model or calculated as follows for coupled wellbore/reservoir model:

$$PI_j = \frac{2\pi \sqrt{k_x k_y} \Delta z}{(0.15802)\left(ln \frac{r_o}{r_w} + S \right)}, \tag{9.2}$$

where, r_o is the equivalent radius of well block which is calculated by either Peaceman (1983) or Babu and Odeh's (1989) models for vertical and horizontal wells, k_x and k_y are the permeability in x and y directions, Δz is the grid block size, r_w is the wellbore size in perforation zone, and S is the skin factor. Asphaltene plugging in the perforation zones, also changes r_w in the productivity index calculation.

Other concerns remaining in explicit coupling of UTWELL to UTCOMP are the time-step sizing and tight coupling for the convergence of both systems. Since the time-step sizes in the transient wellbore models are very small (in order of several seconds) in comparison to the reservoir models, synchronization between these two domains is necessary. For this purpose, an additional criterion is included in the time-step control method of both models to select the minimum time-step sizes of all calculations. Thus, for the coupled transient wellbore model time-step sizes are in the order of several seconds at the beginning of the simulation.

Moreover, for steady-state wellbore model coupling, an iterative solution must be used to march large time-step sizes in the simulation. UTCOMP is an Implicit Pressure and Explicit Concentration (IMPEC) simulator and solves the pressure equation with one iteration. For this reason, convergence issues may occur if the wellbore model is not tightly coupled. In our tight coupling, we perform iterations for pressure solution with the new feeds of wellbore model. In fact, the solution of wellbore model changes the bottom-hole pressure of the well and the amount of influx. Several iterations should be performed until complete convergence is observed for both wellbore and reservoir systems mass influx/outflux. Our experience shows that without tight coupling the reservoir time-steps should be very small to overcome the numerical instabilities. Otherwise, oscillatory results are obtained, which may stop the simulation later. Figure 9.2 shows the comparison of iteratively coupled wellbore model and non-iteratively coupled wellbore model for oil rate. As can be seen, with tight coupling the oscillatory results are diminished.

9.3 COUPLED WELLBORE / RESERVOIR MODEL RESULTS

In this section, we present two case studies to show the simulation of asphaltene deposition in a coupled wellbore / reservoir model. In the first case, we assume a scenario that asphaltene is not formed in the reservoir and it is only precipitated in the wellbore. In the second case, we use a version of UTCOMP that has asphaltene deposition module (Darabi et al., 2012) and assumes asphaltene is deposited in the reservoir and the wellbore.

9.3.1 Asphaltene Deposition Case One

In this case, the fluid composition and reservoir condition are properly chosen to avoid asphaltene precipitation in the reservoir and near-wellbore. Table 9.1 illustrates the configuration of the well and reservoir setup. Fluid composition is similar to the one in Section 8.5.3. For the given fluid type, the asphaltene onset pressure at the reservoir temperature, 220 ^{o}F, is 7250 psi. Hence, we expect the precipitation and deposition of asphaltene to be initiated inside the wellbore, where the pressure and temperature decline below the reservoir condition.

Furthermore, we assume a vertical well with 6000 ft depth which produces at a constant wellhead pressure of 5200 psi (Table 9.1). We keep the wellhead pressure large enough to make sure that reservoir pressure does not go below the onset pressure. We perform the simulation for 100 days and monitor the results in the wellbore. Figure 9.3 shows the pressure and temperature route for different time-steps along the well. As can be seen the bottom-hole pressure of the well is always above the onset pressure line and increases with time and when we go further toward the wellhead, the pressure and temperature decline in a way that fluid invades to asphaltene unstable zone. In most parts of the well, we expect asphaltene deposition in this system. Once asphaltene destabilized in the fluid, it begins to precipitate and aggregate where it can become large enough to diffuse toward the well surface. As discussed previously, the amount of asphaltene particle concentration, the transport coefficient, and sticking factor are the deriving forces for deposition rate in the deposition models. These parameters are non-linearly coupled functions of temperature, velocity, and pressure fields. Hence, we expect non-uniform deposition rate profile in the well from bottom to the top of the well.

Figure 9.4 shows snap shots of the evolution of asphaltene solid deposition in the wellbore in different time-steps. As can be seen, our simulation results can capture how asphaltene is accumulated in the wellbore and build up starting from a particular point in the well. This figure confirms our expectation that at a depth of about 4000 ft we have maximum accumulation of asphaltene. Asphaltene accumulation smoothly reduces in the upper part of the wells where we have less adhesion force and more drag force, which facilitates the asphaltene detachment from the well surface.

Figure 9.5 also shows the oil flow rate in our well versus time. This figure compares the productivity of the well, producing the same fluid if asphaltene was not destabilized (became unstable) and blocked the well. As can be seen, asphaltene blockage has significantly reduced the oil rate and decreased the productivity of the well.

9.3.2 Asphaltene Deposition Case Two

We selected fluid sample similar to Section 8.5.1 for this case. Table 9.2 shows the main parameters of the wellbore and reservoir configuration setup. Appendix E.5 also shows the sample input data for the coupled wellbore reservoir model. In contrast to previous case in Section 9.2.1, we lower the pressure of the wellbore to below the bubble point pressure of the fluid (2900 psi at 212 ^{o}F) and maintain the wellhead pressure at 1000 psi. We perform the simulation for 50 days to monitor the asphaltene deposition and transportation in the wellbore and reservoir.

Figure 9.6 shows the propagation of pressure profile in the reservoir at the early stage of the production. As can be seen, reservoir pressure declines from 5000 psi the initial pressure in the area far from producer to 3116 psi near the well bottom-hole pressure in the producer. Since the pressure in the near-wellbore reaches to the value below asphaltene onset pressure, asphaltene components are stripped out in this area and begin to deposit on the surface of the rock. Figures 9.7 and 9.8 show the concentration of the precipitated asphaltene in the near wellbore and the amount of deposited asphaltene.

Within 50 days of production, about 100 ft of around wellbore area is damaged with asphaltene precipitation. Although in this time period the amount of deposited asphaltene is small but with time progression asphaltene precipitates can accumulate more in these blocks.

Figure 9.9 shows the production rates for oil, water and gas, respectively. The fluid production rates are declined fast due to a low pressure that we assign to the wellhead. Additionally, once the reservoir starts to deplete the fluids, its pressure also decline as shown in Figure 9.10. Due to the average reservoir pressure decline, plus the blockage of the bottom-hole area and the near wellbore zone, the bottom-hole pressure (P_{bh}) increases as shown in Figure 9.11. Bottom-hole pressure reaches to below the bubble-point pressure from the beginning of the production. Hence, we always observe two-phase flow in the wellbore.

The pressure and temperature path in the wellbore (Figure 9.12) shows that asphaltene components can be stabilized in the crude oil with moving to the upper part of the well. When more gas is released from oil, the solubility of oil increases and dissolves the asphaltene components. Figure 9.13 shows the concentration of asphaltene flocculates. As can be seen, above the depth of 3500 ft asphaltene disappears from oil and dissolves back in the oil.

Finally, Figure 9.14 shows the deposition of asphaltene in the wellbore. Since most of the precipitated asphaltene are available in the bottom of the well and the flow rate is the lowest there, asphaltene mostly settles in the bottom of the well. As we discussed earlier, the deposited asphaltene in the perforation zone decrease the productivity index of the well.

Table 9.1 Input parameters for simulation case one of asphaltene deposition in the coupled wellbore/reservoir system

Reservoir dimension	4080ft ×4080ft×4080ft	Fluid composition	N2-C1 = 0.0000321
Gridblocks	51×51×3		CO_2 = 0.0000409
Area	382 acre		C_2-C_3 = 0.0175432
Reservoir initial pressure	8000 psi		IC_4-NC_5 = 0.1114261
Reservoir initial saturation	0.17		C_6-C_9 = 0.3627861
Reservoir temperature	220 °F		C_{10}-C_{19} = 0.3516170
Reservoir permeability	10 md		C_{20}-C_{29} = 0.1154219
Wellbore pressure	5200 psi		C_{30+} = 0.0411327
Wellbore depth	6000 ft		
Wellbore diameter	0.2 ft		
Well roughness	0.0008		

Table 9.2 Input parameters for simulation case two of asphaltene deposition in the coupled wellbore/reservoir system

Reservoir dimension	400ft ×400ft×60ft	Fluid composition	CO_2 = 0.0246
Gridblocks	20×20×3		C_1-C_2 = 0.4041
Area	3.67 acre		C_3-C_5 = 0.0755
Reservoir initial pressure	5000 psi		C_6-C_{19} = 0.2719
Reservoir initial saturation	0.2		C_{20}-C_{30} = 0.1064
Reservoir temperature	220 °F		C_{31+} = 0.0774
Reservoir permeability	500 md		Asphaltene = 0.0401
Wellbore pressure	1000 psi		
Wellbore depth	5000 ft		
Wellbore diameter	0.229 ft		
Well roughness	0.0008		

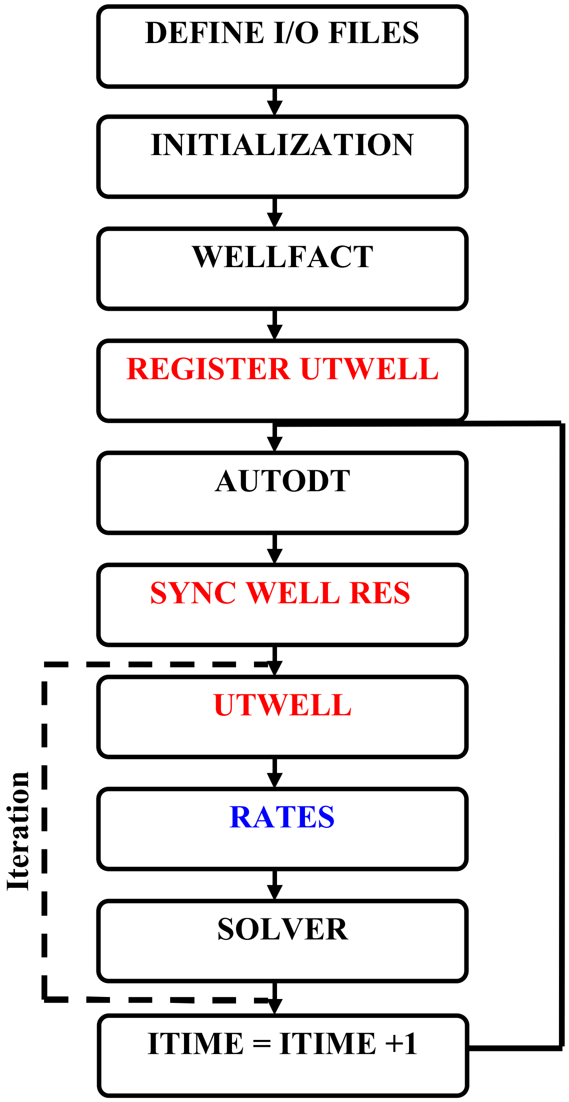

Figure 9.1 The sequence of subroutines in the UTCOMP and inclusion of UTWEL calculation (red boxes). The iteration is used for tight coupling of UTWELL and UTCOMP.

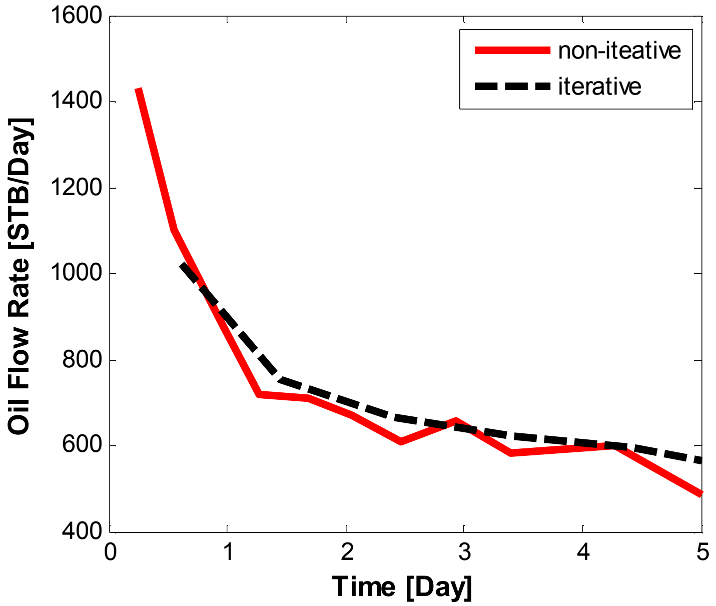

Figure 9.2 Comparison of an example rate solution for iterative and non-iterative coupling approaches in wellbore/reservoir system.

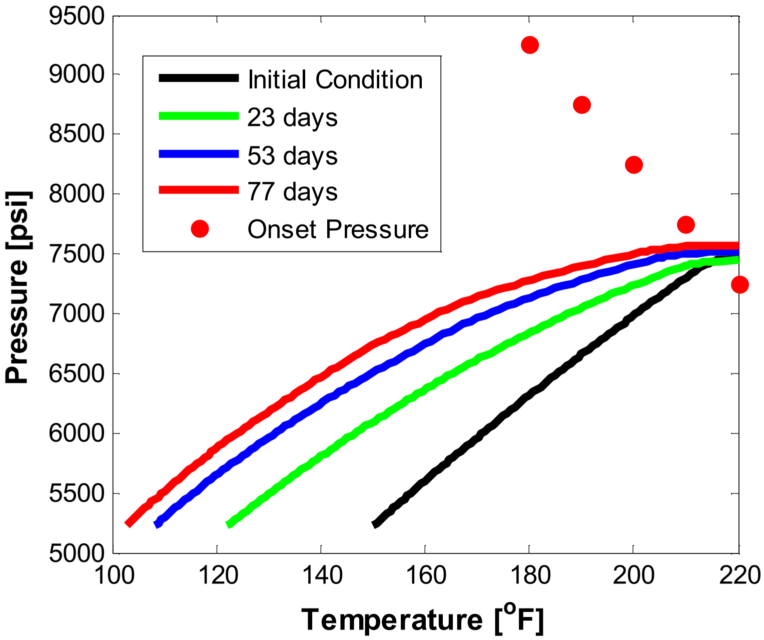

Figure 9.3 Pressure and temperature route in the wellbore for different time-steps.

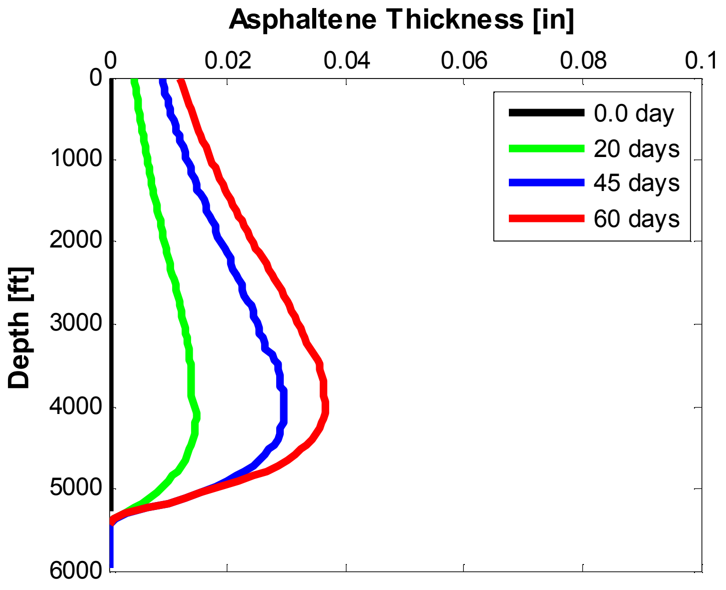

Figure 9.4 Thickness of asphaltene deposit on the inner surface of the wellbore for different times.

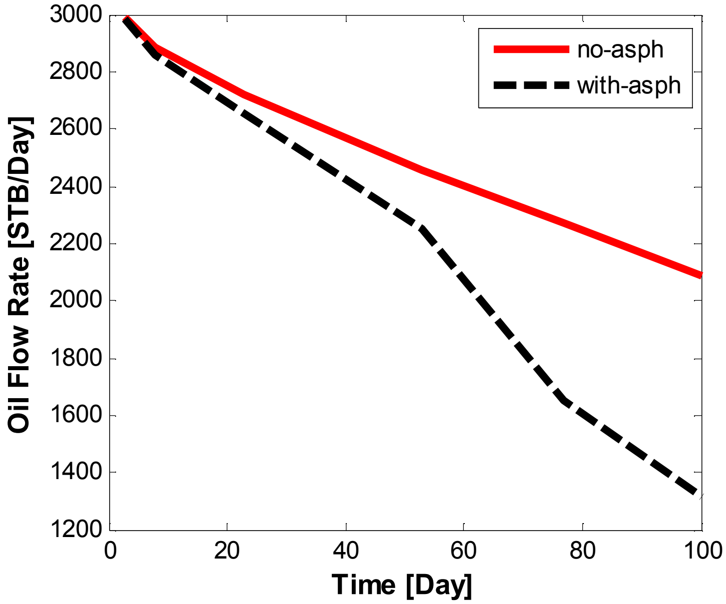

Figure 9.5 Oil flow rate change and effect of asphaltene plugging in the wellbore.

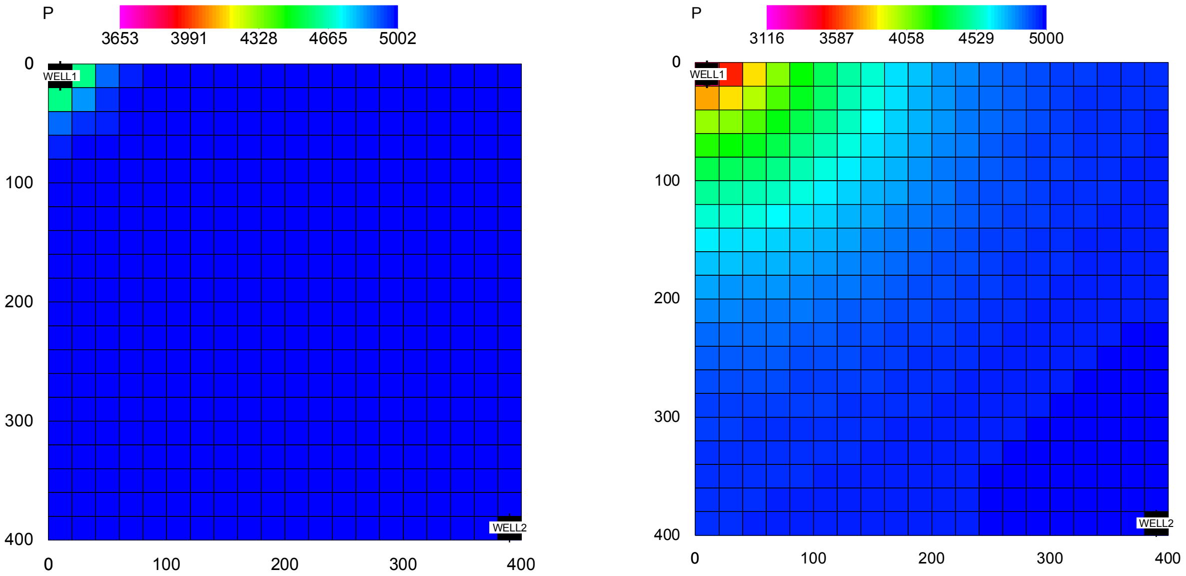

(a)

(b)

Figure 9.6 Reservoir pressure profiles after (a) 1 day of production (b) 50 days of production.

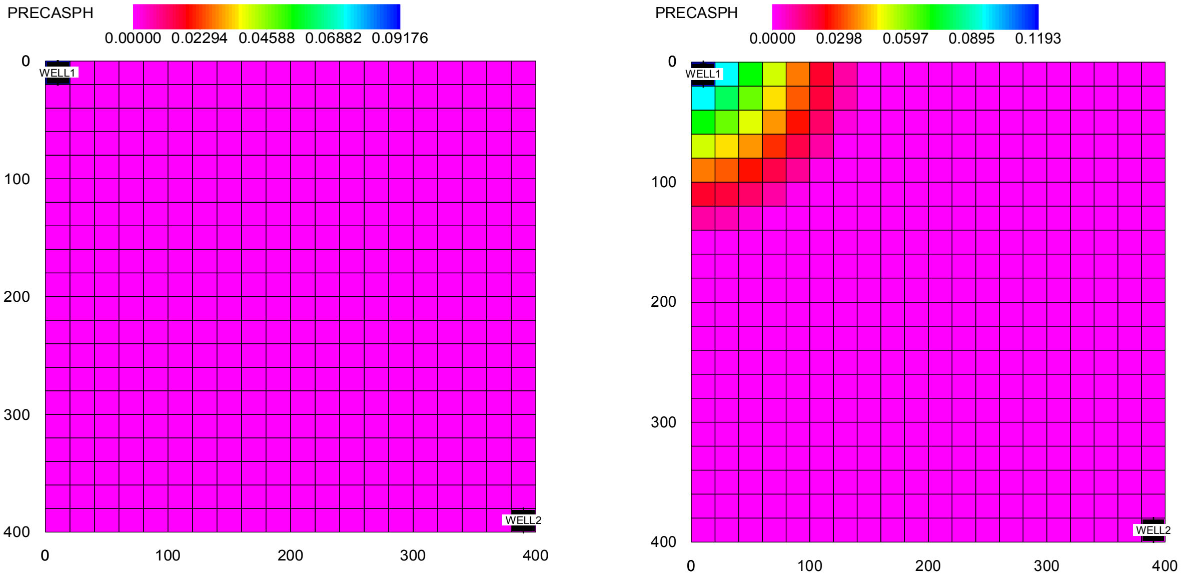

(a)

(b)

Figure 9.7 Asphaltene flocculates concentration (lb/ft^3) profiles in the reservoir after (a) 1 day of production (b) 50 days of production.

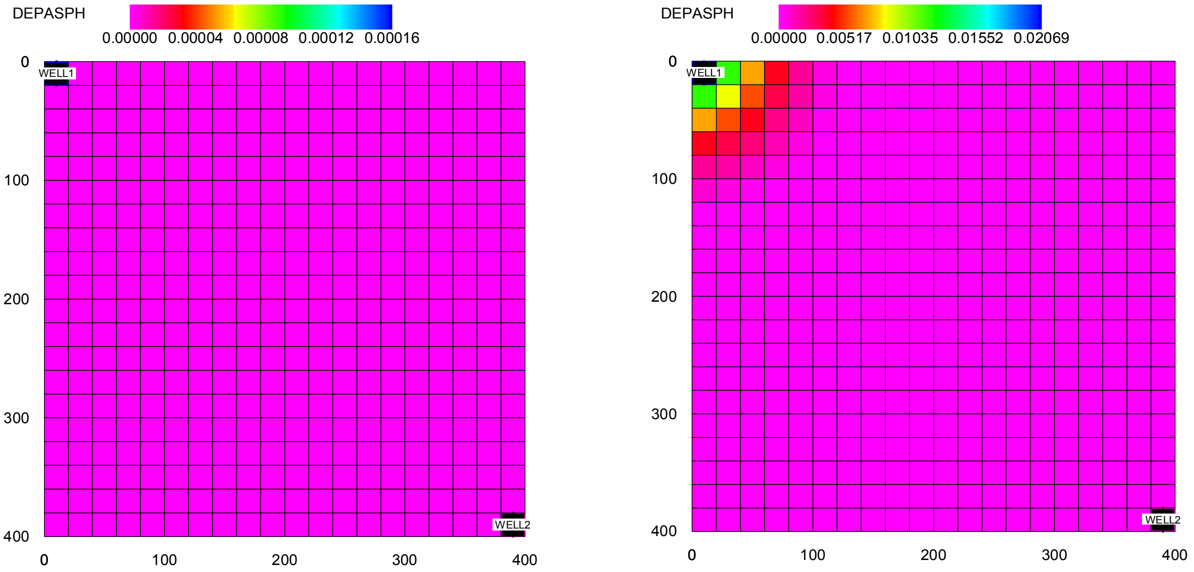

(a)

(b)

Figure 9.8 Asphaltene deposition (lb/ft^3) profiles in the reservoir after (a) 1 day of production (b) 50 days of production.

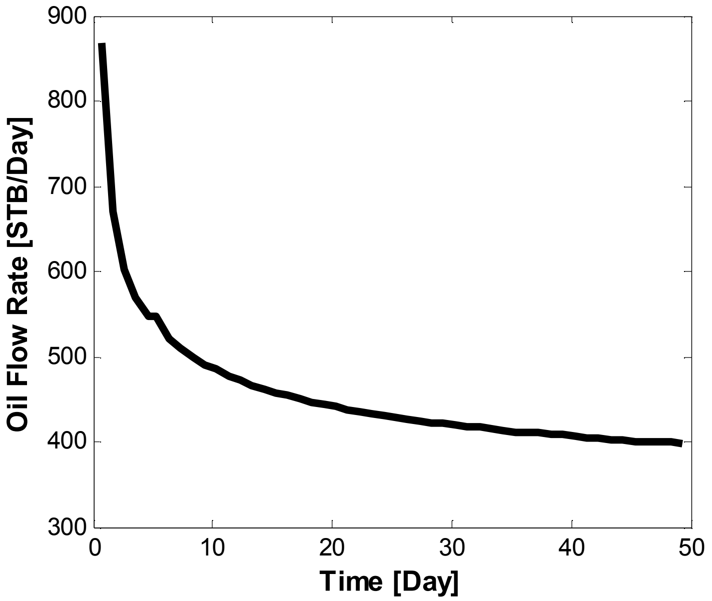

(a)

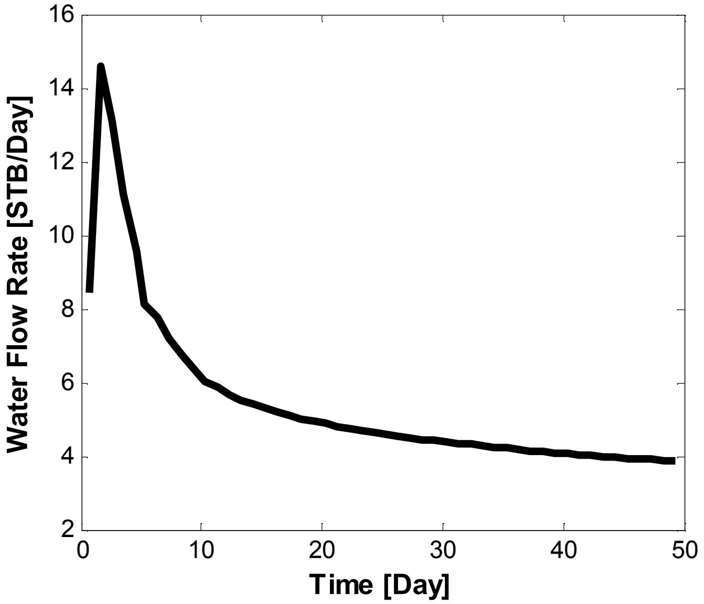

(b)

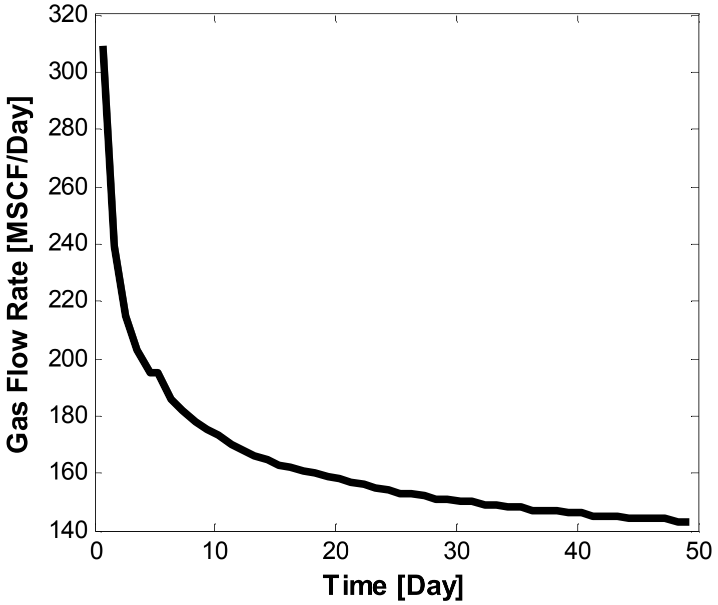

(c)

Figure 9.9 Oil, water and gas flow rate curves for 50 days of production.

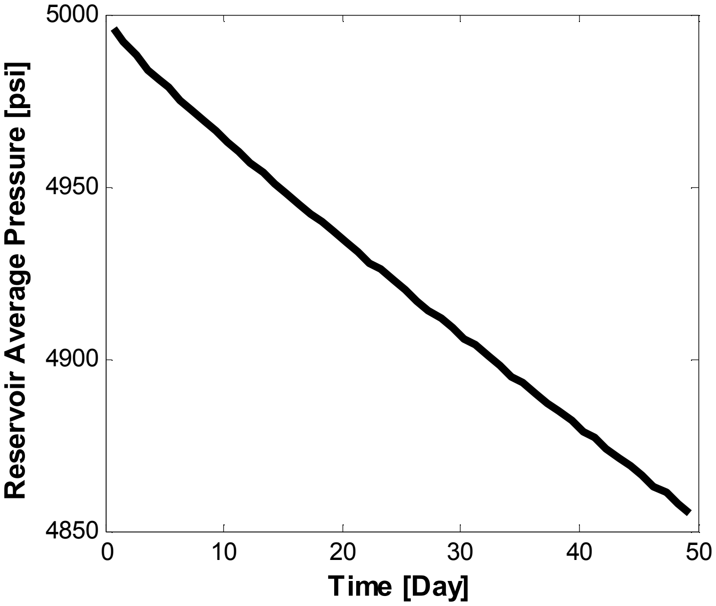

Figure 9.10 Average reservoir pressure versus time.

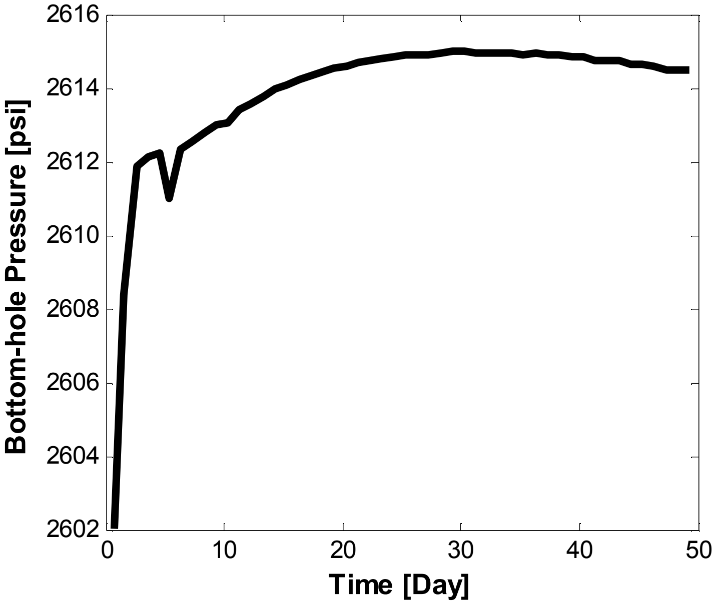

Figure 9.11 Bottom-hole pressure versus time.

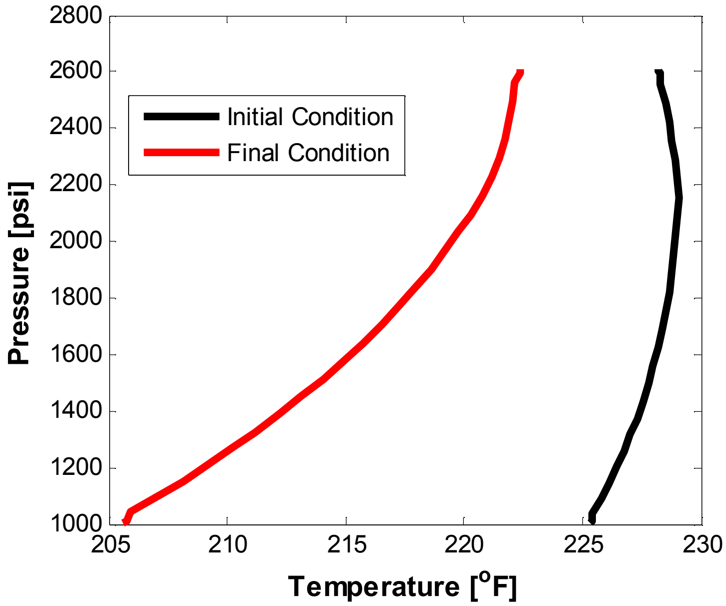

Figure 9.12 Pressure and temperature for initial and final time-steps.

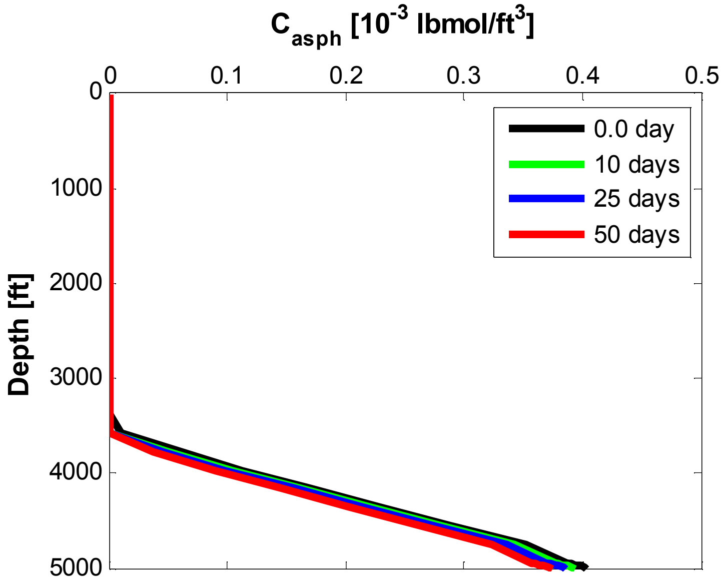

Figure 9.13 Asphaltene flocculates concentration profiles in the wellbore.

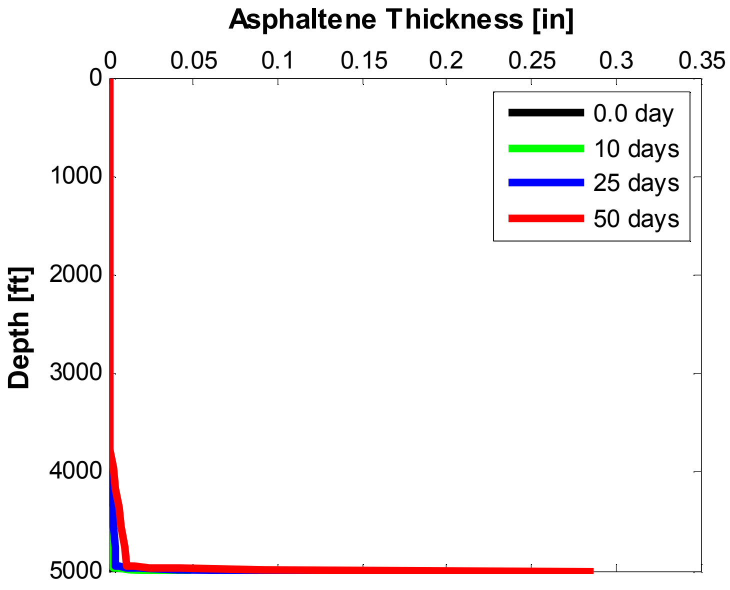

Figure 9.14 Asphaltene deposition thickness profiles in the wellbore.

Chapter 10: Remediation and Prevention Procedures for Asphaltene Deposition

Various events in field operations can trigger asphaltene precipitation and deposition. As such, acid flow back, CO_2 breakthrough, gas breakout, treatment with simple alcohols, and depressurizing reservoir are the main reasons for observing asphaltene problems. In all the processes listed above, molecular destabilization of asphaltene is involved.

There are many reports in the literature that address the methods that can be utilized in reservoir development to reduce asphaltene issues. In this chapter, we briefly list the common field practices of asphaltene prevention and remediation procedures and discuss the efficiency of each method.

Furthermore, we apply our developed tool (UTWELL) to perform some simulation analyses for asphaltene deposition preventions. A series of sensitivity analysis on different parameters, such as wellhead pressure, tubing size, and well heat transfer coefficient, are investigated to complete our simulation studies.

10.1 ASPHALTENE DEPOSITION PREVENTION PROCEDURES

Asphaltene remediation is a very costly endeavor in the field. For this reason, it is always desirable to take any steps initially to prevent asphaltene deposition. In some occasions, modification of the operation condition and screening the mechanisms of the processes can eliminate asphaltene deposition.

Once it is recognized that a reservoir has a high potential for asphaltene deposition, different production scenarios should be evaluated to encounter the minimum of asphaltene problems. Predicting and understanding the phase behavior of asphaltenes in crude oils and pressure and temperature profiles along the wellbores are crucial to test the different production scenarios before applying on the real field.

Other approaches to prevent asphaltene deposition are using asphaltene inhibitors. Asphaltene inhibitors are designed to interact with asphaltene components of crude oil to inhibit aggregation and deposition, and ensure enhanced flow. These chemicals can be circulated in the wellbore or injected into the formation to combine with asphaltene components. Since the injected inhibitors in the formation can be pushed out by produced oil, its application for preventing asphaltene deposition in near-wellbore is limited. However, Nalco Energy Services claim that they can inject asphaltene inhibitors to the formation with activating chemical agents to enhance the adsorption of the inhibitors on the rock. With this method, they can keep inhibitors in near wellbore region for a long time and prevent asphaltene deposition in those sites.

Although inhibitors have shown promises for preventing asphaltene deposition in the fields, they have not been used widely for all field applications so far. In fact, the inhibitors should be designed for the specific conditions of the reservoirs and should be applied at the right time.

10.2 ASPHALTENE DEPOSITION REMEDIATION PROCEDURES

The practical methods for asphaltene deposition treatment are mechanical cleaning of the well, chemical cleaning by circulation of solvents, pressure and temperature manipulation to reduce asphaltene deposition issues. The most desirable time to start remediation process is before the well plugs up completely. Otherwise, the accessibility to the wellbore and the formation becomes impossible and well must be abandoned.

Scrapping the wellbore by coil tubing (CT) is the most traditional method of asphaltene deposition remediation. This method is often slow and costly, particularly if the asphaltene blockage is long and hard. Although this approach is used in different fields worldwide, in many cases it either fails or actually decreases the production. For instance, in the Hassi-Messaoud filed (Haskett and Tartera, 1965) it was reported that cutting the deposits from the tubing by wire-line methods was too time-consuming and sometimes impractical.

Chemical clean-up methods are the next best alternative approach for asphaltene removal. This method is utilized when the CT method is not successful. Solvent treatment with circulation of hot oil has been tried for asphaltene deposition prevention and removal along wellbores. In this procedure, the solvent is injected through the production tubing or through a chemical injection line. The latter is more beneficial since no well shut-in is required and it can be used in a continuous way along with production.

Numerous solvents, additives, co-solvents, dispersants, and many other commercial chemicals have been offered by chemical companies for diluting the asphaltene deposits. Generally, pure aromatic solvents, such as toluene or xylene, are the best candidates for chemical treatment. However, these solvents have limited applicability due to costs, environmental issues, and safety risks of flammability.

Approximately 8 to 10 grams of asphaltene deposits can be dissolved per hundred cc's of xylene. The rate of removal can also become very slow when the solubility limit is reached. At this point using co-solvents can be beneficial to both dissolve and disperse asphaltene deposits (Trbovich and King, 1991). In some cases, the chemical treatment is used to soften the deposit before performing mechanical scraping.

Recently, the use of deasphalted oil injection for asphaltene deposits removal is being tried. This technique has some advantages, since it is less expensive than other solvents and it is not harmful to the environment.

10.3 SIMULATION STUDIES

Regardless of the method used, remediation measures for asphaltene deposition are expensive. For this reason, pressure, temperature and flow rate manipulations, along with on-regular-basis tubing washes are the most preferable methods to overcome asphaltene problems.

In this section, we perform several case studies to investigate the effect of different parameters on evolution of asphaltene deposition. These parameters are listed as

1) effect of wellhead pressure
2) effect of tubing size
3) effect of heat loss and tubing temperature

These simulations aim to find a better solution for operation conditions before proceeding for remediation practices.

10.3.1 Effect of Wellhead Pressure

Adjusting the wellhead pressure can drastically affect both the phase behavior and the transport mechanisms of hydrocarbon fluid in the wellbore. The profile of asphaltene deposition not only depends on the type of the fluid but also on the operation condition of the well. In some circumstances, the asphaltene deposition interval is shrunk or lowered to the bottom of the well by changing the pressure condition of the well.

Effect of wellhead pressure on progression of asphaltene deposition and its damage on the wellbore cannot be generalized. However, in some reservoirs such as, Hassi Messaoud field and Ventura field in California (Leontaritis and Mansoori, 1987), it was reported that changing the operating pressure had removed asphaltene deposition in the wells. In those fields, the bottom-hole pressure was maintained below the bubble point of the crude oil to avoid asphaltene precipitation. On Lake Maracaibo field in Venezuela (Leontaritis and Mansoori, 1987) also asphaltene problems were diminished by manipulating the wellhead pressure and increasing the production flow rates.

In this section, we tested the effect of wellhead pressure on the example case that we discussed in Chapter 8, Section 8.5.1. We used the same fluid, wellbore, and reservoir configuration but changed the wellhead pressure from 1800 psi to 1000 psi. Figure 10.1 shows the asphaltene thickness profiles for different pressures after 3 months of production. Figures 10.2 through 10.4 also show the pressure, temperature and asphaltene concentration profiles, respectively, for various operation conditions in the well. As we observe in this example, the reduction of wellhead pressure causes the shrinkage in the asphaltene deposition interval and minimizes the asphaltene problem.

Nevertheless, we may not be able to maintain the wellhead pressure very low since the flow capacity of the tubing is limited. In such situations, we may need to change the tubing size to be able to lower the pressure to below a certain value.

10.3.2 Effect of Tubing Size

Tubing size can directly affect the velocity of the fluids and the asphaltene particles deposition mechanisms in the wellbore. In this section, we perform simulations for a production well similar to that in Section 8.5.1 to investigate the effect of tubing size on asphaltene deposition profiles. We chose tubings with API 31/2 P110 12.95 lb/ft , API 41/2 L80 26 lb/ft, API 41/2 C90 17 lb/ft and inner radius of 0.1145, 0.135 and 0.1558 ft, respectively, for our simulations.

Figure 10.5 shows the asphaltene deposition thickness profile on the surface of the well for different tubing sizes. As we can see, the smaller tubing has less deposition. In fact, the shear force in smaller tubing is larger, which can remove most of the asphaltene deposits from the surface of the well. Figures 10.6 through 10.9 also show the asphaltene concentration, pressure, temperature, and oil superficial velocity profiles at the end of simulation time (90 days). We do not see any significant difference in asphaltene flocculates concentration in the wellbore for different tubing sizes. However, the velocity profiles are significantly different. Thus, we can infer that the main contributing mechanism for the asphaltene deposition in different tubing sizes is the transport coefficients and asphaltene removal due to drag forces.

10.3.3 Effect of Wellbore Heat Transfer Coefficient

Temperature has dual effects on asphaltene deposition just like pressure. Insulating the well completion can maintain the hydrocarbon temperature and keep the asphaltene components stable in the crude oil. However, the well surface temperature and the fluid temperature also control the adhesion forces between the solid surface and the aggregation of asphaltene particles on the well surface. Higher the temperature is higher the probability of sticking solid particles on the surface of the well.

Effects of temperature on solid precipitation, asphaltene phase behavior, and solid deposition mechanisms always compete in the wellbore. In case a significant amount of asphaltene has been stripped out of the crude oil, temperature effect on the deposition process becomes more important.

In this section, we performed simulation cases for different wellbore overall heat transfer coefficients to evaluate the effect of temperature on asphaltene deposition. Figure 10.10 shows the profile of asphaltene deposition for overall heat transfer coefficients of 1.0, 2.0, and 3.0 (Btu/ft^2-hr-^{o}F). As can be seen, the larger heat transfer coefficient case has a smaller asphaltene deposition rate. In fact, the colder the surface of the well is, the smaller the particles energy is to adhere on the surface.

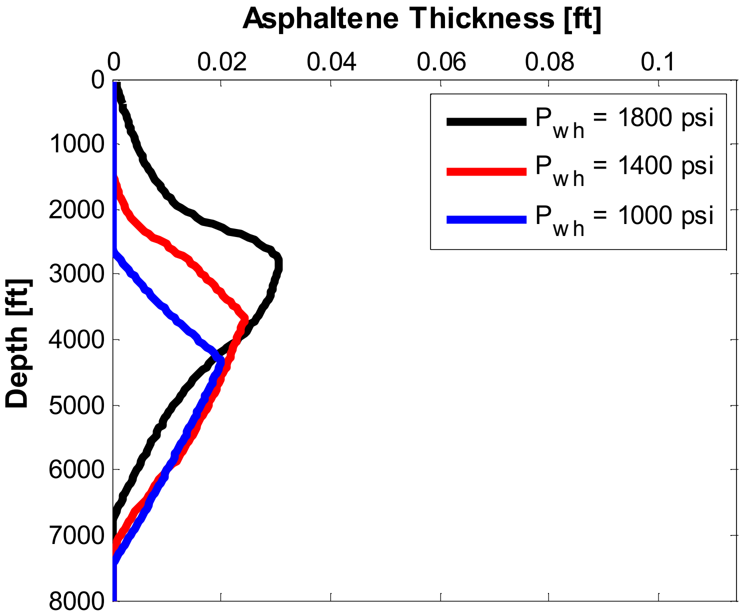

Figure 10.1 Asphaltene deposition thickness profiles for different wellhead pressure at the end of 90 days of production.

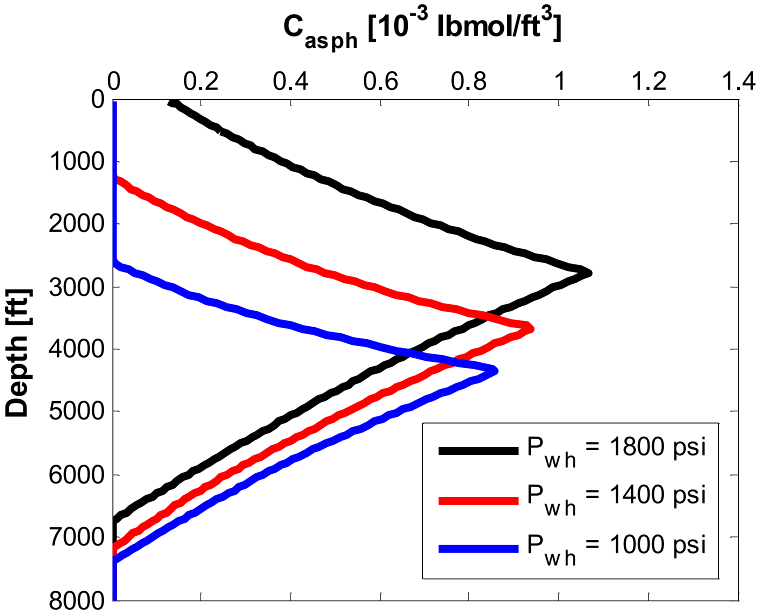

Figure 10.2 Asphaltene flocculate concentration profiles for different wellhead pressure at the end of 90 days of production.

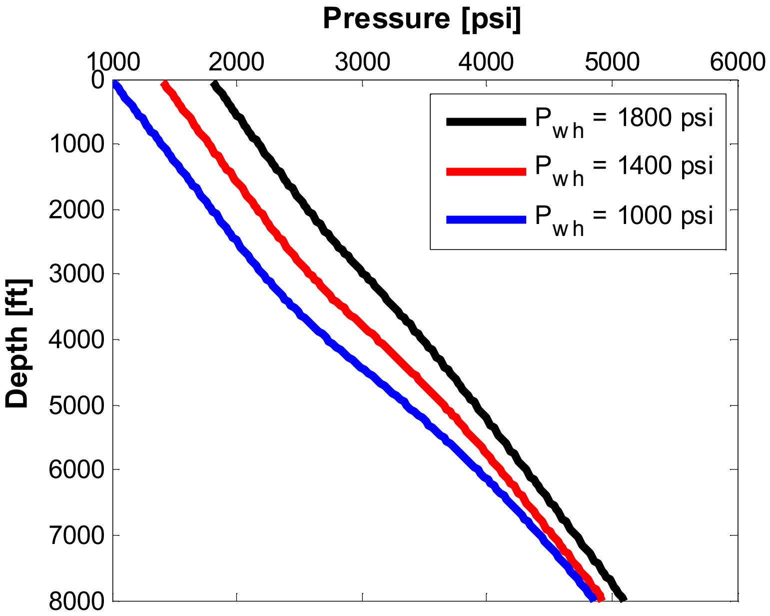

Figure 10.3 Pressure profiles for different wellhead pressure at the end of 90 days of production.

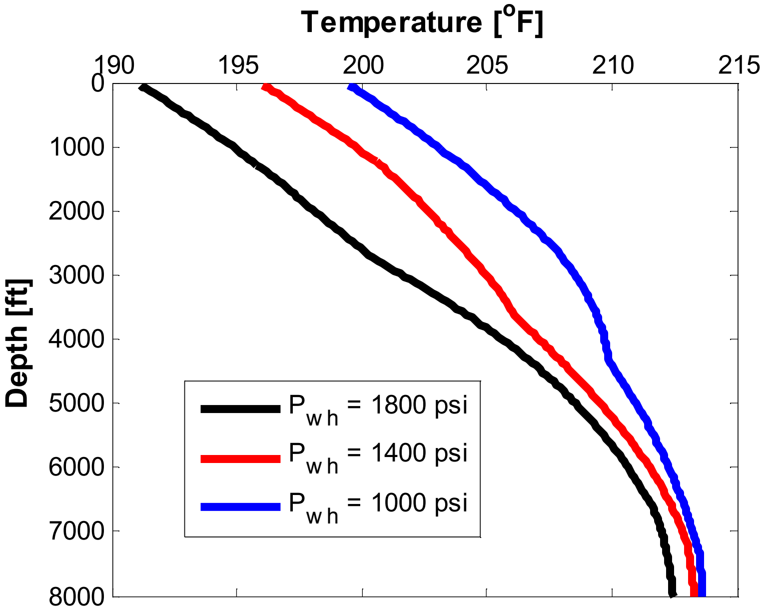

Figure 10.4 Temperature profiles for different wellhead pressure at the end of 90 days of production.

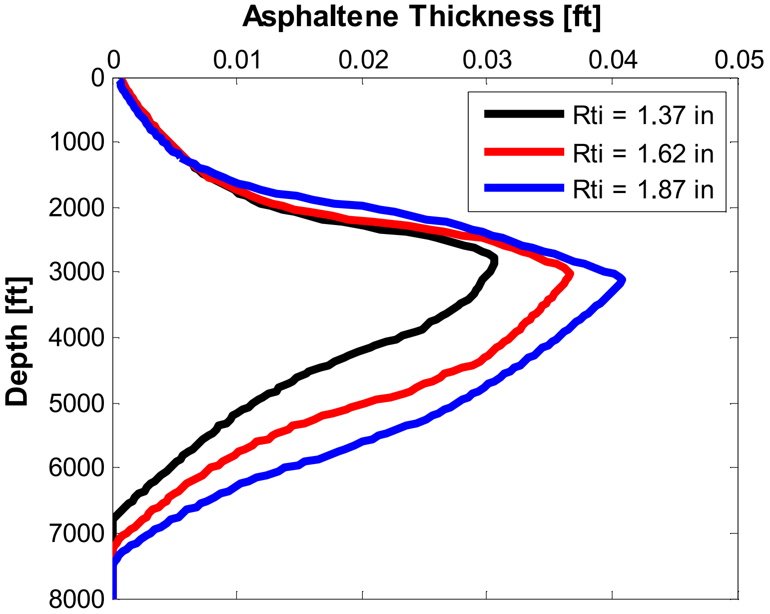

Figure 10.5 Asphaltene deposition thickness profiles for different tubing sizes at the end of 90 days of production.

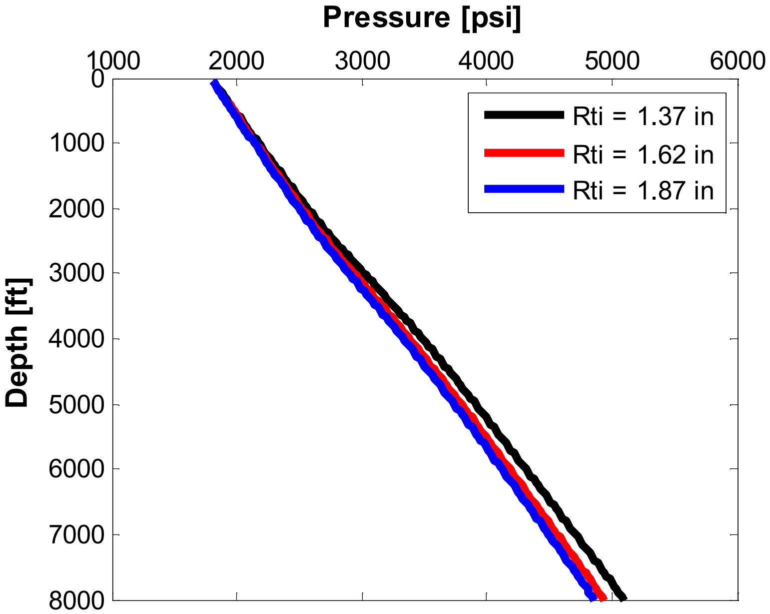

Figure 10.6 Pressure profiles for different tubing sizes at the end of 90 days of production.

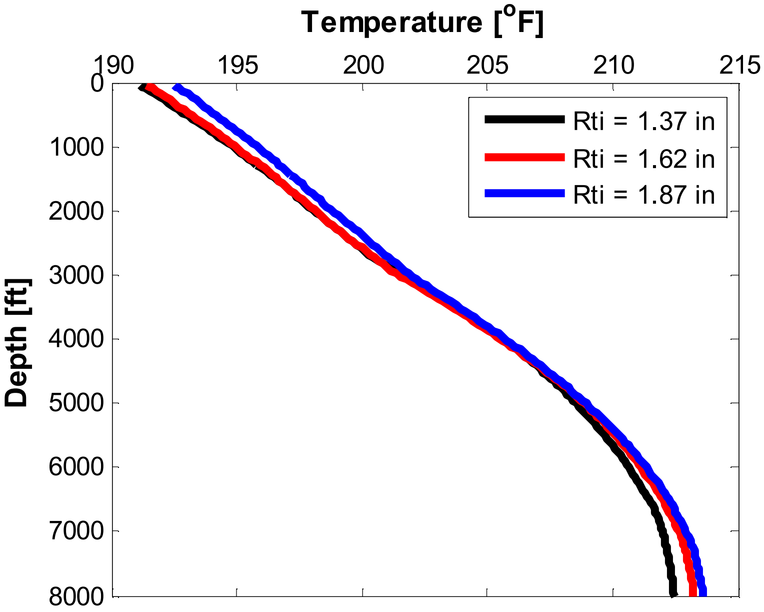

Figure 10.7 Temperature profiles for different tubing sizes at the end of 90 days of production.

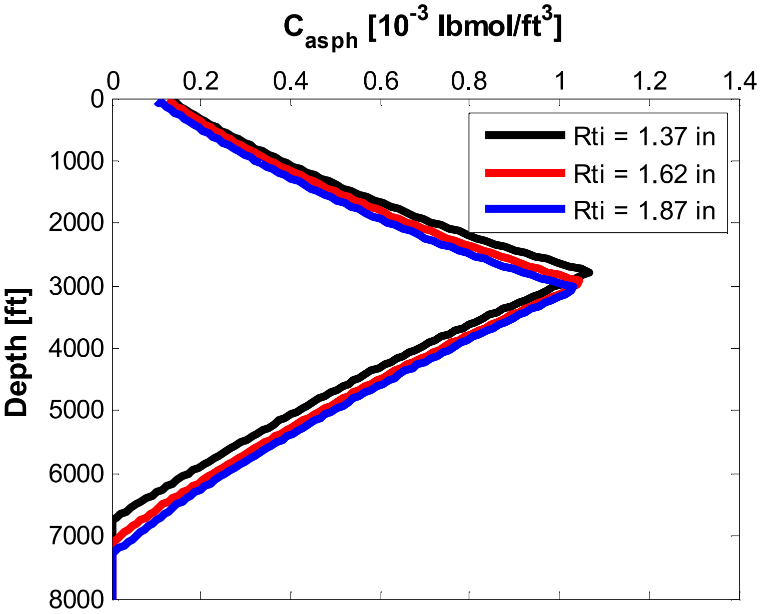

Figure 10.8 Asphaltene flocculate concentration profiles for different tubing sizes at the end of 90 days of production.

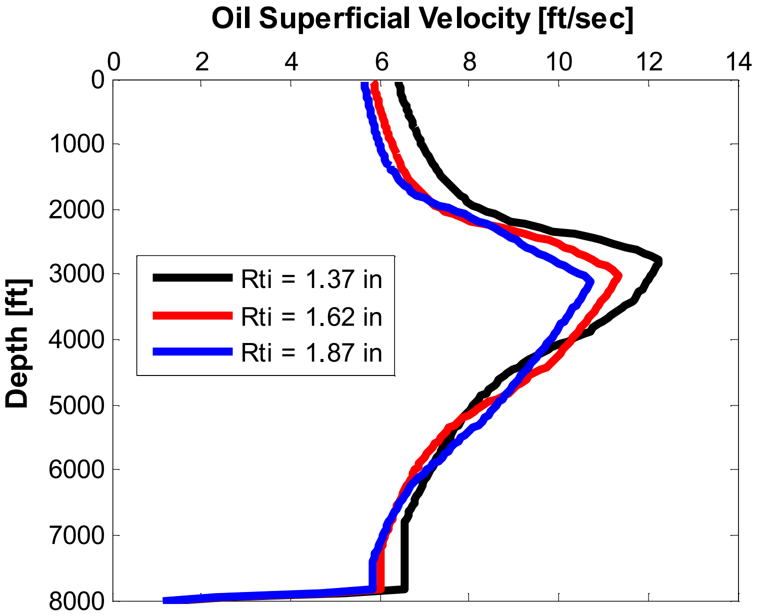

Figure 10.9 Oil superficial velocity profiles for different tubing sizes at the end of 90 days of production.

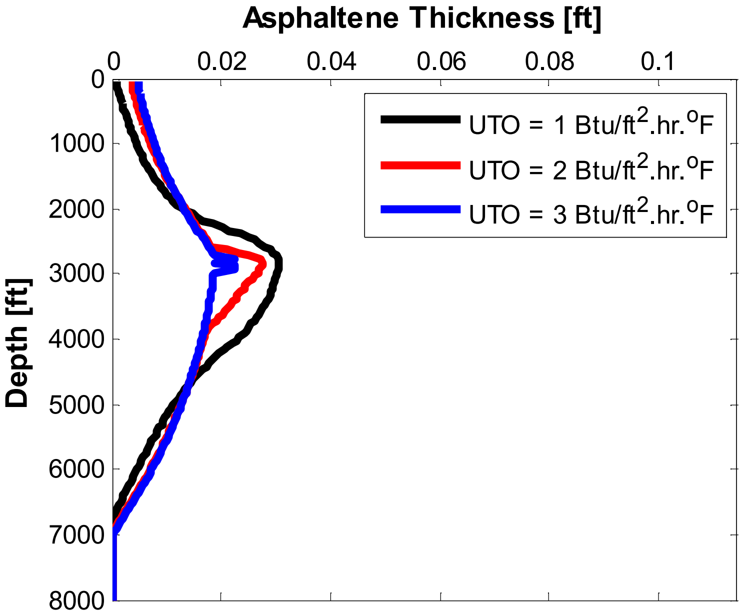

Figure 10.10 Asphaltene thickness profiles for different overall heat transfer coefficient at the end of 90 days of production.

Chapter 11: Summary, Conclusions and Recommendations

This chapter presents the summary and the conclusions of this research and gives recommendations for further extensions of this work.

11.1 SUMMARY

In the following, we summarize the work presented in this study.

- Different modeling approaches for transient and steady state multiphase flow calculation in the wellbore were presented in detail.
- All the formulations for the conservation equations were derived. Constitutive relations for interphase interaction and fluid/wall friction, plus flow regimes transition were discussed and reproduced.
- Drag force and interphase momentum transfer models were implemented in the momentum equations to mimic the effect of different flow regimes.
- Numerical stability and hyperbolicity of different multiphase flow models, such as homogenous, drift-flux, and two-fluid for momentum equations, were discussed in detail.
- Eigenvalue analysis was performed for different multiphase flow models and the regularization methods were applied in two-fluid models.
- Fluid properties were calculated using EOS compositional model or blackoil model.
- Mass transfer between phases was considered by either blackoil models or EOS compositional models.
- Wellbore heat-transfer model was presented with consideration of accurate analytical and numerical models for surrounding materials temperature calculation.

- The energy equation was solved numerically based on the enthalpy calculation.
- Wellbore model solutions with consideration of semi-implicit, nearly-implicit, and fully implicit methods were derived.
- Final wellbore model solution was calculated for pressure, oil, water, and gas volume fractions, temperature and water, oil and gas velocities.
- Wellbore model solutions for different modeling approaches were compared against each other for similar case studies. Computation time and accuracy of results were evaluated for various models and numerical schemes.
- The wellbore model was validated against analytical solutions and commercial multiphase flow simulators. Model results were successfully compared against other commercial simulators.
- Thermodynamic modules were developed for wax and asphaltene precipitation based on cubic EOS.
- Phase behavior modules for asphaltene and wax were compared against experimental data and a commercial phase behavior simulator (Winprop, CMG, 2008).
- A chemical reaction package (PHREEQC) was coupled to the wellbore model for simulating geochemical scales reaction and transportation in the wellbore.
- Application of different particle fouling models for asphaltene and scale deposition were discussed.
- The deposition models for scale and asphaltene were derived for turbulent and laminar flow regimes. For scale and asphaltene particles, two different approaches, the classical stopping distance treatment and the stochastic modeling were described. Consistency of derivations of the models was compared against two sets of experiments.
- Wax deposition model was regenerated from available models in the literature.
- Particle transportation and depositions were extended to multiphase flow systems.

- Model results for asphaltene deposition during primary production and CO_2 enhanced oil recovery were presented and compared.
- Different types of wellbore-reservoir coupling were discussed and an explicit coupling was implemented.
- A coupled horizontal and vertical wellbore model was also developed in which the boundary condition could be assigned in the wellhead or bottom-hole.
- An Equation-of-State compositional reservoir simulators (UTCOMP) were used for the coupling purpose.
- Asphaltene deposition in wellbore and in reservoir during the primary production scenario was studied using a coupled wellbore/reservoir simulator.
- Finally, the remediation procedure for asphaltene deposits removal was discussed briefly. The developed wellbore model was also used for remediation and prevention procedures with manipulation of the well operation conditions.

11.2 CONCLUSIONS

The conclusions from this study can be listed as follows:

- For accurate and more realistic modeling of multiphase flow problems, two-fluid model is the best choice. It is the most suitable approach for the co-current and counter-current flows. Two-fluid models can consider the physics correctly. However, this model is computationally more expensive. For this reason, the drift-flux models with tuning for the slippage ratio can also be used for multiphase flow simulations in the wellbore. Nevertheless, the drift-flux models are mostly appropriate for the dispersed flows.

- Regularization approaches are essential for two-fluid models to avoid stability issues in numerical solutions. Additionally, discretization algorithms are crucial for the computation time and the robustness of two-fluid models.
- Modeling the phase behavior and the equilibrium condition of the hydrocarbon fluids is the most important part of simulation of flow assurance issue in the wellbore. Correct phase envelope calculation for the hydrocarbon fluids can qualitatively describe whether or not the flow assurance problems can occur. In our phase behavior module, we used cubic EOS. Using cubic EOS, we need proper tuning and fluid characterization procedures to be able to capture the precipitation of asphaltene and wax.
- In addition to solid particles concentration in the flow, the transportation of the particles in radial direction controls the particles deposition rate. Transportation of particles in radial direction is a function of different parameters, such as particles size, velocity field, temperature, and viscosity of the continuous fluid. More importantly, the radial transportation is a function of flow regimes (turbulent or laminar). Flow regimes can affect the mechanisms of depositions significantly. For instance, eddy currents exist in the turbulent flow which can enhance particle diffusion in the transverse direction. However, in the laminar flow, the momentum on the particles is only transferred via viscose forces.
- We achieved fairly good agreement for conditions at which the deposition models are valid. In addition, our comparison shows that the described models in Chapter 7 are applicable to asphaltene deposition in oil flow streams as well as particles deposition in gas flow streams.
- We observed that increasing the flow velocity and decreasing the tubing surface temperature decreases the deposition rate significantly. From this observation, we

conclude that in the wellbore system, where velocity increases due to expansion and temperature decreases due to thermal gradient from bottom-hole to the surface, the deposition rate decreases remarkably.

- Combination of transport coefficient in the radial direction and concentration of the solid particles calculated from thermodynamic models determine the deposition rate in the flow line. In any point in the wellbore where the combination of these two parameters is maximum, the deposition rate is maximum. Consequently, the wellbore cross-sectional area becomes a minimum at this point.
- Our simulation studies reveal that the maximum deposition rate of asphaltene occurs in a depth where pressure is close to the bubble point pressure. In addition, above that depth, since light hydrocarbons flash out from crude oil, asphaltene becomes stable and dissolves in the oil. For this reason, we observe a bell shaped profile for asphaltene deposition in the wellbore.
- Asphaltene deposition rate is not only a function of temperature and pressure, but also of crude oil composition. Our results show that existence of light components like CO_2 can significantly increase asphaltene problem in the wellbore. CO_2 destabilizes asphaltene in the phase envelope and increases both the bubble point pressure and the asphaltene onset pressure. For this reason, when CO_2 is mixed with an asphaltic crude oil, it lowers the deposition sites in the wellbore to bottom-hole where the pressure is larger. Our wellbore model can quantitatively determine how CO_2 can change the deposition of asphaltene in the wellbore.
- Our simulation studies show that geochemical scales deposition mostly occurs in the bottom of the well where the shear forces are low and particles can stick on the surface of the well more easily.

- Simulation of wax deposition shows that these components are very sensitive to temperature. Since wax deposition occurs at very low temperatures, we mostly expect to have this problem in the wellhead or in offshore pipelines that have significantly lower temperature than the reservoir temperature.
- For modeling flow assurance problems in the reservoir simulators, a coupled wellbore/reservoir model is necessary. Our simulation results show that the asphaltene deposition problem is more significant in the wellbore than in the reservoir. The damage of asphaltene occurs in the reservoir when pressure goes below the onset pressure. The precipitated asphaltene in the reservoir can flocculate to the wellbore and cause more problems in the bottom of the well.
- The coupled wellbore/reservoir simulator is capable of modeling multiple-zone production from horizontal and vertical wells.
- Finally we discussed remediation procedures for asphaltene problems in the wellbore. Our simulation analyses show that manipulation of pressure and temperature can be a possible method to reduce the asphaltene deposition problem. Operation condition of the well can affect the thermodynamic equilibrium of asphaltene, as well as dynamic transportation of these particles. We observed that decreasing the wellhead pressure to below bubble-point pressure causes the asphaltene deposition interval to shrink and be pushed to a lower part of the well.

11.3 RECOMMENDATIONS

The recommendations for further study in this area are presented in the following:

- Since asphaltene components in the crude oil are the most polar components, they exert molecular forces in their polar sites. This distinction of asphaltene components makes the phase behavior of crude oil more complicated. In this study, we used compositional flash calculation with cubic Equation-of-State to predict asphaltene precipitation at different pressures and temperatures. Although this approach is more reliable than most other solubility models for asphaltene, it lacks the consideration of correct molecular interactions. In the Peng-Robnison Equation-of-State, in order to incorporate the effect of molecular interactions in non-ideal solutions, binary interactions are used. Tuning binary interaction coefficients may not be a mechanistic approach for asphaltene phase behavior prediction, especially in cases where the crude oil composition is changed. Recent developments in SAFT Equation-of-States have shown promising results in modeling the phase equilibrium of systems containing heavy hydrocarbons such as asphaltene (Gonzalez et al., 2005; Gonzalez et al., 2007). Since this Equation-of States considers the interaction of the molecules correctly, this has better prediction capacity for asphaltene precipitation. As a future work, we recommend implementation of SAFT EOS for modeling asphaltene precipitation in the wellbore. Since UTWELL has been developed in a way that can use different phase behavior models and Equations-of-State for fluid property calculations, implementation of SAFT EOS in wellbore calculations will be a simple task.

- Particles deposition rate not only depends on the concentration but also on the speed of particles traveling in the radial direction. The later term in the deposition models has significant effect on the profile of deposits on the surface of the wellbore. In this dissertation, we presented two types of deposition models for turbulent and laminar flows. In those models, we used the classical analogy between mass transfer and momentum transfer in radial direction for one-dimensional flow. Although the deposition models that we applied in our wellbore calculation were validated against experimental data, more validation for different flow situation is still owed. In addition, for the sticking probability and attachment process of the solid particle, we used simplified models which can be further improved and elaborated in the future.

- In our wellbore model, we assume solid particles are small enough that can move with the same speed of fluids in axial direction. In fact, we did not include the slip ratio of fluid and solid particles in our calculations. Although our assumption is valid for light and small particles, it is not appropriate for large particles. For this reason, we recommend development of a similar liquid/gas drift-flux model for solid particles and liquid drift velocity. Having this model, the convection terms of the mass conservation equation for solid particle would be modified based on solid particle velocities.
- The model we developed for geochemical scale deposition was only applied for the standalone wellbore model. However, we know that the source of geochemical scales is mostly the reactions that occur in the reservoir and the near wellbore region where incompatible ions are mixed. In this scenario, a coupled wellbore/reservoir model is needed to fully address the geochemical scales formation and transportation. For this purpose, the development of geochemical reactions in the reservoir is necessary for calculating the flocculated scales into the wellbore. This task requires coupling of geochemical reaction module (PHREEQC) with transportation of solid particles in the reservoir simulator.
- To study the effect of light components in the crude oil for asphaltene deposition mechanisms, we used our standalone wellbore model. Dynamic simulation of CO_2 from the reservoir to the wellbore gives better insight of the effect of CO_2 on asphaltene deposition. A series of simulations are recommended to be performed using the coupled wellbore/reservoir simulator to observe the effect of injected CO_2 on asphaltene formation in the reservoir and wellbore. Since CO_2 flooding can be

combined with water injection, studying Water Alternative Gas injection is also proposed for completeness of our simulation.

- One of the remediation methods that were discussed in Chapter 10 is solvent circulation. Aromatic agents or deasphalted oils are the main solvents that can be circulated through injection annulus in the production wells to remove asphaltene blockage from the surface of the wellbore. This process can be modeled combining the thermodynamic modeling of solvent phase behavior with crude oil and the coupled annulus / tubing fluid flow models. We recommend as a future work to develop an annulus flow path for solvent injection to the wellbore. In this model, the effect of temperature should be carefully modeled in the tubing and the annulus. Developing annulus flow model can also be applied for other purposes such as gas-lift process modeling in future.
- There are some circumstances where asphaltene, geochemical scale, and wax formations are combined in the flow line. These aspects might occur at the same time in the mixing junctions of surface facilities or pipelines. In the current version of our code, we only consider each flow assurance issue (asphaltene, wax, and scale) separately. We also recommend combining these three flow assurance modules together for such complicated scenarios.
- The trajectory of our wellbore model is only a flow line with different angles. In the current version of our code, we do not handle multiple junctions in the wellbore. We recommend further development of UTWELL to implement the branches and junctions for the application of multilateral wells, surface gathering systems, and platforms. Developing this option can provide a complete surface facility network for the realistic modeling of reservoir simulators.

- Finally, we recommend developing analytical solutions for flow rate decline curves and pressure transient models during asphaltene deposition in the wellbore. These models can be used as diagnostic tools for detecting flow assurance problems in the wellbore without full simulation of the wellbore flow.

Appendix A : Reservoir Simulation Model (UTCOMP)

In our coupled wellbore-reservoir model, we use a compositional reservoir simulator called UTCOMP. This simulator, developed at The University of Texas, is an isothermal, three dimensional, equation-of-state (EOS) IMPES (implicit pressure and explicit phase saturations and compositions) compositional reservoir simulator. UTCOMP is used to simulate a variety of important enhanced oil recovery processes, such as immiscible and miscible gas flooding.

The following are some of the main features currently available in UTCOMP (User's Manual, 2003):

- Three-dimensional EOS IMPES compositional
- Rigorous and simplified flash calculations (including three-phase flash-calculation capability)
- K-value method for phase-behavior calculations
- Higher-order total variation diminishing (TVD) finite-difference method
- Full physical-dispersion tensor
- Variable-width cross-section option
- Vertical or horizontal well capability
- Tracer-flood capability
- Polymer-flood capability
- Dilute-surfactant option with both equilibrium and non-equilibrium mass transfer
- Gas-foam-flood capability (Pc^* model and table-look-up approach)
- Black-oil model
- Asphaltene precipitation model

- CO_2 sequestration in aquifers

A.1 RESERVOIR GOVERNING EQUATIONS

Multi-component, multiphase flow in porous media occurs as a transport of chemical species in multiple homogeneous phases under the influence of four predominant forces: viscous, gravity, capillary and dispersion forces. The conservation equation for each species should hold at each point of the medium. The general mass conservation equation for component *i* can be presented as the following equation:

$$V_b \frac{\partial N_i}{\partial t} - V_b \nabla . \left[\Sigma \xi_j \lambda_j x_{ij} \left(\nabla P_j - \gamma_j \nabla D \right) + \phi \xi_j S_j \vec{\vec{K}}_{ij} \nabla x_{ij} \right] - q_i = 0 \quad i = 1,\ 2,\ ..., n_c \tag{A.1}$$

The above equation is written in terms of moles per unit time, in which N_i is the number of moles for component *i* per bulk volume, and q_i is the molar injection (positive) or production (negative) rate for component *i*. The mobility for phase j is defined as follows:

$$\lambda_j = k \frac{k_{r_j}}{\mu_j} \tag{A.2}$$

Physical dispersion is modeled using the full dispersion tensor as presented in equation (A-3):

$$\vec{\vec{K}}_{ij} = \begin{bmatrix} K_{xx} & K_{xy} & K_{xz} \\ K_{yx} & K_{yy} & K_{yz} \\ K_{zx} & K_{zy} & K_{zz} \end{bmatrix}_{ij} \qquad \text{(A-3)}$$

The elements of above tensor contain contributions from two sources of molecular diffusion and mechanical dispersion.

A.1.1 Volume Constraint

The volume constraint states that the pore volume in each of the cells must be filled completely by the total fluid volume. This allows us to write the following equation:

$$\sum_{i=1}^{n_c} N_i \sum_{j=1}^{n_p} L_j \bar{v}_j - V_p = 0\,, \tag{A.4}$$

where L_j is a ratio of moles in phase j to the total number of moles in the mixture. Equation (A.1) and (A.4) combined with phase equilibrium equations (Appendix B) are solved at each time step for a set of independent variables to be mentioned later.

A.1.2 Pressure Equation

Because of the IMPES nature of the UTCOMP simulator, the gridblock pressures need to be implicitly solved first. The pressure equation used in UTCOMP is derived on the premise that the pore volume should be filled completely by the total fluid volume:

$$V_t(P, N) = V_p(P) \tag{A.5}$$

where the fluid is assumed to be a function of pressure and total number of moles of each component and the pore volume are related to pressure only.

Assuming that the formation is slightly compressible, differentiating both volumes with respect to time, using the chain rule to expand both terms against their independent variables, and then rearranging and substituting Equation (A.1) into the resultant equations yields the final pressure equation:

$$\begin{aligned}
&\left(V_p^0 c_f - \frac{\partial V_t}{\partial P}\right)\left(\frac{\partial P}{\partial t}\right) - V_b \sum_{i=1}^{n_c+1} \bar{V}_{ti} \vec{\nabla} \cdot \sum_{j=1}^{n_p} \vec{\vec{k}} \lambda_{rj} \xi_j x_{ij} \nabla P \\
&= V_b \sum_{i=1}^{n_c+1} \bar{V}_{ti} \bar{\nabla} \cdot \sum_{j=1}^{n_p} \vec{\vec{k}} \lambda_{rj} \xi_j x_{ij} \left(\nabla P_{c2j} - \gamma_j \nabla D\right) \\
&\quad + V_b \sum_{i=1}^{n_c+1} \bar{V}_{ti} \vec{\nabla} \cdot \sum_{j=1}^{n_p} \phi \xi_j S_j \vec{\vec{K}} \nabla x_{ij} + \sum_{i=1}^{n_c+1} \bar{V}_{ti} q_i .
\end{aligned} \tag{A.6}$$

The above equation is solved for pressure (P) at a given time t. For the rest of the physical quantities, values at the previous time level are taken. Note that the computation of the derivatives $\frac{\partial V_t}{\partial P}$ and $\bar{V}_{ti}$ involves the solution of two different sets of linear systems with the size equal to the number of hydrocarbon components and constructed on the basis of the phase-equilibrium relationship.

A.1.3 Overall Computational Procedure of UTCOMP

The overall solution scheme of UTCOMP follows a two-step procedure, which is determined by the nature of the governing equations and solution strategy:

Solve implicitly the pressure equation, Equation (A.6), that involves the variables in the adjacent gridblocks for the pressures of all the gridblocks using explicit saturation- and phase-composition-dependent terms; those terms are computed using the physical properties at the previous time level.

Compute overall number of moles for each component in each of the gridblocks using the component molar-balance Equation (A.1). The flash calculations are then performed to determine the phase amounts and compositions.

It should be noted that a set of linear equations is formed in the first step because pressure is the only unknown in Equation (A.6). This distinct feature results in the formulation of UTCOMP being non-iterative over a time-step. The detailed solution procedure over a time-step is given below:

- Compute the derivatives and coefficients necessary for Equation (A.6).
- Solve implicitly Equation (A.6) for pressure at each of the gridblocks.
- Update gridblock porosity at the new pressure.
- Compute overall number of moles of component in each of the gridblocks using Equation (A.1) with the new pressure and porosity.
- Determine the equilibrium phase compositions and molar amount in each of the gridblocks from the flash calculations.
- Evaluate the phase saturations using phase molar amounts and molar densities.
- Compute all other physical properties and desired injection/production streams.
- Check if further calculation is needed by applying user-provided termination criteria. If continuation is permitted, go to step (1) for the next time-step; otherwise, terminate the simulation.

A.2 WELL MODEL

Well models in UTCOMP relate fluid influx/outflux between wellbore and the reservoir through perforation zone. In general, a functional relation between the well rates and flowing bottom-hole pressures is required to couple both reservoir and wellbore models. In our coupled wellbore/reservoir simulator, the well models are based on

Peaceman (1991) and Babu et al. (1991). In addition, wellbore can handle different basic well conditions such as

- Constant bottom-hole flowing pressure injector
- Constant molar rate injector
- Constant volume rate injector
- Constant bottom-hole flowing pressure producer
- Constant molar rate production wells
- Constant volume oil rate production wells
- Constant wellhead pressure production wells

Generally, the relationship between volumetric flow rate, flowing bottom-hole pressure, and gridblock pressure is expressed as

$$Q_j = PI_j \left(P_{wf} - P_j \right), \tag{A.7}$$

where PI_j is the phase productivity index for phase j. Chang (1990) showed that for a one-dimensional case simulation the productivity index can be expressed as a function of gridblock permeability and size as follows:

$$PI_j = \frac{\sqrt{k_x k_y}\,\Delta z \lambda_{rj}}{25.15 \ln\left(\frac{r_o}{r_w} \right)} \quad j = 1, \cdots, n_p \tag{A.8}$$

This equation is valid for a well completed parallel to the *z* direction. The same productivity index is defined for a well completed parallel to the *y* direction. In this equation, permeabilities in the *x* and *z* directions (k_x and k_z) are used:

$$PI_j = \frac{\sqrt{k_x k_z}\,\Delta y \lambda_{rj}}{25.15 \ln\left(\frac{r_o}{r_w}\right)} \qquad j=1,\cdots,n_p \tag{A.9}$$

where $\Delta z, \Delta y$ are gridblock sizes (ft) in z and y directions, respectively. λ_{rj} is the relative mobility in cp^{-1}. For rectangular well blocks in anisotropic reservoirs, an equivalent radius is defined based on the well block dimensions. If the well is completed parallel to the *z* axis (vertical well), then

$$r_o = 0.28 \frac{\left[\left(\frac{k_y}{k_x}\right)^{\frac{1}{2}} \Delta x^2 + \left(\frac{k_x}{k_y}\right)^{\frac{1}{2}} \Delta y^2\right]^{\frac{1}{2}}}{\left(\frac{k_y}{k_x}\right)^{\frac{1}{4}} + \left(\frac{k_x}{k_y}\right)^{\frac{1}{4}}} \tag{A.10}$$

Then, the same equation is used for a horizontal well parallel to the *y* axis

$$r_o = 0.28 \frac{\left[\left(\frac{k_z}{k_x}\right)^{\frac{1}{2}} \Delta x^2 + \left(\frac{k_x}{k_z}\right)^{\frac{1}{2}} \Delta z^2\right]^{\frac{1}{2}}}{\left(\frac{k_z}{k_x}\right)^{\frac{1}{4}} + \left(\frac{k_x}{k_z}\right)^{\frac{1}{4}}} \tag{A.11}$$

For equivalent radius equations, we assume that the grid spacing and permeability in different directions are uniform (i.e., constant Δx, Δz, k_x, and k_z).

A.2.1 Constant Flowing Bottom-hole Pressure Injector

In this operation condition of the well, the flowing bottom-hole pressure for one reference point is known. Well blocks pressure, component flow rates, and phase flow rates at different perforation zones are calculated accordingly.

As a simplified assumption, considering pressure change with gravity only, the perforation layer pressure becomes

$$P_{wfz} = P_{wf,ref} - \gamma_{inj}(z - z_{ref}), \tag{A.12}$$

where $P_{wf,ref}$ is the known bottom-hole pressure at location z_{ref}. γ_{inj} is the specific gravity of the injected fluid at the well pressure. The injected fluid can have water phase with fraction equal to f_1 , and a hydrocarbon phase. Hydrocarbon component flow rates in the perforation layers are calculated by

$$(q_i)_z = [1 - f_1] z_i (q_t)_z . \quad i = 1, ..., n_c \tag{A.13}$$

For water phase also,

$$(q_{nc+1})_z = f_1 (q_t)_z , \tag{A.14}$$

where $(q_t)_z$ is the total flow rate into layer z

$$(q_t)_z = \frac{(Q_t)_z}{(v_t)_{inj}} . \tag{A.15}$$

$(Q_t)_z$ is the total volumetric flow rate into layer z

$$(Q_t)_z = \sum_{j=1}^{np} (PI_j)_z[(P_{wf})_z - (P_j)_z], \tag{A.16}$$

and

$$(v_t)_{inj} = (\frac{f}{\xi_1}) + (1-f)\left[(\frac{L_2}{\xi_2})_{inj} + (\frac{L_3}{\xi_3})_{inj}\right], \tag{A.17}$$

where $(\xi_j)_{inj}$ is the molar density of phase j. $j=1$ refers to the molar density of water, $j=2$ is the molar density of oil and $j=3$ is the molar density of gas phases. $(L_j)_{inj}$ is a ratio of moles in hydrocarbon phase j to the total number of hydrocarbon moles in the injection fluid.

A.2.2 Constant Molar Rate Injector

In this case, well constraint is the constant total molar rate q_t. In contrast to constant bottom-hole pressure scenario, for constant molar rate injectors first we distribute the total molar flow rate into each layer, and then calculate pressure near the perforated zones. We define molar flow rate for each hydrocarbon component as

$$q_i = [1-f_1](z_i)_{inj} q_t, \qquad i = 1,\ldots,n_c \tag{A.18}$$

and for water phase as

$$q_{nc+1} = f_1 q_t \tag{A.19}$$

In multiple layer reservoirs, the total injection rates can be allocated to the individual layers, according to a total mobility allocation scheme. This can be expressed as the productivity index ratio. Hence,

$$(q_i)_z = \frac{q_i (PI_t)_z}{\sum\limits_{m=z_f}^{z_b} (PI_t)_m}, \qquad i = 1, \ldots, n_c + 1 \qquad z = z_f, \ldots, z_l \tag{A.20}$$

where z_f and z_l are the first and last layer numbers of a well, respectively. The total productivity index of a layer z is defined as a summation of the productivity index for all phases,

$$(PI_t)_z = \sum_{j=1}^{n_p} (PI_j)_z \tag{A.21}$$

where $\sum\limits_{m=zt}^{zb} (PI_t)_m$ is the summation of the total productivity index over all communicating layers for a well in a multi-layer reservoir. By knowing each layer molar flow rate, it is possible to compute total volumetric flow rate as

$$(Q_t)_z = \sum_{j=1}^{3} (Q_j)_z = (q_t)_z (v_t)_{inj}, \tag{A.22}$$

where $(v_t)_{inj}$ is defined as Equation (A.17).The bottom-hole pressure is then calculated using the main definition of the productivity index

$$(P_{wf})_z = P_z + \frac{(Q_t)_z}{(PI_t)_z}. \tag{A.23}$$

A.2.3 Constant Volume Rate Injector

The computational procedure for the constant volume rate injector well is similar to that of a constant molar injection well. In this operation condition the gas injection rate, Q_g (MSCF/D) and the water injection rate, Q_w (STB/D) are given at standard condition. In addition, the hydrocarbon composition of the injected fluid z_i is specified. First, we convert the known hydrocarbon volumetric rates to molar flow rates using the following equation:

$$q_i = 2.636 Q_g (z_i)_{inj}. \qquad i = 1, \ldots, n_c \tag{A.24}$$

Similarly for water phase as

$$q_{nc+1} = 19.466 Q_w. \tag{A.25}$$

Afterward, we follow the same procedure as described in Section A.2.2.

A.2.4 Constant Molar Rate Production Well

The total molar production rate, q_t, is specified. The total production rate for each layer is calculated using

$$(q_t)_z = \frac{q_t \sum_{j=1}^{np} (\xi_j PI_j)_z}{\sum_{m=zf}^{zl} \sum_{j=1}^{np} (\xi_j PI_j)_m} \qquad z = z_f, \ldots, z_l \tag{A.26}$$

Again, we assume that the total production rates are allocated to the individual layers according to a total mobility allocation scheme. Thus, at each layer, the component rate can be calculated from

$$(q_i)_z = \frac{(q_t)_z \sum_{j=2}^{np} (\xi_j x_{ij} PI_j)_z}{\sum_{j=}^{np} (\xi_j PI_j)_z}, \qquad z = z_f, \ldots, z_l \quad i = 1, \ldots, n_c \tag{A.27}$$

and for water phase from

$$(q_{nc+1})_z = \frac{(q_t)_z (\xi_1 PI_1)_z}{\sum_{j=1}^{np} (\xi_j PI_j)_z}. \qquad z = z_f, \ldots, z_l \tag{A.28}$$

Finally, the volumetric rates and molar rates are related by

$$(Q_t)_z = \frac{(q_t)_z (PI_t)_z}{\sum_{j=1}^{np} (\xi_j PI_j)_z} \tag{A.29}$$

Calculating the volumetric flow production from each layer, the productivity index definition can be used to obtain perforation layer pressure as

$$(P_{wf})_z = P_z + \frac{(Q_t)_z}{(PI_t)_z}. \tag{A.30}$$

A.2.5 Constant Flowing Bottom-hole Pressure Producer

This operation condition of the well is similar to constant bottom-hole injection well. Likewise, ignoring the friction pressure and acceleration terms, pressure in perforation layers can be obtained from Equation (A.12). Additionally, the layer component flow rate is calculated by

$$(q_i)_z = \sum_{j=2}^{np} (\xi_j x_{ij} PI_j)_z (P_{wf} - P_j)_z \qquad z = z_f, ..., z_l \quad i = 1, ..., n_c \tag{A.31}$$

and

$$(q_{nc+1})_z = (\xi_1 PI_1)_z (P_{wf} - P_1)_z \qquad z = z_f, ..., z_l \tag{A.32}$$

A.2.6 Constant Volume Oil Rate Producer

In this case, the oil rate production, Q_o is specified in standard condition. A flash calculation is performed at separator conditions to determine the molar fraction of oil phase in the produced hydrocarbon fluid using the overall hydrocarbon composition computed from

$$(z_i)_{prod} = \frac{\sum\limits_{m=zt}^{zb} \sum\limits_{j=2}^{np} (\xi_j x_{ij} PI_j)_m}{\sum\limits_{m=zt}^{zb} \sum\limits_{j=2}^{np} (\xi_j PI_j)_m}. \qquad i = 1, ..., n_c \tag{A.33}$$

The total molar flow rate is then calculated using

$$q_t = \frac{5.61 Q_o}{(L_o)_{prod} (v_o)_{prod}} \frac{\sum\limits_{m=zt}^{zb} \sum\limits_{j=1}^{np} (\xi_j PI_j)_m}{\sum\limits_{m=zt}^{zb} \sum\limits_{j=2}^{np} (\xi_j PI_j)_m} \qquad \text{(A.34)}$$

The same allocation scheme for constant molar rate production wells is used to compute the layer component rates. The same procedure discussed in section A.2.4 is used to obtain the perforation layer pressure.

A.2.7 Constant Wellhead Pressure Producer/Injector

This boundary condition is common for the wells. However, this option in UTCOMP is only available with the wellbore model. In fact, in this approach, well blocks pressures are calculated from wellbore module, and then using similar approach to Section A.2.1 or Section A.2.5 for injector or producer wells, well/reservoir influx or outflux is calculated.

Using wellbore module, all the operation conditions at the wellhead, such as constant flow rates or constant pressures, can be interpreted as constant bottom-hole pressure condition. In fact, wellbore model can calculate the bottom-hole pressure for any specified boundary condition and pass it to the reservoir simulator as constant bottom-hole pressure for the source/sink calculation.

Appendix B: Compositional PVT Models

B.1 COMPRESSIBILITY FACTOR

A cubic EOS model is used to calculate pressure, temperature, and volume relation of compositional PVT model as follows:

$$p=\frac{RT}{V-b}-\frac{a}{V^2+Vb(1+c)-cb^2}, \tag{B.1}$$

or,

$$p=\frac{RT}{V-b}-\frac{a}{(V+\delta_1 b)(V+\delta_2 b)}, \tag{B.2}$$

where $2\delta_1=(1+c)-\sqrt{(1+c)^2+4c}$, (B.3)

and $\delta_1\delta_2=-c$. (B.4)

Using c = 1, Equation (B.2) becomes the Peng-Robinson Equation-of-State and using c = 0, it becomes the Soave-Redlich-Kwong Equation-of-State.

The Peng-Robinson Equation-of-State (Peng and Robinson, 1976) is given as follows:

$$P=\frac{RT}{V\text{-}b}\text{-}\frac{a(T)}{V(V+b)+b(V\text{-}b)}. \tag{B.5}$$

The parameters, a and b , for a pure component are computed from

$$a(T)=0.45724\frac{R^2T_c^2}{P_c}\alpha(T) \tag{B.6}$$

$$b=0.07780\frac{RT_c}{P_c} \quad \text{(B.7)}$$

$$\sqrt{\alpha}=1+\kappa\left(1-\sqrt{\frac{T}{T_c}}\right) \quad \text{(B.8)}$$

$$\kappa=0.37464+1.54226\omega-0.26992\omega^2 \ \mathit{if}\ \omega<0.49 \quad \text{(B.9)}$$

$$\kappa= 0.379640 + 1.485030\ \omega - 0.164423\ \omega^2 + 0.016666\ \omega^3 \ \mathit{if}\ \omega\geq 0.49 \quad \text{(B.10)}$$

For a multi-component mixture, a and b are obtained by mixing rules as follows:

$$a = \sum_{i=1}^{n_c} \sum_{j=1}^{n_c} x_i x_j \sqrt{a_i a_j}(1-k_{ij}), \quad \text{(B.11)}$$

$$b= \sum_{i=1}^{N_c} x_i b_i, \quad \text{(B.12)}$$

where a_i and b_i are for pure components. The constant k_{ij} is the binary interaction coefficient between components i and j.

Considering that $Z=\frac{PV}{RT}$, the Peng-Robinson Equation-of-State can be written in the form:

$$Z^3+\alpha Z^2+\beta Z+\gamma=0. \quad \text{(B.13)}$$

In Equation (B.13), α, β, and γ are calculated as

$$\alpha=-1+B, \tag{B.14}$$

$$\beta=A-3B^2-2B, \tag{B.15}$$

$$\gamma=-AB+B^2+B^3, \tag{B.16}$$

where $A=\dfrac{aP}{(RT)^2}$ and $B=\dfrac{bP}{RT}$.

Solving Equation (B.13), we obtain three roots of which two are real. Hence, we can calculate the Z-factors for gas and oil phases.

B.2 PHASE EQUILIBRIUM

One of the criteria for phase equilibrium is the equality of the partial molar Gibbs free energies, or the chemical potentials, which can be expressed as fugacity (Sandler, 1999). Hence, in the thermodynamic equilibrium between phases we have

$$f_{ij}=f_{i\ell} \qquad i=1,\ldots,n_c \textit{ and } j=2,\ldots,n_p(j\neq\ell). \tag{B.17}$$

f_{ij} is the fugacity of component i in phase j, which is a function of pressure, temperature, and phase composition, $f_{ij}=f_{ij}(P,T,x_{ij})$.

The fugacity equation, (B.17), is combined with the phase composition constraints and Rachford-Rice equation in order to solve for each phase composition (Pedersen and Christensen, 2007).

$$\sum_{i=1}^{n_c} x_{ij}-1=0, \qquad (j=1,2,\ldots n_p), \tag{B.18}$$

$$\sum_{i=1}^{n_c} \frac{z_i(K_i-1)}{1+v(K_i-1)}=0. \tag{B.19}$$

Phase composition is used for density and other properties calculation of the phases.

B.3 DENSITY

After calculating the gas compressibility factor, the gas density $(\frac{lbm}{ft^3})$ can be obtained as follows:

$$\rho_g = \frac{MW_g P}{Z_g RT}. \tag{B.20}$$

where, MW_g is the gas molecular weight in $(\frac{lbm}{lbmol})$, P is pressure in (psi), R the universal gas constant ,10.73, and T is the temperature (^oR).

Oil density is also obtained from compositional flash calculation. In fact, at a given temperature, pressure, and overall composition, oil phase Z-factor, oil molar weight are calculated and used in Equation (B.21) to obtain oil density.

$$\rho_o = \frac{MW_o P}{Z_o RT}. \tag{B.21}$$

In Equation (B.21), MW_o is the oil molecular weight in $(\frac{lbm}{lbmol})$, P is pressure in (psi), R is universal gas constant 10.73, and T is temperature in (^oR).

The dissolved gas-oil ratio (R_s) and the oil formation volume factor (B_o) are also obtained by performing flash calculation at standard conditions $(P = 14.7 psi,\ T = 520\ ^oR)$ and calculating the amount of oil and gas volume change from a given condition to standard condition.

B.4 VISCOSITY

Lohrenz et al. (1964) presented different correlations for compositional oil and gas viscosities calculation. Following are the equations.

$$\mu_\beta = \begin{cases} \mu_\beta^* + 0.000205 \dfrac{\xi_{\beta r}}{\eta_\beta} & \xi_{\beta r} \le 0.18 \\ \mu_\beta^* + \dfrac{\left(\chi_\beta^4 - 1\right)}{10^4 \eta_\beta} & \xi_{\beta r} > 0.18 \end{cases} \tag{B.22}$$

where

$$\xi_{\beta r} = \rho_\beta \sum_{i=1}^{n_c} x_{i\beta} V_c(i) \tag{B.23}$$

$$\chi_\beta = 1.023 + 0.2336 \xi_{\beta r} + 0.58533 {\xi_{\beta r}}^2 - 0.40758 {\xi_{\beta r}}^3 + 0.09332 {\xi_{\beta r}}^4, \tag{B.24}$$

$$\eta_\beta = \frac{5.44 \left[\sum_{i=1}^{n_c} x_{i\beta} T_{ci} \right]^{\frac{1}{6}}}{\left[\sum_{i=1}^{n_c} x_{i\beta} WM_i \right]^{\frac{1}{2}} \left[\sum_{i=1}^{n_c} x_{i\beta} P_{ci} \right]^{\frac{2}{3}}}, \tag{B.25}$$

$$\mu_{\beta}^{*} = \frac{\sum_{i=1}^{n_c} x_{i\beta}\,\tilde{\mu}_i\sqrt{MW_i}}{\sum_{i=1}^{n_c} x_{i\beta}\sqrt{MW_i}}. \tag{B.26}$$

The low-pressure pure component viscosity is calculated as follows:

$$\hat{\mu}_i = \frac{0.0001776(4.58T_{ri}-1.67)^{5/8}}{\zeta_i}, \tag{B.27}$$

where

$$\zeta_i = \frac{5.44T_{ci}^{1/6}}{MW_i^{1/2}P_{ci}^{2/3}}. \tag{B.28}$$

B.5 ENTHALPY

In the compositional calculation, the enthalpy is obtained from the excess enthalpy (h^E) as follows:

$$h^E = h - h^{*} = pv - RT + \frac{T(\partial a/\partial T)-a}{\delta_2-\delta_1}\ln\left(\frac{v+\delta_2 b}{v+\delta_1 b}\right). \tag{B.29}$$

where, h is the system enthalpy and h^{*} is the enthalpy at the ideal gas state. h^{*} is calculated from

$$h^{*} = \sum_i x_i h_i^{*}, \tag{B.30}$$

where, $h_i^{*} = H_A + H_B T + H_C T^2 + H_D T^3 + H_E T^4 + H_F T^5.$ (B.31)

In Equation (B.31), h_i^* is only a function of temperature (${}^oR$) and cannot be derived from an Equation-of-State. Passut and Danner (1972) have compiled the values of H_A through H_F for components commonly encountered in petroleum engineering. In most practical applications, the important variables are the enthalpy differences and not the absolute enthalpies. Thus, the reference point for H can be chosen, arbitrarily. Equation (B.29) can also be written in other form as

$$h=\frac{T\frac{\partial a_{m,j}}{\partial T}-a_{m,j}}{2\sqrt{2}b_{m,j}}Ln\left(\frac{Z_j+(\sqrt{2}+1)B_j}{Z_j-(\sqrt{2}-1)B_j}\right)+RT(Z_j-1)+h^*, \tag{B.32}$$

where $\frac{\partial a_{m,j}}{\partial T}$ is

$$\frac{\partial a_{m,j}}{\partial T}=\frac{1}{2}\sum_{i=1}^{n_c}\sum_{k=1}^{n_c}x_{ij}\,x_{kj}\,(a_i a_k)^{-\frac{1}{2}}(a_i\frac{\partial a_k}{\partial T}+a_k\frac{\partial a_i}{\partial T})(1-\delta_{ik}), \tag{B.33}$$

Since in the energy equation the derivative of enthalpy respect to temperature is required in the Jacobian matrix this term can also be calculated as

$$\frac{\partial h}{\partial T}=\frac{T\frac{\partial^2 a_{m,j}}{\partial T^2}}{2\sqrt{2}\,b_{m,j}}Ln\left(\frac{Z_j+(\sqrt{2}+1)B_j}{Z_j+(\sqrt{2}-1)B_j}\right)+\frac{T\frac{\partial a_{m,j}}{\partial T}-a_{m,j}}{2\sqrt{2}b_{m,j}}\frac{2\sqrt{2}\left(Z_j\frac{\partial B_j}{\partial T}-B_j\frac{\partial Z_j}{\partial T}\right)}{(Z_j+(\sqrt{2}-1)B_j)(Z_j+(\sqrt{2}+1)B_j)}$$
$$+R[(Z_j-1)+T\frac{\partial Z_j}{\partial T}]+\frac{\partial h^*}{\partial T}. \tag{B.34}$$

$$\frac{\partial^2 a_{m,j}}{\partial T^2} = \sum_{i=1}^{n_c} \sum_{k=1}^{n_c} x_{ij}\, x_{kj} [-\frac{1}{4}(a_i a_k)^{-\frac{3}{2}}(a_i \frac{\partial a_k}{\partial T} + a_k \frac{\partial a_i}{\partial T}) +$$

$$\frac{1}{2}(a_i a_k)^{-\frac{1}{2}}(a_i \frac{\partial^2 a_k}{\partial T^2} + 2\frac{\partial a_i}{\partial T}\frac{\partial a_k}{\partial T} + a_k \frac{\partial^2 a_i}{\partial T^2})](1-\delta_{ik}), \tag{B.35}$$

$$\frac{\partial a_i}{\partial T} = -\frac{0.45748 R^2 T_{C_i} \kappa}{P_{C_i} \sqrt{T_{r_i}}}[1+\kappa(1-\sqrt{T_{r_i}})], \tag{B.36}$$

$$\frac{\partial^2 a_i}{\partial T^2} = \frac{0.45748 R^2 \kappa}{2 P_{C_i} T_{r_i}^{1.5}}[1+\kappa], \tag{B.37}$$

To validate the enthalpy calculation, we have compared our results with Computer Modeling Group software (CMG, WINPROP version 2008.10) for a fluid mixture of 50% C1 and 50% NC10, at T = 100 ^{o}F. As can be observed in Figures (B.1) and (B.2), there is a good agreement between our results and the CMG calculation.

B.6 INTERFACIAL TENSION

The general equation for calculating the interfacial tension is (Reid et al, 1977)

$$\sigma^{1/4} = P_{ar}(\rho_l - \rho_g), \tag{B.38}$$

where σ is the interfacial tension in dyne/cm between the liquid and gas phases. ρ_j is the molar density in mol/cm^3 of phase j and p_{ar} is the parachor. For multi-component systems Equation (B.38) becomes

$$\sigma^{1/4} = \sum_{i=1}^{n_c} P_{ar}(x_i \rho_l - y_i \rho_g). \tag{B.39}$$

where x_i and y_i are the composition of competent *i* in liquid and gas phases.

For hydrocarbon systems parchor can be a user-defined value or can be calculated as

$$P_{ari} = \xi CN_i \tag{B.40}$$

$$\xi = \begin{cases} 40 & CN_i \le 12 \\ 40.3 & CN_i > 12 \end{cases} \tag{B.41}$$

CN is the carbon number of the component i.

Table B.1 Fluid properties calculation for a mixture of 50% C1 and 50% NC10 at 100 °F and 1000 psi

Liquid z-factor Z_o	0.437
Gas z-factor Z_g	0.886
Oil mole fraction $V_o (lbmol / lbmol)$	0.280
Oil mole fraction at standard condition $V_{so} (lbmol / lbmol)$	0.301
Oil molecular weight $MW_o (lbm / lbmol)$	103.68
Gas molecular weight $MW_g (lbm / lbmol)$	16.13
Oil density $\rho_o (lbm / ft^3)$	39.51
Gas density $\rho_g (lbm / ft^3)$	3.01
Bubble point pressure $Pb(psi)$	1915
Solution gas oil ratio $R_s (scf / stb)$	273.94
Oil viscosity $\mu_o (cp)$	0.28
Gas viscosity $\mu_g (cp)$	0.00127
Oil formation volume factor $B_o (rbbl / stb)$	1.12
Gas formation volume factor $B_g (ft^3 / scf)$	0.00140

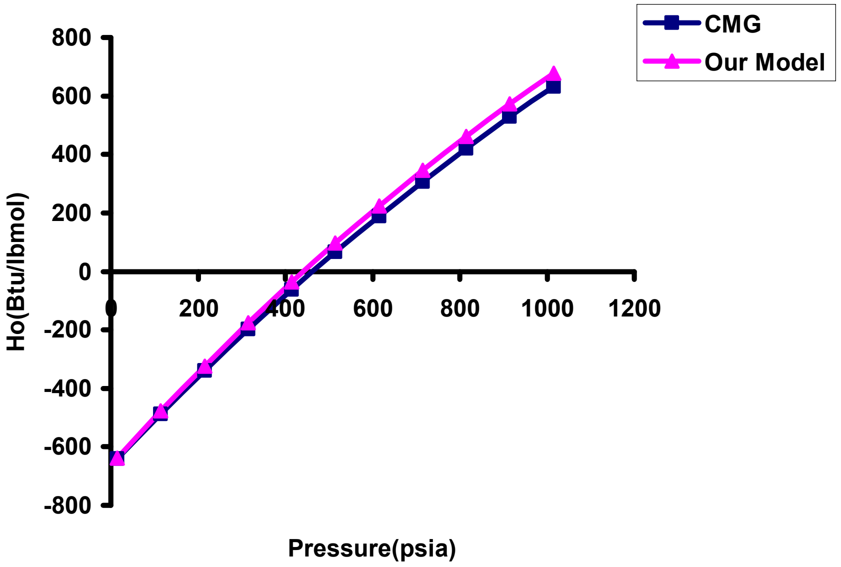

Figure B.1 Oil phase enthalpy calculation and comparison with CMG for the mixture of 50% C1 and 50% NC10, at 100 °F

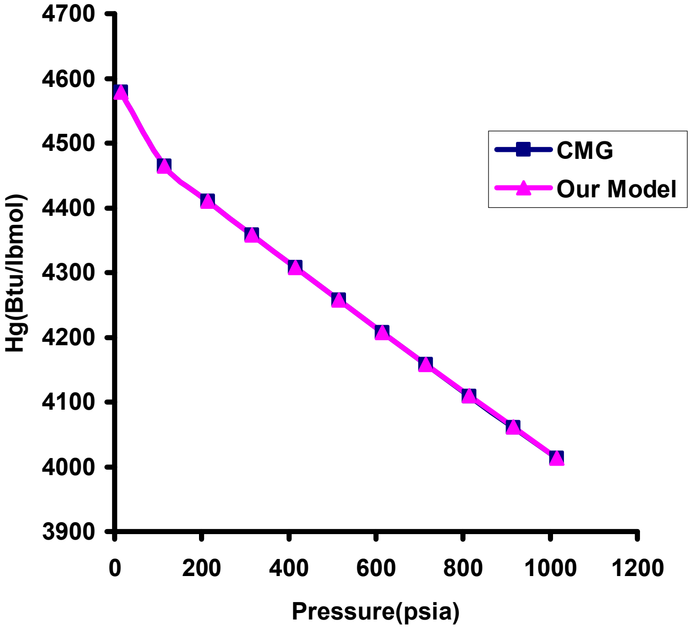

Figure B.2 Gas phase enthalpy calculation and comparison with CMG for the mixture of 50% C1 and 50% NC10, at 100 °F

Appendix C: Black Oil PVT Models

C.1 GAS COMPRESSIBILITY FACTOR

For gas Z-factor calculation, there are different correlations in the literature. Dranchuk and Abou-Kassem (1975) introduced the expression

$$Z=1+\left(A_1+\frac{A_2}{T_r}+\frac{A_3}{T_r^3}+\frac{A_4}{T_r^4}+\frac{A_5}{T_r^5}\right)\rho_r+\left(A_6+\frac{A_7}{T_r}+\frac{A_8}{T_r^2}\right)\rho_r^2$$
$$-\mathrm{A}_9\left(\frac{A_7}{T_r}+\frac{A_8}{T_r^2}\right)\rho_r^5+A_{10}\left(1+A_{11}\rho_r^2\right)\frac{\rho_r^2}{T_r^3}\exp(-A_{11}\rho_r^2)\,. \tag{C.1}$$

where

$$\rho_r=0.27\frac{P_r}{ZT_r}, \tag{C.2}$$

$$T_r=\frac{T}{T_c}, \tag{C.3}$$

$$P_r=\frac{P}{P_c}, \tag{C.4}$$

$$T_c=187.0+330\gamma_g-71.5\gamma_g^2, \tag{C.5}$$

$$P_c=706.0-51.7\gamma_g-11.15\gamma_g^2, \tag{C.6}$$

$$\mathrm{A}=\begin{bmatrix}0.3265,\ \text{-}1.0700,\ \text{-}0.5339,\ 0.01569,\text{-}0.05165\\ 0.5475,\ \text{-}0.7361,\ 0.1844,\ 0.1056,0.6134,0.7210\end{bmatrix}.$$

Benedict et al. (1940) also introduced the expression (C.7) for gas compressibility factor.

$$Z = 1 + \left(A_1 + \frac{A_2}{T_r} + \frac{A_3}{T_r^3} \right) \rho_r + \left(A_4 + \frac{A_5}{T_r} \right) \rho_r^2 +$$
$$\left(\frac{A_5 A_6}{T_r} \right) \rho_r^5 + A_7 \left(1 + A_8 \rho_r^2 \right) \frac{\rho_r^2}{T_r^3} \exp(-A_8 \rho_r^2), \tag{C.7}$$

where

$$A = \begin{bmatrix} 0.31506237, -1.0467009, -0.57832729, -0.53530771, \\ -0.61232032, -0.10488813, 0.68157001, 0.68446549 \end{bmatrix}.$$

C.2 DENSITY

After calculating the gas compressibility factor, the gas density $\left(\frac{lbm}{ft^3} \right)$ can be obtained as follows:

$$\rho_g = \frac{MW_g P}{Z_g R T}, \tag{C.8}$$

where MW_g is the gas molecular weight in $\left(\frac{lbm}{ft^3} \right)$, P is pressure in (psi), R the universal gas constant ,10.73, and T is the temperature (^oR).

Oil density, by using the oil specific gravity (γ_o), the oil formation volume factor (B_o), and dissolved solution gas-oil ratio (R_s) can also be calculated from blackoil models. The Standing's correlation (Standing, 1947) is used to estimate the dissolved gas-oil ratio for saturated oils as follows:

$$R_s = \gamma_g \left(\frac{P}{18 \times 10^{y_g}}\right)^{1.204}, \tag{C.9}$$

where

γ_g = Gas gravity (air =1)

y_g = Gas mole fraction $= 0.00091T - 0.0125\gamma_{API}$

T = Reservoir temperature, °F.

For the saturated oil formation volume factor $B_o\left(\frac{bbl}{stb}\right)$, Standing (1947) presented

$$B_o = 0.972 + 0.000147F^{1.175}, \tag{C.10}$$

where

$$F = R_s\left(\frac{\gamma_g}{\gamma_{OSC}}\right)0.5 + 1.25T. \tag{C.11}$$

Using Equations (C.9) and (C.10), we can obtain the oil density as follows:

$$\rho_o = \frac{62.37\gamma_o + 0.0136 R_s \gamma_g}{B_o}, \tag{C.12}$$

where γ_o is the oil gravity (for water equals to 1).

Other correlations have also been embedded in UTWELL for solution gas oil ratio and oil formation volume factor. De Ghetto et al. (1994) and Vasquez and Beggs (1980) correlations can also be selected for the solution gas oil ratio calculation. Vasquez and Beggs (1980) correlation can also be used for the oil formation volume factor calculation.

C.3 VISCOSITY

For the blackoil model, there are two steps to calculate the oil viscosity. First, the gas-free oil viscosity is obtained and then the gas-saturated oil viscosity is computed. For the first step, Egbogah and Ng (1983) correlations can be applied:

$$log\left(log(\mu_{oD}+1)\right)=1.8653-0.025086\gamma_{API}-0.5644log(T) \tag{C.13}$$

In Equation (C.13), μ_{oD}, is the gas-free oil viscosity, at 14.7 psia. To calculate oil viscosity, μ_{oD} is used in the Beggs and Robinson (1975) correlation, such as

$$\mu_o=A\mu_{oD}^{B}, \tag{C.14}$$

$$A=10.715(R_s+100)^{-0.515}, \tag{C.15}$$

$$B=5.44(R_s+150)^{-0.338}. \tag{C.16}$$

For the gas viscosity calculation, Lee et al. (1966) introduced the following equations:

$$\mu_g=K\exp[X\rho_g{}^{Y}], \tag{C.17}$$

where

$$K = \frac{(9.4+0.02MW_g)T^{1.5}}{209+19MW_g+T}, \tag{C.18}$$

$$X = 3.5+\frac{986}{T}+0.01MW_g, \tag{C.19}$$

$$Y = 2.4-0.2X. \tag{C.20}$$

In Equations (C.17) through (C.20), μ_g is the gas viscosity (μP), ρ_g is the gas density $(\frac{g}{cc})$, MW_g is the gas molecular weight and T is the temperature $({}^oR)$. Other correlations for viscosity of live oil, dead oil, and under-saturated oil from De Ghetto et al. (1994) can be also used in UTWELL blackoil PVT.

C.4 ENTHALPY

The enthalpy is a function of pressure and temperature, via the heat capacity ($C_p\left(\frac{Btu}{{}^oFlbm}\right)$) and Joule-Thomson coefficient ($\eta(\frac{{}^oF}{\frac{Btu}{ft^3}})$), as shown in Equation (C.21).

$$d\bar{h}_j = C_{pj}dT_j - (\frac{144}{J_c})\eta_j C_{pj}dP. \tag{C.21}$$

Hence, enthalpy needs to be calculated with respect to a reference pressure and temperature.

$$\bar{h}_j(T,P) = \bar{h}_j(T_{ref},P_{ref}) + \int_{T_{ref}}^{T} C_{pj}dT - \int_{P_{ref}}^{P} (\frac{144}{J_c})\eta_j C_{pj}dP, \tag{C.22}$$

$$\bar{h}_j(T,P) = \int_{T_{ref}}^{T} C_{pj}dT - \int_{P_{ref}}^{P} (\frac{144}{J_c})\eta_j C_{pj}dP. \tag{C.23}$$

In Equation (C.23) J_c is the conversion factor, η_j is the phase j Joule - Thomson coefficient, and C_{pj} is phase j heat capacity. The Joule-Thomson coefficient can be calculated as follows:

$$\eta_j = \frac{1}{Cp_j}\left(T\left(\frac{\partial}{\partial T}\left(\frac{1}{\rho_j}\right) \right)_p - \frac{1}{\rho_j} \right). \tag{C.24}$$

The heat capacity can be calculated by different correlations for water, oil, and gas. Holman (1958) has reported the following equation for specific heat capacity of water for the range of 20 °C to 290 °C.

$$Cp_w(J/kg.K) = \frac{4245 - 1.841T}{\rho_w}. \tag{C.25}$$

Gambill (1957) has presented the following equation to calculate the specific heat capacity of oil as a function of temperature and oil-specific gravity:

$$Cp_o(J/kg.K) = \frac{1684 + 3.389T}{\sqrt{\gamma_{oil}}}. \tag{C.26}$$

Waples D.W and Waples J.S (2004) presented the temperature dependence of the specific heat capacity for natural gas using a fourth-order polynomial:

$$Cp_g(Btu/lbm.^oF) = AT^4 + BT^3 + CT^2 + DT + E. \tag{C.27}$$

The coefficients in Equation (C.27) are functions of pressure. For instance, the following polynomials are used for methane:

$$A(P) = -2.52\times10^{-22} P^3 + 1.34\times10^{-18} P^2 + -9.15\times10^{-16} P + 1.62\times10^{-13}$$
$$B(P) = 5.37\times10^{-19} P^3 - 2.85\times10^{-15} P^2 + 1.37\times10^{-12} P - 4.67\times10^{-10}$$
$$C(P) = -3.47\times10^{-16} P^3 + 1.86\times10^{-12} P^2 + 2.01\times10^{-11} P + 3.95\times10^{-17}$$
$$D(P) = 7.70\times10^{-14} P^3 - 4.21\times10^{-10} P^2 - 5.96\times10^{-7} P + 3.70\times10^{-4}$$
$$E(P) = -1.03\times10^{-11} P^3 + 5.24\times10^{-8} P^2 + 1.55\times10^{-4} P + 4.88\times10^{-1}.$$

C.5 INTERFACIAL TENSION

For gas and oil interfacial tension the correlation by Baker and Swerdloff (1955)

$$\sigma_{og} = \left(37.7 - 0.05(T - 100.0) - 0.26 API\right)\left(1.0 - 7.1\times10^{-4} P + 2.1\times10^{-7} P^2 + 2.37\times10^{-11} P^3\right). \tag{C.28}$$

For gas and water the correlation by Katz (1955) is used

$$\sigma_{wg} = 70.0 - 0.1(T - 74.0) - 0.002P. \tag{C.29}$$

Appendix D: Derivation of Balance Equations

In many transport systems, field equations are derived to solve the motion of fluids. These equations are usually described based on the conservation laws for mass, momentum, energy, charge, etc. In addition, the constitutive relations and state relations are combined with the conservation laws to explain the interaction and the property of phases respectively.

In this appendix, we briefly discuss the derivation of field equations for single-phase and multi-phase flow systems as shown in Chapters 3 and 4. We follow similar approach discussed in Ishii and Hibiki (2011) for the derivation of these equations.

D.1 GENERAL BALANCE EQUATIONS IN SINGLE-PHASE FLOW

The conceptual models in single-phase flow systems are well-established in continuum mechanics. Single-phase systems are homogenous media with defined boundaries around the fluid.

We can derive the differential balance equation of single-single phase flow system from general integral balance. Assuming a bulk of fluid with density of ρ , Figure D.1, the general integral balance for any quantity of X becomes

$$\frac{d}{dt}\int_{V_m} \rho X\, dV = -\oint_{A_m} nJdA + \int_{V_m} \rho\phi dV, \tag{D.1}$$

where V_m is the material bulk volume, A_m is the material surface area , J is the flux of X from the surface of material and ϕ is the body source of quantity X . Equation (D.1) explains that summation of body source change of quantity X plus the integration of mass flux through the surface boundary of the control volume, V_m, is equal to the accumulation of quantity X in the bulk of fluid. Using the Leibnitz rule for the left hand side integration of Equation (D.1), we obtain

$$\int_{V_m} \frac{\partial \rho X}{\partial t} dV + \int_{A_m} \rho X u.n dA = - \oint_{A_m} n.J dA + \int_{V_m} \rho \phi dV. \tag{D.2}$$

Differentiating Equation (D.2) respect to dV, we obtain

$$\frac{\partial \rho X}{\partial t} + \nabla.\left(u \rho X\right) = -\nabla.J + \rho \phi. \tag{D.3}$$

Equation (D.3) is the differential balance equation for single-phase flow. This equation can be converted to the mass, momentum and energy equations with proper definitions for the quantity X, the flux gradient, J, and the body source and sink terms, ϕ.

For example, assuming $X = 1, J = 0$, $\phi = 0$, Equation (D.3) becomes mass conservation equation as

$$\frac{\partial \rho}{\partial t} + \nabla.\left(u \rho\right) = 0. \tag{D.4}$$

Accordingly, introducing $X = u$ (actual velocity), $J = -T = pI - \tau$ (pressure and viscous stress tensor) and $\phi = g$ (gravity acceleration), we obtain momentum conservation equation as

$$\frac{\partial \rho u}{\partial t} + \nabla.\left(u \rho\right) = -\nabla P + \nabla.\tau + \rho g. \tag{D.5}$$

Finally for $X = e + \frac{u^2}{2}$, $J = q - T.u$, $\phi = g.u + \frac{\dot{q}}{\rho}$, we achieve the energy conservation equation as

$$\frac{\partial \rho \left(e + \frac{u^2}{2} \right)}{\partial t} + \nabla . \left(\rho \left(e + \frac{u^2}{2} \right) u \right) = -\nabla . q + \nabla . \left(T.u \right) + \rho g.u + \dot{q}, \tag{D.6}$$

where e is the internal energy, q is the heat flux, $\dot{q}$ body heat loss/gain.

D.2 GENERAL BALANCE EQUATIONS IN MULTIPHASE FLOW

In multiphase flow systems, a great deal of difficulties is encountered for derivation of field equations due to discontinuity of the bulk of fluids. In contrast to single-phase flow, multiphase flow systems are no longer homogeneous media and consequently are not continuously differentiable in the integration region. In fact, the presences of interface between fluids (such as bubble and liquid or droplet and gas) in a bulk of fluids causes source of discontinuities. Thus, to derive the field equations in the multiphase flow systems the continuity of flow parameters should be maintained by averaging the bulk of fluids. For this reason, in multiphase flow systems understanding the local characteristic of the flow and methods for up-scaling (averaging) the microscopic phenomena between multiphase fluids are crucial.

Averaging procedures of parameters can be classified into three groups:

1) Eulerian Mean Value

Function: $F = F(t, x)$

Time mean value: $\frac{1}{\Delta t}\int_{\Delta t} F(t,x)dx$

Spatial mean value: $\frac{1}{\Delta Z}\int_{\Delta Z} F(t,x)dZ(x)$

Volume: $\frac{1}{\Delta V}\int_{\Delta V} F(t,x).dV$

2) Lagrangian Mean Value

Function: $F = F(t,X),\ \ X = X(x,t)$

Time mean value: $\frac{1}{\Delta t}\int_{\Delta t} F(t,X)dx$

3) Boltzman Statistical Average

Particle density function: $f = f(x,\xi,t)$

Transport properties: $\psi(t,x) = \frac{\int \psi(\xi) f d\xi}{\int f d\xi}$

In this section, our goal is to average fluid properties and field equations in order to obtain a continuum media for the multiphase flow system. Let us assume a reference point x_0 in the flow path that phase 1 and phase 2 passes frequently this location. As can be seen in Figure D.2, the properties that are recorded at this location change with time as step functions. Hence, we observe a heterogonous media in the multiphase flow system which the fluid varies by location and time.

In order to derive the global balance equations in multiphase flow system we are required to establish continuously differentiable functions for the flow variables. Assuming function $F_k = F_k(x_0,t)$ as one of the flow variables (i.e. volume fraction) of phase k at time t and location x_0, function $\overline{F}_k$ can be defined as average value of F_k for time period Δt, which $\overline{F}_k$ is continuous and differentiable

$$\overline{F_k} = \frac{1}{\Delta t} \int_{\Delta t} F_k(x_0, t) dt. \tag{D.7}$$

In other word, our interpretation from $\overline{F_k}$ is the probability of seeing phase k at location x_0 at neighborhood of time t. This definition actually scales the microscopic phase dynamics phenomena to macroscopic scale with continuum attribution. Using Equation D.7 for phase volume fraction we obtain

$$\alpha_k(x_0, t) = \frac{1}{\Delta t} \int_{\Delta t} M_k(x_0, t) dt, \tag{D.8}$$

where $M_k(x_0, t)$ is one when phase k exist at location x_0 and is zero when it does not exist. Hence, $\alpha_k(x_0, t)$ means the probability of existence of phase k at location x_0. $\alpha_k(x_0, t)$ can also be defined as $\overline{M_k}$ according to Equation D.7.

Using the following definitions, we can also obtain the volume and mass average functions as

$$\overline{\overline{F_k}} = \frac{\overline{M_k F_k}}{\overline{M_k}} = \frac{\overline{F_k}}{\alpha_k}, \tag{D.9}$$

$$\hat{\psi} = \frac{\overline{\rho_k \psi_k}}{\overline{\rho_k}} = \frac{\overline{\overline{\rho_k \psi_k}}}{\overline{\overline{\rho_k}}}. \tag{D.10}$$

Using the definitions explained in Equations D.7 through D.10, Ishii and Hibiki (2011) derived the general balance equation for multiphase flow system as follows:

$$\frac{\partial \alpha_k \overline{\overline{\rho_k}}\, \widehat{X_k}}{\partial t} + \nabla.\left(\alpha_k \overline{\overline{\rho_k}}\, \widehat{X_k}\, \widehat{u_k}\right) = -\nabla.\left[\alpha_k \left(\overline{\overline{J_k}} + J_k^T\right)\right] + \alpha_k \overline{\overline{\rho_k}}\, \widehat{\phi_k} + I_k, \tag{D.11}$$

where $\widehat{X_k}$ is weighted quantity mean value, $\widehat{u_k}$ weighted mean velocity of phase k , $\overline{\overline{J_k}}$ is surface flux of phase k, J_k^T is turbulent flux, $\widehat{\phi_k}$ is body source and I_k is interfacial source term.

Consequently, similar to the single-phase model, Equation D.11 can be converted to mass, momentum and energy balance equations with appropriate definitions for the quantity variables. Assuming $\widehat{X_k} = 1$, $\overline{\overline{J_k}} = 0$, $J_k^T = 0$, $\widehat{\phi_k} = 0$ and $I_k = \Gamma_k$ (interphase mass transfer rate), mass balance equation for phase k becomes

$$\frac{\partial \alpha_k \overline{\overline{\rho_k}}}{\partial t} + \nabla.\left(\alpha_k \overline{\overline{\rho_k}}\, \widehat{u_k}\right) = \Gamma_k. \tag{D.12}$$

Like-wise for $X_k = u_k$ (actual velocity), $J_k = -T_k = P_k I - \vec{\tau}_k$ (pressure and viscous shear tensor), $J_k^T = \bar{\tau}_k^T$ (turbulent shear tensor), $\widehat{\phi_k} = g_k$ (gravity acceleration), and $I_k = M_k$ (interphase momentum transfer rate), momentum balance equation for phase k becomes

$$\frac{\partial \alpha_k \overline{\overline{\rho_k}}\, \widehat{u_k}}{\partial t} + \nabla.\left(\alpha_k \overline{\overline{\rho_k}}\, \widehat{u_k}\, \widehat{u_k}\right) = -\nabla.\left[\alpha_k P_k\right] + \nabla.\left[\alpha_k \left(\overline{\overline{\tau_k}} + \bar{\tau}_k^T\right)\right] + \alpha_k \overline{\overline{\rho_k}}\, \widehat{g_k} + M_k. \tag{D.13}$$

For energy balance equation we use $X_k = e_k + \frac{u_k^2}{2}$ (internal energy and kinetic energy), $J_k = q_k - T_k.u_k$ (condition and friction heat flux), $J_k^T = q_k^T$ (turbulent heat flux),

$\widehat{\phi_k} = g_k . u_k + \frac{\dot{q}_k}{\rho_k}$ (gravity potential and heat loss/gain) and $I_k = E_k$ (interfacial heat transfer) to obtain

$$\begin{aligned} &\frac{\partial}{\partial t}\left[\alpha_k \overline{\overline{\rho_k}}\left(\widehat{e_k} + \frac{\widehat{u_k^2}}{2}\right)\right] + \nabla .\left(\alpha_k \overline{\overline{\rho_k}}\left(\widehat{e_k} + \frac{\widehat{u_k^2}}{2}\right)\widehat{u_k}\right) = \\ &-\nabla .\left[\alpha_k\left(\overline{\overline{q_k}} + q_k^T\right)\right] + \nabla .\left(\alpha_k \overline{\overline{T_k}}\,\widehat{u_k}\right) + \alpha_k \overline{\overline{\rho_k}}\,\widehat{g_k} . \widehat{u_k} + E_k . \end{aligned} \qquad \text{(D.14)}$$

Equations D.12 through D.14 are the differential balance equations for multiphase flow systems that have been used in our multiphase flow calculations with some simplifications.

D.3 BASIC ASSUMPTIONS

In Chapters 3 and 4, we added the following assumptions to the general balance equations in Section D.1 and D.2 to obtain the final format of our conservation equations for single-phase and multiphase flow models:

- One-dimensional flow with Eulerian coordination is used.
- Flow path can have arbitrary cross section (with defined hydraulic diameter) and arbitrary trajectory in (*x, y, z*) coordination.
- Field units are considered in the equations of Chapters 3 and 4. Conversion factors such as g_c and J_c are included in the equations.
- Flow path can be surrounded by reservoir as a tank model. Hence the influx terms for each phase from reservoir ($\dot{\psi}_k$) is added to the mass balance equations (Equation D.12).

- Deposition rate ($\dot{m}_{d,s}$) for the solid phase is also considered in the mass balance equation for solid phase.
- Physical dispersion for mass transfer is neglected in the axial direction.
- Phases are liquid (mixture of oil and water) and gas in the momentum equation.
- Oil and water slippage in the liquid system is considered via drift-flux models.
- Momentum interface models in Equation D.13 is replaced by RELAP5 (2011) one-dimensional models as $M_k = \Gamma_k u_{ki} - \alpha_k \rho_k \left(u_k - u_i \right) FIK$.
- Shear tensor ($\overline{\overline{\tau_k}}$) and turbulent tensor ($\overline{\tau}_k^T$) momentum transfer terms in momentum balance equations are neglected and one-dimensional wall-phase shear forces are included using RELAP5 (2011) approach, $\tau_k = -\alpha_k \rho_k u_k FWK$.
- Phase pressures are all assumed to be the same $P_k = P, \quad k = 1, ..., n.$
- We use the summation of energy balance equations for each phase to obtain the temperature in the fluids.
- Enthalpy is used instead of internal energy in the energy equation.
- Enthalpy influx terms for each phase from reservoir ($\dot{H}_k$) is added to the total energy balance equation.
- Phase temperatures are all assumed to be the same $T_k = T, \quad k = 1, ..., n.$
- Interfacial heat transfer is neglected.
- Conduction heat transfer in axial direction ($-\nabla.q$) in the energy equation is neglected.
- Shear stress (friction) heat transfer term ($\nabla.\left(T.u\right)$) in the energy equation is neglected.
- Turbulent heat flux in axial direction (q^T) in the energy equation is neglected.
- Local equilibrium and negligible capillary pressure effect on hydrocarbon thermodynamic equilibrium is considered in the system.
- Up to four phases are allowed to exist in the model as water, oil, gas, and precipitated solids.

- Hydrocarbon mixture is assumed as *nc* components with no water.
- The aqueous phase is pure water plus dissolved ions and solid precipitates.
- The bubbles coalescence and break up is neglected.

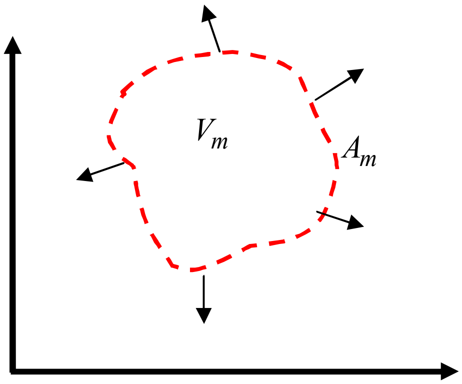

Figure D.1 Fluid bulk control volume

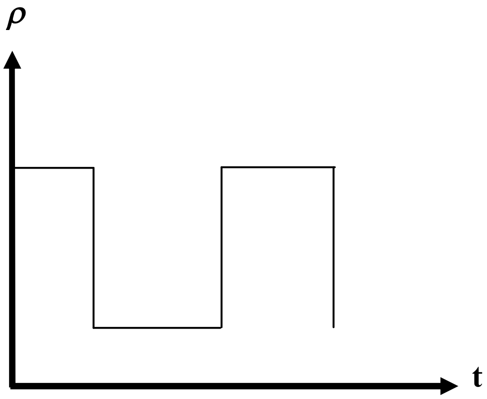

Figure D.2 Density change with time at point x_0

Appendix E : Unit Conversions

$$1(psi) = 1\left(\frac{lbf}{in^2}\right)$$

$$144\left(in^2\right) = 1\left(ft^2\right)$$

$$J_c\left(ft - lbf\right) = 1\left(Btu\right), J_c = 778.16926$$

$$g_c\left(ft / \sec^2\right) = 1\left(lbf\right), g_c = 32.174049$$

$$1\left(bbl\right) = 42\left(Gal\right)$$

$$1\left(bbl\right) = 5.61458\left(ft^3\right)$$

$$1\left(Btu\right) = 1055.05585\left(J\right)$$

$$1\left(lbm\right) = 0.45359237\left(kg\right)$$

$$1\left(ft\right) = 30.48\left(cm\right)$$

$$1\left(lbmole\right) = 453.59237\left(gmole\right)$$

$$1\left(psi\right) = 6894.744825\left(Pa\right)$$

Appendix F: UTWELL Keywords

The main UTWELL input file (INPUT.CFG) consists of comment lines (starting with CC) and keyword lines (starting with *). The UTWELL simulator ignores all comment lines.

If more than one well is introduced in the input data include files can be defined and the wells input data can be stored in the include files separately.

Input variables are read in the following order:

- Well trajectory, casing data, tubing data and formation data
- Fluid properties
- Reservoir data
- Process condition
- Initial condition
- Boundary conditions
- Output options
- Numerical options

F.1 FLOW PATH DEFINITION AND TRAJECTORY

F.1.1 NWLBR, FLOWPATH, INCLUDE

NWLBR - Total number of wells/flow-paths in the simulation
FLOWPATH - Type of flow paths
Possible values:
WELL
PIPELINE
INCLUDE - Name of the include files for each well

F.1.2 LW, WNAME

LW - Well index
WNAME - Well/flow path name

F.1.3 MAXGRIDSIZE, WSURFACE

MAXGRIDSIZE - Maximum size of the wellbore gridblock, [ft]

WSURFACE – Wellbore surface datum, [ft]

F.1.4 TRAJINTVL, MD, TVD, INCLINATION, AZIMUTH

TRAJINTVL - Number of the trajectory intervals in the wellbore
MD - Measured depth of well's intervals, [ft]
TVD - True vertical depth of well's intervals, [ft]
INCLINATION - Inclination of each interval of the well trajectory, [deg]
AZIMUTH - Azimuth angle of each interval of the well trajectory, [deg]

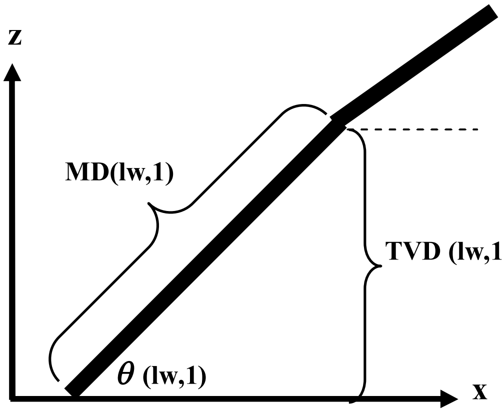

F.1.5 CASEINTVL, HANGERDEPTH, SETTINGDEPTH, RCI, RCO, RWB

CASEINTVL - Number of casing surrounding the well
HANGERDEPTH - Hanger depth of each casing, [ft]
SETTINGDEPTH - Setting depth of each casing, [ft]
RCI - Inner radius of each casing, [ft]
RCO - Outer radius of each casing, [ft]
RWB - Wellbore radius around each casing, [ft]

F.1.6 CEMENTOP, EPSCI, EPSCO, KCASE, KCEM, HCFC, CASEANLSFLUID

CEMENTOP - Top elevation of the cement, [ft]
EPSCI - Inner emissivity of the casing, [ft]
EPSCO - Outer emissivity of the casing
KCASE - Casing heat transfer conductivity, [Btu/hr-ft-^{o}F]
KCEM, Cement heat transfer conductivity, [Btu/hr-ft-^{o}F]
HCFC, Tuning factor for the total heat transfer in the casing
CASEANLSFLUID, Type of the fluid ID between annulus and casing, which is chosen from Annuls fluid database

F.1.7 OPENHOLE_LENGTH, OPENHOLE_RWB, OPENHOLE_ROUGHNESS

OPENHOLE_LENGTH - Length of open hole perforation zone, [ft]
OPENHOLE_RWB - Diameter of flow path in the open-hole zone, [ft]
OPENHOLE_ROUGHNESS - Flow path roughness in the perforation zone, [ft/ft]

F.1.8 TUBINTVL, TUBETOP, TUBEBOTT, RTI, RTO

TUBINTVL - Number of tubing intervals in the well trajectory
TUBETOP - Top depth of tubing interval, [ft]
TUBEBOTT - Bottom depth of tubing interval, [ft]
RTI - Inner radius of tubing interval, [ft]
RTO - Outer radius of tubing interval, [ft]

F.1.9 EPSTO, KTUB, CKNESS, KINS, HCFT, TUBANLSFLUID, ROUGHNESS

EPSTO - Outer emissivity of the tubing
KTUB - Tubing heat transfer conductivity, [Btu/hr-ft-°F]
INSTHICKNESS - Thickness of the insulator around the tubing, [ft]
KINS - Insulator heat transfer conductivity, [Btu/hr-ft-°F]
HCFT - Tuning factor for overall heat transfer factor of tubing
TUBANLSFLUID - Type of the fluid between annulus and tubing
ROUGHNESS - Surface roughness of the tubing, [ft/ft]

F.1.10 FORMINTVL, FORMATIONTOP, FORMATIONBOTT

FORMINTVL - Number of different formation types
FORMATIONTOP - Top depth of the formation, [ft]
FORMATIONBOTT - Bottom depth of formation type, [ft]

F.1.11 FORMATIONTVD, KEARTH, DENEARTH, CEARTH, TAMBTOP, TAMBOTT

FORMATIONTVD - True vertical depth of the formation, [ft]
KEARTH - Surrounding formation heat transfer conductivity, [Btu/hr-ft-°F]
DENEARTH - Surrounding formation density, [lbm/ft^3]
CEARTH - Surrounding formation heat capacity, [Btu/lb.°F]
TAMBTOP - Ambient temperature at the surface of the interval, [°F]
TAMBOTT - Ambient temperature at the bottom of the interval, [°F]

F.1.12 IUTO, UTOTAL

IUTO - Heat transfer coefficient flag
Possible values
0: internal calculation
1: constant user specified value

UTOTAL - Total heat transfer coefficient for IUTO = 1, [Btu/ft^2-sec-°F]

F.2 FLUID PROPERTY

F.2.1 NPHASE, NCOMP, PVTYPE, PHASEID

NPHASE - Number of phase in the EOS calculation
NCOMP - Number of hydrocarbon components
PVTYPE - Type of phase behavior
Possible values
1: compositional
2: steam
3: blackoil
PHASEID - Flag for type of fluid in single
Possible values
0: mixture
1: gas
3: oil
4: water

F.2.2 ICOMPLIB, EOSTYPE, IENTH

ICOMPLIB - Flag for reading the fluid characterization data
Possible values
0: read from input data
1: read from components database
EOSTYPE - Number of hydrocarbon components
Possible values
1: cubic EOS PR
2: cubic EOS PR plus Asphaltene
3: cubic EOS PR plus Wax
IENTH - Type of phase behavior
Possible values
1: ideal gas enthalpy
2: heat capacity coefficients

F.2.3 COMPNAME, PC, TC, VC, WT, OM, PARACHOR, VSP

COMPNAME - Defines he components name in the crud oil mixture
PC - Critical pressure, [psi]
TC - Critical temperature [^{o}F]
VC - Critical volume [ft^3/lbmole]
WT - Components molecular weight [lbm/lbmole]
OM - Components Acentric factor
PARACHOR - Compoenents parachor
VSP - Components volume shift

F.2.4 HA, HB, HC, HD, HE, HF

HA - Components first enthalpy coefficient
HB - Components second enthalpy coefficient
HC - Components third enthalpy coefficient
HD - Components fourth enthalpy coefficient
HE - Components fifth enthalpy coefficient
HF - Components sixth enthalpy coefficient

F.2.5 DELTA(IC, IC)

DELTA(IC, IC) - Components binary interaction coefficients

F.2.6 RSCORR, RSCALIBRATE, ZGCORR, DOVCORR, VISGCORR, IFTOGCORR, IFTWGCORR, ETNHCORR

RSCORR - Correlation flag for solution gas oil ratio
Possible values
1: De Ghetto
2: Vazquez / Beggs
RSCALIBRATE - Flag for calibration of the solution gas oil ratio
Possible values
0: No scaling
1: Scaling
ZGCORR - Correlation flag for the gas compressibility factor
Possible values
1: Robinson
2: Yarborough / Hall
3: Dranchuck / Abu-Khassem
DOVCORR - Correlation flag for dead oil viscosity
Possible values
1: De Ghetto
VISGCORR - Correlation flag for gas viscosity
Possible values
1: Lee-Gonzalez –Eakin (1)
2: Lee-Gonzalez –Eakin (2) – PIPESIM 2011
IFTOGCORR - Correlation flag for gas and oil interfacial tension
Possible values
1: Baker / Swerdloff
IFTWGCORR - Correlation flag for water gas interfacial tension
Possible values
1: Katz
ENTHCORR - Correlation flag for enthalpy calculation
Possible values
1: Default method
2: PIPESIM 1983 method (no Joule Thomson effect)
3: PIPESIM 2009 method (with Joule Thomson effect)

F.2.7 PSEP, TSEP, PBUB, TBUB, RSBUB

PSEP - Separator pressure [psi]
TSEP - Separator temperature [^{o}F]
PBUB - Bubble point pressure [psi]
TBUB - Bubble point temperature [^{o}F]
RSBUB - Solution gas oil ration at the bubble point pressure [ft^3/bbl]

F.2.8 CPW, CPO, CPG, CPWMETHOD, CPOMETHOD, CPGMETHOD, DHVAP

CPW - User specified water heat capacity
CPO - User specified oil heat capacity
CPG - User specified gas heat capacity
CPWMETHOD - Correlation flag for water specific heat capacity calculation
Possible values
1: User input
2: Holman model
CPOMETHOD - Correlation flag for water specific heat capacity calculation
Possible values
1: User input
2: Gambill model
CPGMETHOD - Correlation flag for water specific heat capacity calculation
Possible values
1: User input
2: Waples model
DHVAP - Latent heat of vaporization

F.2.9 GW, GG, API

GW - Water specific gravity in balckoil model
GG - Gas specific gravity in balckoil model
API - Oil API gravity in balckoil model

F.2.10 IASPH, IWAX, ISCALE

IASPH - Flag for asphaltene flow assurance
Possible values
0: off
1: on
IWAX - Flag for wax flow assurance
Possible values
0: off
1: on

ISCALE - Flag for scale flow assurance
Possible values
0: off
1: on

F.2.11 VBS, KCONDASPH, KS1S2, IDEPOSIT, DPS1, DPS2, KDLMNAR KDS1, KDS2, EAS1, EAS2, TAWK, TAW

VBS - Asphaltene solid molar volume, [ft3/lbmol]
KCONDASPH - Asphaltene solid phase heat transfer conductivity, [Btu/hr-ft-^{o}F]
KS1S2 - First order asphaltene aggregation kinetic rate between particle S1 and S2
IDEPOSIT - Flag for different models for particle transportation in radial direction
Possible values
1: Friedlander
2: Beal
3: Mansoori 1993
4: Mansoori 1995

5: Clever and Yates
DPS1 - Smallest asphaltene particle size, [cm]
DPS2 - Largest asphaltene particles size, [cm]
KDLMNAR - Transport coefficient tuning factor for laminar flow
KDS1 - Transport coefficient tuning factor for turbulent flow for the smallest particles
KDS2 - Transport coefficient tuning factor for turbulent flow for the largest particles
EAS1 - Activation energy for smallest particles adhesion forces on the surface, [kJ]
EAS2 - Activation energy for the largest particles adhesion forces on the surface, [kJ]
TAWK - Shear force removal tuning factor
TAWA - Shear force removal power coefficient
TAWMAX – Maximum shear force for deposit removal, [psi]

F.2.12 PORMAX, PORCB, PORCZ, TAWA, SURFCOEF, HLDPCOEF, KDWAX, KCONDWAX

PORMAX – Wax crystal maximum porosity
PORCB – Wax porosity power coefficient
PORCZ – Wax shear stress power coefficient for porosity reduction
SURFCOEF – Wetted surface area power coefficient for wax multiphase flow deposition rate
HLDPCOEF - Holdup power coefficient for wax multiphase flow deposition rate
KDWAX - Transport coefficient tuning factor for wax deposition
KCONDWAX – Wax solid phase heat transfer conductivity, [Btu/hr-ft-^{o}F]

F.2.13 KCONDSCALE, IDEPOSITAQ, DPSAQ, KDLMNRAQ, KDAQ, EAQ

KCONDSCALE - Scale solid phase heat transfer conductivity, [Btu/hr-ft-^{o}F]
IDEPOSITAQ - Flag for different models for scale transportation in radial direction
Possible values
1: Friedlander
2: Beal
3: Mansoori 1993
4: Mansoori 1995
5: Clever and Yates
DPSAQ - Scale particle size, [cm]
KDLMNRAQ - Transport coefficient tuning factor for scale deposition in laminar flow
KDAQ - Transport coefficient tuning factor for scale deposition in turbulent flow
EAQ - Activation energy for scale adhesion forces on the surface, [kJ]

F.2.14 NONSET, PSTAR, TSTAR

NONSET - Number of aspahltene precipitation onset data
PSTAR - Asphaltene onset pressure, [psi]
TSTAR - Asphaltene onset temperature, [^{o}F]

F.2.15 WAXCOMP, HFI, TFI, VFI, WAXPREF

WAXCOMP - Wax forming components ID number
HFI - Fusion enthalpy for liquid/solid conversion, [Btu/lbmol]
TFI - Melting Temperature [^{o}R]
VFI - Wax solid shrinkage factor

WAXPREF - Wax formation reference pressure, [psi]

F.2.16 AQELEMENT, AWSPECIES, AQSOLID, DENAQSOLID, MWAQSOLID

AQELEMENT - Name of elements in the geochemical scale reaction
AWSPECIES - Name of specious in the geochemical scale reaction
AQSOLID - Name of solids in the geochemical scale reaction
DENAQSOLID - Density of solid phase, [lbm/ft^3]
MWAQSOLID - Molecular weight of solid phases, [lbm/lbmol]

F.2.17 REFPRESS, REFTEMP

REFPRESS - Reference pressure, [psi]
REFTEMP - Reference temperature, [^{o}F]

F.3 PROCESS CONDITION

F.3.1 IRESERVOIR

IRESERVOIR - Flag for wellbore/reservoir coupling
Possible values
0: Static coupling
1: Dynamic coupling

F.3.2 RESINTVL, RESERVOIRTOP, RESERVOIRBOTT, PERFSHOT

RESINTVL - Number of reservoir intervals along the well
RESERVOIRTOP - Reservoir top (MD) for an interval, [ft]
RESERVOIRBOTT - Reservoir bottom (MD) for an interval, [ft]
PERFSHOT - Number of perforation in an interval

F.3.3 RESTIME, PRESERVOIR, TRESERVOIR, PIO, PIW, PIG, Z(IC), CELET (IC), MOLESLD

RESTIME - Times for the variation reservoir conditions, [day]
PRESERVOIR - Reservoir pressure, [psi]
TRESERVOIR - Reservoir temperature, [^{o}F]
PIO - Reservoir productivity index for oil phase, [ft^3/psi-ft]
PIW- Reservoir productivity index for water phase, [ft^3/psi-ft]
PIG - Reservoir productivity index for gas phase, [ft^3/psi-ft]
Z(IC) - Fluid composition influx to the reservoir
CELET (IC) - Geochemical Elements concentration influx to the reservoir, [lbmol/kg]
MOLESLD - Mole of geochemical solid influx to the reservoir, [lbmol/kg]

F.3.4 IPROD, ITHERMAL, ITRANSIENT, IMODEL, ISLIPOW, ISLIPGL, IFI, IFWL, IFWG, ICVRM

IPROD - Flag for production or injection well
Possible values
1: injector
-1: producer
ITHERMAL - Flag for energy equation solution
Possible values
0: off
1: on
ITRANSIENT - Flag for transient solution
Possible values
0: off
1: on
IMODEL - Flag for different numerical solutions in transient simulation
Possible values
0: fully implicit homogenous model (FIMPHM)
1: fully implicit drift-flux model (FIMPDF)
2: semi-implicit two-fluid model (SIMPTF)
3: nearly-implicit two-fluid model (NIMPTF)
4: semi-implicit homogenous model (SIMPHM)

ISLIPOW - Flag for slippage between oil and water in liquid system
Possible values
0: no slip
1: slip

ISLIPGL - Flag for slippage between gas and liquid
Possible values
0: no slip
1: slip
IFI – Interphase drag force tuning factor
IFWL – Wall / liquid drag force tuning factor
IFWG – Wall / gas drag force tuning factor
ICVRM – Virtual mass coefficient tuning factor

F.4 INITIAL CONDITION

F.4.1 TINIT, PINIT, HLDPHC, HLDPW, UGINIT, UOINIT, UWINIT

TINIT - Wellbore initial temperature, [^{o}F]
Possible values
0: equilibrium with reservoir condition
Cnst: user specified constant value
PINIT - Wellbore initial pressure, [psi]
Possible values
0: equilibrium with reservoir condition

Cnst: user specified constant value

HLDPHC - Wellbore initial oil volume fraction
HLDPW - Wellbore initial water volume fraction
UGINIT - Wellbore initial gas superficial velocity
UOINIT - Wellbore initial oil superficial velocity
UWINIT - Wellbore initial water superficial velocity

F.5 BOUNDARY CONDITION

F.5.1 IBCTIME, IBCTYPE, IBCP, IBCT, IBCMASSO, IBCMASSW, IBCMASSG, IBCFLOWO, IBCFLOWG, IBCFLOWW, IBCWCUT, IBCGLR, BCF

IBCTIME - Inlet boundary condition time variation
IBCTYPE - Type of inlet boundary condition
Possible values
PRESSURE: pressure node
MASS: mass node
FLOW: flow node
CLOSE: close node
BHP: constant bottom-hole pressure producer
IBCP - Inlet boundary condition pressure, [psi]
IBCT - Inlet boundary condition temperature, [^{o}F]
IBCMASSO - Inlet boundary condition oil mass flow rate, [lbm/sec]
IBCMASSW - Inlet boundary condition water mass flow rate, [lbm/sec]
IBCMASSG - Inlet boundary condition gas mass flow rate, [lbm/sec]
IBCFLOWO - Inlet boundary condition oil flow rate, [ft^3/sec]
IBCFLOWW - Inlet boundary condition water flow rate, [ft^3/sec]
IBCFLOWG - Inlet boundary condition gas flow rate, [ft^3/sec]
IBCWCUT - Inlet boundary condition water cut
IBCGLR - Inlet boundary condition gas/liquid ratio
BCF - Boundary condition factor. This factor shows that how fast the boundary value is assigned to system. This value is between 0 and 0.9. 0 is the immediate boundary condition. 0.9 is variable boundary condition, where after about 100 time step of calculation the boundary condition is set to boundary value.

F.5.2 OBCTIME, OBCTYPE, OBCP, OBCT, OBCMASSO, OBCMASSW, OBCMASSG, OBCFLOWO, OBCFLOWG, OBCFLOWW

OBCTIME - Outlet boundary condition time variation
OBCTYPE - Type of outlet boundary condition
Possible values
PRESSURE: pressure node
MASS: mass node
FLOW: flow node
CLOSE: close node

PRODWHP: constant wellhead pressure producer
INJWHP: constant wellhead pressure injector
PROWHQ: constant wellhead flow rate producer
INJWHQ: constant wellhead flow rate injector

OBCP - Outlet boundary condition pressure, [psi]
OBCT - Outlet boundary condition temperature, [^{o}F]
OBCMASSO - Outlet boundary condition oil mass flow rate, [lbm/sec]
OBCMASSW - Outlet boundary condition water mass flow rate, [lbm/sec]
OBCMASSG - Outlet boundary condition gas mass flow rate, [lbm/sec]
OBCFLOWO - Outlet boundary condition oil flow rate, [ft^3/sec]
OBCFLOWW - Outlet boundary condition water flow rate, [ft^3/sec]
OBCFLOWG - Outlet boundary condition gas flow rate, [ft^3/sec]

F.6 OUTPUT OPTIONS

F.5.1 TPRINT

TPRINT - Frequency of reporting the variables profile in .PRF and .ASR files

F.5.1 IPVT, PLOTTEMP1, PLOTTEMP2, PLOTPRES1, PLOTPRES2

IPVT - Flag for PVT output files
Possible values
0: off
1: on

PLOTTEMP1 - Pressure interval beginning value for PVT plot, [psi]
PLOTTEMP2 - Pressure interval ending value for PVT plot, [psi]
PLOTPRES1 - Temperature interval beginning value for PVT plot, [^{o}F]
PLOTPRES2 - Temperature interval beginning value for PVT plot, [^{o}F]

F.7 NUMERICAL OPTIONS

F.5.1 WTOLP, WTOLT, WTOLQ, WMAXITER

WTOLP - Pressure convergence tolerance in steady state models, [psi]
WTOLT - Temperature convergence tolerance in steady state models, [^{o}F]
WTOLQ - Temperature convergence tolerance in steady state models, [ft^3/day]
WMAXITER - Maximum iteration for balance equations convergence

F.5.2 WTOLM, WTOLE, RME, WMAXITER, CFLCHECK

WTOLM - Material balance and momentum balance convergence tolerance in transient model

WTOLE - Energy balance convergence tolerance in transient model
RME - Residual mass balance error. This value is critical for adaptive time step sizing
CFLCHECK - Courant number check for time step sizing in semi-implicit methods
Possible values
0: off
1: on

F.5.3 STARTIME, ENDTIME, DTMIN, DTMAX

STARTIME - Start time for simulation, [day]
ENDTIME - End time for the simulation, [day]
DTMIN - Minimum time step size for automatic time step sizing, [day]
DTMAX - Maximum time step size for automatic time step sizing, [day]

Appendix G: Sample Input Data

G.1 TRANSIENT THREE PHASE FLOW SIMULATION

The following is a sample input data file for the standalone wellbore simulator. We used this case in Chapter 5 for three-phase flow model. The program language is FORTRAN 90 and it is run on windows.

```
CC ==================================================================*
CC  WELLBORE MODEL INPUT DATA                                        *
CC ================================================================= *
CC                                                                   *
CC CASE NAME:  NIMPTF - MODEL, THREE PHASE BLACKOIL                  *
CC CREATED BY: Mahdy Shirdel 08/13/2012                              *
CC                                                                   *
CC ==================================================================*
CC
CC MAXIMUM NUMBER OF WELLS IN CALCULATION AND FLOWPATH TYPE
* NWLBR  FLOWPATH
   1        WELL

CC********************************************************************
CC WELL #01 DATA                                                     *
CC********************************************************************

CC
CC CASE DEFINITION: {WELL ID}
* LW      WNAME
   1      TEST
CC
CC MESH GRID SIZE [FT]
* MAXGRIDSIZE
     80.0
CC
CC WELL SURFACE [FT]
* WSURFACE
          0.0
CC
CC WELL PROFILE AND SURVEY
* TRAJINTVL  MD        TVD     INCLINATION     AZIMUTH
     1       2000.0    2000.0      90.0        0.0
CC
CC WELL CASING AND COMPLETION {Default RWB=RCO+0.041665}  (CODE:7")
* CASEINTVL HANGERDEPTH  SETTINGDEPTH  RCI         RCO       RWB      CEMENTOP
     1        0              2000       0.21      0.25      0.2541       0

* EPSCI  EPSCO    KCASE    KCEM    HCFC   CASEANLSFLUID
 0.9      0.9      26.0     4.02    1.0        19

CC
CC WELL OPEN HOLE
* OPENHOLE_LENGTH  OPENHOLE_RWB  OPENHOLE_ROUGHNESS
           0.0        0.3333              0.0
```

```
CC
CC WELL TUBING COMPLETION (CODE:API 3 1/2" )(0.1 ft Black Aerogel)
* TUBINTVL  TUBETOP   TUBEBOTT     RTI          RTO          EPSTO    KTUB
      1       0.0       2000.0    0.1145      0.14583       0.0001     26.0

* INSTHICKNESS   KINS   HCFT  TUBANLSFLUID      ROUGHNESS
    0.0         0.002   1.0    19            0.0008

CC
CC FORMATION HEAT TRANSFER COEFFICIENTS
CC  {IUTO = 1 USES ONLY UTO AS THE TOTAL HEAT TRANSFER COEFFICIENT WUTO=Kavg/log(ro/ri)}
* FORMINTVL   FORMATIONTOP      FORMATIONBOTT  FORMATIONTVD   KEARTH  DENEARTH
    1             0.0               2000.0          2000.0        1.0      132.0

* CEARTH  TAMBTOP      TAMBOTT     IUTO   UTOTAL
  0.264     60.0         180.0       1     1.0

CC FLUID NUMBER OF PHASES TO HANDLE NP
CC {1:FLUID MIXTURE, 2:LIQ/GAS}, NUMBER OF COMPONENTS,PVTYPE{1:COMPOSITIONAL, 2:STEAM
3:BLACKOIL}
CC  PHASEID:{0:MIXTURE, 1:GAS   2:OIL 3:WATER }
* NPHASE  NCOMP PVTYPE  PHASEID
   3       3     3        0

CC
CC FLUID BLACK-OIL CORRELATIONS FLAGS (PVTYPE=3)
* RSCORR   RSCALIBRATE   ZGCORR    OFVFCORR   DOVCORR   LOVCORR   UOVCORR   VISGCORR
        2       0             2       1          1         1         1         2
*IFTOGCORR   IFTWGCORR
   1           1
CC
CC FLUID BLACK-OIL FLUID CHARACTERIZATION
*  GW     GG    API    PBUB
    1.0   0.6     30.0    2000.0
CC
CC FLUID BLACK-OIL THERMAL FLAGS
* ENTHCORR    CPWMETHOD   CPOMETHOD   CPGMETHOD
        1           1           1           1
CC
CC FLUID BLACK-OIL THERMAL CHARACTERIZATION
*  CPW   CPO      CPG
   1.0   0.45     0.55
CC
CC FLUID REFRENCE PRESSURE, TEMPERATURE
* REFPRESS      REFTEMP
     14.7         60.0
CC
CC FLUID FLOW ASSURANCE TYPE: {0:OFF, 1:ON}
* IASPH             IWAX              ISCALE
    0                0                 0
CC
CC RESERVOIR COUPLING:
CC {0: STATIC, 1:DYNAMIC} {RESINTVL: NUMBER OF RESERVOIR INTERVAL}{NTIME: NUMBER OF PI
VARIATION DATA}
* IRESERVOIR
   0
CC
CC RESERVOIR INTERVALS {VALUES ARE MD VALUES}
* RESINTVL  RESERVOIRTOP   RESERVOIRBOTT    PERFSHOT
   1           1850.0         2000.0            10

CC RESERVOIR PRODUCTIVITY INDEX: {FOR IRESERVOIR=0} {TIME INTERVAL SHOULD MATCH START/END
TIMES}
* RESTIME  PRESERVOIR     TRESERVOIR      PIO   PIW   PIG
   0.0      2000.0         180.0          0.1    0.1  1.0
```

```
CC
CC PROCESS CONDITIONS
CC IPROD {1:INJECTION, -1:PRODUCTION} IMODEL {0:no slip, 1:FIMPDF, 2:SIMPTF, 3:NIMPTF,
4:SIMPHM}
* IPROD     ITHERMAL ITRANSIENT    IMODEL    ISLIPOW ISLIPGL
    -1        1          1           1          0     1
CC
CC INITIAL CONDITIONS {ZERO IS STATIONARY EQUILIBRIUM WITH RESERVOIR}
* TINIT   PINIT   HLDPHC   HLDPW   UGINIT  UOINIT  UWINIT
   0       0.0      0.1    0.1    0.0001   0.0001  0.0001
CC
CC BOUNDARY CONDITIONS IN BOTTOM-HOLE {BHP: AUTOMATICALLY CLOSED INLET AND CONNECTS TO
RESERVOIR}
* IBCTIME    IBCTYPE
   0.0        CLOSE
CC
CC BOUNDARY CONDITIONS IN WELLHEAD {OPEN: AUTOMATIC COMBINED WITH BHP}
* OBCTIME    OBCTYPE    OBCP        BCF
   0.0       PRODWHP     1000.0     0.999
CC
CC OUTPUT PRINT FREQUENCY
* TPRNT
    500
CC
CC OUTPUT PVT PLOTS {0: OFF, 1: ON}
* IPVT PLOTTEMP1   PLOTTEMP2 PLOTPRES1   PLOTPRES2
   0     120.0       600.0      500.0     2500.0

CC
CC NUMERICAL CONVERGENCE TOLERRANCE
* WTOLM    WTOLE    RME       WMAXITER CFLCHECK
    1E-6     1E-3    0.005       50       0

CC * WTOLP    WTOLT    WTOLQ    WMAXITER
CC   1.0     0.1      0.1       20

CC
CC NUMERICAL SIMULATION TIME
CC {TIME STEP SIZE SHOUDL BE SETUP LESS THAN TIME INTERVALS FOR RESERVOIR CONDITION}
* STARTIME  ENDTIME     DTMIN      DTMAX
      0.0    0.083333    1.0E-9    0.0001
CC
CC END OF INPUT.
```

G.2 STANDALONE ASPHALTENE DEPOSITION SIMULATION

The following is a sample input data file for the standalone wellbore simulator for asphaltene deposition. We used this case in Chapter 8.

```
CC ==================================================================*
CC               WELLBORE MODEL INPUT DATA                           *
CC ================================================================= *
CC                                                                   *
CC CASE NAME:  7COMP ASPH FLUID PROD WELL                            *
CC             THIS CASE IS USED FOR TESTING THE CODE FOR ASPH       *
CC             DEPOSITION SYSTEM.                                    *
CC             THE FLUID IS FROM BURK ET AL.(1999)                   *
CC                                                                   *
CC UNITS:      FIELD                                                 *
CC             FT, DEGREE, BTU/HR.F.FT, BBL/PSI.FT.DAY               *
CC             LB/FT3, PSI, F, FT3/LBMOLE, LBM/LBMOLE, BTU/LB, DAY   *
CC                                                                   *
CC CREATED BY: Mahdy Shirdel 04/21/2013                              *
CC                                                                   *
CC ==================================================================*

CC
CC MAXIMUM NUMBER OF WELLS IN CALCULATION AND FLOWPATH TYPE
* NWLBR  FLOWPATH
   1        WELL


CC*******************************************************************
CC WELL #01 DATA                                                     *
CC*******************************************************************

CC
CC CASE DEFINITION: {WELL ID}
* LW      WNAME
   1      ASPH
CC
CC MESH GRID SIZE [FT]
* MAXGRIDSIZE
    50.0
CC
CC WELL SURFACE [FT]
* WSURFACE
          0.0

CC
CC WELL PROFILE AND SURVEY
* TRAJINTVL  MD        TVD     INCLINATION     AZIMUTH
     1       8000.0    8000.0      90.0        0.0


CC
CC WELL CASING AND COMPLETION {Default RWB=RCO+0.041665}  (CODE:7")
* CASEINTVL HANGERDEPTH  SETTINGDEPTH  RCI         RCO        RWB       CEMENTOP
      1     0.0              50.0        0.78       0.833      0.8749      0.0
      2     0.0              1000.0      0.51722    0.55725    0.59891     0.0
      3     0.0              8000.0      0.3648     0.4010     0.4427      0.0

* EPSCI    EPSCO    KCASE           KCEM          HCFC    CASEANLSFLUID
 0.9      0.9          26.0          4.02          1.0     19
 0.9      0.9          26.0          4.02          1.0     19
```

```
 0.9      0.9          26.0          4.02          1.0     19


CC
CC WELL OPEN HOLE
* OPENHOLE_LENGTH  OPENHOLE_RWB  OPENHOLE_ROUGHNESS
          0.0        0.3333              0.0
CC
CC WELL TUBING COMPLETION
* TUBINTVL  TUBETOP   TUBEBOTT     RTI          RTO        EPSTO    KTUB
      1       0.0       8000.0    0.1145    0.14583      0.0001     26.0

* INSTHICKNESS   KINS   HCFT  TUBANLSFLUID      ROUGHNESS
    0.0          0.002   1.0    19            0.0008

CC
CC FORMATION HEAT TRANSFER COEFFICIENTS
CC  {IUTO = 1 USES ONLY UTO AS THE TOTAL HEAT TRANSFER COEFFICIENT WUTO=Kavg/log(ro/ri)}
* FORMINTVL   FORMATIONTOP      FORMATIONBOTT  FORMATIONTVD   KEARTH  DENEARTH
    1             0.0               8000.0          8000.0        1.0      132.0

* CEARTH  TAMBTOP      TAMBOTT     IUTO   UTOTAL
  0.264     60.0         212.0       1     1.0

CC FLUID NUMBER OF PHASES TO HANDLE NP
CC {1:FLUID MIXTURE, 2:LIQ/GAS}, NUMBER OF COMPONENTS,PVTYPE{1:COMPOSITIONAL, 2:STEAM
3:BLACKOIL}
CC  PHASEID:{0:MIXTURE, 1:GAS 3:OIL 4:WATER }
* NPHASE  NCOMP PVTYPE  PHASEID
   2       7     1        0
CC
CC FLUID DATA FOR ONLY PVTYPE = 1, {DEFINES COMPONENTS}
CC {ICOMPLIB: 0:OFF,1:ON- TAKES THE COMPNAMES AND READ FROM COMP LIB}
CC {EOSTYPE: 1:PR, 2:CUBIC_ASPH, 3:CUBIC_WAX} {IENTH: 1 IDEAL GAS ENTHALPY 2:ACPI }
* ICOMPLIB     EOSTYPE    IENTH
    0             2         1
CC
CC FLUID DATA FOR ONLY PVTYPE=1,
CC {DEFINES COMPONENTS PROPERTIES, 0.0 VALUES MOEANS INTERNAL CORRELATION}
* COMPNAME   PC       TC        VC          WT        OM          PARACHOR     VSP
   CO2     1070.0    547.56   1.5071        44.01      0.225        168.17       0.0
   C1-2    668.51   360.61    1.6431        17.417      0.015127     92.19        0.0
   C3-5    573.15   732.89    3.8098        53.516      0.179313     195.33       0.0
   C6-19   291.41   1135.31   13.7197      164.423      0.655007     512.21       0.0
   C20-30  175.41   1419.29   29.033       340.927      1.064023     1016.51      0.0
   C31+    143.17   1682.93   56.5486      665.624      1.371778     1944.21       0.0
   ASPH     143.17   1682.93   56.5486     665.624      1.371778     1944.21      0.0

*    HA         HB             HC           HD              HE            HF
   4.78E+00  1.14E-01       1.01E-04     -2.65E-08      3.47E-12      -1.31E-16
 -5.58E+00   5.65E-01      -2.83E-04      4.17E-07     -1.53E-10      1.96E-14
  -5.58E+00  5.65E-01      -2.83E-04      4.17E-07     -1.53E-10      1.96E-14
  -5.58E+00  5.65E-01      -2.83E-04      4.17E-07     -1.53E-10      1.96E-14
  -5.58E+00  5.65E-01      -2.83E-04      4.17E-07     -1.53E-10      1.96E-14
  0.00E+00 -2.780970E-02   4.091065E-04 -5.955861E-08   0.000000E+00  0.000000E+00
  0.00E+00 -2.780970E-02   4.091065E-04 -5.955861E-08   0.000000E+00  0.000000E+00

CC
CC FLUID DATA FOR ONLY PVTYPE=1, {DEFINES COMPONENTS BIC}
* DELTA(1)  DELTA(2)     DELTA(3)   DELTA(4)    DELTA(5)   DELTA(6)    DELTA(7)
   0.0000   0.0001       0.0068     0.0375      0.0651      0.0945     0.2200
   0.0001   0.0000       0.0056     0.0347      0.0616      0.0905     0.2200
   0.0068   0.0056       0.0000     0.0130      0.0319      0.0548     0.2200
   0.0375   0.0347       0.0130     0.0000      0.0045      0.0158     0.0000
   0.0651   0.0616       0.0319     0.0045      0.0000      0.0035     0.0000
   0.0945   0.0905       0.0548     0.0158      0.0035      0.0000     0.0000
```

```
   0.2200   0.2200       0.2200     0.0000      0.0000      0.0000     0.0000
CC
CC FLUID DATA FOR WATER PARAMETERS
* GW    IFTWGCORR   ENTHCORR    CPWMETHOD    CPW
  1.0     1            1            1         1.0
CC
CC FLUID REFRENCE PRESSURE, TEMPERATURE
* REFPRESS      REFTEMP
     14.7         60.0
CC
CC FLUID FLOW ASSURANCE TYPE: {0:OFF, 1:ON}
* IASPH             IWAX              ISCALE
    1                0                 0

CC
CC FLUID FLOW ASSURANCE ASPHALTENE ONSET DATA

* VBS       KCONDASPH    KS1S2   IDEPOSIT    DPS1    DPS2
   10.3           1.0     0.0     4         5.0E-6  5.0E-6

* KDLMNAR    KDS1      KDS2       EAS1    EAS2    TAWK          TAWA
   1.0E14   1.0E11    1.0E11       65.3   65.3   1E-8        1.0

CC
CC FLUID FLOW ASSURANCE ASPHALTENE ONSET DATA
*  NONSET    PSTAR      TSTAR
1 4600  212
2 5046  200
3 5451  190
4 5961  180
5 6659  170
6 7581  160
7 8650  150
8 9543  145



CC
CC RESERVOIR COUPLING:
CC {0: STATIC, 1:DYNAMIC} {RESINTVL: NUMBER OF RESERVOIR INTERVAL}{NTIME: NUMBER OF PI
VARIATION DATA}
* IRESERVOIR
   0
CC
CC RESERVOIR INTERVALS {VALUES ARE MD VALUES}
* RESINTVL  RESERVOIRTOP   RESERVOIRBOTT    PERFSHOT
   1           7800.0         8000.0            10

CC RESERVOIR PRODUCTIVITY INDEX: {FOR IRESERVOIR=0} {TIME INTERVAL SHOULD MATCH START/END
TIMES}
* RESTIME  PRESERVOIR TRESERVOIR PIO PIW PIG    Z(1) Z(2) Z(3) Z(4)  Z(5)    Z(6)   Z(7)
    0.0     5200.0      212.0    0.2 0.0  0.0  0.0246  0.4041  0.0755 0.2719 0.1064
0.0774  0.0401

CC
CC PROCESS CONDITIONS
CC IPROD {1:INJECTION, -1:PRODUCTION} IMODEL {0:no slip, 1:drift flux, 2:two-fluid}
* IPROD     ITHERMAL  ITRANSIENT    IMODEL    ISLIPOW  ISLIPGL
    -1        1          0            0          0         0
CC
CC INITIAL CONDITIONS {ZERO IS STATIONARY EQUILIBRIUM WITH RESERVOIR}
* TINIT   PINIT   HLDPHC   HLDPW   UGINIT   UOINIT  UWINIT
   0.0     0.0     0.0      0.0      0.0      0.0     0.0
CC
CC BOUNDARY CONDITIONS IN BOTTOM-HOLE {BHP: AUTOMATICALLY CLOSED INLET AND CONNECTS TO
RESERVOIR}
```

```
* IBCTIME    IBCTYPE        IBCP
   0.0        CLOSE         4500
CC
CC BOUNDARY CONDITIONS IN WELLHEAD {OPEN: AUTOMATIC COMBINED WITH BHP}
* OBCTIME    OBCTYPE      OBCP
  0.0         PRODWHP  1800.0
CC
CC OUTPUT PRINT FREQUENCY
* TPRNT
    1
CC
CC OUTPUT PVT PLOTS {0: OFF, 1:ON}
* IPVT  PLOTTEMP1   PLOTTEMP2  PLOTPRES1   PLOTPRES2
   0     120.0       600.0      500.0     2500.0
CC
CC NUMERICAL CONVERGENCE TOLERRANCE
* WTOLP    WTOLT    WTOLQ    WMAXITER
    0.1     0.1      0.1       20
CC
CC NUMERICAL SIMULATION TIME
CC {TIME STEP SIZE SHOUDL BE SETUP LESS THAN TIME INTERVALS FOR RESERVOIR CONDITION}
* STARTIME  ENDTIME     DTMIN   DTMAX
      0.0    90.0       0.1      5.0
CC
CC END OF INPUT.
```

G.3 STANDALONE WAX DEPOSITION SIMULATION

The following is a sample input data file for the standalone wellbore simulator for wax deposition in the horizontal pipeline. We used this case in Chapter 8.

```
CC =================================================================*
CC               WELLBORE MODEL INPUT DATA                          *
CC ================================================================ *
CC                                                                  *
CC CASE NAME:  8COMP WAX FLUID HORIZONTAL OFFSHORE PIPE              *
CC             THIS CASE IS USED FOR TESTING THE CODE FOR WAX       *
CC             DEPOSITION SYSTEM.                                   *
CC                                                                  *
CC UNITS:      FIELD                                                *
CC             FT, DEGREE, BTU/HR.F.FT, BBL/PSI.FT.DAY              *
CC             LB/FT3, PSI, F, FT3/LBMOLE, LBM/LBMOLE, BTU/LB, DAY   *
CC                                                                  *
CC CREATED BY: Mahdy Shirdel 04/21/2013                             *
CC                                                                  *
CC =================================================================*

CC
CC MAXIMUM NUMBER OF WELLS IN CALCULATION AND FLOWPATH TYPE
* NWLBR  FLOWPATH
   1        WELL


CC*****************************************************************
CC WELL #01 DATA                                                  *
CC*****************************************************************

CC
CC CASE DEFINITION: {WELL ID}
* LW      WNAME
   1      WAX
CC
CC MESH GRID SIZE [FT]
* MAXGRIDSIZE
     50.0
CC
CC WELL SURFACE [FT]
* WSURFACE
          0.0

CC
CC WELL PROFILE AND SURVEY
* TRAJINTVL  MD        TVD     INCLINATION     AZIMUTH
     1       1000.0    0.0      0.0            0.0

CC
CC WELL CASING AND COMPLETION {Default RWB=RCO+0.041665}
* CASEINTVL HANGERDEPTH  SETTINGDEPTH  RCI         RCO        RWB       CEMENTOP
      1     0.0              1000.0    0.78       0.833      0.8749      0.0


* EPSCI    EPSCO    KCASE           KCEM          HCFC    CASEANLSFLUID
 0.9      0.9          26.0          4.02          1.0     19


CC
CC WELL TUBING COMPLETION
```

```
* TUBINTVL  TUBETOP   TUBEBOTT     RTI          RTO          EPSTO    KTUB
      1       0.0       1000.0    0.1145      0.14583       0.0001     26.0

* INSTHICKNESS   KINS   HCFT  TUBANLSFLUID      ROUGHNESS
    0.0            0.002   1.0    19            0.0008

CC
CC FORMATION HEAT TRANSFER COEFFICIENTS
CC  {IUTO = 1 USES ONLY UTO AS THE TOTAL HEAT TRANSFER COEFFICIENT WUTO=Kavg/log(ro/ri)}
* FORMINTVL   FORMATIONTOP      FORMATIONBOTT  FORMATIONTVD   KEARTH  DENEARTH
    1             0.0               1000.0          1000.0        1.0      132.0

* CEARTH  TAMBTOP      TAMBOTT     IUTO   UTOTAL
  0.264     40.0         40.0        1   20.0

CC FLUID NUMBER OF PHASES TO HANDLE NP
CC {1:FLUID MIXTURE, 2:LIQ/GAS}, NUMBER OF COMPONENTS,PVTYPE{1:COMPOSITIONAL, 2:STEAM
3:BLACKOIL}
CC  PHASEID:{0:MIXTURE, 1:GAS 3:OIL 4:WATER }
* NPHASE  NCOMP PVTYPE  PHASEID
   2       8     1        0
CC
CC FLUID DATA FOR ONLY PVTYPE=1, {DEFINES COMPONENTS}
CC {ICOMPLIB: 0:OFF,1:ON- TAKES THE COMPNAMES AND READ FROM COMP LIB}
CC {EOSTYPE: 1:PR, 2:CUBIC_ASPH, 3:CUBIC_WAX} {IENTH: 1 H_COEFF 2:ACPI }
* ICOMPLIB     EOSTYPE    IENTH
    1             3         1
CC
CC FLUID DATA FOR ONLY PVTYPE=1,
CC {DEFINES COMPONENTS PROPERTIES, 0.0 VALUES MOEANS INTERNAL CORRELATION}
* COMPNAME
   C1
   C2
   NC4
   NC5
   FC6
   FC14
   FC17
   FC33

CC
CC FLUID DATA FOR ONLY PVTYPE=1, {DEFINES COMPONENTS BIC}
* DELTA(1)  DELTA(2)     DELTA(3)   DELTA(4)    DELTA(5)   DELTA(6)  DELTA(7)  DELTA(8)
   0.0         0.0         0.0         0.0        0.0        0.0       0.0        0.0
   0.0         0.0         0.0         0.0        0.0        0.0       0.0        0.0
   0.0         0.0         0.0         0.0        0.0        0.0       0.0        0.0
   0.0         0.0         0.0         0.0        0.0        0.0       0.0        0.0
   0.0         0.0         0.0         0.0        0.0        0.0       0.0        0.0
   0.0         0.0         0.0         0.0        0.0        0.0       0.0        0.0
CC
CC FLUID DATA FOR WATER PARAMETERS
* GW    IFTWGCORR   ENTHCORR    CPWMETHOD    CPW
  1.0     1            1            1         1.0
CC
CC FLUID REFRENCE PRESSURE, TEMPERATURE
* REFPRESS      REFTEMP
     14.7         60.0
CC
CC FLUID FLOW ASSURANCE TYPE: {0:OFF, 1:ON}
* IASPH             IWAX              ISCALE
    0                1                 0
CC
CC FLUID WAX COMPONENT {0.0 VALUES MEANS FROM INTERNAL CORRELATION}
* WAXCOMP     HFI       TFI        VFI       WAXPREF
    6          15000.0   460.0     -0.7        14.60
    7          19000.0   590.0     -1.1        14.60
```

```
    8          37000.0   680.0      -2.1        14.60
CC
CC FLUID WAX DEPOSITION
* PORMAX  TAWMAX    PORCB   PORCZ    TAWK   TAWA   SURFCOEFF   HLDPCOEFF  KDWAX  KCONDWAX
   0.7     1.0       2.3     1.0      0.0    1.9     0.5         0.5       0.0005     1.0
CC
CC RESERVOIR COUPLING:
CC {0: STATIC, 1:DYNAMIC} {RESINTVL: NUMBER OF RESERVOIR INTERVAL}{NTIME: NUMBER OF PI
VARIATION DATA}
* IRESERVOIR
   0
CC
CC RESERVOIR INTERVALS {VALUES ARE MD VALUES}
* RESINTVL  RESERVOIRTOP   RESERVOIRBOTT    PERFSHOT
   1           900.0         1000.0            10

CC RESERVOIR PRODUCTIVITY INDEX: {FOR IRESERVOIR=0} {TIME INTERVAL SHOULD MATCH START/END
TIMES}
* RESTIME  PRESERVOIR     TRESERVOIR      PIO    PIW   PIG    Z(1)  Z(2)  Z(3) Z(4)  Z(5)
Z(6)   Z(7) Z(8)
   0.0      1100.0          60.0           0.5    0.0  0.0    0.6   0.1  0.05   0.05   0.05
0.05  0.05  0.05

CC
CC PROCESS CONDITIONS
CC IPROD {1:INJECTION, -1:PRODUCTION} IMODEL {0:no slip, 1:drift flux, 2:two-fluid}
* IPROD     ITHERMAL  ITRANSIENT    IMODEL    ISLIPOW  ISLIPGL
    -1        1          0            0          0         0
CC
CC INITIAL CONDITIONS {ZERO IS STATIONARY EQUILIBRIUM WITH RESERVOIR}
* TINIT   PINIT   HLDPHC   HLDPW   UGINIT   UOINIT  UWINIT
   0.0     0.0     0.0      0.0      0.0      0.0     0.0
CC
CC BOUNDARY CONDITIONS IN BOTTOM-HOLE {BHP: AUTOMATICALLY CLOSED INLET AND CONNECTS TO
RESERVOIR}
* IBCTIME    IBCTYPE
   0.0        CLOSE
CC
CC BOUNDARY CONDITIONS IN WELLHEAD {OPEN: AUTOMATIC COMBINED WITH BHP}
* OBCTIME    OBCTYPE      OBCP
   0.0       PRODWHP   1000.0
CC
CC OUTPUT PRINT FREQUENCY
* TPRNT
    1
CC
CC OUTPUT PVT PLOTS {0: OFF, 1:ON}
* IPVT  PLOTTEMP1   PLOTTEMP2  PLOTPRES1   PLOTPRES2
   0     120.0       600.0      500.0     2500.0
CC
CC NUMERICAL CONVERGENCE TOLERRANCE
* WTOLP    WTOLT    WTOLQ    WMAXITER
    0.1     0.1      0.1       20
CC
CC NUMERICAL SIMULATION TIME
CC {TIME STEP SIZE SHOUDL BE SETUP LESS THAN TIME INTERVALS FOR RESERVOIR CONDITION}
* STARTIME  ENDTIME     DTMIN   DTMAX
      0.0    10.0       1.0     1.0
CC
CC END OF INPUT.
```

G.4 STANDALONE GEOCHEMICAL SCALE DEPOSITION SIMULATION

The following is a sample input data file for the standalone wellbore simulator for geochemical scale deposition. We used this case in Chapter 8.

```
CC ==================================================================*
CC               WELLBORE MODEL INPUT DATA                           *
CC ================================================================= *
CC                                                                   *
CC CASE NAME:  3COMP SCALE FLUID                                     *
CC             THIS CASE IS USED FOR TESTING THE CODE FOR SCALE      *
CC             DEPOSITION SYSTEM.                                    *
CC                                                                   *
CC UNITS:      FIELD                                                 *
CC             FT, DEGREE, BTU/HR.F.FT, BBL/PSI.FT.DAY               *
CC             LB/FT3, PSI, F, FT3/LBMOLE, LBM/LBMOLE, BTU/LB, DAY   *
CC                                                                   *
CC CREATED BY: Mahdy Shirdel 04/21/2013                              *
CC                                                                   *
CC ==================================================================*

CC
CC MAXIMUM NUMBER OF WELLS IN CALCULATION AND FLOWPATH TYPE
* NWLBR  FLOWPATH
   1        WELL


CC********************************************************************
CC WELL #01 DATA                                                     *
CC********************************************************************

CC
CC CASE DEFINITION: {WELL ID}
* LW      WNAME
   1      SCALE
CC
CC MESH GRID SIZE [FT]
* MAXGRIDSIZE
     50.0
CC
CC WELL SURFACE [FT]
* WSURFACE
          0.0

CC
CC WELL PROFILE AND SURVEY
* TRAJINTVL  MD        TVD     INCLINATION     AZIMUTH
     1       5000.0    5000.0      90.0            0.0

CC
CC WELL CASING AND COMPLETION {Default RWB=RCO+0.041665}  (CODE:7")
* CASEINTVL HANGERDEPTH  SETTINGDEPTH  RCI         RCO        RWB       CEMENTOP
      1     0.0              5000.0        0.78       0.833      0.8749      0.0


* EPSCI    EPSCO    KCASE           KCEM          HCFC    CASEANLSFLUID
 0.9      0.9          26.0          4.02          1.0     19
```

```
CC
CC WELL TUBING COMPLETION (CODE:API 3 1/2" )(0.1 ft Black Aerogel)
* TUBINTVL  TUBETOP   TUBEBOTT     RTI          RTO          EPSTO    KTUB
      1       0.0       5000.0    0.1145      0.14583       0.0001     26.0

* INSTHICKNESS   KINS   HCFT  TUBANLSFLUID      ROUGHNESS
    0.0            0.002   1.0    19            0.0008

CC
CC FORMATION HEAT TRANSFER COEFFICIENTS
CC  {IUTO = 1 USES ONLY UTO AS THE TOTAL HEAT TRANSFER COEFFICIENT WUTO=Kavg/log(ro/ri)}
* FORMINTVL   FORMATIONTOP      FORMATIONBOTT  FORMATIONTVD   KEARTH  DENEARTH
    1             0.0               5000.0          5000.0        1.0      132.0

* CEARTH  TAMBTOP      TAMBOTT     IUTO   UTOTAL
  0.264     60.0         180.0        1   20.0

CC FLUID NUMBER OF PHASES TO HANDLE NP
CC {1:FLUID MIXTURE, 2:LIQ/GAS}, NUMBER OF COMPONENTS,PVTYPE{1:COMPOSITIONAL, 2:STEAM
3:BLACKOIL}
CC  PHASEID:{0:MIXTURE, 1:GAS 3:OIL 4:WATER }
* NPHASE  NCOMP PVTYPE  PHASEID
   3       3     3        0

CC
CC FLUID BLACK-OIL CORRELATIONS FLAGS (PVTYPE=3)
* RSCORR   RSCALIBRATE   ZGCORR    OFVFCORR   DOVCORR   LOVCORR   UOVCORR   VISGCORR
IFTOGCORR   IFTWGCORR
   2      0             2       1          1         1         1         2           1
1
CC
CC FLUID BLACK-OIL FLUID CHARACTERIZATION
*  GW     GG    API    PBUB
    1.0   0.6   30.0   500.0
CC
CC FLUID BLACK-OIL THERMAL FLAGS
* ENTHCORR    CPWMETHOD   CPOMETHOD   CPGMETHOD
         1           1           1           1
CC
CC FLUID BLACK-OIL THERMAL CHARACTERIZATION
*  CPW   CPO      CPG
   1.0   0.45     0.55


CC
CC FLUID REFRENCE PRESSURE, TEMPERATURE
* REFPRESS      REFTEMP
     14.7         60.0
CC
CC FLUID FLOW ASSURANCE TYPE: {0:OFF, 1:ON}
* IASPH             IWAX              ISCALE
    0                0                 1

CC
CC FLUID AQUEOUSE PHASE ELEMENTS
* AQELEMENT
    Ca
    S(6)
    Na

CC
CC FLUID AQUEOUSE PHASE SPECIES
*  AQSPECIES
    Ca+2
    SO4-2
    Na+
```

```
CC
CC FLUID AQUEOUSE PHASE SOLIDS
*  AQSOLID       DENAQSOLID    MWAQSOLID
    Anhydrite        65.4         100.0

CC
CC FLUID SCALE DEPOSITION PARAMETERS
* KCONDSCALE    IDEPOSITAQ    DPSAQ    KDLMNRAQ    KDAQ     EAQ
    1.0          4            5.0E-6     1E-3    5E-6   0.0

CC
CC RESERVOIR COUPLING:
CC {0: STATIC, 1:DYNAMIC} {RESINTVL: NUMBER OF RESERVOIR INTERVAL}{NTIME: NUMBER OF PI
VARIATION DATA}
* IRESERVOIR
   0
CC
CC RESERVOIR INTERVALS {VALUES ARE MD VALUES}
* RESINTVL  RESERVOIRTOP   RESERVOIRBOTT    PERFSHOT
   1           4800.0         5000.0            10

CC RESERVOIR PRODUCTIVITY INDEX: {FOR IRESERVOIR=0} {TIME INTERVAL SHOULD MATCH START/END
TIMES}  {CONCENTRATIONS IN MOLE/KG}
* RESTIME  PRESERVOIR     TRESERVOIR      PIO   PIW   PIG    CELET(1)  CELET(2)  CELET(3)
MOLESLD(1)
   0.0      2500.0         180.0           0.5    0.1  0.0      0.001   0.003    0.1
0.1

CC
CC PROCESS CONDITIONS
CC IPROD {1:INJECTION, -1:PRODUCTION} IMODEL {0:no slip, 1:drift flux, 2:two-fluid}
* IPROD     ITHERMAL  ITRANSIENT    IMODEL    ISLIPOW  ISLIPGL
    -1        1          0            0          0         0
CC
CC INITIAL CONDITIONS {ZERO IS STATIONARY EQUILIBRIUM WITH RESERVOIR}
* TINIT   PINIT   HLDPHC   HLDPW   UGINIT   UOINIT  UWINIT
   0.0     0.0     0.0      0.99      0.0      0.0     0.0
CC
CC BOUNDARY CONDITIONS IN BOTTOM-HOLE {BHP: AUTOMATICALLY CLOSED INLET AND CONNECTS TO
RESERVOIR}
* IBCTIME    IBCTYPE     IBCP
   0.0        CLOSE      1100.0
CC
CC BOUNDARY CONDITIONS IN WELLHEAD {OPEN: AUTOMATIC COMBINED WITH BHP}
* OBCTIME    OBCTYPE     OBCP
   0.0       PRODWHP    500.0
CC
CC OUTPUT PRINT FREQUENCY
* TPRNT
    1
CC
CC OUTPUT PVT PLOTS {0: OFF, 1:ON}
* IPVT  PLOTTEMP1   PLOTTEMP2  PLOTPRES1   PLOTPRES2
   0     120.0       600.0      500.0     2500.0
CC
CC NUMERICAL CONVERGENCE TOLERRANCE
* WTOLP    WTOLT    WTOLQ    WMAXITER
    0.1     0.1      0.1       20
CC
CC NUMERICAL SIMULATION TIME
CC {TIME STEP SIZE SHOUDL BE SETUP LESS THAN TIME INTERVALS FOR RESERVOIR CONDITION}
* STARTIME  ENDTIME     DTMIN   DTMAX
      0.0    90.0     1.0        5.0
CC
CC END OF INPUT.
```

G.5 COUPLED WELLBORE/RESERVOIR SIMULATION

The following is a sample input data file for the coupled wellbore/reservoir simulator asphaltene deposition. We used this case in Chapter 9.

```
CC********************************************************************
CC                                                                  *
CC                                                                      *
CC                                                                      *
CC********************************************************************
CC                                                                      *
CC                                                                      *
CC                                                                   *
CC LENGTH(FT):2000                        INJECTION FLUID  :oil        *
CC HEIGHT(FT):1                      INJECTION RATE   :8.3(cu ft/D)      *
CC WIDTH (FT):2000                     W/O REL. PERM    : none          *
CC POROSITY  :0.2                     G/O REL. PERM    : none           *
CC ABS. PERM :1.5                     3-PHASE REL. PERM: none           *
CC TEMP(F)   :200                    WETTIBILITY:       none            *
CC PRE(PSI)  :2000                     W/O CAP. PRESSURE: none          *
CC SOR       :                     G/O CAP. PRESSURE: none              *
CC SWC       :0.2                     DISPLACEMENT TYPE:                *
CC Grid Dim. :25×25×1              Trapping Model   : no                *
CC                                                                      *
CC                                                                      *
CC                                                                      *
CC                                                                      *
CC                                                                      *
CC                                                                      *
CC********************************************************************
CC                                                                      *
CC                                                                      *
CC                                                                      *
CC********************************************************************
CC
CC..+....1....+....2....+....3....+....4....+....5....+....6...+...7..
CC***********SOME CONSTANTS AND MAXIMUM VALUES FOR MODELS**************
CC
CC NXM, NYM, NZM, NPM, NCM, NWM, post_processor
   20   20    3    3     7    2        2
CC
CC NS1M,NBWM,NPRM,NPFM,NCTM,NHSM
    1    401   50    10   10   10000
CC
CC IC2,NCMT,NREG,NTAB
    2  4    6   25
CC
CC EE, NZPM
   0.5761 3
CC
CC TOLP, TOLVOL, QLIM
   0.5D-1 0.5D-4 1.0D-30
CC
CC NUMAX,INQUA,INCON,INVEL,NOSWTM,NUMPRE,NUMOUT,NUMPVT,NST,IFLIP
    10     3     3     5     10     30     12     30    20   0
CC*********************************************************************
CC CASE NAME WITH FORMAT ( 17A4, A2 ) OF TOTAL 70 COLUMNS.
*----HEADER
 2D Compressible Flow
CC
CC
```

```
* IENERGY
    0
CC
CC NUMBER OF COMPONENTS.
*--------NC
         6
CC COMPONENT NAMES WITH FORMAT ( 1X, A8 ), NC CARDS.
CC..+..8
*----NAME
   CO2
   C1-C2
   C3-C5
   C6-C19
   C20-C30
   C31+
CC
CC BLACK OIL OPTION; AQUIFER SALINITY (ppm); AQUIFER OPTION
*-----IBOST     SLNTY    IAQUIF
          0        0.         0
CC CRITI  1AL PRESS. (PSI), TEMP. (R) AND  VOL. (CU FT/LB-MOLE),
CC MOLECULAR WT. (LB/LB-MOLE), ACENTRIC FACTOR, PARACHOR. NC CARDS.
*--------PC       TC        VC         MW      OM    PARACH  VSP
       1070.0     547.56    1.5071  44.01    0.225    168.17  0.0
       668.51     360.61    1.6431  17.417   0.015127 92.19   0.0
       573.15     732.89    3.8098  53.516   0.179313 195.33  0.0
       291.41     1135.31   13.7197 164.423  0.655007 512.21  0.0
       175.41     1419.29   29.0333 340.927  1.064023 1016.51 0.0
       143.17     1682.93   56.5486 665.624  1.371778 1944.21 0.0
CC EOS parameters (Ac and Bc)
CC NC CARDS.
*----PARAA               PARAB
   0.457235529        0.077796074
   0.457235529        0.077796074
   0.457235529        0.077796074
   0.457235529        0.077796074
   0.457235529        0.077796074
   0.457235529        0.077796074
CC
CC BINARY INTERACTION COEFFICIENTS, CIJ. NC CARDS.
*-----DELTA
0.0000
0.0001 0.0000
0.0068 0.0056 0.0000
0.0375 0.0347 0.0130 0.0000
0.0651 0.0616 0.0319 0.0045 0.0000
0.0945 0.0905 0.0548 0.0158 0.0035 0.0000
CC
CC BINARY INTERACTION COEFFICIENTS, DIJ. NC CARDS.
*-------DIJ
0.000
0.000 0.000
0.000 0.000 0.000
0.000 0.000 0.000 0.000
0.000 0.000 0.000 0.000 0.000
0.000 0.000 0.000 0.000 0.000 0.000
CC
CC reduction method: (0: OFF, 1: ON)
*-------IFLASHTYPE  irfla  irsa
          1           0      0
CC
CC MAXIMUM NUMBER OF PHASES ( 3 OR 4 )
*--------NP     IVISC  IVISC_COEF   ISINGL   ISOLU
         3         1        0    0    0
CC IEOS: 1,    IPEM: 0 OR 1
CC ISTAM: -1, 0 OR 1, IEST: 0 OR 1  KI: 0, 1 OR 2
*---IEOS   IPEM     ISTAM   IEST  IVSP   KI
```

```
     1      0         0      1      0     0
CC
CC ITERATION TOLERANCES FOR PERSCHKE'S FLASH ROUTINES.
*----TOLFLA    TOLFLM     TOLPD    TOLSAM    TOLSAS    TOLSUM
     1.0E-10  1.0E-10    1.0E-10  1.0E-08   1.0E-08   1.0E-05
CC
CC MAXIMUM NUMBER OF ITERATIONS FOR PERSCHKE'S FLASH ROUTINES.
*----MAXFLA    MAXFLM     MAXPD    MAXSAM    MAXSAS
     1000       1000      1000       1000        1000
CC
CC VECTOR FLASH OPTION
*-----IVCFL    TOLVFL    MAXVFL
          0     1.E-8        20
CC
CC SWITCHING PARAMETERS FOR PERSCHKE'S FLASH ROUTINES.
*----SWIPCC    SWIPSA
      .001       1.0
CC
CC PHASE IDENTIFICATION PARAMETERS FOR PERSCHKE'S FLASH ROUTINES.
*------IOIL      ITRK   DMSLIM
          1        1      25.
CC
CC IFLAGT ( 0 : OFF,   1 : ON )
*------IFLAGT    IASPR
            0        2
CC
CC PERMEABILITY MODEL USED FOR ASPHALTENE PRECIPITATION
*------1: SOLID: 2: RELATIVE; 3: RELATIVE WITH ADJUSTABLE PARAMETER
     2      4600       10.3
CC
CC BINARY INTERACTION COEFFICIENT OF THE PRECIPITATED COMPONENT
*------ DELTA
0.22   0.22    0.22    0.00    0.00    0.00   0.00
CC
CC FLOOCULATION AND DEPOSITION MODEL
*------ IWETTAB, K12, K21,ALPHA,BETA,GAMA,VCRIT
         0       0.    1    0   6.    0.  0.    0.
CC
CC***********************************************************************
CC                                                                  *
CC OUTPUT OPTIONS                                                   *
CC                                                                  *
CC***********************************************************************
CC
CC
CC HISTORY PRINTING PARAMETER FOR <<HISTORY.CPR>>.
*---NHSSKIP   NSTSKIP     IPV
        10        50          0
CC
CC REFERENCE CONCENTRATION, CONC0, USED FOR EFFLUENT CONCENTRATION.
*-----CONC0
  1.0   1.0   1.0   1.0   1.0   1.0  1.0   1.0   1.0   1.0   1.0   1.0
CC
CC NUMBER OF PRINTS FOR <<.TAB>> (ALSO FOR TRAPPING & ASPHALTENE DATA)
*-------NPR
         11
CC
CC TIME(DAYS) AND FLAGS ( 0 OR 1 ) FOR <<TABLE.CPR>>. NPR CARDS.
*-------TPR      MPRP    MPRSAT   MPROMFR   MPRPMFR    MPRPRO  MPRATES
       1.         1         1         1         1         1        1
       5.         1         1         1         1         1        1
       10.        1         1         1         1         1        1
      15.         1         1         1         1         1        1
      20.         1         1         1         1         1        1
      25.         1         1         1         1         1        1
       30.        1         1         1         1         1        1
```

```
       35.        1         1         1         1         1        1
       40.        1         1         1         1         1        1
       45.        1         1         1         1         1        1
       50.        1         1         1         1         1        1
CC
CC NUMBER OF PRINTS FOR <<PROFILE.CPR>>.
*-------NPF
          3
CC
CC TIME(DAYS) AND FLAGS ( 0 OR 1 ) FOR <<.PRF>>. NPF CARDS.
*-------TPF    MPFSAT   MPFOMFR   MPFPMFR   MPFPROP
         1.         1         1         1         1
       100.         1         1         1         1
       365.         1         1         1         1
CC
CC NUMBER OF PRINTS FOR <<CONTOUR.CPR>>.
*-------NCT
          11
CC
CC TIME(DAYS) AND FLAGS ( 0 OR 1 ) FOR <<.CON>>. NCT CARDS.
*-------TCT      MCTP    MCTSAT   MCTOMFR   MCTPMFR    MCTPRO
       1.         1         1         1         1         1        1
       5.         1         1         1         1         1        1
       10.        1         1         1         1         1        1
      15.         1         1         1         1         1        1
      20.         1         1         1         1         1        1
      25.         1         1         1         1         1        1
       30.        1         1         1         1         1        1
       35.        1         1         1         1         1        1
       40.        1         1         1         1         1        1
       45.        1         1         1         1         1        1
       50.        1         1         1         1         1        1
CC
CC***********************************************************************
CC                                                                 *
CC RESERVOIR AND WELL DATA                                         *
CC                                                                 *
CC***********************************************************************
CC
CC A FLAG FOR RESERVOIR GEOMETRY:
CC 1-D: 11(Y), 12(X), 13(Z), 2-D: 21(XY), 22(YZ), 23(XZ), 3-D: 31
*-----IGEOM       INUG
         31         0
CC
CC NUMBER OF GRID BLOCKS IN X, Y, AND Z.
*--------NX        NY        NZ
         20        20         3
CC
CC NUMBER OF WELLS
*--------NW       IWM
          2         2
CC
CC WELLBORE RATIUS (FT). NW NUMBERS.
*--------RW: (NW)
       0.25  0.25
CC
CC WELL LOCATIONS. NW CARDS.
*-------LXW       LYW    IDIR   LZWF      LZWL
         1       1       3      1         3
         20      20      3      1         3
CC
CC A FLAG ( 0 OR 1 ) FOR GRID BLOCK SIZE IN X-DIRECTION.
*-------MDX
         0
CC
CC CONSTANT GRID BLOCK SIZE IN X-DIRECTION (FT).
```

```
*--------DX
         20
CC
CC A FLAG ( 0 OR 1 ) FOR GRID BLOCK SIZE IN Y-DIRECTION.
*-------MDY
        0
CC
CC CONSTANT GRID BLOCK SIZE IN Y-DIRECTION (FT).
*--------DY
         20
CC
CC A FLAG ( 0 OR 1 ) FOR GRID BLOCK SIZE IN Z-DIRECTION.
*-------MDZ
        0
CC
CC CONSTANT GRID BLOCK SIZE IN Z-DIRECTION (FT).
*--------DZ
         20
CC
CC A FLAG ( 0 OR 1 ) FOR FORMATION DEPTH.
*--------MD
         0
CC
CC DEPTH (FT) OF THE MOST UPPER LAYER.
*---------D
       5000.0
CC
CC A FLAG ( 0 OR 1 ) FOR FORMATION POROSITY.
*------MPOR
       0
CC
CC HOMOGENEOUS POROSITY (FRACTION) AT PF.
*----PORSTD
     0.2
CC
CC A FLAG ( 0 OR 1 ) FOR PERMEABILITY IN X-DIRECTION.
*----MPERMX
       0
CC
CC HOMOGENEOUS PERMEABILITY (MD) IN X-DIRECTION.
*-----PERMX
       500
CC
CC A FLAG ( 0 OR 1 ) FOR PERMEABILITY IN Y-DIRECTION.
*----MPERMY
       0
CC
CC HOMOGENEOUS PERMEABILITY (MD) IN Y-DIRECTION.
*-----PERMY
       500
CC
CC FLAG ( 0 OR 1 ) FOR PERMEABILITY IN Z-DIRECTION.
*----MPERMZ
       0
CC
CC HOMOGENEOUS PERMEABILITY (MD) IN Z-DIRECTION.
*-----PERMZ
       100
CC
CC FORMATION COMPRESSIBILITY (1/PSI) AND REFERENCE PRESSURE (PSI).
*--------CF           PF
      5.0E-4           1500
CC H2O COMPRESSIBILITY (1/PSI), REFERENCE PRESSURE (PSI) AND
CC MOLAR DENSITY (LB-MOLE/CU FT).
*--------CW       PW     DENMWS
     0.0         14.696    3.468
```

```
CC
CC WATER MOLECULAR WT. (LBM/LBM-MOLE) AND VISCOSITY (CP).
*-------WTW     VISCW
        18.      1.0
CC
CC FORMATION TEMPERATURE (F).
*-----TEMPF
       220.0
CC
CC STANDARD TEMPERATURE (F) AND STANDARD PRESSURE (PSI).
*-----TFSTD      PSTD
        60.      14.696
CC
CC A FLAG ( 1, 2, 3 OR 4 ) FOR NUMERICAL DISPERSION CONTROL.
*----IUPSTW
          1
CC
CC ITC ( 0 : NO 2ND ORDER TIME,   1 : 2ND ORDER TIME ON )
*----ITC
       0
CC RESTART OPTIONS.
CC ISTART ( 1 OR 2 ), ISTORE ( 0 OR 1 ).
*----ISTART    ISTORE
          1         0
CC
CC A FLAG ( 0 OR 1 ) FOR AUTOMATIC TIME-STEP SELECTION ( = 1 ).
*-------MDT
          1
CC
CC A FLAG ( 0 OR 1 ) FOR PHYSICAL DISPERSION CALCULATION.
*-----MDISP
        0
CC FLAGS FOR RELATIVE PERMEABILITY MODEL AND CAPILLARY PRESSURE.
CC IPERM ( 1 OR 2 ), ICPRES ( 0 OR 1 ).
*-----IPERM    ICPRES      ICAP    IRPERM
       4        0           2          0
CC CAPILLARY PRESSURE PARAMETERS AND
CC WATER/OIL INTERFACIAL TENSION (DYNES/CM).
*-------EPC       CPC    RIFTWO    RIFTWG    RIFTWL
         2.        2.0    0.        0.       0.
CC
CC HIGH IFT RESIDUAL SATURATIONS.
*------S1RW     S2RW1     S2RW2      S3RW     S4RW1     S4RW2
        0.2      .1       .0      0.0      0.0     0.0
CC
CC LOW IFT RESIDUAL SATURATIONS.
*------S1RC     S2RC1     S2RC2      S3RC     S4RC1     S4RC2
       0.2     .1       .0         0.0        0.0        0.0
CC
CC HIGH IFT END POINT RELATIVE PERMEABILITY.
*------P1RW      P2RW      P3RW      P4RW
       0.4       1.0       1.0       1.0
CC
CC LOW IFT END POINT RELATIVE PERMEABILITY.
*------P1RC          P2RC        P3RC     P4RC
       0.4          1.0         1.0      1.0
CC
CC HIGH IFT EXPONENT OF RELATIVE PERMEABILITY.
*-------E1W      E2W1      E2W2       E3W      E4W1      E4W2
        3.0       2.0      2.0       1.0      1.0       1.0
CC
CC LOW IFT EXPONENT OF RELATIVE PERMEABILITY.
*-------E1C      E2C1      E2C2       E3C      E4C1      E4C2
       3.0       2.0       2.0       1.0       1.0       1.0
CC
CC WATER AND L1 PHASE CAPILLARY DESATURATION PARAMETERS.
```

```
*-------T11       T12      T211      T221      T212      T222
         250.        1.        3000.        1.        3000.        1.
CC
CC GAS AND L2 PHASE CAPILLARY DESATURATION PARAMETERS.
*-------T31       T32      T411      T421      T412      T422
         0.        0.        0.        0.        0.        0.
C
CC A FLAG FOR PRESSURE EQUATION SOLVER ( 1, 2, 3, 4 OR 5 ).
*----IPRESS    IPREC   METHSL   OMEGA
         4      2       1       1.0
CC
CC ITERATIVE PRESSURE SOLVER PARAMETERS.
*-----ITMAX  LEVLIT  IDGTS   NS1       NS2      ZETA
      1000      1      -1      5      1000000   1.E-07
CC
CC INITIAL TIME (DAYS).
*---------T
          0
CC
CC A FLAG ( 0 OR 1 ) FOR INITIAL PRESSURE.
*--------MP
         0
CC
CC CONSTANT INITIAL PRESSURE (PSIA).
*---------P
        5000.0
CC
CC A FLAG ( 0 OR 1 ) FOR INITIAL WATER SATURATION.
*------MSAT
        0
CC
CC CONSTANT INITIAL WATER SATURATION (FRACTION).
*-------SAT
        0.2
CC
CC A FLAG ( 0 OR 1 ) FOR INITIAL OVERALL COMPOSITION.
*-----MOMFR
        0
CC
CC CONSTANT INITIAL COMPOSITION (MOLE FRACTION).
*------OMFR
0.0246  0.4041  0.0755  0.2719  0.1064  0.0774  0.0401
CC
CC***********************************************************************
CC                                                                  *
CC RECURRENT DATA                                                       *
CC                                                                  *
CC***********************************************************************
CC
CC
CC MAXIMUM TIME (DAYS), TIME STEP (DAYS) AND WELL DATA.
*----TM            DT       NWELLS    GORLIM    WORLIM
    60.0      0.05        2           -1.        -1.
CC
CC PARAMETERS FOR TIME STEP SELECTORS.
*-----DTMAX     DTMIN     DSLIM      DPLIM      DVLIM    DMFACT
       0.1     1e-5           0.05       0.01       .05      .05
CC
CC WELL NO. AND WELL TYPE.
*--------LW    IQTYPE   IWELLBORE (0:OFF, 1:0N)
          1      -5       1
CC
CC   (MOLES/D)
*----QTMLC(1)   FWMLC(1)   NCOMP   ISWITCH   PBHC
                                             1000
CC
```

```
CC WELL NO. AND WELL TYPE.
*--------LW    IQTYPE   IWELLBORE (0:OFF, 1:0N)
         2      2         0
CC
CC   (MOLES/D)
*----P   FWMLC(1)   NCOMP
      100  0           1
CC
CC INJECTION COMPONENT NO. AND COMPOSITION (FRACTION). NCOMP CARDS.
*--------KC Z1
         1 1
CC
CC END OF INPUT.
*--------TM DT    NWELLS    GORLIM    WORLIM ----------------
        -1.  -1.  -1.       -1.E10    -1.E10



CC ================================================================*
CC  WELLBORE MODEL INPUT DATA                                      *
CC =============================================================== *
CC                                                                 *
CC CASE NAME:  7COMP ASPHALTENE FLUID PROD WELL (BURK ETAL DATA)     *
CC CREATED BY: Mahdy Shirdel 11/15/2012                            *
CC                                                                 *
CC ================================================================*
CC
CC*****************************************************************
CC WELL #01 DATA                                                   *
CC*****************************************************************
CC
CC CASE DEFINITION: {WELL ID}
*-----LW     WELL NAME
      1       TEST
CC
CC MESH GRID SIZE
*--------MAX_GRID_SIZE[FT]
          200.0
CC
CC WELL SURFACE
*--------WSURFACE[FT]
          0.0
CC
CC WELL PROFILE AND SURVEY
*--------INTERVAL MD[FT]  TVD[FT]  INCLINATION[DEGREE]      AZIMUTH[DEGREE]
          1       5000    5000      90                   0
CC
CC WELL CASING AND COMPLETION {Default RWB=RCO+0.041665}  (CODE:7")
*--------INTERVAL HANGER_DEPTH[FT]  SETTING_DEPTH[FT]   RCI[FT]    RCO[FT]    RWB[FT]
CEMENT_TOP[FT]  EPSCI    EPSCO    KCASE[BTU/HR.FT.F]   KCEM[BTU/HR.FT.F]  HC
ANNULUS_FLUID_ID [SELECT FROM TABLE]
            1     0                 50                 0.78       0.833      0.8749
0               0.9      0.9          26                4.02             1.0     19
            2     0                 1000               0.51722    0.55725    0.59891
0               0.9      0.9          26                4.02             1.0     19
            3     0                 5000               0.3648     0.4010     0.4427
0               0.9      0.9          26                4.02             1.0     19
CC
CC WELL OPEN HOLE
*--------OPENHOLE_LENGTH[FT]  OPENHOLE_RWB[FT]  OPENHOLE_ROUGHNESS[FT/FT]
          0                   0.3333              0.0
CC
CC WELL TUBING COMPLETION (CODE:API 3 1/2" )(0.1 ft Black Aerogel)
*--------INTERVAL  TUBE_TOP[FT]  TUBE_BOTT[FT]    RTI[FT]         RTO[FT]         EPSTO
KTUB[BTU/HR.FT.F]  INS_THICKNESS[FT]  KINS[BTU/HR.FT.F]  HC    ANNULUS_FLUID_ID
ROUGHNESS
```

```
          1        0             5000        0.1145         0.2      0.0001
26.0                 0.0             0.002         1.0      19               0.0008

CC
CC FORMATION HEAT TRANSFER COEFFICIENTS {IUTO = 1 USES ONLY UTO AS THE TOTAL HEAT
TRANSFER COEFFICIENT WUTO=Kavg/log(ro/ri)}
*--------INTERVAL   FORMATION_TOP[FT]     FORMATION_BOTT[FT] FORMATION_TVD[FT]
KEARTH[BTU/HR.FT.F]  DENEARTH[LBM/FT3]       CEARTH[BTU/LBM.F]  TAMBIENT_TOP[F]
TAMBIENT_BOTT[F]    IUTO   UT0[BTU/HR.FT.F]
        1           0                   5000               5000                 1.0
           132                 0.2649              60            180            1
0.2
CC
CC FLUID NUMBER OF PHASES TO HANDLE NP{1:FLUID MIXTURE, 2:LIQ/GAS}, NUMBER OF
COMPONENTS,PVTYPE{1:COMPOSITIONAL, 2:STEAM 3:BLACKOIL} PHASEID:{0:MIXTURE, 1:IDEAL-GAS
2:NONEIDEAL-GAS 3:OIL 4:WATER }
*--------NP  NC PVTYPE  PHASEID
        3   7    1      0
CC
CC FLUID DATA FOR ONLY PVTYPE=1, {DEFINES COMPONENTS}
*-------- ICOMPLIB     EOSTYPE    IENTH    {ICOMPLIB: 0:OFF,1:ON- TAKES THE COMPNAMES AND
READ FROM COMP LIB} {EOSTYPE: 1:PR, 2:CUBIC_ASPH, 3:CUBIC_WAX} {IENTH: 1 H_COEFF 2:ACPI }
           0             2         1
CC
CC FLUID DATA FOR ONLY PVTYPE=1, {DEFINES COMPONENTS PROPERTIES}
*-------- NAME[]   PC[PSI]   TC[R]      VC[FT3/LBM]   WT[LB/LBMOL]  OM[]
PARACHOR[]   VSP[]         HA[BTU/LB]      HB             HC           HD              HE
HF
   CO2    1070.09   547.56    1.5071        44.01      0.225       168.17        0.0
4.78E+00        1.14E-01       1.01E-04     -2.65E-08       3.47E-12     -1.31E-16
   C1-2   668.51    360.61    1.6431        17.417     0.015127    92.19         0.0
-5.58E+00        5.65E-01      -2.83E-04      4.17E-07      -1.53E-10      1.96E-14
   C3-5   573.15    732.89    3.8098        53.516     0.179313    195.33        0.0
-5.58E+00        5.65E-01      -2.83E-04      4.17E-07      -1.53E-10      1.96E-14
  C6-19   291.41    1135.31   13.7197            164.423      0.655007    512.21
0.0        -5.58E+00        5.65E-01      -2.83E-04      4.17E-07      -1.53E-10
1.96E-14
   C20-30   175.41    1419.29   29.033           340.927      1.064023    1016.51
0.0        -5.58E+00        5.65E-01      -2.83E-04      4.17E-07      -1.53E-10
1.96E-14
   C31+     143.17    1682.93   56.5486          665.624      1.371778    1944.21
0.0         0.00E+00       -2.780970E-02   4.091065E-04 -5.955861E-08   0.000000E+00
0.000000E+00
   ASPH     143.17   1682.93   56.5486           665.624      1.371778    1944.21
0.0         0.00E+00       -2.780970E-02   4.091065E-04 -5.955861E-08   0.000000E+00
0.000000E+00
CC
CC FLUID DATA FOR ONLY PVTYPE=1, {DEFINES COMPONENTS BIC}
*-------- DELTA
0.0000
0.0001 0.0000
0.0068 0.0056 0.0000
0.0375 0.0347 0.0130 0.0000
0.0651 0.0616 0.0319 0.0045 0.0000
0.0945 0.0905 0.0548 0.0158 0.0035 0.0000
0.2200 0.2200 0.2200 0.0000 0.0000 0.0000 0.0000
CC
CC FLUID DATA FOR WATER PARAMETERS
*-------GW[]   IFTWGCORR[]  ENTHWCORR[]   CPWMETHOD[]   CPW[BTU/LBM.F]
        1.0     1             1              1          1.0
CC
CC FLUID REFRENCE PRESSURE, TEMPERATURE
*--------PRESSURE[PSI] TEMPERATURE[F]
        14.7         60
CC
CC FLUID FLOW ASSURANCE TYPE: {0:OFF, 1:ON}
```

```
*-------- IASPH            IWAX              ISCALE
           1                0                 0
CC
CC FLUID FLOW ASSURANCE ASPHALTENE ONSET DATA
*-------- VBS[FT3/LBM]  KCOND_ASPH KS1S2   IDEPOSIT  DPS1[cm]  DPS2     KD_LMNAR[cm/SEC]
KDS1      KDS2       EAS1    EAS2[KJ]
          10.3           1.0       0.0     4         5.0E-6  5.0E-6       1.0E11
1.0E9     1.0E9        65.3     65.3
CC
CC FLUID FLOW ASSURANCE ASPHALTENE ONSET DATA
*-------- NONSET    PSTAR[PSI]    TSTAR[F]
   1    4600   212
   2    5046   200
   3    5451   190
   4    5961   180
   5    6659   170
   6    7581   160
   7    8650   150
   8    9543   145
CC
CC RESERVOIR COUPLING: {0: STATIC, 1:DYNAMIC}
*-------- IRESERVOIR
           1
CC
CC PROCESS CONDITIONS
*-------- IPROD[] {1:INJECTION, -1:PRODUCTION}   ITHERMAL[]  ITRANSIENT[]   IMODEL[]{0:no
slip, 1:drift flux, 2:two-fluid}  ISLIPOW[] ISLIPGL[]
          -1                                     1           0              0
0         0
CC
CC INITIAL CONDITIONS {ZERO IS STATIONARY EQUILIBRIUM WITH RESERVOIR}
*-------- TINIT[F]  PINIT[PSI]  HLDPHC[]  HLDPW[]  UGINIT[FT/SEC]  UOINIT[FT/SEC]
UWINIT[FT/SEC]
           0.0       0.0        0.01      0.01       0.0             0.0             0.0
CC
CC OUTPUT PRINT FREQUENCY
* ------TPRNT
          1
CC
CC OUTPUT PVT PLOTS {0: OFF, 1:ON}
* ------  IPVT TEMP1[F]  TEMP2[F] PRES1[PSI]    PRES2[PSI]
           0   120       600      500          2500
CC
CC NUMERICAL CONVERGENCE TOLERRANCE
*--------WTOLP[PSIA]   WTOLT[F]   WTOLQ[LBM/HR]   WMAXITER
          0.1         0.1            0.1          20
CC
CC NUMERICAL SIMULATION TIME
*--------START_TIME[DAY]   END_TIME [DAY]    DTMIN[DAY]  DTMAX[DAY] {TIME STEP SIZE
SHOUDL BE SETUP LESS THAN TIME INTERVALS FOR RESERVOIR CONDITION}
          0.0                   30             0.1         0.1
CC
CC END OF INPUT.
```

G.6 PHREEQC SAMPLE DATABASE

```
#***********************************************
#***************WATER***************************
#***********************************************
SOLUTION_MASTER_SPECIES

H       H+           -1.     H         1.008
H(0)     H2           0.0     H
H(1)     H+           -1.     0.0
E       e-           0.0     0.0             0.0
O       H2O         0.0     O          16.00
O(0)     O2           0.0     O
O(-2)    H2O         0.0     0.0

#*************************************************
#*************************************************

Ca       Ca+2      0.0     Ca         40.08
Na       Na+        0.0    Na        22.9898
Ba       Ba+2      0.0     Ba         137.34

Cl       Cl-            0.0     Cl              35.453

C        CO3-2          2.0     HCO3            12.0111
C(+4)    CO3-2          2.0     HCO3

S        SO4-2     0.0     SO4        32.064
S(6)     SO4-2    0.0      SO4


#*************************************************
#*************************************************
#*************************************************

SOLUTION_SPECIES

e- = e-
        log_k      0.000

H2O = H2O
        log_k      0.000
        -gamma    10e9    0.0

H+ = H+
        log_k      0.000
        -gamma    10e9    0.0

H2O = OH- + H+

        log_k      -14.000
        -gamma     10e9   0.0

2 H2O = O2 + 4 H+ + 4 e-
       log_k      -86.08
2 H2O = O2 + 4 H+ + 4 e-
       log_k      -86.08
2 H+ + 2 e- = H2
        log_k      -3.15

#*************************************************
```

```
#**************************************************

H+ = H+
        log_k           0.000


Na+ = Na+
        log_k      0.000
        -gamma     10e9   0.0

Ba+2 = Ba+2
        log_k      0.000
        -gamma    10e9  0.0

Ca+2 = Ca+2
        log_k      0.000
        -gamma     10e9   0.0

Cl- = Cl-
        log_k           0.000
        -gamma    3.5000    0.0150


SO4-2 = SO4-2
        log_k      0.000
        -gamma    10e9    0.0

CO3-2 = CO3-2
        log_k           0.000
        -gamma    5.4000    0.0000


CO3-2 + H+ = HCO3-
        log_k           10.329
        -gamma    5.4000    0.0000

CO3-2 + 2 H+ = CO2 + H2O
        log_k           16.681


Ba+2 + SO4-2 = BaSO4
        log_k           2.700

Ba+2 + CO3-2 = BaCO3
        log_k           2.71

Ca+2 + SO4-2 = CaSO4
        log_k           2.300

Ca+2 + CO3-2 = CaCO3
        log_k           3.224


#**************************************************
#**************************************************
#**************************************************

PHASES

Calcite
        CaCO3 = CO3-2 + Ca+2
        log_k           -8.480


Witherite
        BaCO3 = Ba+2 + CO3-2
```

```
        log_k           -8.562


Barite
        BaSO4 = Ba+2 + SO4-2
        log_k      -14.85


Anhydrite
        CaSO4 = Ca+2 + SO4-2
        log_k      -14.480000
```

G.7 PHREEQC SAMPLE INPUT DATA

```
PRINT
     -RESET                 TRUE
 SELECTED_OUTPUT
  -RESET                 FALSE
 USER_PUNCH
          -headings                                    Ca
          -headings                                    Ba
          -headings                                    Na
          -headings                                    Cl
          -headings                                    S(6)
          -headings                                    C(+4)
          -headings                                    Ca+2
          -headings                                    Ba+2
          -headings                                    Na+
          -headings                                    CO3-2
          -headings                                    HCO3-
          -headings                                    CO2
          -headings                                    SO4-2
          -headings                                    BaSO4
          -headings                                    BaCO3
          -headings                                    CaSO4
          -headings                                    CaCO3
          -headings                            Anhydrite
          -headings                            Calcite
          -headings                            Witherite
          -headings                            Barite

    -start
          10   PUNCH TOT("Ca")
          20   PUNCH TOT("Ba")
          30   PUNCH TOT("Na")
          40   PUNCH TOT("Cl")
          50   PUNCH TOT("S(6)")
          60   PUNCH TOT("C(+4)")
          70   PUNCH MOl("Ca+2")
          80   PUNCH MOL("Ba+2")
          90   PUNCH MOL("Na+")
         100   PUNCH MOL("CO3-2")
         120   PUNCH MOL("HCO3-")
         120   PUNCH MOL("CO2")
         130   PUNCH MOL("SO4-2")
         140   PUNCH MOL("BaSO4")
         150   PUNCH MOL("BaCO3")
         160   PUNCH MOl("CaSO4")
         170   PUNCH MOl("CaCO3")
         180 PUNCH EQUI("Anhydrite")
         190 PUNCH EQUI("Calcite")
         200 PUNCH EQUI("Witherite")
         200 PUNCH EQUI("Barite")
    -end



 TITLE   FOUR SCALE PERCIPITATION
 SOLUTION           1


 -units mol/kgw
 -pH 7.0
 -temp 25.0
```

```
   Ca           0.0500
   Ba           0.0500
   Na           0.2000
   Cl           0.2000
   S(6)         0.0500
   C(+4)        0.0500



REACTION_TEMPERATURE 1
   50.0
EQUILIBRIUM_PHASES



   Anhydrite  0.     0.000000E+00
   Calcite    0.     0.000000E+00
   Witherite  0.     0.000000E+00
   Barite     0.     0.000000E+00


END
```

Glossary

The following list of nomenclature includes only the generalized symbols used in the text. Symbols which have been used to represent different quantities have been defined as they were used in the text.

A	Wellbore / pipe cross section area (ft^2)
B	Gravity force gradient (ft/sec^2)
B_o	Oil formation volume factor (rbbl/stb)
C^{vm}	Virtual mass parameter
C_0	Drift flux profile parameter
C_b	Average bulk particle concentration (lbm/ft^3)
C_s	Average surface particle concentration (lbm/ft^3)
D	Wellbore/pipe diameter (ft)
D_B	Brownian diffusivity (m^2/sec)
D^+_{pipe}	Non-dimensional pipe diameter
d_p	Particle diameter (m)
f	Friction factor
f_i	Fugacity of component i in the hydrocarbon mixture
FIG	Interphase gas friction force factor (1/sec)
FIL	Interphase liquid friction force factor (1/sec)
FWG	Wall/Gas friction force factor (1/sec)
FWL	Wall/Liquid friction force factor (1/sec)
g	Gravity acceleration (ft/sec^2)
h	Fluid height in the cross section (ft)
$\overline{h}$	Fluid enthalpy (Btu/lbm)
j	Spatial variable numerical index (junction)
K	Spatial variable node center index
K_t	Transport coefficient (m/sec)
L	Spatial variable node center index
M	Spatial variable node center index
$\dot{m}_d$	Mass deposition flux (lbm/sec. ft^2)

n	Time variable numerical index
N_k	Molar per bulk volume of hydrocarbon component k in the mixture (lbmol /ft^3)
n_c	Number of hydrocarbon components
P	Pressure (psi)
$\dot{Q}$	Wellbore gridblock heat loss (Btu/sec.ft)
R_s	Solution gas oil ratio (scf/stb)
r^+_{avg}	Non-dimensional average radial distance
S	Wellbore wetted perimeter (ft)
SP	Sticking probability
S^+_p	Non-dimensional stopping distance
T	Temperature (^{o}F)
t	Time variable (sec)
u	Actual velocity (ft/sec)
v	Drift velocity (ft/sec)
$VISL$	Liquid viscous -like term in momentum equation
$VISG$	Gas viscous-like term in momentum equation
Vb	Wellbore grid bulk volume (ft^3)
x	Well trajectory spatial variable (ft)
y	Liquid height from center of pipe (ft)
y^+	Non-dimensional distance from the wellbore / pipe wall
z	Wellbore gridblock overall composition of fluid mixture

Greek Symbols

α	Fluid volume fraction
$\dot{\psi}$	Fluid mass influx per gridblock bulk volume (lbm/ft^3.sec)
$\dot{H}$	Fluid enthalpy influx per gridblock bulk volume (Btu/ ft^3.sec)
ρ	Fluid density (lbm/ft^3)
σ	Liquid/gas interfacial tension
μ	Viscosity (Cp)
θ	Well trajectory angle (radian)
τ	Shear stress (lbm/sec^2.ft)
Γ	Interphase mass transfer per bulk volume (lbm/sec.ft^3)

Subscripts

d	Drift

g	Gas
gi	Gas interphase
i	Interphase
l	Liquid
li	Liquid interphase
m	Mixture
mx	Maximum
o	Oil
TB	Taylor bubble
sl	Superficial variable for liquid phase (i.e. superficial liquid velocity)
sg	Superficial variable for gas phase
sp	Single phase
tp	Two phase
w	Water

References

Akbarzadeh, K., Hammami, A., Kharrat, A., Zhang, D., Allenson, S., Creek, J., Kabir, S., Jamaluddin, A., Marshall, A.G., Rodgers, R.P., Mullins, O.C., and Solbakken, T.: "Asphaltene – Problematic but Rich in Potential," Schlumberger Oil Field Review, pp. 22- 43, Summer 2007.

Ali, M.A. and Islam, M.R.: "The Effect of Asphaltene Precipitation on Carbonate-Rock Permeability: An Experimental and Numerical Approach," SPE Production and Facilities, pp. 178– 183, Aug 1998.

Almehaideb, R.A., Aziz, K., and Pedrosa Jr., O.J.: "A Reservoir/Wellbore Model for Multiphase Injection and Pressure Transient Analysis," Paper SPE 17941, presented at 6th Middle East Oil Technical Conference and Exhibition, Manama, Bahrain, Mar 11-14, 1989.

Ansari, A.M., Sylvester, N.D., Sarica, C., Shoham, O., and Brill, J. P.: "A Comprehensive Mechanistic Model for Upward Two-Phase Flow in Wellbores," SPE Production & Facilities Journal, pp. 143-151, 1994.

Aziz, K., Govier, G.W., and Fogarasi, M.: "Pressure Drop in Wells Producing Oil and Gas," JCPT, pp. 38-47, July-Sept 1972.

Babu, D.K. and Odeh, A.S.: "Productivity of a Horizontal Well," Soc. Pet. Eng. Reservoir Eng., 4, pp. 417-421, Nov 1989.

Baker, O. and Swerdloff, W.: "Calculation of Surface Tension," Oil and Gas Journal, 141, Dec 1955.

Barnea, D., Shoham, O., and Taitel, Y.: "Flow Pattern Transition for Vertical Downward Two-Phase Flow," Chem. Eng. Sci., 37, pp. 741, 1982.

Banerjee, S. and Chan, A.M.C.: "Separated Flow Models I. Analysis of the Averaged and Local Instantaneous Formulations," International Journal of Multiphase Flow, 6, pp.124, 1980.

Beal, S., K.: "Deposition of Particles in Turbulent Flow on Channel or Pipe Walls," Nuclear Science and Engineering, 40, pp. 1-11, 1970.

Bedrikovestsky, P.G., Lopes, R.P. Jr., Rosario, F.F., Bezerra, M.C., and Lima, E.A.: "Oilfield Scaling Part I: mathematical and Laboratory Modeling," Paper SPE 81127, Presented at the Latin American and Caribbean Petroleum Engineering conference, Port-of-Spain, Trinidad, West India, pp. 27-30, Apr 2003.

Behie, A., Collins, D., Forsyth, P.A., and Sammon, P.H.: “Fully Coupled Multiblock Wells in Oil Simulation,” Paper SPE 11877, Journal of Petroleum Technology, pp. 535-542, Aug 1985.

Beggs, H.D. and Brill, J.P.: “A Study of Two-Phase Flow in Inclined Pipes,” Journal of Petroleum Technology, pp. 607-617, May 1973.

Beggs, H.D. and Robinson, J.R.: “Estimating the Viscosity of Crude Oil Systems,” Journal of Petroleum Technology, 27, pp. 1140–1141, Sep 1975.

Bendiksen, K.H., Malnes, D., Moe, R., and Nuland, S.: “The Dynamic Two-Fluid Model OLGA: Theory and Application,” SPE Production Engineering, 6, pp. 171-180, May 1991.

Benedict, M., Webb, G.B., and Rubin L.C.: “An Empirical Equation for Thermodynamic Propertied of Light Hydrocarbons and their Mixture,” Journal of Chem. Phys, 8, pp. 334-45, 1940.

Bird, R., B., Stewart, W., and E., Lightfoot, E., N.: *Transport Phenomena*, 2nd Edition, John Wiley & Sons, 2002.

Brown, T.S., Niesen, V.G., and Erickson, D.D.: “Measurement and Prediction of Kinetics of Paraffin Deposition,” Paper SPE 26548, 68th Annual Technical Conference and Exhibition, Houston, TX, Oct 3-6, 1993.

Burke, N.E., Hobbs, R.D., and Kashou, S.F.: "Measurement and Modeling of Asphaltene Precipitation,” JPT, pp. 1440-1446, 1990.

Carbognani, L., Orea, M., and Fonseca, M.: “Complex Nature of Separated Solid Phases from Crude Oils,” Energy & Fuels, 13, pp. 351-358, 1999.

Carnahan, N. F.: “Precipitation of Asphaltene in Heavy Oil and Tar Sands,” in Asphaltenes and Asphalts, Elsevier Science B.V., 2000.

Chang, Y.B.: “*Development and application of an Equation of States Compositional Simulator*,” Ph.D. Dissertation, The University of Texas at Austin, 1990.

Chapman, W.G, Gubbins, K.E., Jackson, G., and Radosz, M.: “New Reference Equation of State for Associating Liquids,” Ind. Eng. Chem. Res., 29(8), pp. 1709-1721, 1990.

Chokshi, R.N: "*Prediction of Pressure Drop and Liquid Holdup in Vertical Two-Phase Flow through Large Diameter Tubing*," Ph.D. Dissertation, The University of Tulsa, 1994.

Chung, T.H.: "Thermodynamic Modeling for Organic Solid Precipitation," Paper SPE 24851, Washington D.C, USA, Oct. 4-7, 1992.

Cleaver, J., W. and Yates, B.: "A Sub-layer Model for the Deposition of Particles from a Turbulent Flow," Chem. Eng. Sci., 30, pp. 983-992, 1975.

Crabtree, M.: "Fighting Scale-Removal and Prevention," Schlumberger Oilfield Review, pp. 30-40, Autumn 1999.

Darabi, H., Sepehrnoori, K., and Kalaei, H.: "Modeling of Wettability Alteration Due to Asphaltene Deposition in Oil Reservoirs," SPE Paper 159554, Presented at Annual Technical Conference and Exhibition, San Antonio, Texas, USA, Oct 8-10, 2012.

Davis, J.T.: "A New Theory of the Deposition of Colloidal Particles from Turbulent Fluids," Annals of the New York Academy of Science, 404, pp. 313-326, 1983.

Dinh, T.N., Nourgaliev, R.R., and Theofanous, T.G.: "Understanding The Ill-posed Two-Fluid Model," NURETH, Seoul, Korea, Oct 59, 2003.

De Ghetto, G., Paone F., and Villa M.: "Reliability Analysis on PVT Correlations," Paper SPE 28904, Presented at the European Petroleum Conference, London, UK, Oct 25-27, 1994.

Delshad, M. and Pope, G.: "Effect of Dispersion on Transport and Precipitation of Barium and Sulfate in Oil Reservoirs," SPE Paper 80253, Presented at the International Symposium on Oilfield Scale, Houston, Feb 5-8, 2003.

Dranchuk, P.M. and Abou-Kassem, J.H.: "Calculation of Z-factor for Natural Gases Using Equations of State," Journal of Canadian Petroleum Technology, 34, Jul 1975.

Drew, D. A. and Lahey, R.T.: "Application of General Constitutive Principles to the Derivation of Multidimensional Two-Phase Flow Equations," Int. J. Multiphase Flow, Vol.5, pp.243264, 1979.

Dukler, A.E., Wicks. M. III., and Cleveland, R.G.: "Frictional Pressure Drop in Two-Phase Flow: An Approach through Similarity Analysis," AIChE Journal, 10, 44, 1964.

Duns, H.Jr. and Ros, N.C.J.: "Vertical Flow of Gas and Liquid Mixtures in Wells," Paper 22-PD6 of the Sixth World Petroleum Congress, Frankfurt, Germany, Jun 1963.

Eaton, B.A., Andrews, D.E., Knowles, C.R., Silberberg, I.H., and Brown, K.E.: "The Prediction of Flow Patterns, Liquid Holdup and Pressure Losses Occurring During Continuous Two-Phase Flow in Horizontal Pipelines," Journal of Petroleum Technology, pp. 815, Jun 1967.

Egbogah, E.O. and Ng, J.T..: "An Improved Temperature-Viscosity Correlation for Crude Oil Systems," Journal of Petroleum Science and Engineering, 4, pp. 197-200, Jul 1990.

Erickson, D.D., Niesen, V.G., and Brown, T.S.: "Thermodynamic Measurement and Prediction of Paraffin Precipitated in Crude Oil," Paper SPE 26604, Presented at SPE ATCE, Houston, TX, Oct 3-6, 1993.

Erickson, D.D. and Mai, M.C.: "A Transient Multiphase Temperature Prediction Program," Paper SPE 24790, Presented at SPE ATCE, Washington D.C, Oct 4-7, 1992.

Epstein, N.: "Particulate Fouling of Heat Transfer Surface: Mechanisms and Models" Fouling Science and Technology, 145, pp. 143-164, 1988.

Escobedo, J.: "*Mexican Crude Oils and the Asphaltene Deposition Problem*" M.Sc. thesis, The University of Illinois at Chicago, Chicago, IL, 1993.

Escobedo, J. and Mansoori, G.A.: "Asphaltene and Other Heavy-Organic Particle Deposition during Transfer and Production Operation," Paper SPE 29488, Production Operation Symposium, Oklahoma City, Oklahoma, USA, Apr 2-4, 1995.

Eskin, D., Ratulowski, J., Akbarzadeh, K., and Pan, S.: "Modeling Asphaltene Deposition in Turbulent Pipeline Flows," The Canadian Journal of Chemical Engineering , pp. 421-441, June, 2011.

Fair, W.B. Jr.: "Pressure Buildup Analysis with Wellbore Phase Redistribution," Paper SPE 8206, SPE Journal, 21, 2, pp. 259-270, Apr 1981.

Fan, L., Lee, W.J., and Spivey, J.P.: "Semi-Analytical Model for Thermal Effect on Gas Well Pressure Buildup Tests," Paper SPE 56612, presented at SPE Annual Technical Conference and Exhibition, Houston, Texas, Oct 3-6, 2000.

Fazelipour, W.: "*Development of a Fully Implicit, Parallel, Equation-of-State Compositional Simulator to Model Asphaltene Precipitation in Petroleum Reservoirs*," M.Sc. Thesis, the University of Texas at Austin, 2007.

Friedlander, S.K. and Johnstone, H.F.: "Deposition of Suspended Particles from Turbulent Gas Streams," Ind. Eng. Chem., 49, pp. 1151-1156, 1957.

Frenier., W. and Ziauddin, M.: *Formation, Removal, and Inhibition of Inorganic Scale in the Oilfield Environment*, SPE Book, pp.59-85, 2008.

Gambill, W. R.: “You Can Predict Heat Capacities,” Chemical Engineering, pp. 243–248, Jun 1957.

Gidaspow, D.: “Modeling of Two Phase Flow,” Proceedings of the 5th International Heat Transfer Conference VII, 1974.

Gomez, L.E., Shoham, O., and Taitel, Y.: “Prediction of Slug Liquid Holdup-Horizontal to Upward Vertical Flow,” International Journal of Multiphase Flow, 26, 3, pp. 517, Mar 2000.

Gonzalez, D.L, Ting, P.D., and Hirasaki, G.J., Chapman, W.G.: “Prediction of Asphaltene Instability under Gas Injection with the PC-SAFT Equation of State,” Energy & Fuels, 19(4), pp. 1230-1234, 2005.

Gonzalez, D.L., Hirasaki, G.J., Creek, J., and Chapman, W.G.: “Modeling of Asphaltene Precipitation Due to Changes in Composition Using the Perturbed Chain Statistical Associating Fluid Theory Equation of State,” Energy & Fuels, 21(3), pp. 1231-1242, 2007.

Gross, J. and Sadowski, G.: “Perturbed-Chain SAFT; An Equation of State Based on a Perturbation Theory for Chain Molecules,” Ind. Eng. Chem. Res., 40(4), pp. 1244-1260, 2001.

Hagedorn, A.R. and Brown, K.E.: “Experimental Study of Pressure Gradients Occurring During Continuous Two-Phase Flow in Small-Diameter Vertical Conduits,” Journal of Petroleum Technology, pp. 475, Apr 1965.

Hammami, A., Ferworn, K.A., Nighswander, J.A., Overa, S., and Stange, E.: “Asphaltenic Petroleum Fluid Oil Characterization: An Experimental Investigation of the Effect of Resins on the Stability of Asphaltenes,” Pet. Sci. Technol., 16(3– 4), 227, 1998.

Hamouda, A.: “An Approach for Simulation of Paraffin Deposition in Pipelines as a Function of Flow Characteristics with a Reference to Teesside Oil Pipeline,” Paper SPE 28966, Presented at SPE Int. Symposium on Oilfield Chemistry, San Antonio, 14-17, Feb 1995.

Han, C., Delshad, M., Sepehrnoori, K., and Pope, G.: “A Fully Implicit, Parallel, Compositional Chemical Flooding Simulator,” Society of Petroleum Engineering Journal, 12, 3, pp. 322-338, 2007.

Hasan, A.R. and Kabir, C.S.: "A Study of Multiphase Flow Behavior in Vertical Wells," SPE Production Engineering Journal, pp. 263–272, May 1988.

Hasan, A.R. and Kabir, C.S.: "Predicting Multiphase Flow Behavior in Deviated Wells," SPE Production Engineering Journal, pp. 474–482, Nov 1988.

Hasan, A.R. and Kabir, C.S.: "A Wellbore/Reservoir Simulator for Testing Gas Wells in High-Temperature Reservoirs," SPE Formation Evaluation Journal, pp. 128-135, Jun 1996.

Hasan, A.R. and Kabir, C.S.: "A Mechanistic Model for Computing Fluid Temperature Profiles in Gas-Lift Wells," SPE Production Facilities Journal, pp. 179, Aug 1996.

Hasan, A.R., Kabir, C.S., and Wang, X.: "Development and Application of a Wellbore/Reservoir Simulator for Testing Oil Wells," SPE Formation Evaluation Journal, pp. 182-188, Sep 1997.

Hasan, A.R., Kabir, C.S., and Wang, X.: "Wellbore Two-Phase Flow and Heat Transfer during Transient Testing," Society of Petroleum Engineering Journal, 3, 2, pp. 174-180, Jun 1998.

Hasan, A.R., Kabir, C.S., and Sayarpour, M.: "A Basic Approach to Wellbore Two-Phase Flow Modeling," Paper SPE 109868, Presented at SPE Annual Technical conference and Exhibition, Anaheim, CA, USA, 11-14 Nov, 2007.

Haskett, C.E. and Tartera, M.: "A Practical Solution to the Problem of Asphaltene Deposits – Hassi Messaoud Field, Algeria," J. Pet. Tech., pp. 387-391, Apr 1965.

Hayduk, W. and Minhas, B.S.: "Correlations for Predictions of Molecular Diffusivities in Liquids," The Canadian Journal of Chemical Engineering, 60, 295, 1982.

Hernandez, O.C., Hensley, H., Sarica, C., Brill, J.P., Volk, M., and Delle-Case, E.: "Improvements in Single-Phase Paraffin Deposition Modeling," SPE Production and Facilities, 237, 2004.

Holman, J.P.: *Heat Transfer,* 4th ed., McGraw-Hill Book Co, New York, 1958.

Hutchinson, P.C., Hewitt, G.F., and Dukler, A.E.: "Deposition of Liquid or Solid Dispersions from Turbulent Gas Streams: A Stochastic Model," Chem. Eng. Sci., 26, pp. 419-439, 1971.

Hwang, Y-H.: "Upwind Scheme for Non-Hyperbolic Systems," J. Comput. Phys. 192, pp. 643–676, 2003.

Issa, R.I. and Kempf, M.H.W.: "Simulation of Slug Flow in Horizontal and Nearly Horizontal Pipes with the Two-Fluid Model," Int. J. Multiphase. Flow 29, pp. 69–95, 2003.

Ishii M.: "One-Dimensional Drift-flux Model and Constitutive Equations for Relative Motion between Phases in Various Two-Phase Regimes," Argonne National Laboratory, Oct 1977.

Ishii M. and Hibiki. T.: *Thermo-fluid Dynamics of Two-Phase Flow,* 2nd ed., Springer, New York Dordrecht Heidelberg London, 2011.

Johansen, S., T.: "The Deposition of Particles on Vertical Walls," Int. J. Multiphase Flow" 17, 3, pp. 355-376, 1991.

Jarvis, S. J.: "On the Formulation and Numerical Evaluation of a Set of Two-Phase Flow Equations Modeling the Cooldown Process," Technical Note 301, National Bureau of Standards, Boulder, Colorado, 1965.

Jamialahmadi, M., Soltani, B., Muller-Steinhagen, H., and Rashtchian, D.: "Measurement and Prediction of the Rate of Deposition of Flocculated Asphaltene Particles from Oil," International Journal of Heat and Mass Transfer, 52, pp. 4624-4634, 2009.

Katz, D.L.: *Handbook of Natural Gas Engineering*, McGraw Hill Book Co., New York, 1959.

Kaya, A.S, Sarica, C., and Brill J.P.: "Comprehensive Mechanistic Modeling of Two-phase Flow in Deviated Wells," Paper SPE 56522, Presented at Annual Technical Conference and Exhibition, Houston, Texas, Oct 3-6, 1999.

Kontogeorgis, G.M., Voutsas E.C., Yakoumis, I.V., and Tassios, D.P.: "An Equation of State for Associating Fluids," Ind. Eng. Chem. Res., 35(11), pp. -4318, Nov, 1996.

Kohse, B.F, Nghiem, L.X, Maeda H., and Kenji, O.: "Modeling Phase Behavior Including the Effect of Pressure and Temperature on Asphaltene Precipitation," Paper SPE 64465, Presented at Asia Pacific Oil and Gas Conference and Exhibition, Brisbane, Australia, Oct 16-18, 2000.

Laufer, J., National Advisory Committee for Aeronautics, Technical Note, 2954, 1953.

Lax, P.D.: "Differential Equations, Difference Equations and Matrix Theory," Communications on Pure and Applied Mathematics, Vol. XI, pp. 174-194, 1958.

Lee, A.L., Gonzalez, M.H., and Eakin, B.E.: "The Viscosity of Natural Gases" Journal of Petroleum Technology, pp. 997-1000, Aug 1966.

Leontaritis, K.J. and Mansoori, G.A.: "Asphaltene Deposition: A Survey of Field Experiences and Research Approaches," J. of Pet. Sc. and Eng. 1, 229, 1988.

Lockhart, R. W. and Martinelli, R. C.: "Proposed Correlation of Data for Isothermal Two-phase, Two-Component Flow in Pipes," Chem. Eng. Prog., 45, 39, Jan 1949.

Liao J., Mei, R., and Klausner, J.F: "A Study on the Numerical Stability of the Two-Fluid Model Near Ill-posedness," International Journal of Multiphase Flow 34, pp. 1067–1087, 2008.

Li, Z. and Firoozabadi, A.: "Cubic-Plus-Association (CPA) Equation of State for Water-Containing Mixtures: Is 'Cross Association" Necessary?," AIChE J, 55(7), pp. 1803-1813, 2009.

Livescu, S., Durlofsky, L.J., and Aziz, K.: "Development and Application of a Fully-coupled Thermal Compositional Wellbore Flow Model," Paper SPE 121306, presented at the SPE Western Regional Meeting, San Jose, California, U.S.A., Mar 24-26, 2009.

Lichaa, P.M.: "Asphaltene Deposition Problem in Venezuela Crudes - Usage of Asphaltenes in Emulsion Stability" Can. Pet. Tech. J., Oil Sands, pp. 609-624, 1977.

Lin, C., S., Moulton, R., W., and Putnam, G., L.: "Mass Transfer between Solid and Fluid Streams; Mechanism and Eddy Distribution Relationships in Turbulent Flow," Ind. Eng. Chem, 45, pp. 636-640, 1953.

Lira-Galeana, C., Firoozabadi, A., and Prausnitz J.M.: "Thermodynamics of Wax Precipitin in Petroleum Mixtures," AIChE Journal, 42 (1), pp. 239-248, Jan 1996.

Lohrenz, J., Bray, B.G., and Clark, C.R.: "Calculation Viscosities of Reservoir Fluids from Their Composition," Trans., AIME, V.142, pp. 159-172, 1964.

Lyczkowski, R.W, Gidaspow, D., Solbrig, C.W., and Hughes, E.D.: "Fundamentals of Two-Phase Flow," Annual ASME Meeting, Houston, Nov. 30 – Dec. 4, 1975.

Mamun, C.K.: "Free Energy of Mixing of Cross-linked Polymer Blemds," Langmuir 21, pp. 240-250, 2005.

Mamun, C.K.: "Spatial Modulation in Cross-linked Binary Polymer Blends," Langmuir, 21, pp. 7921-7936, 2005.

Matzain, A.: "Multiphase Flow Paraffin Deposition Modeling," Ph.D. Dissertation, University of Tulsa, Tulsa, OK, 2001.

Micaelli, J.C.: "CATHARE an Advanced Best-Estimate Code for PWR Safety Analysis," SEThiLEML-EM/87-58, 1987.

Mishima, K. and Ishii, M.: "Flow Regime Transition Criteria for Upward Two-Phase Flow in Vertical Tubes," International Journal of Heat and Mass Transfer, 27, pp. 723-737, 1984.

Mukherjee, H. and Brill, J.P.: "Liquid Holdup Correlations for Inclined Two-Phase Flow," Journal of Petroleum Technology, pp. 1003-1008, May 1983.

Nancollas, G.H., White, W., Tsai, F., and Maslow, L.: "The Kinetics and Mechanism of Formation of Calcium Sulfate Scale Minerals: the Influence of Inhibitors," Corrosion, 35 (7), pp. 304-308, 1979.

Nghiem, L.X., Hassarn, M.S., and Nutakki, R.: "Efficient Modeling of Asphaltene Precipitation," SPE Paper 26642, Presented at Annual Technical Conference and Exhibition, Houston, Texas, Oct 3-6, 1993.

No, H.C. and Kazimi M.S.: "The Effect of Virtual Mass on the Characteristics and the Numerical Stability in Two-Phase Flows," MIT Energy Laboratory Report No. MIT-EL 81-023, April 1981.

Orkiszewski, J.: "Predicting Two-Phase Pressure Drops in Vertical Pipe," Journal of Petroleum Technology, pp. 829-838, Jun 1967.

Ozon, P.M., Ferschneider, G., and Chwetzoff, A.: "A New Multiphase Flow Model Predicts Pressure and Temperature Profile," Paper SPE 16535, presented at the SPE Offshore Europe Conference, Aberdeen, Scotland, Sept. 8-11, 1987.

Papavergos, P., G. and Hedly, A., B.: "Particle Deposition Behaviour from Turbulent Gas Streams," Chem. Eng. Res. Des., 62, pp. 275-295, 1984.

Parkhurst, D.L. and Appelo, C.A.J.: "Description of Input and Examples for PHREEQC Version 3--A Computer Program for Speciation, Batch-Reaction, One-Dimensional Transport, and Inverse Geochemical Calculations," U.S. Geological Survey Techniques and Methods, 2013.

Passut, C.A. and Danner, R.P.: "Correlation of Ideal Gas Enthalpy, Heat Capacity, and Entropy," Ind. Eng. Chem. Proc. Des. Development, 11, pp. 543-546, 1972.

Peaceman, D.W.: "Interpretation of Well-Block Pressure in Numerical Reservoir Simulation with Non-square Grid Blocks and Anisotropic Permeability," Journal of Petroleum Technology, pp. 531-543, Jun 1983.

Pedersen, K.S.: "Prediction of Cloud Point Temperature and Amount of Wax Precipitation," SPE Production and Facilities, pp. 46-49, Feb 1995.

Pedersen, K.S. and Christensen, P.L.: *Phase Behavior of Petroleum Reservoir Fluid*, Taylor & Francis Group, LLC, Florida, 2007.

Pedersen, K.S., and Rønningsen, H.P.: "Effect of Precipitated Wax on Viscosity A model for Predicting Non-Newtonian Viscosity of Crude Oils," Journal of Energy and Fuel, 14, pp. 43-51, 2000.

Pedersen, W.B., Hansen, A.B., Larsen, E., Nielsen, A.B., and Rønningsen, H.P.: "Wax Precipitation from North Sea Crude Oils. 2. Solid-phase Content as Function of Temperature Determined by Pulsed NMR," Journal of Energy and Fuel, 5, pp. 908-913, 1991.

Peng, D.Y. and Robinson, D.B.: "A New Two-Constant Equation of State," Industrial. and Engineering Chemical: Fundamentals, 15, pp. 59-64, 1976.

Petalas, N. and Aziz, K.: "A Mechanistic Model for Multiphase Flow in Pipes," Journal of Canadian Petroleum Technology, 39, pp. 43-55, Jun 2000.

PIPESIM.: "PIPESIM Production System Analysis Software User's Manual," Schlumberger, Version 2011.1.

Pourafshary, P.: "*A Coupled Wellbore/Reservoir Simulator to Model Multiphase Flow and Temperature Distribution*," Ph.D. Dissertation, The University of Texas at Austin, 2007.

Pourafshary, P., Varavei, A., Sepehrnoori, K., and Podio, A.L.: "A Compositional Wellbore/Reservoir Simulator to Model Multiphase Flow and Temperature Distribution," Journal of Petroleum Science and Engineering, 69, pp. 40–52, 2009.

Prosperetti, A. and Tryggvason, G.: *Computational Methods for Multiphase Flow*, Cambridge University Press, Cambridge, UK, 2007.

Qin, X.: "*Modeling Asphaltene Precipitation and Implementation of Group Contribution Equation of State into UTCOMP*," MSc Thesis, The University of Texas at Austin, 1998.

Ramastad, K., Tydal, T., Askvik, K. M., and Forland, P.: "Predicting Carbonate Scale in Oil Producers for High-Temperature Reservoirs," SPE Journal, 10 (4), pp. 363-373, 2004.

Ramey H.J., Jr.: "Wellbore Heat Transmission," J. Pet. Tech., 427; Trans., AIME, 225, Apr 1962.

Ramirez-Jaramillo, E., Lira-Galeana, C., and Manero, O.: “Modeling Asphaltene Deposition in Production Pipelines,” Journal of Energy and Fuels, 20, pp. 1184-1196, Dec 2006.

Ramshaw, J.D., and Trapp, J.A.: “Characteristics, Stability and Short Wavelength Phenomena in Two-Phase Flow Equation Systems, Nucl. Sci. Eng., Vol.66, pp.93-102, 1978.

Ransom, V.H.: “Numerical Benchmark Tests,” Multiphase Science and Technology, 3, edited by G.F. Hewitt, J.M. Delhay, and N. Zuber, Hemisphere, Washington, DC, 1987.

RELAP5-3D.: “Code Manual Volume IV: Models and Correlations,” INEEL-EXT-98-00834, Revision 4.0, June 2012.

Richtmyer, R.D. and Morton, K.W.: *Difference Methods for Initial-Value Problem*, Interscience Publishers, Inc., New York, 1967.

Rocha, A. A. , Frydman, M., da Fontoura, S. A. B., Rosario, F.F., and Bezerra, M. C. M.: “Numerical Modeling of Salt Precipitation During Produced Water Reinjection,” SPE Paper, International Symposium on Oilfield Scale, Aberdeen, United Kingdom, 30-31 Jan 2001.

Rygg, O.B., Rydahl, A.K., and Rønningsen, H.P.: “Wax Deposition in Offshore Pipeline Systems,” Proc. 1st North American Conference on Multiphase Technology, Banff, Canada, Jun 1998.

Sandler, S.I.: “*Models for Thermodynamic and Phase Equilibrium Calculations*,” Chemical Industries, v. 52. New York, Dekker, 1999.

Scotti, R. and Montanari, L.: “Molecular Structure and Intermolecular Interaction of Asphaltenes by FT-IR, NMR,” in Structure and Dynamics of Asphaltenes, Plenum Press, New York, 1998.

Shi, H., Homes, J.A., durlofsky, L.J., Aziz, K., Diaz, L.R., Alkaya, B., and Oddie, G.: “Drift-Flux modeling of Two-Phase Flow in Wellbores,” SPE Journal 10 (1): 24-33, 2005a.

Shirdel, M.: “*Development of Coupled Wellbore-Reservoir Compositional Simulator for Horizontal Wells*,” MSc Thesis, The University of Texas at Austin, 2010.

Shirdel, M. and Sepehrnoori, K.: “Development of a Transient Mechanistic Two-Phase Flow Model for Wellbores,” SPE Journal, 17(3), pp. 942-955, Sep 2012.

Shoham, O.: *Mechanistic Modeling of Gas-Liquid Two-phase Flow in Pipes*, Society of Petroleum Engineering, 2005.

Singh, P.: "Gel Deposition on Cold Surfaces," U. of Michigan, Ann Arbor, Michigan, 2000.

Standing, M.B.: "A Pressure-Volume-Temperature Correlation for Mixtures of California Oils and Gases," Drill. and Prod. Prac, API, 1947.

Stone, T.W., Edmund, N.R., and Kristoff, B.J.: "A Comprehensive Wellbore/Reservoir Simulator," Paper SPE 18419, presented at the SPE Reservoir Simulation Symposium, Houston, Texas, U.S.A., Feb. 6-8, 1989.

Sorbie, K.S. and Laing N.: "How scale Inhibitors Work: Mechanism of Selected Barium Sulfate Scale Inhibitors across a Wild Range of Temperatures," Paper SPE 87470, Presented at the International Symposium on Oilfield Scale, Aberdeen, May 26-27, 2004.

Song, J.H. and Ishii, M.: "The Well-posedness of Incompressible One-Dimensional Two-Fluid Model. Int. J. Heat Mass Transf. 43, pp. 2221–2231, 2000.

Taitel, Y. and Dukler, A.E.: "A Model for Predicting Flow Regime Transition in Horizontal and Near Horizontal Gas-Liquid Flow," AIChE Journal, 22, pp. 47-57, 1976.

Taitel, Y., Barnea, D., and Dukler, A.E.: "Modeling Multi-Pattern Transitions for Steady Upward Gas-Liquid Flow in Vertical Tubes," AIChE Journal, 26, pp. 345-354, 1980.

Tomson, M., Fan, C., Lu, H., Alsaiari, H., Kan, A.T.: "Integration of Kinetics into Scale Prediction Software, ScaleSoftPitzer," SPE Paper 121681, Presented at International Symposium on Oilfield Chemistry, The Woodland, Texas, USA, Apr 20-22, 2009.

Trbovich, M.G. and King, G.E.: "Asphaltene Deposit Removal: Long-Lasting Treatment with a Co-Solvent," Paper SPE 21038, Presented Int. Symp. On Oilfield Chemistry, Anaheim, Feb. 20-22, 1991.

Tuttle, R.N.: "High Pour-Point and Asphaltic Crude Oils in Condensates," J. Pet. Tech., pp. 1192-1196, June 1983.

UTCOMP: "*Technical Documentation for UTCOMP 3.8*," Reservoir Engineering Research Program, Center for Petroleum and Geosystems Engineering, The University of Texas at Austin, 2003.

Vargas, F.M.: "*Modeling Asphaltene Precipitation and Arterial Deposition*," Ph.D. Dissertation, Rice University, 2009.

Vasquez, M., and Beggs, H. D.: "Correlations for Fluid Physical Property Prediction," Paper SPE 6719, Presented at the 52nd Annual Technical Conference and Exhibition of the Society of Petroleum Engineers, Denver, Colorado, 1977.

Venkatesan, R.: "The Deposition and Rheology of Organic Gels," U. of Michigan, Ann Arbor, Michigan, 2004.

Victorov, A.I. and Firoozabadi, A.: "Thermodynamics of Asphaltene Precipitation in Petroleum Fluids by a Micellization Model," AIChE J., 42, 1753, 1996.

von Karman, T.: Transaction, American Society of Mechanical Engineering, 61, 705, 1935.

Xiao, J.J., Shoham, O., and Brill, J.P.: "A Comprehensive Mechanistic Model for Two-phase Flow in Pipelines," Paper SPE 20631, Presented at SPE Annual Technical Conference and Exhibition, New Orleans, LA, Sep 23-26, 1990.

Waples, D.W. and Waples, J.S.: "A review and Evaluation of Specific Heat Capacities of Rocks, Minerals, and Subsurface Fluids. Part 2: Fluids and Porous Rocks," Natural Resources Research, 13l, 2, pp. 123-130, Jun 2004.

Wang, P., Balay, S., Sepehrnoori, K., Wheeler, J., Abate, J., Smith, B., and Pope, G.: "A Fully Implicit Parallel EOS Compositional Simulator for Large Scale Reservoir Simulation," Paper SPE 51885, SPE Reservoir Simulation Symposium, Houston, Texas, U.S.A, Feb 14-17, 1999.

Wang, S., and Civan, F.: "Productivity Decline of Vertical and Horizontal Wells by Asphaltene Deposition in Petroleum Reservoirs," Paper SPE 64991, Presented at the International Symposium on Oilfield Chemistry, Houston, Texas, Feb 13-16, 2001.

Watkinson, P. and Epstein, N.: "Particulate Fouling of Sensible heat Exchangers," Presented at the Fourth International Heat Transfer Conference, Versailles, France, 1970.

Winterfeld, P.H.: "Simulation of Pressure Buildup in a Multiphase Wellbore Reservoir System," SPE Formation Evaluation Journal, 4, 2, pp. 247-252, Jun 1989.

Won, K.W.: "Continuous Thermodynamics for Solid-Liquid Equilibria: Wax Formation from Heavy Hydrocarbon Mixtures," Fluid Phase Equilibria, 30, pp. 265-279, 1986.

Yuan, M. and Zhou, D.: "Evaluation of Two-phase Flow Correlation and Mechanistic Models for Pipelines at Horizontal and Inclined Upward Flow," Paper SPE 101929, SPE Production and Operation Symposium, Oklahoma city, Oklahoma, U.S.A., Apr 4-8, 2009.

Yuan, M. D. and Todd, A. C.: "Prediction of Sulfate Scaling Tendency in Oilfield Operations," SPE Paper 18484, pp. 63-72, 1991.

Vita

Mahdy Shirdel was born in 1984, in Tehran, Iran. He received two B.Sc. degrees: Mechanical Engineering and Petroleum Engineering, from Sharif University of Technology in 2007. Subsequently, he joined the Department of Petroleum and Geosystems Engineering of The University of Texas at Austin in fall 2007 and earned his M.S.E degree in December 2010 under the supervision of Dr. Kamy Sepehrnoori. Mahdy's research interest include reservoir simulation, thermal and compositional, wellbore modeling, thermodynamics and geochemistry.

Permanent address: 2501 Lake Austin Blvd Apt A107, Austin, Texas, 78703

This dissertation was typed by the author.